Organic Carbon in Hydrothermal Systems: From Phototrophy to Aldehyde Transformations

by

Kristopher Michael Fecteau

A Dissertation Presented in Partial Fulfillment
of the Requirements for the Degree
Doctor of Philosophy

Approved October 2016 by the
Graduate Supervisory Committee:

Everett L. Shock, Chair
Ian R. Gould
Hilairy E. Hartnett

ARIZONA STATE UNIVERSITY

December 2016

ABSTRACT

Hydrothermal environments are important locales for carbon cycling on Earth and elsewhere in the Universe. Below its maximum temperature (~73 °C), microbial photosynthesis drives primary productivity in terrestrial hydrothermal ecosystems, which is thought to be performed by bacterial phototrophs in alkaline systems and eukaryotic algae in acidic systems, yet has received little attention at pH values intermediate to these extremes. Sequencing of 16S and 18S rRNA genes was performed at 12 hot springs with pH values 2.9-5.6 and revealed that cyanobacteria affiliated with the genus *Chlorogloeopsis* and algae of the order *Cyanidiales* coexisted at 10 of the sites. Cyanobacteria were present at pH values as low as 2.9, which challenges the paradigm of cyanobacteria being excluded below pH 4. Presence of the carotenoid β-cryptoxanthin in only 2 sites and quantitative PCR data suggest that algae were inactive at many of the sites when sampled. Spatial, but perhaps not temporal, overlap in the habitat ranges of bacterial and eukaryal microbial phototrophs indicates that the notion of a sharp transition between these lineages with respect to pH is untenable.

In sedimentary basins, biosphere-derived organic carbon is subjected to abiotic transformations under hydrothermal conditions. Benzaldehyde was experimentally evaluated as a model to assess the chemistry of aldehydes under these conditions. It was first demonstrated that gold, a traditional vessel material for hydrothermal experiments, caused catalysis of benzaldehyde degradation. Experiments in silica tubes were performed at 250, 300, and 350 °C yielding time-dependent data at several starting concentrations, which confirmed second-order kinetics. Therefore, disproportionation was expected as a major reaction pathway, but unequal yields of benzoic acid and benzyl alcohol were

inconsistent with that mechanism. Consideration of other products led to development of a putative reaction scheme and the time dependencies of these products were subjected to kinetic modeling. The model was able to reproduce the observed yields of benzoic acid and benzyl alcohol, indicating that secondary reactions were responsible for the observed ratios of these products. Aldehyde disproportionation could be an unappreciated step in the formation of carboxylic acids, which along with hydrocarbons are the most common organic compounds present in natural systems.

This dissertation is dedicated to my parents, Karen and Timothy. Without you, I would not have been able to take the path that has led me to this point. This dissertation is yours as well.

ACKNOWLEDGMENTS

Many people have contributed to not only the results presented herein, but also my personal and professional development. First, my undergraduate education was guided by my academic advisors in biology, Professor Theresa Theodose, and in chemistry, Professor Henry Tracy. Both ensured I obtained strong, broad training in both of these important fields, and collectively, though perhaps unintentionally, fostered my interdisciplinary philosophy that I was able to pursue in this dissertation. As my first research mentor, Professor Tracy also offered a venue for me to not only succeed, but more importantly to fail and learn from my mistakes, and in doing so, taught me how research is really done.

In addition to the many individuals who contributed results for the following projects who are acknowledged in the following chapters, several warrant additional recognition. My thesis advisor, Everett Shock, shares most significantly in this work and I will forever be grateful for his countless hours writing proposals to make these great projects possible, for showing me Yellowstone National Park and its intriguing complexities, for his unique perspective on the interdisciplinary questions tackled in this work, and for his wisdom, scientific and otherwise. Ian Gould served ably and faithfully to help anchor my work in physical organic chemistry and made the results truly interdisciplinary. Hilairy Hartnett graciously welcomed me into her lab for use of her muffle furnace and LC-MS instrument, both of which were essential to this work. Professor Eric Boyd of Montana State University is a collaborator in the truest sense who made the Yellowstone results possible and I am deeply indebted for the many trips to his laboratory to accomplish research that would not otherwise be possible and for many hours spent discussing science.

I deeply appreciate members of GEOPIG, both past and present, who have influenced me during my time at ASU, especially Grayson Boyer, Peter Canovas, Alysia Cox, Randall Debes, Jeff Dick, Christopher Glein, Jeff Havig, Alta Howells, Kristin Johnson, Jordan Okie, Apar Prasad, Panjai Prapaipong, Kirtland Robinson, Brian St. Clair, and Ziming Yang. I similarly must thank members of other labs, including Bennett Addison, Christiana Bockisch, Jesse Coe, Steve Davidowski, Sarah Frey, Alex Hamilton, Aurelie Marcotte, Rumit Maini, Adam Monroe, Katie Noonan, Josh Nye, Amisha Poret-Peterson, Ryan Schmaltz, Meg Schmierer, Jessie Shipp, Brian Woodrum, Jinwei Zhang, and Natasha Zolotova for their assistance and support. Professors Ariel Anbar, Pierre Herckes, Robert Marzke, Kevin Redding, and Wim Vermaas also contributed to my graduate career both directly and indirectly. I must also thank Tom Hand for mentoring me over the years in ion chromatography and teaching me so much on that subject.

I must acknowledge my colleague and roommate of 5 years, Dr. Trevor Bozeman, for his support and assistance in ways too numerous to describe, both during our years as undergraduates and at ASU. Finally, I must thank my family, including my parents, Karen and Tim, my sisters, Nicole and Jen, my niece, Lily, my late grandparents, Robert, Helen, Warren, and Dolores, and many uncles, aunts, and cousins for your years of love and support along this journey.

TABLE OF CONTENTS

Page

CHAPTER Page

CHAPTER Page

LIST OF TABLES

LIST OF FIGURES

Figure Page

Figure Page

I. INTRODUCTION

Water is an ubiquitous chemical compound on Earth and is essential for life. When heated, liquid water exhibits properties quite different from those encountered at the ambient surface conditions that are most familiar. Heated water leads to hydrothermal conditions, which for the purposes of this dissertation shall be broadly defined as any system containing water heated in excess of ambient conditions. Natural hydrothermal environments, heated geothermally via heat flow from the mantle, exist at Earth's surface in both terrestrial and marine settings, creating conditions conducive to highly specialized microbial life known as thermophiles. Thermophiles have evolved biochemically to cope with the physical stresses of high temperatures and have temperature optima well above ambient conditions. Numerous examples of thermophilic microbial communities exist in the thermal features of Yellowstone National Park (YNP; Wyoming, USA) which exceed 12,000 in number (Nordstrom *et al.*, 2005). In addition to temperature, the chemical nature of hot water is relevant to microbes. For example, neutral pH at the boiling point for the elevation of YNP (~93 °C) is ~6.2 due to the greater dissociation of water at elevated temperatures, meaning that the commonly encountered hot springs with pH values of 7-8 are actually somewhat alkaline rather than neutral.

As water is heated further, conditions are eventually reached that are inconducive to life. Such temperatures (> ~150 °C) are reached in sedimentary basins and other subsurface environments on Earth. Though life is excluded, these hydrothermal conditions have profound effects on the cycling of organic carbon derived from the biosphere. While the elevated temperatures facilitate dramatically enhanced kinetics when compared with ambient conditions, the properties of water also have important consequences. In addition

to the aforementioned decrease in neutral pH, which reaches a minimum of ~5.6 around 250 °C, the dielectric constant decreases rapidly as temperature increases. For example, at 250 °C the dielectric constant is ~30 (Akiya and Savage, 2002), giving it solvent properties comparable to ethanol at room temperature. Additionally, hydrogen bonding is less prevalent at higher temperatures (Kruse and Dinjus, 2007). Thus, water is a more robust solvent for organic compounds at elevated temperatures and may also facilitate acid/base chemistry due to the higher activities of hydronium and hydroxide ions.

The effects of water on organic compounds under hydrothermal conditions are profound. Numerous reactions of organic compounds have been observed in hot water ((Kuhlmann *et al.*, 1994; Katritzky *et al.*, 1996; An *et al.*, 1997; Savage, 1999; Katritzky *et al.*, 2001), yet much remains to be done in order to gain kinetic and mechanistic understanding of these reactions. This reactivity has implications for the formation and evolution of petroleum and other fossil fuels, as well as for the alteration of biomass for biofuel production (Kruse and Dahmen, 2015). Hydrothermal conditions may also facilitate abiotic synthesis of organic compounds from inorganic precursors (Shock and Schulte, 1998; McCollom and Seewald, 2007), which may support subsurface microbial ecosystems.

This dissertation tackles several disparate questions regarding organic carbon under hydrothermal conditions. First, the transition in primary production via microbial photosynthesis between eukaryotes and bacteria is examined in mildly acidic hot springs in YNP. Second, catalysis of benzaldehyde reactions by gold in hydrothermal organic experiments is demonstrated, contradictory to conventional wisdom that gold offers an inert surface for such experiments. Lastly, a thorough investigation of the hydrothermal

chemistry of aldehydes is described, using benzaldehyde as a model compound, with discussion of implications for transformations of organic carbon in natural systems.

1.1 Phototrophy in Mildly Acidic Hot Springs

Phototrophy in hot spring habitats is traditionally thought to be performed by bacterial phototrophs in alkaline systems and by eukaryotic algae in acidic systems, yet has received little attention at pH values intermediate to these extremes. Sequencing of 16S and 18S rRNA genes was performed at 12 hot springs in Yellowstone National Park (Wyoming, USA) with pH values ranging from 2.9 to 5.6 and revealed that cyanobacteria affiliated with the genus *Chlorogloeopsis* and algae of the order *Cyanidiales* (phylum Rhodophyta) coexisted in 10 of the sites. Cyanobacteria were present as low as pH 2.9, which challenges the paradigm of cyanobacteria being excluded below pH 4. Sequences associated with *Chloracidobacterium thermophilum*, an anoxygenic phototroph, were also observed at 2 of the sites. The carotenoid β-cryptoxanthin, a biosynthetic intermediate, was only found in the pigment extracts from 2 sites, suggesting *Cyanidiales* were only active in those sites when sampled. Chlorophyll degradation products were identified at all sites; no intact chlorophyll *a* was observed in 2 of the samples, which also did not exhibit light-driven carbon fixation at the time of sampling. Quantitative PCR analyses confirmed that cyanobacteria were more abundant than *Cyanidiales* by up to 3 orders of magnitude, with algae only approaching cyanobacteria in abundance at the most acidic sites. Collectively, these observations show that many of the algal sequences represent populations that were no longer active.

Geochemically, these hot spring fluids are derived from hydrothermal vapor and meteoric water and are therefore dilute and weakly buffered. Variability in the supply of

meteoric water likely contributes to dynamic conditions at these sites, leading to transitions in the phototrophic communities. Spatial, but perhaps not temporal, overlap in the habitat ranges of bacterial and eukaryal microbial phototrophs indicates that the notion of a sharp transition between these lineages with respect to pH is untenable.

1.2 Catalysis of the Cannizzaro Reaction by Bulk Gold

Though traditionally base-catalyzed, the Cannizzaro reaction of benzaldehyde was shown to be catalyzed by bulk gold in superheated water. At 200 °C for ~48 hours, 0.1 molal solutions of benzaldehyde exhibited conversions that depended linearly on the amount of gold present at low amounts of gold, but this trend reversed at the highest gold loadings. Ratios of benzoic acid to benzyl alcohol greatly exceeded unity, increasing with increasing amounts of gold. These observations were attributed to the reactivity of benzyl alcohol in the presence of gold, which was proposed to react via cross-disproportionation with benzaldehyde to yield toluene and benzoic acid, transitioning to benzyl alcohol disproportionation resulting in toluene and the reformation of benzaldehyde at higher gold loadings. Benzene was also formed via gold-catalyzed decarbonylation of benzaldehyde. Turnover frequencies for both benzaldehyde (0.00013 s^{-1}) and benzyl alcohol (0.0011 s^{-1}) were quite low and attributed to coagulation of the gold powder under the experimental conditions. The concentration dependence of the yields of the major products indicated aqueous benzaldehyde is involved at the rate-determining step. The gold-catalyzed reactivity of organic compounds at conditions typical of hydrothermal experiments implies that gold may not always be the most inert choice as an experimental vessel.

1.3 Kinetics and Chemistry of Aldehydes under Hydrothermal Conditions

Aldehydes represent an intermediate redox state of organic carbon and may be the precursors to carboxylic acids, which together with hydrocarbons are the most common organic compounds in natural systems. A model aldehyde, benzaldehyde, was subjected to hydrothermal experiments (250-350 °C, saturation pressure) in clear fused quartz (CFQ) autoclaves to assess the kinetics and mechanisms of the reactions leading to carboxylic acids. The concentration dependence unequivocally demonstrates the kinetics are second-order in benzaldehyde, consistent with the putative disproportionation reaction of benzaldehyde, which is reminiscent of the base-catalyzed Cannizzaro reaction known at lower temperatures. Arrhenius parameters for these rate constants trend well with published values for the reaction under supercritical conditions from one study (Tsao *et al.*, 1992) though the activation energy is larger in the supercritical region. However, the pre-exponential factor is approximately 4 orders of magnitude smaller than that derived from another study under supercritical conditions (Ikushima *et al.*, 2001). Additionally, fitting the rate constants from this study with the Eyring equation yields an entropy of activation ($\Delta S^{\ddagger}$) of -178 J mol^{-1} K^{-1}, which is consistent with a bimolecular transition state at the rate-limiting step. In contrast, the rates of Ikushima *et al.* (2001) yield a positive value of $\Delta S^{\ddagger}$, which is inconsistent with the putative mechanism for the reaction. The change in activation energy near the critical point for the decomposition of benzaldehyde indicates that experimentally derived rates in subcritical, not supercritical, conditions should be used for extrapolation to conditions where diagenesis, alteration, metamorphism, and other hydrothermal processes of interest occur in natural systems.

An experiment with benzaldehyde-carbonyl-^{13}C analyzed by ^{13}C-NMR demonstrated the production of benzyl alcohol, benzoic acid, and carbon dioxide, though the yields of benzoic acid and benzyl alcohol were not equal, as expected for the disproportionation reaction. It was therefore necessary to consider secondary reactions that would lead to unequal yields of benzyl alcohol and benzoic acid. Benzene and carbon dioxide are primarily produced via decarboxylation of benzoic acid, the rates of which were measured in separate experiments at 300 °C and 350 °C. Benzyl alcohol undergoes facile dehydration to yield the stable benzyl cation, which acts as an effective electrophile in electrophilic aromatic substitution reactions. These and other pathways invoked from the product suites of the experiments were developed into a plausible reaction scheme and their time dependencies were subjected to kinetic modeling. The kinetic model was able to reproduce the observed yields of benzyl alcohol and benzoic acid, indicating that disproportionation and subsequent secondary reactions were able to explain the observed product yields. Experiments at different starting pH values demonstrated that while the reaction can be catalyzed by hydroxide, as traditionally understood, at lower pH water serves as the nucleophile for hydrate formation, which then donates hydride to another benzaldehyde molecule in the rate-limiting step. It is expected that most aldehydes are able to undergo disproportionation, and if present in natural systems, could be the precursor to carboxylic acids. The formation of aldehydes from an alkane requires oxidation of a primary alcohol, which would arise via *anti*-Markovnikov hydration of the corresponding alkene. Though this pathway is less favorable than Markovnikov hydration, which leads to a ketone, on geologic time scales it could be a viable pathway toward metastable carboxylic acids.

II. PHOTOTROPHY IN MILDLY ACIDIC HOT SPRINGS: WHERE BACTERIAL AND EUKARYOTIC PHOTOTROPHS MEET AT THE LIMITS OF PHOTOSYNTHESIS

2.1 Introduction

Microbial photosynthesis is a major contributor to primary production in many aquatic environments. To date, photosynthesis is found in two of the three domains of life, occurring in the bacteria and eukarya while being absent in the archaea (Blankenship, 2014). In aquatic systems, microbial phototrophs from both domains commonly exist together in the same habitat. For example, diatoms often occur together with *Prochlorococcus* and *Synechococcus* cyanobacteria in oligotrophic ocean regions (Biller *et al.*, 2015). In contrast, terrestrial hot springs are environments that span both temperatures and chemical conditions, such as pH, that cross the boundaries of the habitat ranges for specific groups of phototrophs. The distribution of hot springs with respect to pH exhibits a bimodal distribution (Figure 1), which has been demonstrated in Yellowstone National Park (YNP) and elsewhere (Brock, 1971; Brock, 1978; Nordstrom *et al.*, 2009; Amenabar *et al.*, 2015). This distribution is a consequence of two prevailing buffering systems, with alkaline hot springs being bicarbonate buffered and acidic systems being sulfuric acid buffered.

Recent efforts to catalog the distribution of phototrophic microbes with respect to extremes of physical and chemical conditions in YNP hot spring habitats have confirmed an upper temperature limit for phototrophy near 73 °C that is reached in alkaline environments, while acidic environments exhibit lower temperature maxima (Boyd *et al.*, 2010; Cox *et al.*, 2011; Boyd *et al.*, 2012; Hamilton *et al.*, 2012). The upper temperature

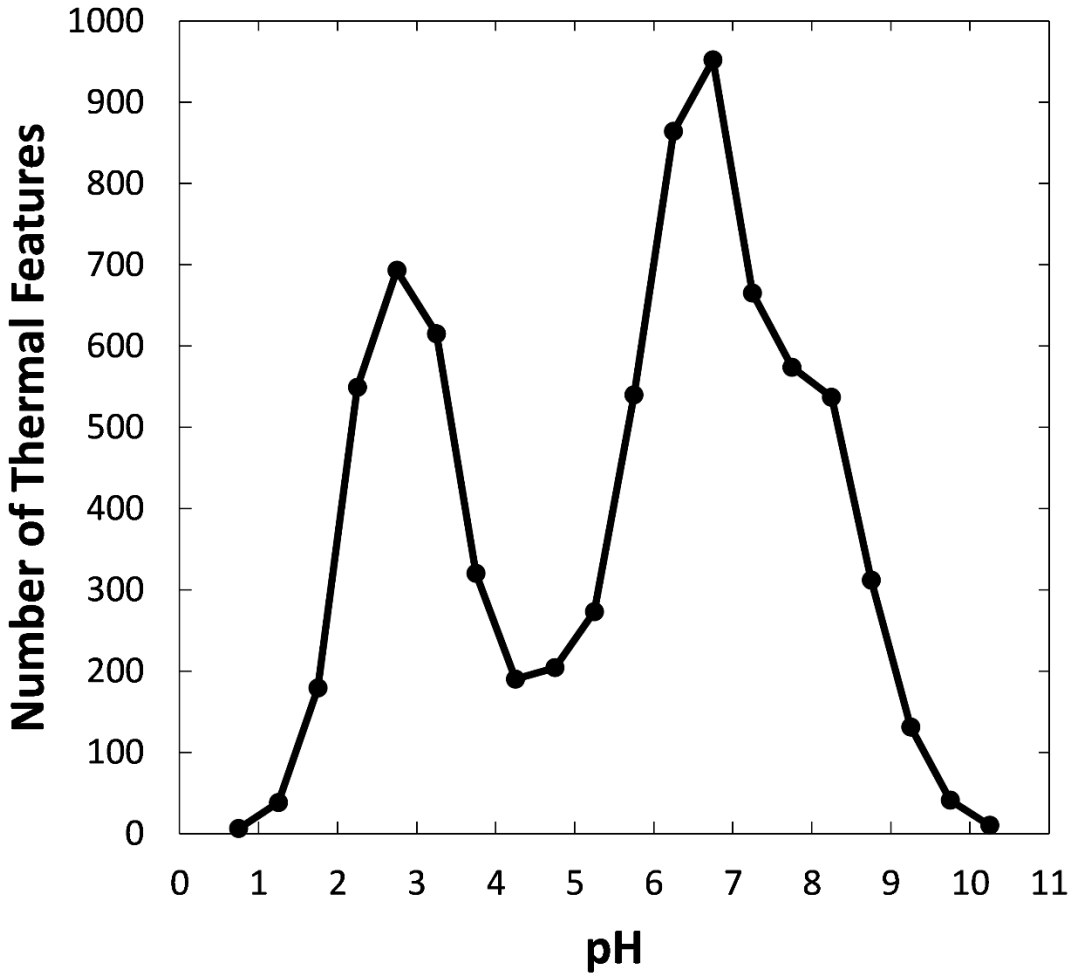

Figure 1. Abundance of thermal features in Yellowstone National Park with respect to their pH values. Data were obtained from an extensive survey of Yellowstone hot springs (www.rcn.montana.edu). Springs are binned every 0.5 pH units and plotted at the midpoint of each pH interval.

limit in alkaline locations is reached only by certain strains of cyanobacteria of the genus *Synechococcus* (Brock, 1967; Brock and Brock, 1968; Brock, 1978). Isolates from alkaline mats in Yellowstone exhibit several phylotypes, each with highly specialized temperature niches (Allewalt *et al.*, 2006). At cooler temperatures that are typically encountered further downstream in outflow channels of alkaline hot springs, a variety of other bacterial phototrophs flourish. These include other cyanobacteria such as *Mastigocladus laminosus* (Miller *et al.*, 2006; Miller *et al.*, 2009) and green non-sulfur bacteria such as *Chloroflexus auranticus* (Pierson and Castenholz, 1974; Brock, 1978) and *Roseiflexus* sp. (Boomer *et al.* 2002), which is more abundant than *C. auranticus* in molecular surveys of these communities (van der Meer *et al.*, 2010). A preponderance of evidence suggests that anoxygenic bacteria grow photomixotrophically in these systems, inhabiting mat layers beneath a thin top layer of cyanobacteria and utilizing light wavelengths in the near-infrared not used by oxygenic phototrophs (Bauld and Brock, 1973; Brock, 1978; van der Meer *et al.*, 2005; Klatt *et al.*, 2007; Klatt *et al.*, 2013). Alkaline springs with high sulfide concentrations have been described that harbor populations of anoxygenic phototrophs able to employ sulfide as an electron donor, such as *Thermochromatium tepidum* (Madigan, 1984; Madigan, 1986).

In contrast to alkaline systems, phototrophic communities in acidic environments are dominated by eukaryal phototrophs. Doemel and Brock surveyed these systems extensively and concluded that one species of red algae (phylum Rhodophyta), *Cyanidium caldarium*, was the only phototroph present above 40 °C at locations below pH 4 (Doemel, 1970; Doemel and Brock, 1970; Doemel and Brock, 1971; Brock, 1978). This conclusion is based on the absence of other algae growing above ~40 °C, together with observations

of an apparent lack of cyanobacteria below pH 4 in both thermal and non-thermal environments (Brock, 1973). Below ~40 °C a variety of other algae are commonly present, including *Chlorella*, *Chlamydamonas*, *Euglena*, and diatoms (Doemel and Brock, 1971). With the advent of molecular biology and its application to microbial ecology, it became clear the organism studied by Doemel and Brock in Yellowstone aquatic environments was *Cyanidioschyzon merolae* of the order *Cyanidiales* within the phylum Rhodophyta (Toplin *et al.*, 2008), which is the only species of these algae found in aquatic environments (Skorupa *et al.*, 2013). The upper temperature limit for these algae, and thus for phototrophs in general in acidic conditions, is 56 °C (Doemel and Brock, 1970).

This dichotomous view of microbial phototrophs in hydrothermal environments, that algae dominate in acidic features and cyanobacteria dominate in circumneutral and alkaline features, has been left largely untested in the half-century since the observations of Brock and colleagues. Cyanobacteria have been observed under mildly acidic, thermal conditions as low as pH 4 (Brock, 1973), while *Cyanidiales* isolates from Yellowstone can grow at pH values approaching 5, above which no growth is observed (Doemel and Brock, 1971). Based on these observations, the habitat ranges for algae and cyanobacteria in thermal environments overlap with respect to pH. Indeed, Brock observed both cyanobacteria and algae present between pH 4 and 5 in the mixing zone created when the effluent from alkaline springs meets the acidic Obsidian Creek in Yellowstone (Brock, 1973; Brock, 1978). Nevertheless, studies to date have not yielded adequate data to further investigate the potential coexistence of algal and cyanobacterial photosynthesis in thermal environments, in spite of including some sample locations within the pH range 4-5. While Doemel (1970) noted cyanobacteria in locations where *Cyanidiales* were absent based on

microscopic observation, it is quite possible cyanobacteria could go unnoticed, especially at sites where algae were identified. Later studies focusing on *Cyanidiales* relied on sequencing of 18S rRNA and *rbcL* genes of cultures (Toplin *et al.*, 2008) or amplified and sequenced *rbcL* genes from natural samples using *Cyanidiales*-specific primers (Skorupa *et al.*, 2013). Cyanobacteria present in the natural system likely would not be enriched for in culture at the pH used (2.0) and amplification of cyanobacterial *rbcL* genes was not reported. Hamilton *et al.* (2012) examined the habitat range of phototrophs, yet the gene they employed, *chlL*, is not present in *C. merolae*, thus they were not able to determine the distribution and abundance of *Cyanidiales* and observations of algae were limited to members of the order *Bangiales* in several acidic locations below 40 °C. Recently, several studies have examined the composition of phototrophic communities in Yellowstone hot springs using metagenomic techniques or amplification of ribosomal genes using universal primers, but these studies did not examine any locations below pH 6.2, nor did they investigate eukarya (Ross *et al.*, 2012; Swingley *et al.*, 2012; Klatt *et al.*, 2013).

Observations of algae and cyanobacteria at temperatures above 40 °C reported in the literature are depicted in pH and temperature space in Figure 2. It is evident that separate observations of algae and cyanobacteria have been made between pH 4 and 5, yet the data in this pH range is sparse. This paucity of data is exacerbated by the rarity of thermal features within this pH range, as illustrated in Figure 1. This study targets Yellowstone hot springs with a pH range from approximately 3 to 6 with temperatures conducive to photosynthesis, indicated in Figure 2. Sequencing of 16S and 18S ribosomal RNA genes (targeting bacteria and eukarya, respectively) is integrated with pigment and geochemical analyses in order to characterize the composition of phototrophic microbial

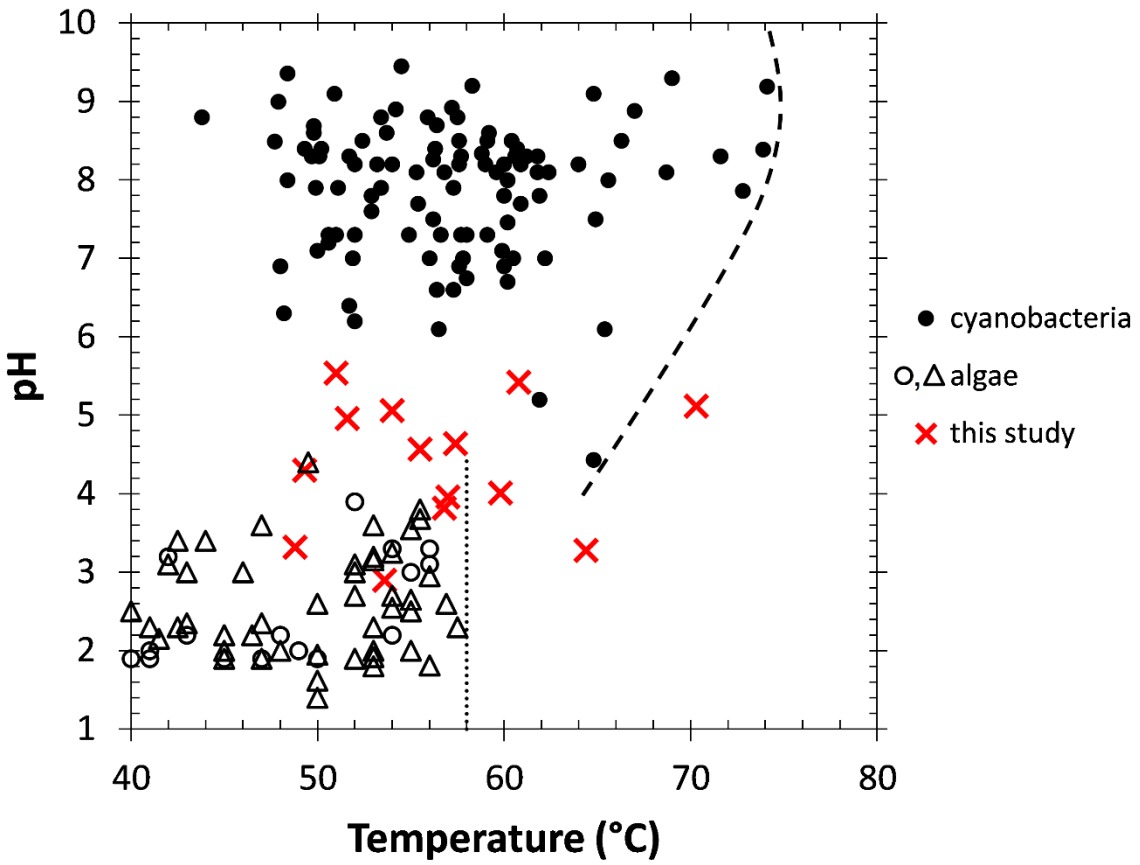

Figure 2. Literature observations of cyanobacteria (filled circles) and algae (open symbols) in thermal aquatic locations with respect to in situ temperature and pH. For algae, circles indicate sequencing-based confirmation of algae while triangles indicate confirmation via microscopy or culturing; all cyanobacteria data are from sequencing. Data are derived from: Doemel, 1970; Brock, 1973; Papke *et al.*, 2003; Toplin *et al.*, 2008; Boomer *et al.*, 2009; Meyer-Dombard *et al.*, 2011; Hamilton *et al.*, 2012; Loiacono *et al.*, 2012; Klatt *et al.*, 2013; Schubotz *et al.*, 2013; Skorupa *et al.*, 2013. Red crosses denote samples from this study. Empirical 'fringe' curves for cyanobacteria (heavy dashes) and algae (light dashes) are drawn to encompass the data. The cyanobacteria curve is not extended below pH 4 due to lack of evidence for cyanobacteria below this pH in thermal environments. The algae fringe is drawn as a line and not extended above pH 4.5 because of the lack of data for algae in thermal environments above this pH. In cases where multiple observations were made of the same system, such as in outflow channels, only the highest temperature observation is plotted. Similarly, the highest temperature is plotted when a temperature range is reported for a particular sample location.

communities where the habitat ranges of phototrophs from each domain overlap and their geochemical setting. Several sites below pH 4 were also included to further examine the transition from putatively algae-only phototrophic systems to those also containing cyanobacteria, as there is a growing body of observations of cyanobacteria in acidic, low temperature environments (Steinberg *et al.*, 1998; Hamilton *et al.*, 2012; Hao *et al.*, 2012; Urbieta *et al.*, 2015) that challenge the paradigm of cyanobacteria being excluded below pH 4 (Brock, 1973). This study aims to determine under what, if any, conditions both thermophilic cyanobacteria and algae coexist, which is a fundamental issue with respect to the habitat range of phototrophs that has been nearly completely unaddressed. The geochemical processes yielding environments of intermediate pH may have facilitated niche differentiation between these two lineages of phototrophs at the edges of their habitat ranges, or competition may prevail, as both cyanobacteria and algae fulfil the same niche metabolically via the same biochemical pathways. This ecological question undoubtedly has evolutionary implications, and could lead to novel insights into the endosymbiotic evolution of algae from a cyanobacterial precursor, an event that could have occurred in a thermal environment where cyanobacteria and a non-phototrophic eukaryote coexisted.

2.2 Materials and Methods

2.2.1 Field Sites and Sample Collection

The sample sites in this study are located within the Midway Geyser Basin and southern portion of the Lower Geyser Basin of YNP. Though these areas are known to harbor primarily alkaline features, several springs have been observed to have pH values within the range of interest here (~3-6) and many of these appear to support phototrophic communities. Specifically, several pools were sampled adjacent to Imperial and Spray

Geysers in the southwest portion of Lower Geyser Basin, as well as many features in the area of Rabbit Creek within Midway Geyser Basin between July 2011 and July 2012. In total, 12 sites were studied; two locations were sampled in both years to begin to evaluate temporal variability. GPS coordinates and sampling dates for each site are reported in Table 1.

Samples for DNA, pigment, and elemental analysis were collected with sterilized spatulas or forceps, placed in sterile specimen containers and then aliquoted to cryovials and immediately frozen in the field by storing them in insulated containers with dry ice. Samples designated for DNA extraction contained 0.8 mL of sucrose lysis buffer (Mitchell and Takacs-Vesbach, 2008). Upon return from the field each day, DNA and pigment samples were transferred to dry shippers charged with liquid nitrogen (approximate temperature, -150 °C) and transferred to a -80 °C freezer upon return to the laboratory for storage until sample processing. Samples for elemental analysis were stored at -20 °C at the end of each sampling day and maintained at that temperature until analysis.

Water sampling and field measurements were conducted as closely as possible to the site of biological sampling and were typically performed immediately prior to collection of samples for DNA, pigments, and elemental analysis. Measurements of pH were performed with a WTW pH meter (model 3300i or 3110) and temperature-compensated WTW probes constructed with a gel electrolyte that are calibrated daily at ambient temperature with buffered pH solutions. Specific conductivity (i.e., conductivity normalized to 25 °C) and temperature were measured using a YSI model 30 meter. Dissolved oxygen and total dissolved sulfide were determined colorimetrically (HRDO and methylene blue methods, respectively) in the field using Hach 2400 or 2800 portable

Table 1. Sample dates, locations, charge balance results, conductivities, and water isotopes

	Sample ID[a]	Easting[b]	Northing	Field pH	Corrected pH[c]	% charge imbalance	Specific Conductivity (µS/cm)	$\delta^{18}O$ vs. VSMOW (‰)	$\delta^{2}H$ vs. VSMOW (‰)
FF1	120720KF	513469	4929044	3.30	3.28	-1.25	462	-4.8	-108.3
IG1	110918R	509797	4930939	3.78	3.96	2.92	365	-8.5	-123.2
IG2	120722TE	509794	4930931	3.13	3.32	13.5	606	-5.4	-111.0
IG3	120722TK	510064	4930948	3.26	2.91	-12.7	914	-14.1	-127.4
RN1-2011	110708C	515110	4929721	3.94	4.64	22.1	69.5	-14.9	-137.7
RN1-2012	120718TJ	515110	4929721	4.91	5.10	1.45	96.7	-15.3	-138.2
RN2	110708D	515110	4929727	4.64	4.57	-0.892	59.0	-12.7	-133.2
RN3	120718TL	515045	4929810	4.43	4.01	-4.17	351.8	-11.7	-131.0
RS1	120713TI	515138	4928593	4.80	5.07	2.99	274.4	-9.1	-124.0
RS2	120713TL	515125	4928566	4.50	4.30	-2.55	171.4	-9.3	-123.4
RS3	110710Y	515146	4928521	4.87	5.43	9.25	155.3	-12.9	-127.8
RS4	110710D	515145	4928523	4.24	5.54	39.9	117.1	-15.3	-139.8
RS5-2011	110720F1	515129	4928550	3.80	3.82	0.908	165.8	-13.5	-134.2
RS5-2012	120713TJ	515129	4928550	4.52	5.12	14.1	224.3	-13.3	-134.8

[a]sample codes are in YYMMDD format. [b]UTM coordinates, all in zone 12T. [c]field pH corrected to achieve charge balance (see methods).

spectrophotometer and Hach reagents on unfiltered water samples. Hach spectrophotometers and reagents were also employed for the measurement of aqueous silica (silicomolybdate method) except these analyses were performed on 0.2 micron-filtered water samples, described below.

Water samples for laboratory analyses were filtered with a series of Supor (Pall Corporation) filters down to 0.2 microns and preserved in bottles designated for various analyses. Samples for water isotope determinations were collected in 30 mL Quorpak square bottles with polymer-lined caps to ensure gas-tight storage. The bottle were rinsed with deionized water and dried prior to use; water isotope samples were stored at room temperature until analysis. Samples for ion chromatography (2 per site) were filtered into 30 mL HDPE Nalgene bottles, which had been thoroughly soaked and rinsed with multiple aliquots of deionized water, and frozen at -20 °C at the end of each sampling day and kept frozen until analysis. Samples for dissolved inorganic carbon (DIC) were preserved in acid-washed 40 mL amber glass vials with black butyl rubber septa. The filtering apparatus consisted of a 140 mL plastic syringe and caulking gun to facilitate filtering. Sample water was collected in 1 L HDPE bottles and loaded into the syringe via plastic tubing and a 3-way stopcock. The entire apparatus was rinsed with at least 100 mL of sample prior to filtering into sample bottles.

2.2.2 Geochemical Analyses

Concentrations of major anions (F^-, Cl^-, SO_4^{2-}, NO_3^-) and major cations (Li^+, Na^+, K^+, Ca^{2+}, Mg^{2+}, NH_4^+) were determined on separate Dionex DX-600 ion chromatography systems using suppressed conductivity detection and operated by Chromeleon software (version 6.8). The anion system employs a potassium hydroxide eluent generator, a

carbonate removal device, and AS11-HC/AG11-HC columns. The hydroxide concentration of the eluent is held isocratically at 5 mM for 5 minutes, followed by a non-linear (Chromeleon curve 8) hydroxide concentration gradient applied over 31 minutes, after which the column is reequilibrated at 5 mM hydroxide for 10 minutes before the next sample injection. The eluent flow rate is held constant at 1.0 mL/min. The cation system is equipped with CS-16 and CG-16 columns and cations are eluted isocratically with 19 mM methanesulfonic acid (MSA) at 0.5 mL/min. Samples for cations were acidified with 6 N MSA to approximately 19 mM final concentration. Both systems are plumbed with an external source of deionized water for suppressor regeneration to improve the signal-to-noise ratio of the analyses. Injection volumes are 100 µL and 75 µL for anions and cations, respectively. Quantification is achieved externally via calibration curves constructed from a series of dilutions of mixed ion standards (Environmental Express, Charleston, SC, USA). Quantification accuracy is verified daily by analysis of an independent mixed ion standard (Thermo Scientific, Waltham, MA, USA). Uncertainties in reported ion concentrations are estimated to be +/- 5%.

Analyses of DIC were conducted using an OI Wet Oxidation TOC analyzer coupled to a Thermo Delta Plus Advantage mass spectrometer as previously described (Havig *et al.*, 2011). The DIC in each sample was converted to CO_2 by addition of phosphoric acid. The ion chromatogram for the CO_2 molecular ion (44 m/z) was used for quantification of CO_2 via comparison to calibration curves constructed with sodium bicarbonate standards encompassing expected concentrations. Water isotopes were determined on a Los Gatos water isotope analyzer that employs cavity ring down spectroscopy. The isotope ratios were standardized with isotope standards encompassing the range of the natural samples.

2.2.3 Correction of pH and Speciation

The major ion data and the DIC data were used with the geochemical speciation code EQ3/6 (Wolery and Jarek, 2003) to speciate each aqueous fluid and assess charge balance using activity coefficients calculated with an extended Debye-Hückel equation and equilibrium constants derived from the revised Helgeson-Kirkham-Flowers equation of state (Shock *et al.*, 1997; Sverjensky *et al.*, 1997). Several of the samples (particularly RN1-2011 and RS4) exhibited charge imbalances (expressed as percent of the mean charge, as defined by Nordstrom *et al.*, 2009) in excess of 20%, which is believed to indicate faulty pH probes in use at the time of sampling. Since hydrogen ions are nearly at the same order of magnitude concentration as the major solutes in these samples, the pH measurements were corrected to achieve charge balance, as indicated in Table 1. These corrected values are believed to be closer to the actual pH of each hot spring at the time of sampling. The DIC concentrations were speciated using the corrected pH values.

2.2.4 DNA Extraction and Ribosomal Gene Sequencing

Samples preserved for DNA extraction were thawed and mat material (~0.5 g) was transferred aseptically to Lysing Matrix E tubes supplied with the FastDNA Spin Kit for Soil (MP Biomedicals, Santa Ana, CA, USA). Extraction was performed according to the manufacturer's instructions except that 250 µL of the phosphate buffer was replaced by 250 µL of tris-buffered phenol (pH 8; Sigma-Aldrich, St. Louis, MO, USA), which is a slight modification of previously described procedures (Boyd *et al.*, 2007). Extracted DNA was quantified using the PicoGreen dsDNA assay kit (Invitrogen, Carlsbad, CA, USA) and a Mx3005P QPCR System (Agilent Technologies, Inc., Santa Clara, CA, USA) operating

in quantitative plate read mode with the FAM filter set (492 nm excitation; 516 nm emission).

Bacterial 16S rRNA and eukaryal 18S rRNA genes were amplified via polymerase chain reaction (PCR) from ~5 ng of genomic DNA using primers 1100F/1492R (annealing temperature of 55 °C) and A7F/570R (annealing temperature of 42 °C), respectively, as previously described (Hamilton *et al.,* 2013). PCRs were subjected to an initial denaturation (4 min., 94 °C) followed by 35 cycles of denaturation (1 min., 94 °C), annealing (1 min., specified annealing temperature), and extension (1 min., 72 °C). A final extension step was performed at 72 °C for 20 min. The PCR was verified via electrophoresis using a 1% agarose gel. All 14 DNA extracts yielded eukaryal 18S rRNA gene amplicons while 13 of the 14 DNA extracts (exception being RS5-2012) yielded bacterial 16S rRNA gene amplicons. Amplicons were purified using the Promega Wizard PCR purification system (Madison, WI), quantified via the Qubit DNA Assay kit (Life Technologies, Grand Island, NY) and a Qubit 2.0 Fluorometer (Life Technologies), and sequenced using an Ion Personal Genome Machine (Life Technologies).

Post-sequencing processing was performed with Mothur (ver. 1.25.1; Schloss *et al.*, 2009) as previously described (Hamilton *et al.,* 2013). Raw bacterial 16S rRNA and eukaryal 18S rRNA gene libraries were trimmed to a maximum length of 215 and 195 bases, respectively, and were subjected to a filtering step using the quality scores file to remove sequences with anomalous base calls. Unique sequences were aligned using the SILVA database and sequences were trimmed using a defined start and end site based on inclusion of 75% of the total sequences; those that started before or after these defined positions were removed without further consideration. The resulting unique sequences

were pre-clustered to remove amplification and sequencing errors and chimeras were identified and removed using UCHIME (Edgar *et al.*, 2011). Operational taxonomic units (OTUs) were assigned at a sequence similarity of 95% (eukarya) or 97% (bacteria) using the furthest-neighbor method. The remaining sequences were randomly sub-sampled in order to normalize the total number of sequences in each library. This processing resulted in a total library size of 861 bacterial rRNA gene sequences and 3307 eukaryal 18S rRNA gene sequences per spring sampled. Sequences were classified using the Bayesian classifier (Wang *et al.*, 2007) and the RDP database, with manual verification using BLASTn (https://blast.ncbi.nlm.nih.gov). Raw untrimmed sequence and quality score files along with a mapping file have been deposited in the NCBI SRA database under the accession number SRR2147823.

2.2.5 Quantitative PCR

Quantitative PCR was performed with the SsoAdvanced Universal SYBR Green Supermix (BioRad, Hercules, CA, USA) according to the manufacturer's protocol, and assayed on a CFX Connect detection system (BioRad) using primers 1100F/1492R (annealing temperature of 55 °C) and A7F/570R (annealing temperature of 42 °C). Reactions were performed in triplicate, with 500 nM forward and reverse primer, in a final reaction volume of 20 μL using the following cycling conditions: initial denaturation at 98 °C (0.5 min.), followed by 35 cycles of denaturation at 98 °C (0.5 min.), annealing and elongation at specified temperature (1 min.), and eventually a melt curve of 65-95 °C in 0.5 °C steps at 5 seconds/step. Control reactions contained no template DNA. Plasmids containing inserts of each amplicon as prepared and reported previously (Hamilton *et al.*, 2013) were used as standards.

2.2.6 Pigment Analyses

Samples (~1 g) preserved for analysis of pigments were thawed, transferred aseptically to Lysing Matrix A tubes (MP Biomedicals), and centrifuged at 21000 x *g* for 5 minutes at 4 °C. After removal of the aqueous supernatant, 250 µL of 7:2 acetone:methanol (v/v) that had been stored over 4 Å molecular sieves (Sigma-Aldrich) was added and the samples were subjected to ballistic bead beating (FastPrep 24; 6.5 speed, 40 s). The samples were subsequently centrifuged and the organic supernatant was transferred to a microcentrifuge tube. Additional aliquots of 7:2 acetone:methanol and pure methanol were homogenized with the solid sample by additional rounds of bead beating and subsequently collected by centrifugation, whereupon the supernatants were pooled. This process was continued until the supernatant became clear and no obvious signs of methanol-soluble pigments remained in the solid sample, typically requiring ~1.5 mL of total solvent. The pooled supernatants were centrifuged and the top 500 µL were transferred to Teflon-sealed amber autosampler vials (Agilent) for analysis. To minimize pigment degradation, all manipulations were conducted in a cold room (4 °C) without direct lighting and the samples were transported on ice in a closed container.

Pigment samples were analyzed immediately after extraction via high pressure liquid chromatography (HPLC) equipped with a photodiode array absorbance detector (Thermo Surveyor) coupled with atmospheric pressure chemical ionization mass spectrometry (Thermo Quantum Discovery MAX triple-quadrupole) operating in positive ion, single quadrupole scanning mode from 200 to 1500 m/z with a scan rate of 1 Hz. Parameters for mass spectrometry were based on those employed by van Breemen *et al.* (2012), specifically a corona discharge of 8 µA, vaporizer temperature of 350 °C, and

capillary temperature of 300 °C. Samples were injected via a 50 µL sample loop onto a YMC Carotenoid C-30 reverse phase column (3 x 250 mm). HPLC conditions were modified from those described by Sander *et al.* (1994). The solvent system was initially isocratic at 81:15:4 methanol:methyl *tert*-butyl ether:water for 30 minutes, followed by a linear gradient to 6:90:4 methanol:methyl *tert*-butyl ether:water at 90 minutes. The solvent system was then returned to initial conditions over 5 minutes and held isocratically for 15 minutes to re-equilibrate the column for the next sample. Chromatograms were obtained at 360, 475, and 665 nm using the diode array detector to track chlorophylls and carotenoids.

Pigment analyte peaks were assigned tentative identifications by synergistic comparison of visible absorption spectra and molecular ions obtained from the mass spectra. These data are reconciled with respect to the retention time of the analyte peaks and knowledge of the elution profile for common carotenoids on the C30 stationary phase (Sander *et al.*, 1994). In the case of carotenoids, the spectral fine structure, specifically the %III/II value and the presence or absence of a *cis*-peak, are particularly important for making identifications (Britton, 1995). In the case of *cis*-isomers, the relative height of the *cis*-peak is especially useful at distinguishing isomers (Muller *et al.*, 1997). Semi-quantitative comparison for specific pigments was performed using integrated peak areas from the diode array chromatograms and normalized per gram dry mass of the sample after extraction and total solvent volume used. These results are then further normalized per µg N using the elemental analysis data as a proxy for the amount of biomass present in each sample. Quantitative results for chlorophyll *a* and β-carotene were obtained using response factors at 665 nm and 475 nm, respectively, determined using a series of pigment solutions

prepared using 7:2 acetone:methanol and authentic samples of each pigment obtained commercially (Sigma-Aldrich).

2.2.7 Elemental Analyses

Samples designated for analysis of total carbon and nitrogen were processed and analyzed as previously described (Havig *et al.*, 2011). Briefly, samples (~5 g) were dried at 80 °C for ~3 days and then uniformly powdered using an agate mortar and pestle. Aliquots of this homogenous powder were weighed in tin capsules for combustion analysis, performed on a Costech model ECS 4010 Elemental Analyzer coupled to a Thermo Delta Plus Advantage mass spectrometer. The CO_2 and N_2 obtained from sample combustion were separated via gas chromatography and quantified using the ion chromatograms at 44 and 28 m/z, respectively. Calibration was based on calibration curves using NIST 2710 (Montana soil). Results are reported as the mean and standard deviation of at least 3 replicate analyses.

2.2.8 Inorganic Carbon Uptake Assays

Total DIC uptake was assessed using slight modifications to methods described previously (Boyd *et al.*, 2009). Microcosms were prepared in pre-sterilized, N_2-purged 24 mL serum bottles. Ten mL of spring water was sampled directly from the spring source and added to each serum bottle using a syringe and needle. Mat samples were collected aseptically using a sterile spatula and were placed in 50 mL falcon tubes. Twenty mL of spring water was added to each tube and it was shaken vigorously to create a homogenized slurry. One mL of this slurry was added to each serum bottle. The gas phase of all microcosms was equalized to atmospheric pressure using a sterile needle prior to injection of 10.0 µCi (20 µM final concentration) of radiolabeled sodium bicarbonate ($NaH^{14}CO_3$).

Triplicate microcosms were wrapped in foil (dark) and triplicate microcosms were allowed access to light (light). A separate series of triplicate light and dark assays was amended with $HgCl_2$ to a final concentration of 500 µM. All microcosms were placed in a sealed bag (secondary containment) and incubated in the source of the spring for <60 minutes. Microcosms were terminated by freezing on dry ice and were stored at -20 °C until processed (described below).

In the laboratory, sealed microcosm assays were thawed at room temperature for approximately 2 hours followed by acidification to pH ~2 by injection of 1.0 mL of 1N HCl to volatize unreacted CO_2 into headspace. After acidification, microcosms were allowed to equilibrate for an additional 2 hours. Acidified samples were filtered onto 0.22 µm polycarbonate membranes, washed with 5 mL of sterile deionized water, and dried overnight at 80 °C. Dried filters were placed in scintillation vials and overlain with 10 ml of CytoScint ES™ liquid scintillation fluid. Radioactivity associated with each of the samples was measured on a Beckman LS 6500 liquid scintillation counter (Beckman Coulter, Inc., Indianapolis, IN). Rates of carbon assimilation based on the ^{14}C tracer were determined using the methods of Lizotte *et al.* (1996). Briefly, uptake rates were calculated by multiplying the uptake of ^{14}C-labeled substrate by the total effective concentration of the substrate (^{14}C-labeled substrate + native substrate) using an isotopic discrimination factor of 1.06.

2.3 Results and Discussion

2.3.1 Ribosomal Gene Sequences

Sequencing of 16S and 18S rRNA gene amplicons from the 14 samples reveals that 11 of the samples contained OTUs associated both with cyanobacteria and with algae of

the order *Cyanidiales* within the phylum Rhodophyta (Figure 3). In these samples, cyanobacteria represented from <1-85% of all 16S rRNA gene sequences, nearly all of which were most closely associated (88-100% sequence similarity; most abundant OTUs 99-100% sequence similarity) with *Chlorogloeopsis* sp. Greenland 5, an isolate from an alkaline, high-salinity hot spring in Greenland (Roeselers *et al.*, 2007). Observations of *Chlorogloeopsis* morphotypes have been briefly reported for springs with pH 4-5 in other areas of YNP, but have not been further investigated (Castenholz, 1996). Site RS1 also contained an OTU associated with the genus *Synechococcus*, representing 15% of the cyanobacterial sequences (9% of all 16S rRNA gene sequences) in that sample. Nearly all Rhodophyta OTUs were most closely related (97-100% sequence similarity) to *Cyanidioschyzon merolae* 10D, which other studies have identified as the most common *Cyanidiales* phylotype in acidic, aquatic environments at YNP (Toplin *et al.*, 2008; Skorupa *et al.*, 2012). The relative abundance of *C. merolae* sequences was quite variable, ranging from <1% to nearly 100% of 18S rRNA gene sequences in these samples. Surprisingly, very few chloroplast sequences were found in the 16S rRNA gene libraries and only in IG2 were they associated with *Cyanidiales*.

Of the remaining samples, 2 samples below a pH of 4 (IG1 and FF1) also yielded sequences associated with the *Cyanidiales* but yielded no cyanobacterial sequences. Several algal mats dominated by *Cyanidiales* in Yellowstone with pH values of ~3 have received considerable attention including Nymph Creek (Ferris *et al.*, 2005; Boyd *et al.*, 2012) and Dragon Spring (Lehr *et al.*, 2007; Boyd *et al.*, 2012), thus this study extends sequencing observations of *Cyanidiales* populations higher in pH. Green algae (Chlorophyta) were also detected at 8 of the sites, representing <1-35% of 18S rRNA gene

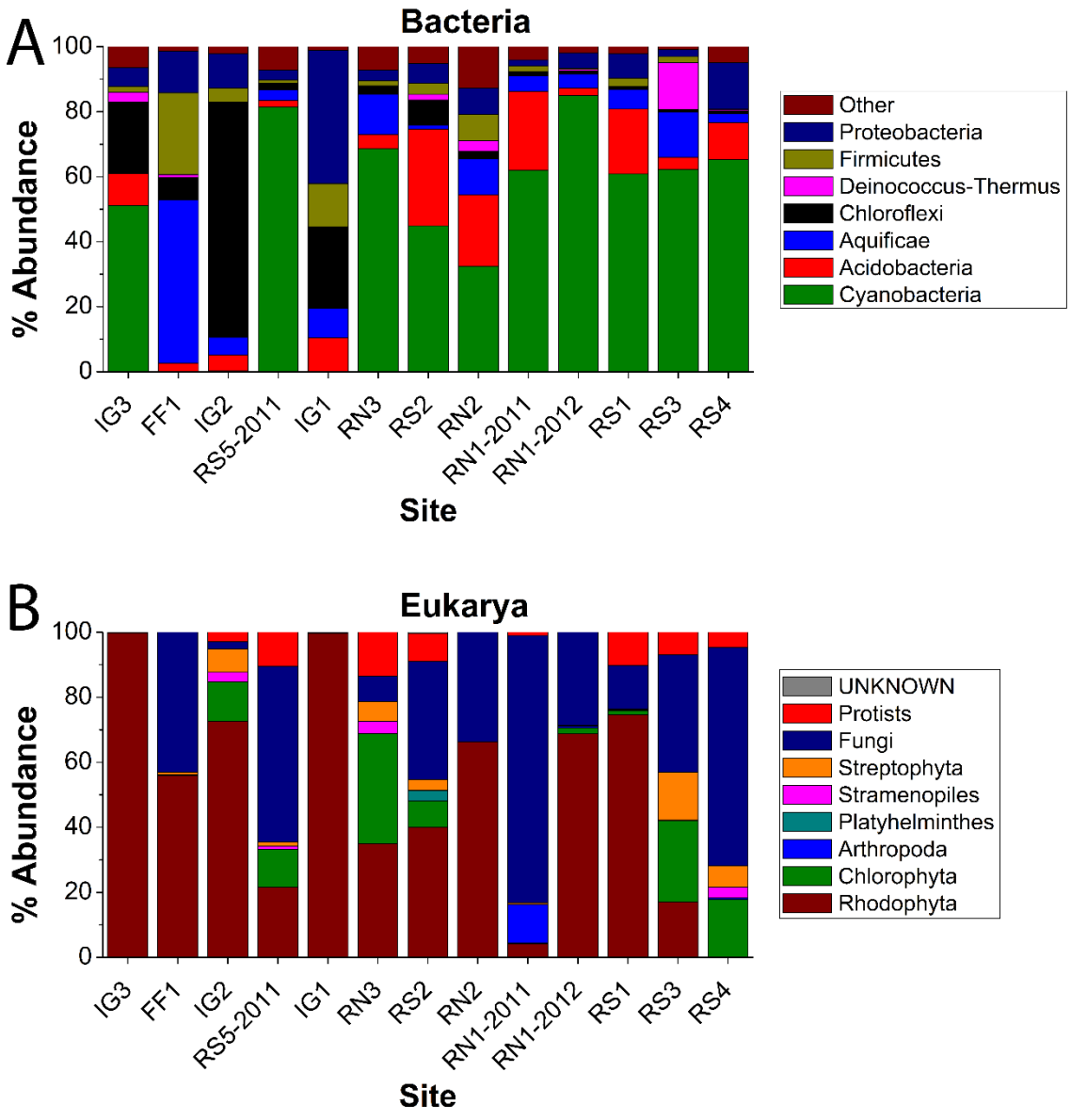

Figure 3. Phylum-level diversity of bacterial 16S (A) and eukaryal 18S (B) rRNA gene sequences. Data are expressed in percent and arranged left to right by increasing pH. OTUs representing less than 0.1% of total OTUs were not included. Sequence data for sample RS5-2012 are not shown as no bacterial 16S rRNA gene amplicons were obtained and the only eukaryal 18S rRNA gene sequences were affiliated with Streptophyta. Though not visible in this depiction, cyanobacteria are present in IG2 and Rhodophyta are present in RS4 in low abundance.

sequences, rivaling *Cyanidiales* in abundance in some samples. One sample (RS5-2012) lacked OTUs associated with any known microbial phototroph. The amount of DNA obtained from this sample was quite low (2.5 ng/μL) and failed to yield any 16S rRNA gene amplicons. All 18S rRNA gene sequences associated with this sample were most closely affiliated with *Ranunculales*, an order of angiosperms, rather than microbial eukaryotes.

Fungi represented a significant proportion of the 18S rRNA gene OTUs in most samples, with the exception of the three sites near Imperial Geyser. The diversity of the fungal OTUs is large, encompassing 6 of the 7 recognized phyla of fungi. Thermotolerant fungi are thought to be more abundant in lower pH environments, and likely represent the most thermotolerant eukarya, having a temperature maximum of ~60 °C (Tansey and Brock, 1972; Brock, 1978). Other 18S rRNA gene sequences are associated with protists, arthropods, and land plants; these sequences in many cases may represent exogenous surface input of biomass rather than indigenous members of the hot spring community. Fungi and protists were also observed in hot spring samples from Lassen, California, again with uncertainty regarding to what extent they represent autochthonous organisms (Brown and Wolfe, 2006). Mildly acidic hot springs at the photosynthetic fringe are excellent targets for further exploration and characterization of the 'eukaryotic fringe' and its constituents.

Interestingly, two sites (RS1 and RS4) yielded 16S rRNA gene sequences most closely associated with *Chloracidobacterium thermophilum* (13% and 2% of 16S rRNA gene OTUs, respectively), an organism first cultivated from an alkaline hot spring and is the only known phototrophic member of the Acidobacteria (Bryant *et al.*, 2007; Tank and

Bryant, 2015). Sequence similarity ranged from 86-99%, yet the most abundant OTU associated with *Cab. thermophilum* in both sites was 99% similar to the cultured representative. While most samples contained an abundance of OTUs associated with phyla containing anoxygenic phototrophs such as Chloroflexi, Proteobacteria, and Firmicutes, none of these OTUs were closely associated with cultured representatives of these phyla known to be phototrophic. Other abundant phyla in these samples include other Acidobacteria, Aquificae, and Deinococcus-Thermus.

2.3.2 Carbon Fixation Assays

In order to demonstrate active photosynthesis by the microbial communities inhabiting hot springs within this pH range, carbon fixation assays were completed at 4 of the study sites at the time of sampling (Figure 4) to measure rates of biological inorganic carbon uptake under both light and dark conditions. Statistically significant differences in carbon uptake rates between light and dark treatments were observed at RS1 and RS2, indicating light-driven carbon uptake (photoautotrophy) was occurring when these springs were sampled. In contrast, rates of carbon uptake were low in experiments coinciding with samples RS5-2012 and FF1 and the rates were not statistically different between light and dark treatments, signifying that light-driven carbon uptake was not occurring when these springs were sampled.

2.3.3 Pigment Compositions of Biofilms

Analysis of pigment extracts of biofilm samples was performed to complement the ribosomal sequence data in assessing the composition of the phototrophic communities at each site. Furthermore, the abundances of pigments and their degradation products can provide insights into the metabolic state (i.e., likely active or inactive) of specific

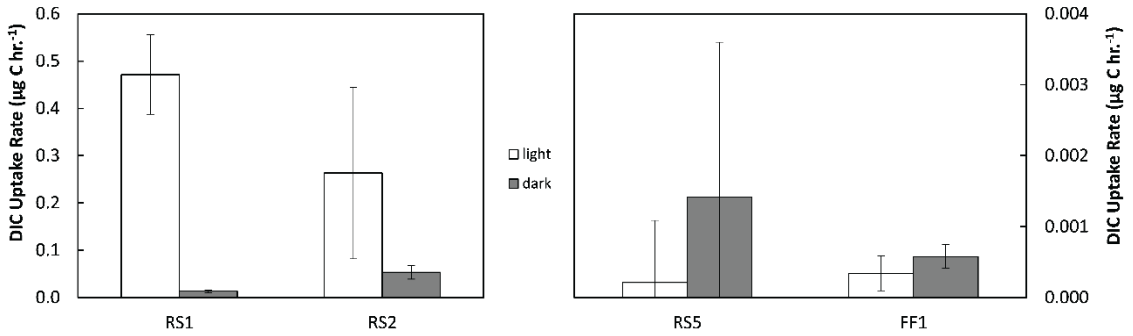

Figure 4. Rates of DIC incorporation into biomass observed under light and dark conditions for 4 of the study sites. The left scale applies to RS1 and RS2, while the scale on the right applies to RS5 and FF1. Rates were measured in July 2012.

phototrophic populations at the time of sampling. The major chlorophyll type in all samples was chlorophyll *a*, the only chlorophyll found in thermophilic cyanobacteria and *Cyanidiales*. Every sample also had significant quantities of compounds related to chlorophyll *a*, including chlorophyll *a'* (epimer at the 13^2 carbon, using IUPAC numbering), pheophytin *a* and its 13^2 derivatives, including its epimer, allomer, and pyrolyzed product (pyropheophytin *a*), and pheophorbide *a* as depicted in Figure 5a. The presence or absence of chlorophyllide *a*, the magnesium-containing analogue of pheophorbide *a*, was more ambiguous, as analyte peaks with retention times and absorbance spectra consistent with this compound were often present, but none yielded mass spectra expected for chlorophyllide *a*. In contrast to the other sites, samples FF1 and RS5-2012 did not yield any intact chlorophyll *a*; the major chlorophyll molecules present were pheophorbide *a* and pyropheophytin *a*, respectively, with smaller amounts of pheophytin *a* and other derivatives. Thus, most of the chlorophyll present at these sites had been demetallated and further degraded and likely was not present in active cells at the time of sampling.

Each of the chlorophyll *a* derivatives observed are likely the result of abiotic processes as depicted in Figure 6. Exposure to acid quickly demetallates chlorophyll *a* to yield pheophytin *a* (reaction 1), which can be further degraded via reactions at the esterified carbon (carbon 13^2) in the E-ring of the macrocycle. Formation of the allomer (reaction 2) is believed to occur through a reaction with molecular oxygen via a radical mechanism (Hynninen *et al.*, 2002). Decarbomethoxylation (reaction 3) to yield pyropheophytin *a* proceeds via hydrolysis of the methyl ester followed by rapid decarboxylation of the resulting β-keto acid (Pennington *et al.*, 1964; Smith, 2013). The phytyl ester was also

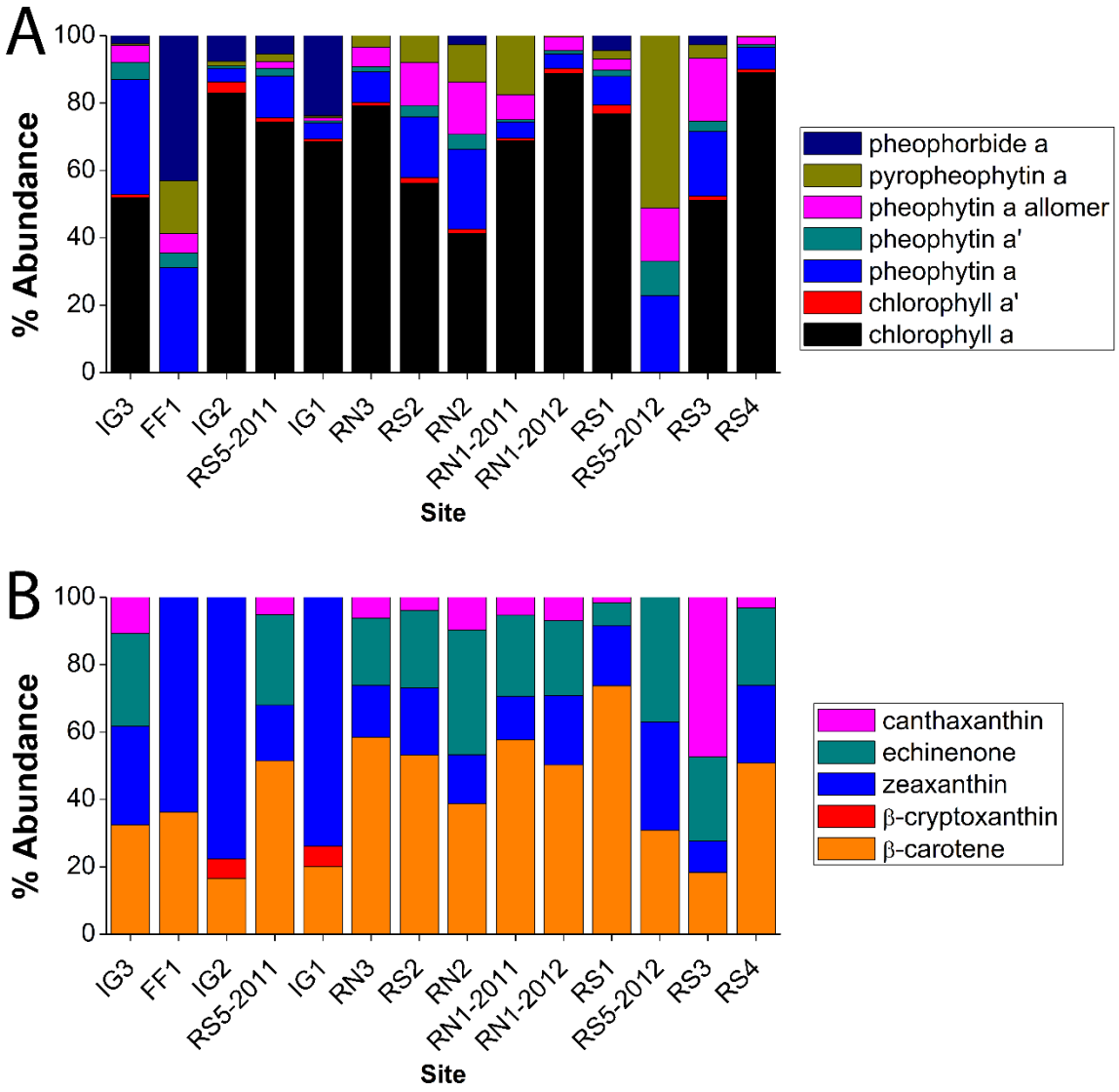

Figure 5. Relative abundances of chlorophyll *a* and its derivatives (A) and relative abundances of major carotenoids (B) in mat samples collected from hot springs in Yellowstone National Park, as determined from integrated peak areas in chromatograms obtained at 665 nm (chlorophylls) and 475 nm (carotenoids) using the diode array detector. As in Figure 3, samples are arranged from left to right by increasing pH. As an approximation, the relative abundance of pheophytin and its derivatives (i.e., all magnesium-free compounds) were corrected by multiplying by the ratio of molar absorptivities of the Q_y absorption maxima for chlorophyll *a* to pheophytin *a* reported by Kobayashi *et al.* (2006) to reflect the weaker absorbance of demetallated chlorophylls. Similarly, the carotenoid relative abundances were corrected by multiplying by the ratio of the molar absorptivity for β-carotene to that of each carotenoid using the molar absorptivities reported by Britton (1995) using light petroleum as solvent.

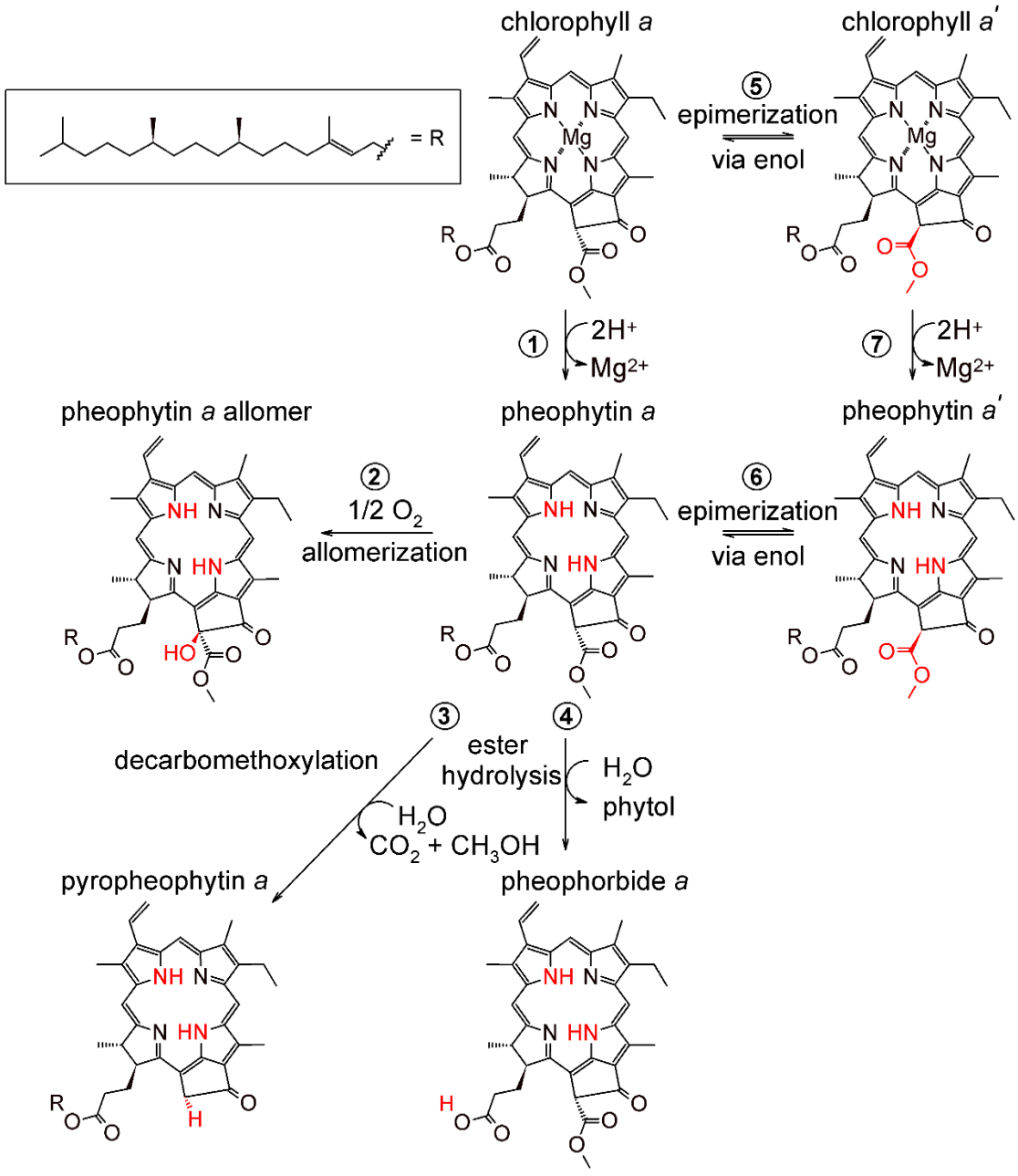

Figure 6. Structures of chlorophyll a and its derivatives detected in samples from this study with putative reaction pathways. Moieties that differ from those of chlorophyll *a* proper are depicted in red.

observed to have been hydrolyzed (reaction 4) in some samples resulting in pheophorbide *a*. Enzymatic catabolism of chlorophyll within phototrophic cells or by heterotrophic grazers may contribute to the observed quantities of these chlorophyll degradation products, or they may also arise as artifacts during the extraction process. However, the products of analogous reactions at the 13^2 carbon of chlorophyll *a* (i.e., magnesium-containing analogues of the products of reactions 2 & 3 in Figure 6) were not observed, strongly suggesting the observed compounds arise via abiotic processes occurring in the hot springs rather than by biological processes or during extraction as described above. Moreover, pigment analysis of a non-thermal sample (a green leaf from an oak tree, *Quercus virginianus*) did not yield chlorophyll degradation products except for small amounts of pheophytin *a*, which is known to occur in the reaction centers of photosystem II (Blankenship, 2014). Carrying a standard solution of chlorophyll *a* through the extraction process performed with hot spring samples yielded none of the degradation products discussed above, offering further evidence that they are not artifacts of the extraction method. Thus, it seems that senescent phototrophic cells, having lost the ability to maintain intracellular pH, rapidly experience acidification of the cytosol via reaction with the hot spring water, leading to demetallation of chlorophyll followed by several slower degradation pathways, the rates of which are enhanced by acid and thermal conditions. The observed chlorophyll degradation products are consistent with the pathways of early pigment diagenesis observed in other systems (Louda *et al.*, 2011).

The epimerization reactions for both chlorophyll *a* and pheophytin *a*, which are reversible reactions via an enol intermediate as depicted in Figure 6 (reactions 5 and 6, respectively), offer further evidence for abiotic pigment degradation. The observed ratios

of epimer pairs for both compounds (chlorophyll *a'*/chlorophyll *a* and pheophytin *a'*/pheophytin *a*) represent the reaction quotients, Q, of the epimerization reactions. These ratios can be compared to equilibrium constants, K, for each reaction at the hot spring temperature derived from the standard state free energy and reaction enthalpy data reported by Mazaki *et al.* (1992), assuming the reaction enthalpy is constant up to the hot spring temperatures (i.e., extrapolating the Van't Hoff plot). The ratios of Q to K, representing the position of the reaction relative to chemical equilibrium, were converted to chemical affinities (Shock *et al.*, 2010) according to the equation

$$A = -RT \ln \frac{Q}{K}$$

where R is the universal gas constant and T represents the Kelvin temperature. The affinities are plotted versus hot spring temperature in Figure 7 where it can be seen that at each sample site the epimerization reaction for chlorophyll *a* always has a larger affinity than does the reaction for pheophytin *a* at the same site. This indicates that the epimerization reaction of chlorophyll *a* is further from equilibrium than the corresponding reaction for pheophytin *a*. Active biosynthesis of chlorophyll *a* likely maintains the chlorophyll *a'*/chlorophyll *a* ratio far from equilibrium, though small amounts of chlorophyll *a*' are found in P700 of photosystem I and may arise via enzymatic conversion of chlorophyll *a* (Blankenship, 2014). In contrast, pheophytin *a*, mostly derived abiotically from chlorophyll *a* in inactive cells, is allowed to approach equilibrium with pheophytin *a'*. Moreover, it is probable that the epimerization reaction is kinetically inhibited for chlorophyll *a* when the molecule is stably bound within proteins or membranes. The epimerization reaction for one sample, RS5-2012, has a negative affinity for pheophytin *a*,

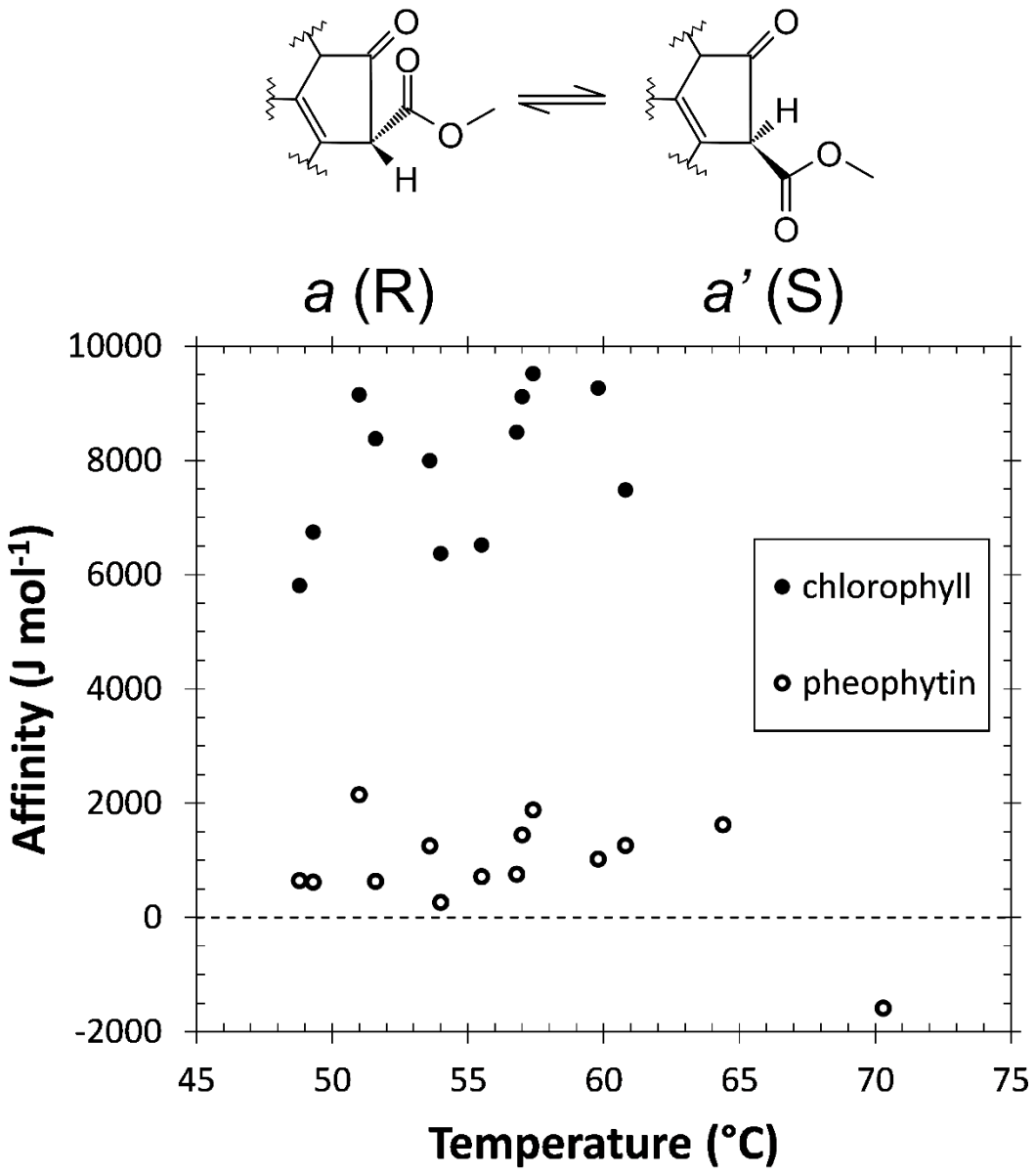

Figure 7. Chemical affinity for the epimerization reaction of the 13^2 carbon of chlorophyll *a* (filled circles) and pheophytin *a* (open circles) as a function of hot spring temperature. The reaction is depicted above with the chirality of each epimer indicated. The horizontal dashed line is plotted at an affinity of zero, which corresponds to equilibrium.

indicating more pheophytin *a'* than would be present at equilibrium and that the reaction should proceed toward pheophytin *a*. It is unclear why pheophytin would exist on this side of equilibrium. The high relative abundance of pyropheophytin *a* in this sample points to the possibility that pheophytin *a* is more susceptible to the pyrolysis reaction than its epimer, pheophytin *a'*, which could maintain the epimerization of pheophytin away from equilibrium. Kinetic studies could elucidate the behavior of each epimer in the observed degradation reactions.

Evidence for small amounts of chlorophylls possessing a chlorophyll *b* chromophore was found in 3 of the sites (IG1, IG2, FF1), including pheophytin *b*. Chlorophyll *b* is found in the Chlorophyta as well as in plants, both of which also synthesize chlorophyll *a* (Blankenship, 2014). There was no evidence of intact chlorophyll *b*, so it is unlikely that these compounds were derived from active cells. While Chlorophyta 18S rRNA gene sequences were present in these samples, sequence abundance was very low in IG1 and FF1, and no pigment peaks exhibiting a chlorophyll *b* chromophore were found in samples from sites with the highest Chlorophyta abundance. Thus, the observed chlorophyll *b* derivatives do not correlate with Chlorophyta sequence abundance and the observed chlorophyll *b* derivatives may largely be derived from exogenous higher plant matter.

Similarly, small amounts of bacteriochlorophyll *a* and its derivatives, such as bacteriopheophytin *a*, were found in 4 of the samples (RS1, RS2, RS4, FF1). Found exclusively in anoxygenic phototrophs to date, the presence of bacteriochlorophyll *a* chromophores suggests the presence of these bacterial phototrophs at those sites. Bacteriochlorophyll *a* was also reported for other sites in the pH range 3-6 in YNP

(Hamilton *et al.*, 2012). Bacteriochlorophyll *a* proper was found at 2 of these sites (RS1 and RS4), which are the two sites where *Cab. thermophilum* sequences were found. Bacteriochlorophyll *a* is present in the reaction centers of *Cab. thermophilum* and thus may be associated with these bacteria at these sites (Tsukatani *et al.*, 2012). Currently, the only known acidophilic anoxygenic phototroph that exhibits some degree of thermotolerance is *Rhodopila globiformis*, which was isolated from a high-sulfide, warm spring near the Gibbon River in YNP (Pfennig, 1974; Madigan, 2003). *R. globiformis* expresses distinct carotenoid pigments (Schmidt and Liaaen-Jensen, 1973) that were not observed in this study, consistent with the low sulfide concentrations of the springs examined here. The observation of bacteriochlorophyll *a* chromophores at other sites (RS2 and FF1) is noteworthy because no 16S rRNA gene OTUs from these sites correspond to known phototrophic bacteria, suggesting that if anoxygenic phototrophs are present they are quite novel.

In contrast to bacteriochlorophyll *a*, no bacteriochlorophyll *c* homologues were detected in any of the samples. *Cab. thermophilum* employs a variety of bacteriochlorophyll *c* structures as the major chlorosome antenna pigments (Garcia-Costas *et al.*, 2012) so it is surprising that none were observed in samples where *Cab. thermophilum* sequences were found. While the similar absorbance spectra of bacteriochlorophyll *c* and chlorophyll *a* make identifying bacteriochlorophyll *c* compounds more ambiguous, a search of unassigned analyte peaks from sample RS1, where *Cab. thermophilum* was most abundant, did not offer any strong evidence for bacteriochlorophyll *c* homologues in the mass spectra. Given the complexity of the mixture

of bacteriochlorophyll *c* species produced by *Cab. thermophilum*, perhaps each individual homologue is below detection in these samples.

A variety of minor peaks with chlorophyll-like spectra that had Q_y maxima of approximately 695 nm were observed in many of the samples. These analytes are proposed to represent chlorophyll *d* chromophores. Chlorophyll *d* is believed to occur only in cyanobacteria (Blankenship, 2014) and is synthesized by cells grown under near-infrared light (Gan *et al.*, 2013). Chlorophyll *d* differs from chlorophyll *a* by substitution of the vinyl group with a formyl group at carbon 3, which extends the Q_y band into the infrared region (Schliep *et al.*, 2013; Chen, 2014). Recently, *C. fritschii* was demonstrated to produce chlorophyll *d* under natural or near-infrared light (Airs *et al.*, 2014). The observation of chlorophyll *d* in this study suggests that the *Chlorogloeopsis* sp. present in mildly acidic hot springs may produce red-shifted chlorophylls to exploit additional wavelengths for photosynthesis, particularly cells growing deeper in the mats. While anoxygenic phototrophs are typically believed to use infrared wavelengths, the lack of anoxygenic phototrophic gene sequences in many of the sites may point to cyanobacteria outcompeting these organisms and thus occupying this niche in these springs.

Carotenoids are present in photosynthetic microbes as accessory light-harvesting pigments and for UV-protection (Blankenship, 2014). The relative abundances of major carotenoids in the 14 samples are shown in Figure 5b. The common carotenoids β-carotene and zeaxanthin (3*R*,3'*R*)-β,β-carotene-3,3'-diol) were present in all samples and are among the most abundant carotenoids. Both carotenoids are known to be present in cultures of *C. merolae* (Cunningham *et al.*, 2007) and *Chlorogloeopsis fritschii* (Evans and Britton, 1983), close relatives of the major phototrophs in these springs. The majority of the sites

exhibited a relatively constant zeaxanthin:β-carotene ratio, while 4 of the most acidic sites deviate from this trend with larger relative amounts of zeaxanthin (Figure 8). This deviation likely indicates *C. merolae* synthesizes zeaxanthin to a greater extent than do cyanobacteria and these algae are most abundant in these 4 sites.

The ketocarotenoid echinenone (β,β-carotene-4-one) was abundant at nearly all sample sites where cyanobacterial 16S rRNA gene sequences were found, with the exception of IG2, where cyanobacterial OTU abundances were relatively low. Echinenone was also absent from pigment analyses from sites without cyanobacteria, suggesting this carotenoid is largely derived from the *Chlorogloeopsis* spp. present at these sample sites and not from *C. merolae*. Smaller amounts of canthaxanthin, a carotenoid similar to echinenone where both rings possess 4-keto groups, were present in the same samples, suggesting canthaxanthin is also associated with the cyanobacteria at these sites. Indeed, echinenone is a major carotenoid in *C. fritschii* cells, with traces of canthaxanthin present as well (Evans and Britton, 1983). The lack of echinenone and canthaxanthin at IG2 may indicate that cyanobacteria were not active there when sampled. These two carotenoids, as well as β-carotene, are also present in cultures of *Cab. thermophilum* (Garcia Costas *et al.*, 2012) and the populations of this phototroph observed at sites RS1 and RS4 likely contribute to the observed abundances of these pigments. Other carotenoids synthesized by *Cab. thermophilum* include γ-carotene, lycopene, and deoxyflexixanthin (Garcia Costas *et al.*, 2012), however there was insufficient spectral evidence to make confident assignments for these carotenoids.

β-cryptoxanthin, a mono-hydroxylated analog of zeaxanthin and its putative biosynthetic precursor, was present at 2 sites (IG1 and IG2) where cyanobacteria were

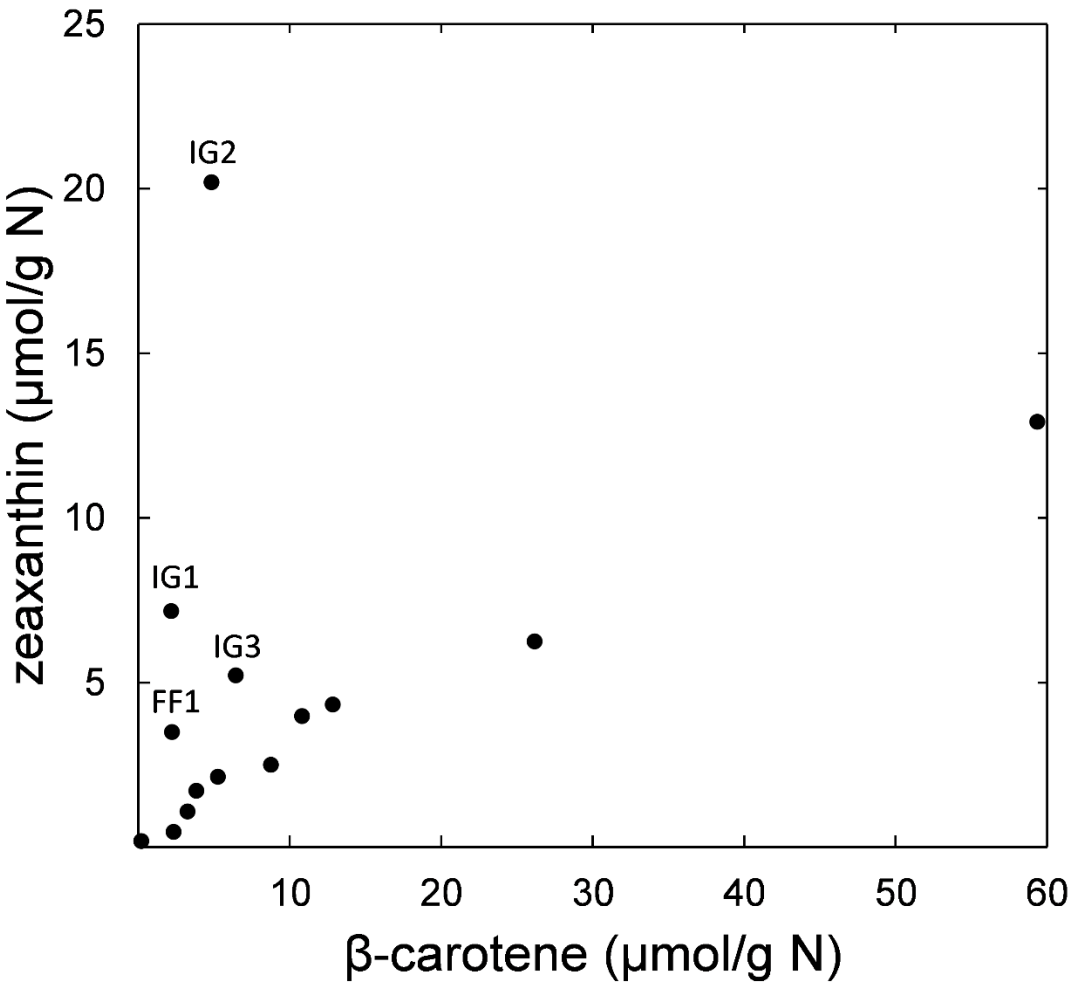

Figure 8. Zeaxanthin versus β-carotene abundance, both expressed as µmol/g N, using data reported in Appendix A. Selected samples are labelled.

either absent or not very abundant. While β-cryptoxanthin is known to occur as a minor carotenoid in both *C. merolae* (Cunningham *et al.*, 2007) and *Chlorogloeopsis fritschii* (Evans and Britton, 1983), its occurrence at only IG1 and IG2 leads to the hypothesis that β-cryptoxanthin is associated with algae in these springs, rather than cyanobacteria. As a corollary, the lack of β-cryptoxanthin at the other sites where *C. merolae* sequences were observed likely indicates that algae were inactive at those sites when sampled. In particular, β-cryptoxanthin was absent at site FF1, where the only putative phototroph was *C. merolae* yet the chlorophyll composition and lack of light-driven carbon fixation indicate that photosynthesis was not occurring under the conditions observed at this site. This observation confirms the relationship of inactive algae and a lack of β-cryptoxanthin and therefore supports the idea that β-cryptoxanthin may be a sensitive indicator of active *C. merolae* populations.

In addition to the predominant *all-trans*-β-carotene, two mono-*cis* isomers of β-carotene were observed: 9-Z- and 13-Z-β-carotene. 9-Z-β-carotene occurred in all 14 samples, while 13-Z-β-carotene was detected in 8 of the 14 samples. While the concerted biosynthesis and incorporation of *cis*-isomers of carotenoids in photosynthetic complexes is known (Bialek-Bylka *et al.*, 1995; Yan *et al.*, 2001; Ye *et al.*, 2008), the abundances of *cis*-carotenes observed here lead to the hypothesis that they are derived mainly from abiotic processes, either thermally or photochemically. Abiotic isomerization leads to only a few sterically unhindered isomers; in the case of β-carotene, 13-Z-β-carotene is the kinetically favored product, while 9-Z-β-carotene is more stable thermodynamically (Doering *et al.*, 1995). Nevertheless, it is unclear precisely to what extent the observed isomerization occurs in the hot spring environment and how much may be attributed to the extraction

process. Subjecting a β-carotene standard to the extraction process yielded peak area ratios of β-carotene to its isomers of 17.2 and 40.4 for the 13-Z- and 9-Z- isomers, respectively, whereas the observed ratios in the hot spring pigment extracts ranged from 4.5-9.5 and 1.9-4.0 for the same isomers, respectively. These ratios indicate that the extraction process induces carotenoid isomerization and contributes to the observed quantities of isomers, but is insufficient to fully explain the observed quantities. Abiotic isomerization *in situ* appears to represent the most prolific source of carotenoid isomers, particularly in the case of the 9-Z-isomer. Alternatively, it is also possible that phototrophic cells in hot springs biosynthesize 9-Z-β-carotene, which is loosely supported by its ubiquity in the samples and its somewhat consistent ratio with *all-trans*-β-carotene, in contrast to the case of 13-Z-β-carotene.

2.3.4 Abundances of Cyanobacteria and Algae

In order to estimate and compare the abundances of cyanobacteria and Rhodophyte algae within the phototrophic communities of each spring, quantitative PCR was performed on samples for which sufficient DNA was obtained (Table 2). For these samples, the ratio of 16S to 18S rRNA gene templates was used to correct the ratio of cyanobacteria to Rhodophyta OTUs, as shown in Figure 9. Since the genomes of both *Chlorogloeopsis fritschii* 9212 (Dagan *et al.*, 2013) and *C. merolae* 10D (Matsuzaki *et al.*, 2004), which represent nearly all the cyanobacterial and Rhodophyta OTUs, respectively, each indicate three copies of ribosomal genes within the nucleus, no correction for nuclear copy number per cell was employed. Cyanobacteria were more abundant than Rhodophyta in all sites analyzed and Rhodophyta only approached the abundance of cyanobacteria in the two most acidic sites examined (IG2 and IG3). Yet, even in these sites, cyanobacteria were more

Table 2. Quantitative PCR results

	Bacterial 16S rDNA		**Eukaryal 18S rDNA**	
	copies/ng DNA	uncertainty	copies/ng DNA	uncertainty
IG1	932380	259017	247250	39037
IG2	584722	64566	76	28
IG3	419087	118978	4619	559
RN1-2012	1208669	228422	4	1
RS1	768018	32323	228	27
RS2	570781	146944	5	1
RS4	397613	62400	131	1
RS5-2011	1410646	23954	14	1

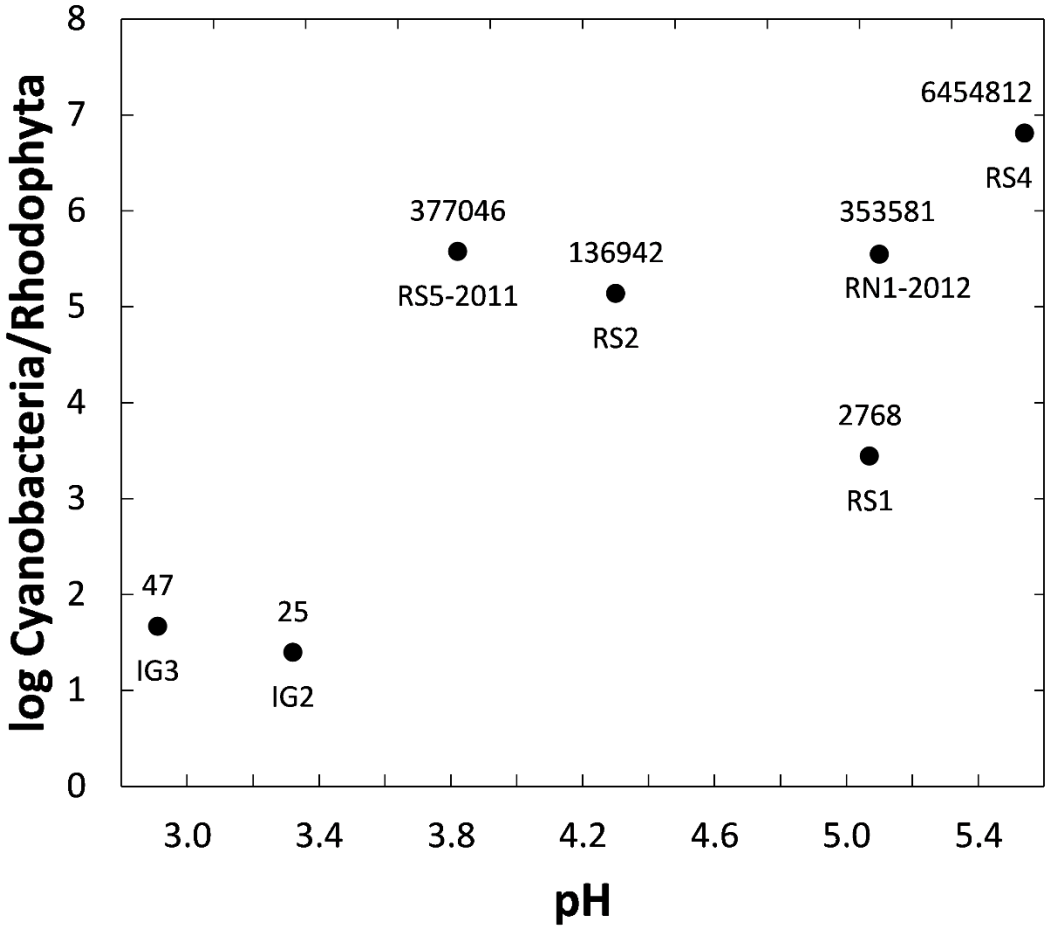

Figure 9. Ratio of cyanobacteria 16S rRNA gene to Rhodophyta 18S rRNA gene abundance (plotted on a logarithmic scale) as a function of pH. The ratio was calculated using the quantitative PCR copy number results for 16S and 18S genes (Table 2) multiplied by the total OTU abundance for each taxonomic group (i.e., those affiliated with cyanobacteria and those affiliated with Rhodophyta). Sites are labeled below each point and the ratio at each site is indicated above each point.

abundant by at least an order of magnitude. Cyanobacteria in the other sites exceeded Rhodophyte algae by 3 to 6 orders of magnitude. These results further substantiate indications from the pigment and carbon uptake data that *Cyanidiales* algae were not significant contributors to primary production at most sites when these springs were studied.

2.3.5 Geochemistry of Mildly Acidic Hot Springs

Geochemical sampling and analysis were completed in order to provide a geochemical context for the dynamic phototrophic microbial communities described above. Major geochemical data are reported in Table 3. The sulfate concentrations of the study sites with respect to chloride concentrations appear in Figure 10, along with the composition of local meteoric water and compositions of other hot springs throughout YNP. Many of the sites are quite dilute and appear in the bottom left portion of the YNP data. Evaporation of approximately 80% of the local meteoric fluid (0.7 log units) could conceivably lead to the observed chloride compositions of many of the mildly acidic springs, which are among the lowest encountered in YNP hot springs, but evaporation cannot explain the intermediate sulfate concentrations observed. Thus, a hydrothermal vapor-phase component from which most of the sulfate is derived is invoked, with the observed chloride concentrations representing a combination of evaporation of the meteoric water component and minor amounts of shallow water-rock reactions. Ratios of chloride to fluoride are also particularly low in many of the 14 sites (Table 3), likely due to a vapor-phase contribution of hydrogen fluoride to these hot spring fluids. Being derived from meteoric water and hydrothermal vapor, these hot springs are classified as MG-type hot springs under the categorization of Nordstrom *et al.* (2009) as are many other acidic

Table 3. Major geochemical measurements and temperatures of the 14 samples in this study

Sample	pH[a]	Temp. °C	O_2 µM	ΣH_2S µM	SiO_2 mM	F^- µM	Cl^- µM	SO_4^{2-} µM	NO_3^- µM	NH_4^+ µM	Li^+ µM	Na^+ µM	K^+ µM	Mg^{2+} µM	Ca^{2+} µM
FF1	3.28	64.4	22	1.7	2.4	45	150	1488	1.2	128	23.7	1663	442	23	61
IG1	3.96	57.0	(31)[b]	(0.5)	(4.9)	13	10	1255	0.3	113	49.4	1944	252	8.9	21
IG2	3.32	48.8	56	0.1	5.7	44	30	1218	0.3	4.0	27.8	1214	380	47	95
IG3	2.91	53.6	84	5.5	2.7	291	378	5089	564	426	117	3902	1567	321	1211
RN1-2011	4.64	57.4	50	1.6	4.3	22	15	195	3.8	21	3.0	234	131	1.8	8.2
RN1-2012	4.96	51.6	113	0.1	3.2	27	15	197	1.5	5.1	2.8	260	135	2.1	8.4
RN2	4.57	55.5	(113)	(0.5)	4.6	18	14	276	3.1	26	1.5	325	174	3.8	13
RN3	4.01	59.8	59	1.2	3.2	89	685	638	0.9	61	46.2	1431	288	14	35
RS1	5.06	54.0	41	0.6	4.1	84	28	601	0.4	13	2.7	747	445	15	69
RS2	4.30	49.3	138	5.1	4.4	76	12	533	0.8	7.0	3.9	625	321	11	59
RS3	5.42	60.8	34	(3.7)	4.8	93	13	476	1.3	27	1.6	844	260	4.9	21
RS4	5.54	51.0	72	1.1	4.0	101	16	275	1.7	10	1.3	603	257	7.8	31
RS5-2011	3.82	56.8	109	0.5	3.6	74	15	470	1.1	22	1.5	479	256	8.1	35
RS5-2012	5.12	70.3	25	2.4	4.0	66	39	379	2.8	35	1.8	562	284	18	50

[a]corrected pH. [b]data in parentheses were estimated from measurements at the site from other years.

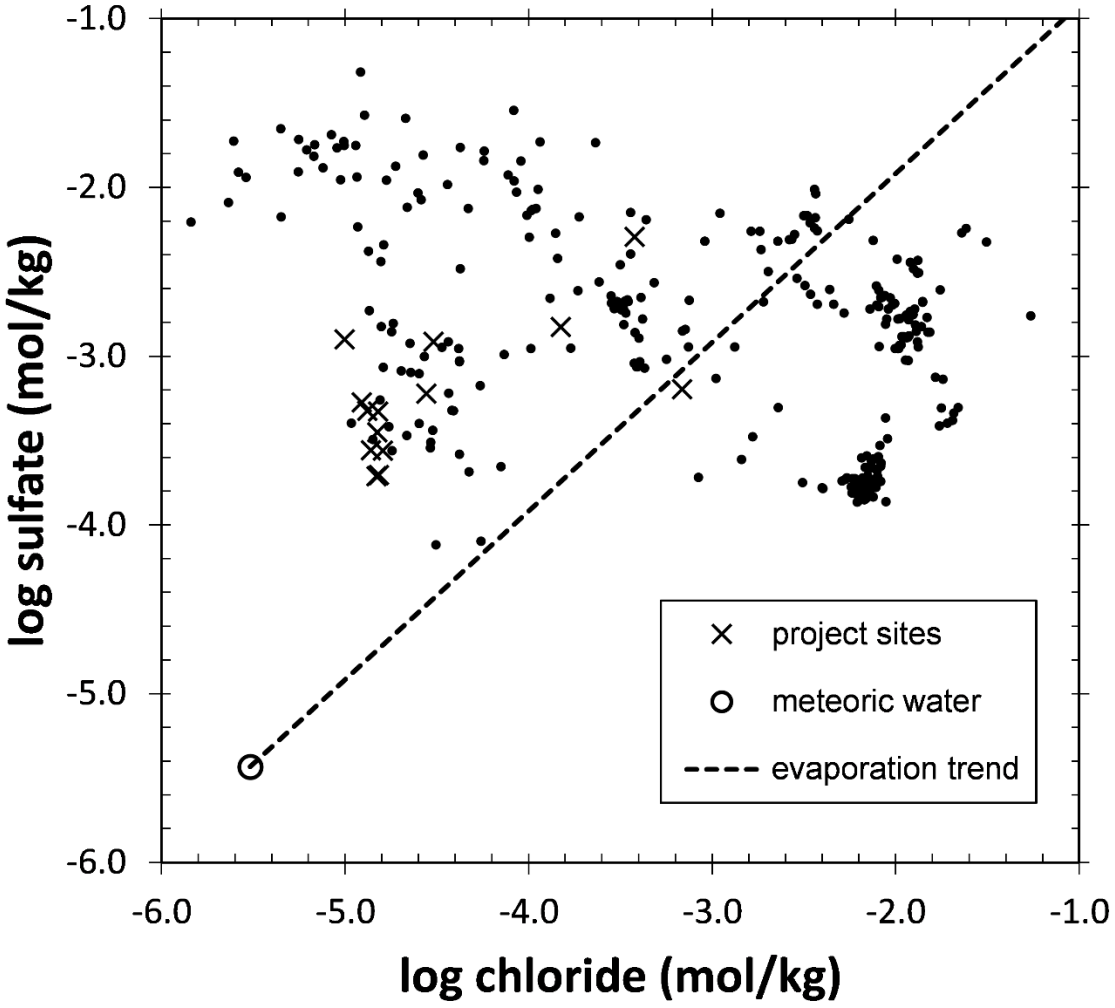

Figure 10. Distribution of hot spring sulfate and chloride compositions in samples from Yellowstone National Park. The 14 samples included in this study (crosses) are plotted along with analyses of 302 other hot spring waters (filled circles) collected from multiple areas in YNP in 2011 & 2012. The composition of local meteoric water (open circle) is the shown as the mean concentrations of sulfate and chloride reported by the National Trend Network of the National Atmospheric Deposition Program for 2012 analyses of precipitation at Tower Falls, YNP (http://nadp.sws.uiuc.edu/data/ntn/); the evaporation trend for this water is plotted across the diagram as a dashed line.

hot springs in YNP. Yet, these sites must be considered extreme cases of this type, as the chloride concentrations for many of the springs are below 1 ppm (< 28 μM), sulfate is often below 100 ppm (< 1 mM), and they are less acidic than the majority of YNP springs in this category.

Several sample sites were appreciably higher in chloride concentration than the others, indicating contributions in addition to meteoric water and hydrothermal vapor. The study sites are all in close proximity to alkaline hot springs, suggesting the possibility that mixing of the deep hydrothermal fluid feeding the alkaline springs is contributing small amounts of chloride and other solutes to the mildly acidic springs. This deep hydrothermal fluid is theorized to have 310-400 ppm chloride, with subsurface processes possibly changing chloride concentrations before mixing (Fournier, 2005). It is likely that mixing occurs in the shallow subsurface where the plumbing of proximal springs are partially connected. For example, site FF1 is approximately 100 meters from a boiling alkaline hot spring, while site IG3 is only about 5 meters from the main source of Spray Geyser (pH = 8.0, unpublished data). In contrast, mixing with fluids enriched in chloride at site RN3 is possibly a surface process, as this small pool is adjacent to the outflow channel of a circumneutral hot spring with a pH of ~6. Nevertheless, these sample sites are still more dilute than sulfidic, mildly acidic springs described elsewhere in YNP (Macur *et al.*, 2013).

The stable isotopic compositions (δ^2H and $\delta^{18}O$) of the hot spring waters in this study are depicted in Figure 11. The data trend away from the local meteoric water line (Kharaka *et al.*, 2002; Holloway *et al.*, 2011) with a slope of approximately 3, typical of other hot springs experiencing non-equilibrium evaporation (Nordstrom *et al.*, 2009). This linear trend intercepts the local meteoric water line very close to δ^2H = -149 ‰ and $\delta^{18}O$ =

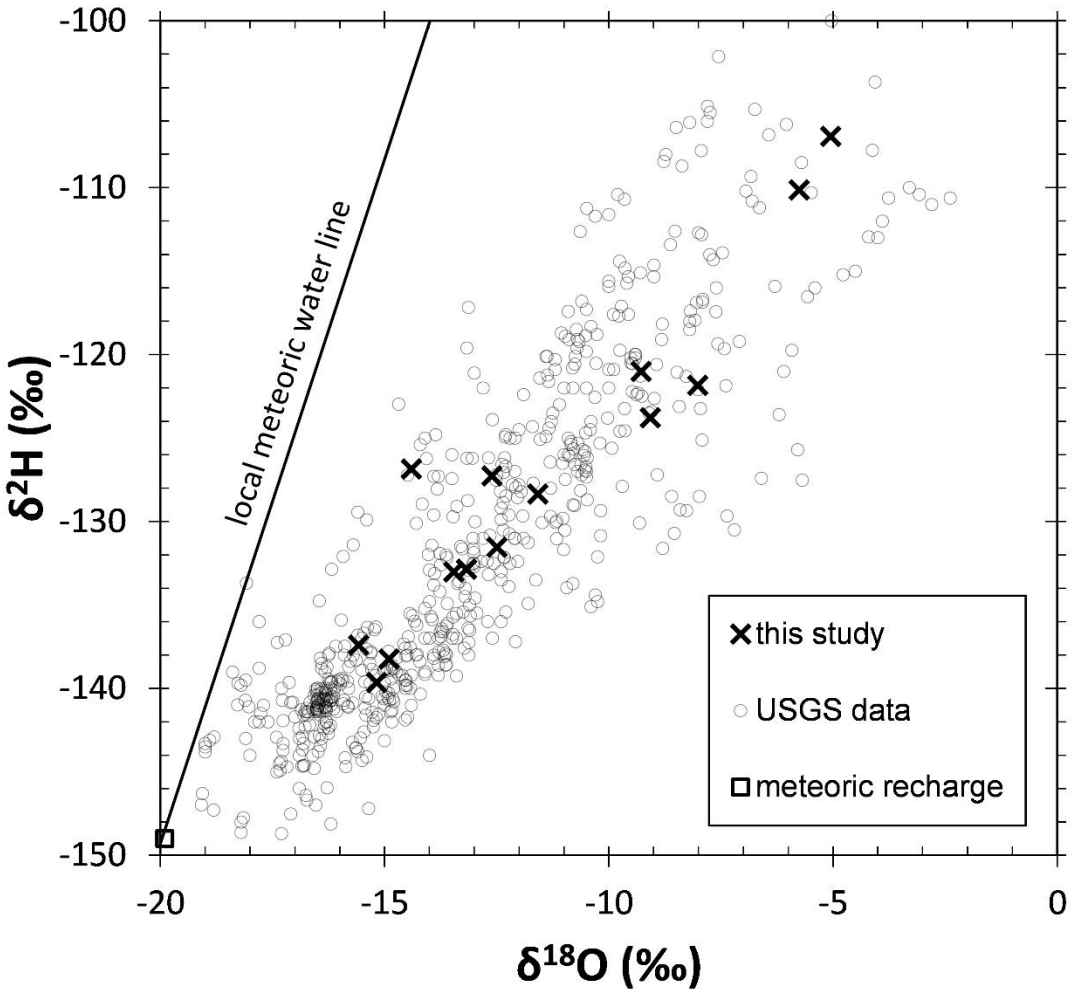

Figure 11. The isotopic composition of hydrogen in hot spring waters (δ^2H) relative to the isotopic composition of oxygen ($\delta^{18}O$) in the same waters. The 14 samples in this study are plotted as crosses along with data derived from USGS reports (open circles) for samples taken throughout YNP from 2003-2013 (Ball *et al.*, 2008; Ball *et al.*, 2010; McCleskey *et al.*, 2014). The local meteoric water line is plotted for reference (Holloway *et al.*, 2009) as is the putative composition of the meteoric recharge water for YNP as reported by Kharaka *et al.* (2002).

-19.9 ‰, which was indicated to be the isotopic composition of meteoric recharge to the geyser basins (Kharaka *et al.*, 2002). The δ^2H and $\delta^{18}O$ values also correlate with sulfate concentrations (Figure 12; only $\delta^{18}O$ shown), though no analogous correlation exists for chloride concentrations. One interpretation of this correlation with sulfate is that the isotopic composition depends most strongly on the amount of hydrothermal vapor input, with relatively uniform extents of surface evaporation and meteoric water isotopic composition. Hydrothermal vapor is predictably isotopically light, but if only a small fraction condenses to form hot spring waters then the resulting fluid would be isotopically heavy. These waters can then be diluted to varying extents with isotopically light meteoric water, concomitantly altering the sulfate and isotopic compositions. This correlation offers additional evidence for mixtures of meteoric water and hydrothermal vapor leading to mildly acidic hot springs waters. Site IG3 does not follow this trend, indicating a different mechanism is required to yield the observed sulfate concentration, which greatly exceeds that of the other samples (*vide infra*).

2.3.6 Carbon and Nitrogen Compositions of Biofilms and Waters

The carbon content of dried biofilm samples ranged from 0.29-9.8 weight percent, while nitrogen content ranged from 0.038-1.35 weight percent (Table 4). It has been demonstrated by analysis of acid-treated samples that the inorganic carbon contents of biofilms and sediments from rhyolite-hosted hot spring locations in YNP are negligible (Havig *et al.*, 2011), therefore this range reflects variation in the amount of biomass between sample sites. Carbon-to-nitrogen ratios were also variable (5.9-12) yet were consistent at sample sites that were sampled in both years.

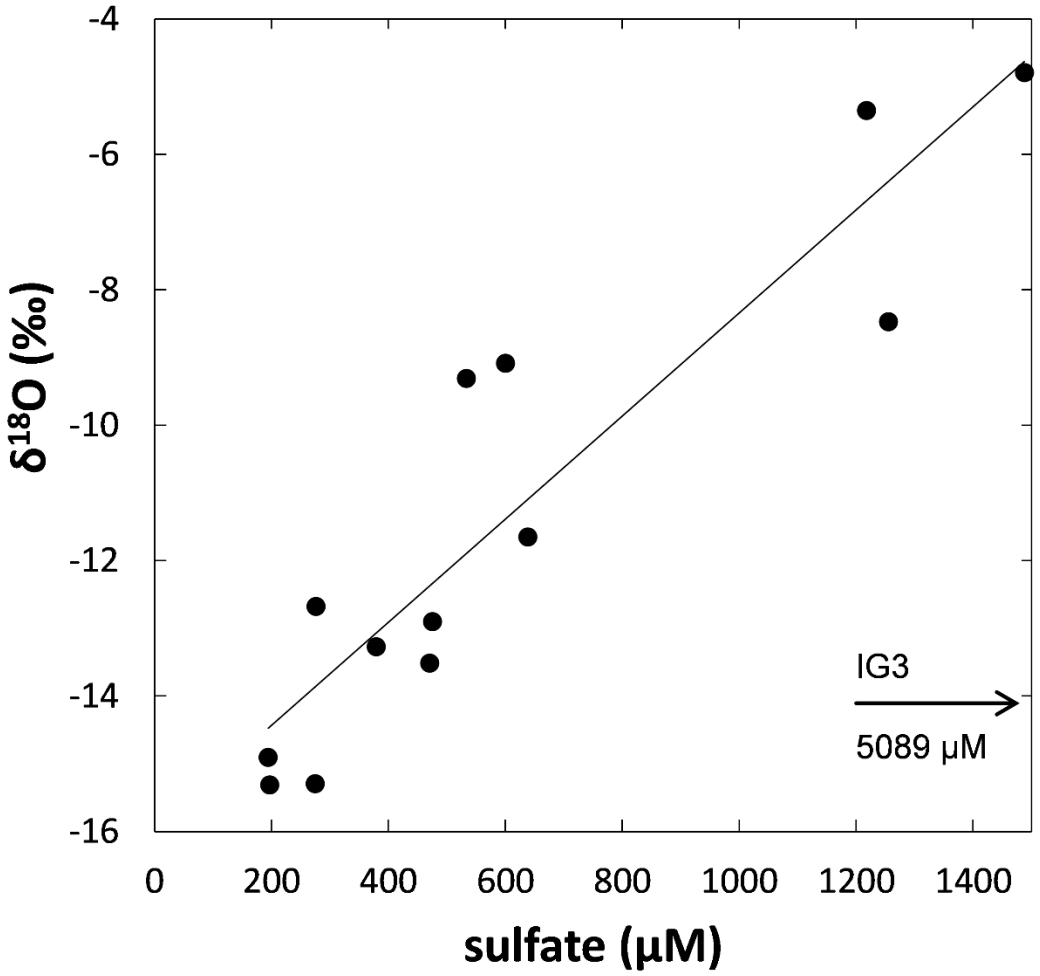

Figure 12. Correlation of $\delta^{18}O$ of hot spring waters with their sulfate concentrations. Site IG3 is indicated with an arrow plotted at its $\delta^{18}O$ value, but its sulfate value is off scale. The least-squares regression line is shown ($R^2 = 0.84$); IG3 is not included in the regression.

Table 4. Carbon and nitrogen composition of biofilms and DIC speciation

Sample	Biofilm wt. % C	SD[a] wt. % C	Biofilm wt. % N	SD wt. % N	Biofilm C:N[b]	DIC µM	SD µM	CO_2 µM	HCO_3^- µM	CO_2/HCO_3^-
FF1	3.37	0.01	0.439	0.001	8.95	573	4	572	0.62	918
IG1	3.15	0.06	0.45	0.01	8.2	537	ND[c]	534	2.8	189
IG2	6.02	0.02	0.707	0.002	9.93	1833	26	1831	2.2	825
IG3	4.97	0.06	0.859	0.005	6.74	92	3	92	0.05	2020
RN1-2011	2.87	0.01	0.545	0.001	6.14	*145*[d]	27	142	3.4	41
RN1-2012	6.9	0.1	1.35	0.04	5.9	73	4	69	3.5	20
RN2	1.08	0.02	0.189	0.003	6.66	*183*	35	180	3.7	48
RN3	0.66	0.01	0.106	0.001	7.3	83	5	83	0.49	169
RS1	1.4	0.2	0.22	0.03	7.4	1125	20	1055	70	15
RS2	1.57	0.01	0.2080	0.0008	8.80	683	22	676	7.6	89
RS3	2.89	0.06	0.300	0.003	11.2	1000	5	869	131	7
RS4	6.1	0.1	0.596	0.008	12	1708	2	1430	278	5
RS5-2011	9.8	0.3	1.27	0.05	9.0	1317	17	1312	4.9	267
RS5-2012	0.29	0.01	0.038	0.003	8.9	2058	ND	1919	139	14

[a]standard deviation. [b]mol:mol ratio. [c]not determined; only a single analysis could be completed. [d]DIC data in italics were below the lowest calibration standard.

Photoautotrophs employ DIC both as a carbon source and an electron acceptor, but do so differently depending on speciation. All sample-site pH values were lower than the pK_a for carbonic acid, implying that DIC concentrations (Table 4) are dominated by aqueous carbon dioxide, as confirmed by speciation calculations. At the highest pH values encountered in this study, ratios of aqueous carbon dioxide to bicarbonate approach unity, but at lower pH, aqueous carbon dioxide dominates by up to 3 orders of magnitude. While it has been suggested that aqueous carbon dioxide may be less bioavailable than bicarbonate, particularly for bacterial phototrophs (Hamilton *et al.*, 2012), it seems unlikely that populations could sustain significant biomass using only bicarbonate at the acidic sites in this study. Indeed, the substrate eventually fixed by RubisCO in the Calvin cycle (i.e., the reductive pentose phosphate cycle) is carbon dioxide (Berg, 2011) and acidophilic *Cyanidiales* appear to rely on free membrane diffusion of carbon dioxide which undergoes an intracellular accumulation mechanism (Zenvirth *et al.*, 1985). Cyanobacteria in this pH regime may also primarily employ aqueous carbon dioxide as an inorganic carbon source for photoautotrophy. Nevertheless, it is possible that the ability to more effectively utilize one substrate or the other may affect niche differentiation between different groups of microbial phototrophs in intermediate pH environments.

Microbial communities require a source of nitrogen to sustain growth, along with other nutrients. While biological fixation of elemental nitrogen is an important process in hot springs (Loiacono *et al.*, 2012; Hamilton *et al.*, 2011a; Hamilton *et al.*, 2011b), this energy-intensive process is observed when concentrations of combined nitrogen are insufficient to support the microbial community (Zehr *et al.*, 2003). Both ammonium and nitrate were detected in all samples, though ammonium exceeded nitrate in all samples

except IG3 (Table 3). Ammonium concentrations are generally higher in acidic springs, as ammonia partitions with the vapor phase during subsurface phase separation and is ionized to ammonium under acidic conditions and is therefore less volatile (Holloway *et al.*, 2011). Ammonium is likely the most important biological nitrogen source in these hot springs.

2.3.7 Dynamics of Mildly Acidic Hot Spring Phototrophic Communities

As described above, hot springs with slightly acidic pH values are dilute and weakly buffered, which is itself a consequence of the derivation of these hot spring fluids largely from meteoric water, an important contributor to hydrothermal fluids in YNP (Hurwitz and Lowenstern, 2014). It is likely that temporal fluctuations in meteoric water availability, perhaps on a seasonal basis, are extensive. Such fluctuations would change the relative contributions of meteoric water and hydrothermal vapor to the hot spring, overwhelming the limited buffering capacity of the fluid and changing the pH. Moreover, as the vapor-phase component increases, additional heat may be added to the system, especially at times of low meteoric water input, resulting in a higher steady-state temperature that can drive additional evaporation, causing lower water levels. It follows that temporal fluctuations in the chemical and physical characteristics of such hot springs may be reflected in the temporal dynamics of the composition and activity of the microbial communities they host, as has been observed in other hot spring systems (Macur *et al.*, 2004; Lacup *et al.*, 2007; Schubotz *et al.*, 2013; Briggs *et al.*, 2014; Wang *et al.* 2014).

Observations of these study sites over several years offer preliminary insights into the dynamics of mildly acidic hot springs. Of particular interest is site IG3, a small (~20 cm diameter) pool near Spray Geyser. This site is presumably closely related to the "small pool near Spray Geyser" studied by Doemel nearly 50 years ago which had the highest pH

reported for an aquatic environment hosting *Cyanidiales* (Doemel, 1970). Modern observations of this site include pH measurements as high as 4.8 (unpublished data), yet at the time of sampling the pH was 2.91. A hailstorm occurred just prior to sampling, which increased the volume of the hot spring and allowed for collection of a complete geochemical sample set. Nevertheless, the aqueous geochemistry indicates the hot spring fluid differs considerably from meteoric water, with the highest concentrations of dissolved solutes (save for oxygen, chloride, and silica) of all samples in this study. In particular, the anomalously high nitrate concentration (564 μM) suggests a significant contribution from sediment pore water, where nitrate is likely produced by nitrifying bacteria. Given the shallow water depth (~2 cm), it is possible that the sediments were disturbed during sampling. Alternatively, it is possible that the hydrology of this hot spring is such that recharge of meteoric water during a rain event leads to an increased flow into the hot spring from the underlying sediments, much like squeezing the water from a sponge. Extensive evaporation due to its especially small volume likely causes the observed enrichments of the major solutes, which accumulate in sediment pore water.

Two of the study sites were sampled in both 2011 and 2012. In 2011, site RS5 yielded DNA, pigment, and carbon/nitrogen data that were comparable to the other sites in the area, while in 2012 the abundances of dissolved oxygen, pigments, and biofilm carbon and nitrogen were substantially lower. No intact chlorophyll *a* was observed, nor was light-driven carbon fixation, indicating that the site was not photosynthetic in 2012. While carbon uptake was not assessed in 2011, the presence of chlorophyll *a* and other data suggest an active phototrophic population at this time. Most notably, the temperature increased from 56.8 °C in 2011 to 70.3 °C in 2012, which apparently exceeded the upper

temperature limit of the phototrophs observed in 2011. The water level in the spring was noticeably lower and the chloride concentration had more than doubled, consistent with a change in the extent of evaporation relative to the fluid supply into the hot spring. The sulfate concentration was lower in 2012 and the pH had increased, suggesting a weaker vapor-phase contribution to the hot spring fluid compared to 2011. A decrease in sulfate could also reflect an increased contribution from microbial sulfate reduction. These observations suggest that the heat flux and temperature of mildly acidic hot springs may not be simply correlated to vapor-phase input as hypothesized above.

In contrast to site RS5, site RN1 was putatively phototrophic in both years of sampling and the water chemistry had not changed appreciably during the year between sampling events (Figure 13). The temperature had slightly increased from 51.6 °C in 2011 to 57.4 °C in 2012, yet in spite of the temperature increase, Rhodophyta represented a larger fraction of the eukaryotic sequences in 2012 than in 2011. Chlorophyta were also observed in 2012 when the temperature was higher, but not in 2011. Nevertheless, the absence of β-cryptoxanthin suggests *Cyanidiales* were not active during either sampling. The temperature in 2012 exceeds the known upper temperature limit for these algae, further substantiating that these algae were inactive. Yet, the increase in the relative abundance of sequences associated with *Cyanidiales* and the appearance of Chlorophyta suggest that these algae may have been active members of the phototrophic community at some point during the intervening period between sampling.

2.3.8 Activity of Phototrophic Populations

Ribosomal gene sequencing indicated the presence of DNA associated with phototrophs from both the Bacteria and the Eukarya in many of the mildly acidic hot

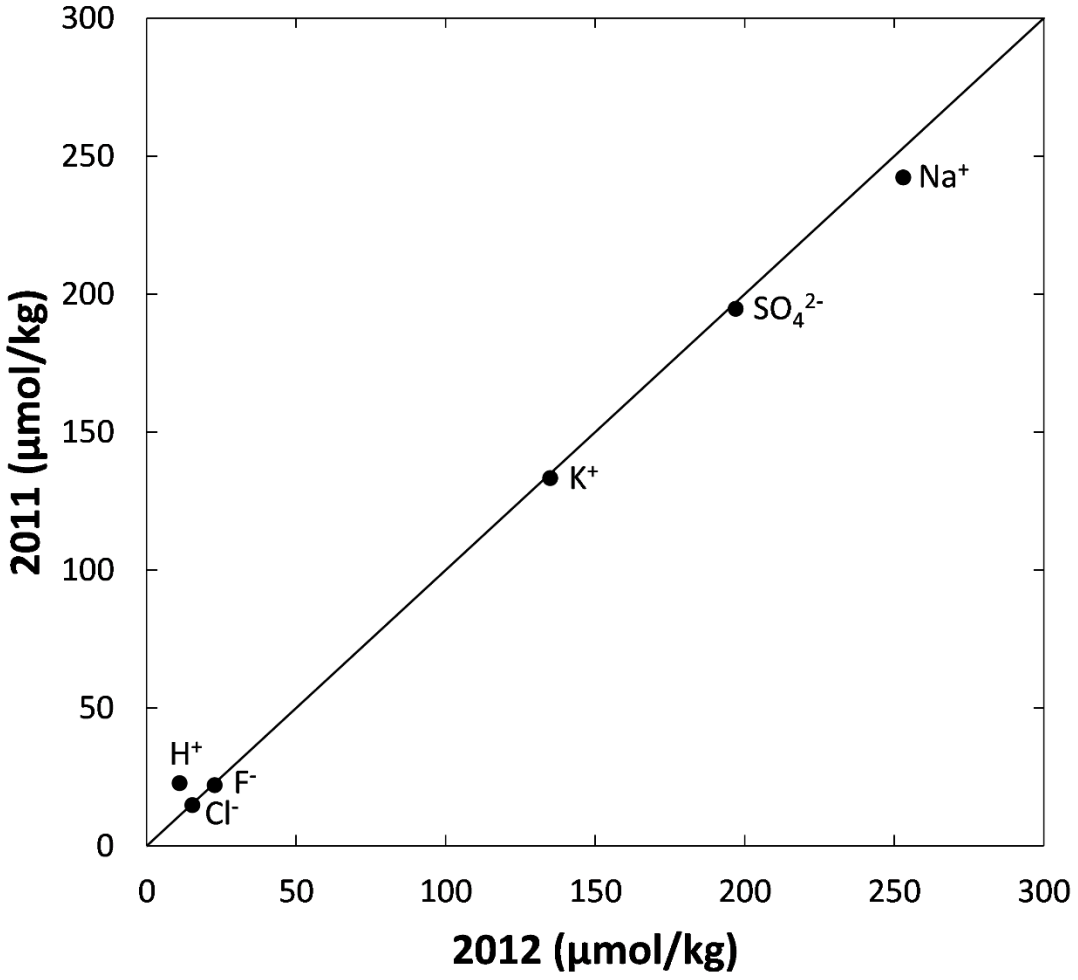

Figure 13. Comparison of major solutes at site RN1 for 2011 and 2012 samples. Corrected H^+ concentrations are shown.

springs studied here, yet the preponderance of the other data enables some conclusions about the activity of these phototrophic populations. The observation of β-cryptoxanthin at only two sites suggests that these may be the only sites where *Cyanidiales* were active when sampling occurred. Site FF1 is particularly noteworthy in that no light-driven carbon fixation was observed, proving that the algae here were inactive. Furthermore, very few chloroplast sequences were identified in the 16S rRNA gene libraries, suggesting that algal chloroplasts had undergone degradation, as illustrated by the observations of chlorophyll degradation products. The temperatures at FF1 as well as RN1-2012, RN3, RS3, RS5-2011, and IG1 all exceeded 56 °C when sampled, which is the known upper temperature limit for *Cyanidiales*. Curiously, β-cryptoxanthin was observed at IG1, suggesting algae were active in spite of the elevated temperature. Perhaps the temperature had only recently, or briefly, exceeded the upper temperature limit of the algae and this biosynthetic intermediate was still present.

In addition to temperature, pH and sulfide can constrain the activity of *Cyanidiales* populations. Sulfide concentrations were relatively low at each of the sample sites and within the documented sulfide tolerance of YNP phototrophs (Cox *et al.*, 2011). Nevertheless, sulfide could at times disfavor algal populations, as *Cyanidiales* algae were found to be less tolerant of sulfide than cyanobacteria (Boyd *et al.*, 2012). The upper pH limit for the alga *C. merolae* exists between a pH of 4 and 5 (Doemel and Brock, 1971), thus pH seems to favor cyanobacteria at many of the sites. The pH for samples RS1, RS3, RS4, and RS5-2012 all exceed 5, suggesting that the algae were inactive when these sites were sampled, as other lines of evidence also indicate. It was observed that *Cyanidiales* isolates are able to lower the ambient pH in culture toward their optimum pH, which was

hypothesized to offer advantages in certain natural settings (Lowell and Castenholz, 2013). Mildly acidic springs are weakly buffered, often small in size, and likely have low fluid fluxes, making them habitats where microbially managed pH may occur in nature. However, indications of inactive algae at many of the sites does not support the utility of this phenomenon at these sites, which if feasible would offer *Cyanidiales* a competitive advantage over cyanobacteria.

Cyanobacteria were present at many of the sites and were likely responsible for phototrophic activity at these sites except those where algae were hypothesized to be active (IG1 and IG2). In contrast to *Cyanidiales*, cyanobacteria are not likely to be constrained by an upper pH limit at these sites and it has been suggested that the upper temperature limit for the *Chlorogloeopsis* spp. present in YNP is near 63 °C (Kallas and Castenholz, 1982; Castenholz, 1996), indicating temperature may also favor cyanobacteria at the geochemical conditions observed during sampling. Additionally, the presence of cyanobacteria below pH 4 at several sites further challenges the validity of this lower pH limit for cyanobacteria. In spite of reports of a sharp pH limit for *Chlorogloeopsis* spp. of 4.5 (Kallas and Castenholz, 1982), these cyanobacteria overwhelmingly outnumbered *Cyanidiales* at site RS5 in 2011 when the pH was 3.82. Intriguingly, cyanobacteria exceeded *Cyanidiales* by over an order of magnitude at IG2 and IG3, both of which had pH values well below 4. While cyanobacteria may not have been active at IG2 given the lack of echinenone and canthaxanthin, IG3 offers an opportunity to assess the extent to which cyanobacteria exhibit metabolic activity below a pH of 4. Unfortunately, the lack of phototrophy at RS5 in 2012 prevented further study of cyanobacteria below pH 4 at this site. Future work targeting the activity of specific populations of phototrophs during different seasons would

help to address these hypotheses regarding the dynamics of phototrophic communities and the activities of their populations.

In addition to cyanobacteria and *Cyanidiales*, other phototrophic groups encountered in the sequence data are Chlorophyta and *Cab. thermophilum*. Though detected in many of the samples, the upper temperature limit for Chlorophyta is likely close to 42 °C, which is the upper temperature limit for a thermotolerant strain of *Chlorella* (Sorokin, 1967). The most thermotolerant strain of *Chlamydamonas* also has a similar upper temperature limit (Gerloff-Elias *et al.*, 2006). Since the ambient spring temperature exceeded 42 °C in each location yielding Chlorophyta sequences, Chlorophyta may have been inactive at the time of sampling and are instead relics of a time when conditions were different, possibly earlier in the year when the temperature was cooler or when the water level was lower and they established populations on the moist walls of the hot spring. The inactivity of these populations is supported by the lack of intact chlorophyll *b*. In contrast, *Cab. thermophilum* was identified at only two sites (RS1 and RS4) along with intact bacteriochlorophyll *a*, yet were significant constituents of those two bacterial communities. It is therefore hypothesized that these phototrophs were active at the time of sampling. Though originally isolated from an alkaline hot spring outflow, *Cab. thermophilum* sequences were also recovered from an acidic, cool location in YNP (Hamilton *et al.*, 2012), so these phototrophs do not appear to be limited to alkaline habitats.

2.3.9 Evolutionary Implications of Phototrophy in Mildly Acidic Hot Springs

The spatial coexistence of cyanobacteria and *Cyanidiales* instigates interesting evolutionary considerations. Indications in this study of inactive algae in the presence of putatively active cyanobacteria suggest the two lineages of phototrophs have achieved

some degree of niche differentiation, separating their niches temporally in response to the physicochemical dynamics of their hot spring habitat, possibly driven largely by seasonal variations. More profoundly, spatial overlap between cyanobacteria and algae makes mildly acidic hot spring candidates for habitats where algae may have originally evolved via endosymbiosis. The endosymbiotic theory for plastid evolution is now widely accepted and all plastids are believed to be monophyletic (Rodriguez-Ezpeleta *et al.,* 2005). Three lineages of algae appear to comprise the primary symbionts that arose via endosymbiosis of a cyanobacterium: the Glaucophyta, Rhodophyta, and Chlorophyta (Gould *et al.*, 2008; Archibald, 2009). While there are some indications that Glaucophyta are the most ancestral (Moreira *et al.,* 2000; Gould *et al.*, 2008), molecular data are equivocal on this point (Rodriguez-Ezpeleta *et al.*, 2005). It is possible that *C. merolae*, very primitive algae that are descendants of the first unicellular Rhodophyta, may have evolved directly via endosymbiosis in a hot spring environment rather than via divergence from other algae such as the Glaucophyta. The phylogeny of the cyanobacterial endosymbiont is also somewhat ambiguous (Criscuolo and Gribaldo, 2011; Falcon *et al.*, 2010, Ochoa de Alda *et al.*, 2014). While the *Chlorogloeopsis* spp. observed in mildly acidic hot springs are filamentous (unpublished observations), this morphology could be a derived trait that evolved from unicellular ancestors and *C. fritschii* isolates are known to exhibit a variety of morphologies, including unicellular forms amenable to endosymbiosis (Evans *et al.*, 1976). One possible selective pressure that could have allowed such an endosymbiosis event to persist evolutionarily would have been a more stable chemical environment for the cyanobacterium once incorporated into the host, perhaps allowing it to withstand more acidic conditions. As suggested by Brock (1973; 1978), this enhanced acid tolerance would

have offered a significant evolutionary advantage if it enabled phototrophs to colonize acidic habitats that were, presumably, previously devoid of phototrophs.

2.4 Conclusions

Overall, the observations here illustrate a spatial overlap in the habitat range of cyanobacteria and algae of the order *Cyanidiales*, yet raise questions regarding the extent to which active populations overlap temporally. Collectively the data offer snapshots of these phototrophic communities and the geochemical conditions in which they live, both of which appear to be undergoing continuous and dynamic change. The ubiquity of *Cyanidiales* sequences across the conditions observed raises fundamental questions concerning the role these populations have in these communities, given the numerical dominance of cyanobacteria. Similarly, the presence of cyanobacterial sequences and pigments well below pH 4 suggests an underappreciated role for cyanobacteria in these acidic habitats. Together, these observations indicate that the concept of a sharp demarcation between eukaryotic and prokaryotic phototrophy with respect to pH is invalid.

2.5 Acknowledgments

This work was supported by the NASA Astrobiology Institute program (grant numbers NNA15BB02A and NAI50018). The results presented here were made possible by Hilairy Hartnett who provided analytical assistance and instrument access and by Amisha Poret-Peterson who provided assistance with DNA extraction and quantification. Extracted DNA was prepared for sequencing my Max Amenabar and sequence data was processed by Professor Eric Boyd, both of Montana State University (MSU); the quantitative PCR data were graciously obtained by Melody Lindsay, also at MSU. Water isotope data for the samples in this work were measured by Randall Debes at ASU.

Cultured biomass for pigment extraction of *Rhodobacter sphaeroides* was graciously provided by Professor Jim Allen's group at ASU. This work would not be possible without the help of numerous assistants who participated in field work, in particular: Alysia Cox, Randall Debes, Jenna Donatelli, Trinity Hamilton, Jeff Havig, Chris Lawler, Jeremy Melton, Adam Monroe, Marc Neveu, Kirtland Robinson, Rebecca Smith, Zachary Smith, and Brian St. Clair. Field work was also made possible through assistance by Christie Hendrix and Stacey Gunther at the Yellowstone Center for Resources (permit YELL-5434).

III. CATALYSIS OF THE CANNIZZARO REACTION BY BULK GOLD

3.1 Introduction

The Cannizzaro reaction (Cannizzaro, 1853) is the base-catalyzed disproportionation of aldehydes and is considered a classic reaction in organic chemistry (Ashby *et al.,* 1987). The rate-limiting step is believed to be bimolecular hydride transfer from the hydrate to another aldehyde equivalent (Swain *et al.,* 1979), though the mechanism has also been suggested to include a radical component. (Ashby *et al.,* 1987; Chung, 1982) While the synthetic utility of this reaction has been supplanted by the advent of metal hydride reducing agents (Swain *et al.,* 1979), it has received renewed interest for its occurrence in supercritical or superheated water in the absence of added base, which has been investigated with benzaldehyde (Ikushima *et al.,* 2001; Nagai *et al.,* 2004a; Tsao *et al.,* 1992), acetaldehyde (Nagai *et al.,* 2003; Nagai *et al.,* 2004b; Nagai *et al.,* 2005; Morooka *et al.,* 2008), and formaldehyde (Tsujino *et al.,* 1999; Watanabe *et al.,* 2003; Morooka *et al.,* 2005; Morooka *et al.,* 2007; Akgul and Kruse, 2013). Here, we report that under hydrothermal conditions the Cannizzaro reaction of benzaldehyde, as well as benzaldehyde decarbonylation and the disproportionation of benzyl alcohol, are catalyzed by bulk gold powder.

Gold finds use in the catalysis of CO oxidation as well as the hydrogenation and oxidation of organic compounds (Stephen *et al.,* 2006), yet bulk gold is traditionally thought to be a poor catalyst (Haruta, 1997; Bond and Thompson, 1999; Bond *et al.,* 2006). Nevertheless, bulk gold has been demonstrated to be an active catalyst in a variety of reactions (Angelici, 2013), including CO oxidation (Ketchie *et al.,* 2007; Zhu and Angelici, 2006), reactions involving isocyanides (Lazar and Angelici, 2006; Lazar *et al.,* 2007;

Klobukowski *et al.,* 2012b), carbenes (Zhou *et al.,* 2009), and amines (Zhou *et al.,* 2010; Zhu and Angelici, 2006; Zhu and Angelici, 2007; Zhu *et al.,* 2008a; Klobukowski *et al.,* 2012a; Klobukowski *et al.,* 2012b; Klobukowski *et al.,* 2011), as well as alcohol oxidations (Ketchie *et al.,* 2007; Guo *et al.,* 2011; Klobukowski *et al.,* 2012a). The current study demonstrates that in the absence of added oxidants or acid/base catalysts, bulk gold catalyzes disproportionations of benzaldehyde and benzyl alcohol in superheated water.

Two commercially available gold powders were employed. Bulk powder was produced from the precipitation of a gold chloride solution with oxalic acid (Salt Lake Metals, Salt Lake City, UT, USA) with particles from ~1 to 1000 microns. A smaller powder with 0.5-0.8 micron particles (Alfa Aesar) was also employed, allowing comparison with a previous study (Ketchie *et al.,* 2007). Experiments were performed in clear fused quartz tubing that was flame sealed under vacuum, analogous to previous work (Yang *et al.,* 2014; Yang *et al.,* 2015). Typical reaction conditions were 100 millilmolal organic concentration held at 200 °C for ~48 hours.

3.2 Experimental Procedures

3.2.1 Materials

All reagents employed in this study were obtained commercially. Benzene (99.9%), toluene (99.9%), benzaldehyde (redistilled, 99.5%), decane (99%), benzyl alcohol (99.8%), benzoic acid (99.5%), diphenylmethane (99%), bibenzyl (99%), and benzyl ether (99%) were all obtained from Sigma-Aldrich (St. Louis, MO, USA) and used as received. 4-methyldiphenylmethane (Matrix Scientific, Columbia, SC, USA) and 2-methyldiphenylmethane (Synquest Laboratories, Alachua, FL, USA) were both obtained at 98% purity while 3-methyldiphenylmethane (97%) was obtained from AK Scientific

(Union City, CA, USA); all were used as received. Dichloromethane (99.9%) was obtained from Fisher Scientific (Pittsburg, PA, USA) and used as received. Deionized water was obtained from a Barnstead Diamond water purification system fed with locally produced reverse osmosis water to yield a final resistivity of 18.2 MΩ•cm.

Bulk gold powder was obtained at 99.995% purity from Salt Lake Metals (Salt Lake City, UT, USA). Before use, the powder was rinsed repeatedly with deionized water in a fine fritted filter, allowed to air dry, then rinsed with multiple aliquots of dichloromethane and allowed to air dry. The powder was then heated overnight at 110 °C before use. For reuse, the used gold was collected on the fritted filter under reduced pressure and the same cleaning procedure was then employed. Gold powder with 0.5-0.8 micron particle size was obtained from Alfa Aesar (Ward Hill, MA, USA) at 99.96% purity. Upon receipt, this powder was transferred to a 4 mL silanized vial with a teflon-lined cap, suspended in deionized water, and allowed to settle. The water was decanted and the procedure was repeated twice. Subsequently, 3 aliquots of methanol (spectroscopy grade) followed by dichloromethane were similarly used and the residual dichloromethane was evaporated under a gentle stream of nitrogen. The surface area of this powder was determined via Brunauer-Emmett-Teller (BET) adsorption of nitrogen using a Micromeritics Tristar 3020 surface area and porosity system with ~2 g of powder.

3.2.2 Methods

All experiments were conducted in clear fused silica tubes (8 mm inner diameter, 12 mm outer diameter) produced from tubing obtained commercially (GM Associates, Oakland, CA, USA). The tubing was cut into ~25 cm lengths, flame-sealed on one end using a glass blowing lathe, and annealed. Each tube was weighed empty using a foam

holder and then weighed again after addition of an aliquot of gold powder. Benzaldehyde (41.0 µL) or benzyl alcohol (41.5 µL) was added dropwise via a 50 µL syringe followed by the addition of water (4.00 mL) via syringe that had been purged with argon for at least one hour, resulting in final organic concentrations of ~100 millimolal. For ~200 millimolal experiments, the volume of organic loaded was doubled. The tube was degassed via 2 freeze-pump-thaw cycles using liquid nitrogen and then frozen and flame-sealed under vacuum with a hydrogen-oxygen flame, resulting in a final experimental tube length of ~14 cm. The tubes were thawed, thoroughly mixed via vortexing, and placed horizontally in the middle of a preheated muffle furnace (Fisher Isotemp) containing a galvanized steel pipe as secondary containment, as previously described (Yang *et al.,* 2015). All experiments were conducted at 200 °C and the temperature was monitored using a thermocouple probe; the variability in temperature over the course of the experiment was estimated to be +/- 2 °C. To end the experiment, the tubes were quenched under tap water, requiring ~2 minutes to reach ambient temperature. The tubes were then frozen at -20 °C until analysis.

Dichloromethane-soluble organics were quantified by liquid-liquid extraction and gas chromatography-flame ionization detection (GC-FID) analysis. Experiment tubes were thawed, scored above the liquid level with a tubing cutter, and broken open, whereupon the contents were poured into a 20 mL amber vial containing ~1.4 g of sodium chloride. 8.00 mL of dichloromethane containing 9.23 mM decane (internal standard) was then added to the vial, with a portion of this solution first being added to the open tube to extract organics adhered to the inside of the tube, then being combined with the other fluids in the vial. Once combined, the vial was sealed with a teflon-lined septum and shaken vigorously

for 45 seconds then allowed to stand for several minutes until phase separation had occurred. The shaking and standing procedure was repeated twice. A portion of the bottom dichloromethane layer was then transferred to 2 mL amber autosampler vials via a Pasteur pipet and sealed with a teflon-lined septum. Samples were then analyzed by GC-FID on either a Varian CP-3800 or Bruker Scion 456 gas chromatograph, both of which were equipped with a Varian CP-8400 autosampler. Injection volumes were 1 µL and all data are based on the means of at least 3 injections. The injector (CP-1177) was isothermal at 275 °C and operated at a split ratio of 15. The carrier gas was helium held constant at 1.5 mL/minute through a capillary column (Supelco 5% phenyl, 95% polydimethylsiloxane, 30 m x 0.25 mm, 0.25 µm film thickness). The column oven was initially 40 °C, but upon injection was increased to 140 °C over 10 minutes, then raised to 300 °C over 32 minutes, after which it was held at 300 °C for 8 minutes. The flame ionization detector temperature was held isothermally at 300 °C.

Integrated peak area ratios of each analyte relative to that of the decane internal standard were expressed in millimolarity units (as dichloromethane solutions) using response factors obtained from calibration curves, which were constructed with at least 4 solutions of known quantities of each analyte and 9.23 mM decane. The response factor of 4-methyldiphenylmethane, determined as described above, was used for all 3 isomers of methyldiphenylmethane. The concentrations of each analyte were then converted to yields of each compound in each experiment. Mass balance was determined via comparison of the equivalents of aromatic rings added to each experiment to the number of equivalents quantified upon analysis, thereby assuming aromatic rings are inert under the experimental conditions.

SEM images of the gold powders were obtained using a FEI XL30 Environmental SEM-FEG to observe surface morphology and particle sizes. The uncoated powders were mounted on 12.7 mm round aluminum pin stubs (Ted Pella, Redding, CA, USA) and adhered to the surface of the mounts by carbon tape. Images were collected in secondary electron mode at 15.00 to 20.00 kV with spot sizes 3.0 to 4.0.

3.3 Results and Discussion

The conversion of benzaldehyde is enhanced by the presence of gold powder (Figure 14) and appears linearly correlated with the amount of gold powder at lower gold loadings. This linear dependence indicates gold is acting as a catalyst under kinetically controlled conditions, which are expected due to the large amount of benzaldehyde relative to the surface area of gold. At higher gold loadings, the linear trend is discontinued, and net conversion of benzaldehyde develops a negative correlation with the amount of gold powder.

The major products in each experiment were benzyl alcohol and benzoic acid (Table 5), which are hypothesized to result from the Cannizzaro reaction (Figure 15, Reaction 1). However, the ratios of acid to alcohol exceeded unity, particularly at higher gold loadings (Figure 16a). Other products observed include benzene and toluene (Figure 17). Benzene is believed to arise from decarbonylation of the aldehyde (Figure 15, Reaction 2). Decarboxylation of benzoic acid could also contribute to the production of benzene, but this reaction is only weakly gold catalyzed (Bell *et al.,* 1994) and its rate is negligible even under more extreme reaction conditions than those studied here (Katritzky *et al.,* 1990a). Unlike benzene, toluene exhibited an induction effect at lower gold loadings (and hence,

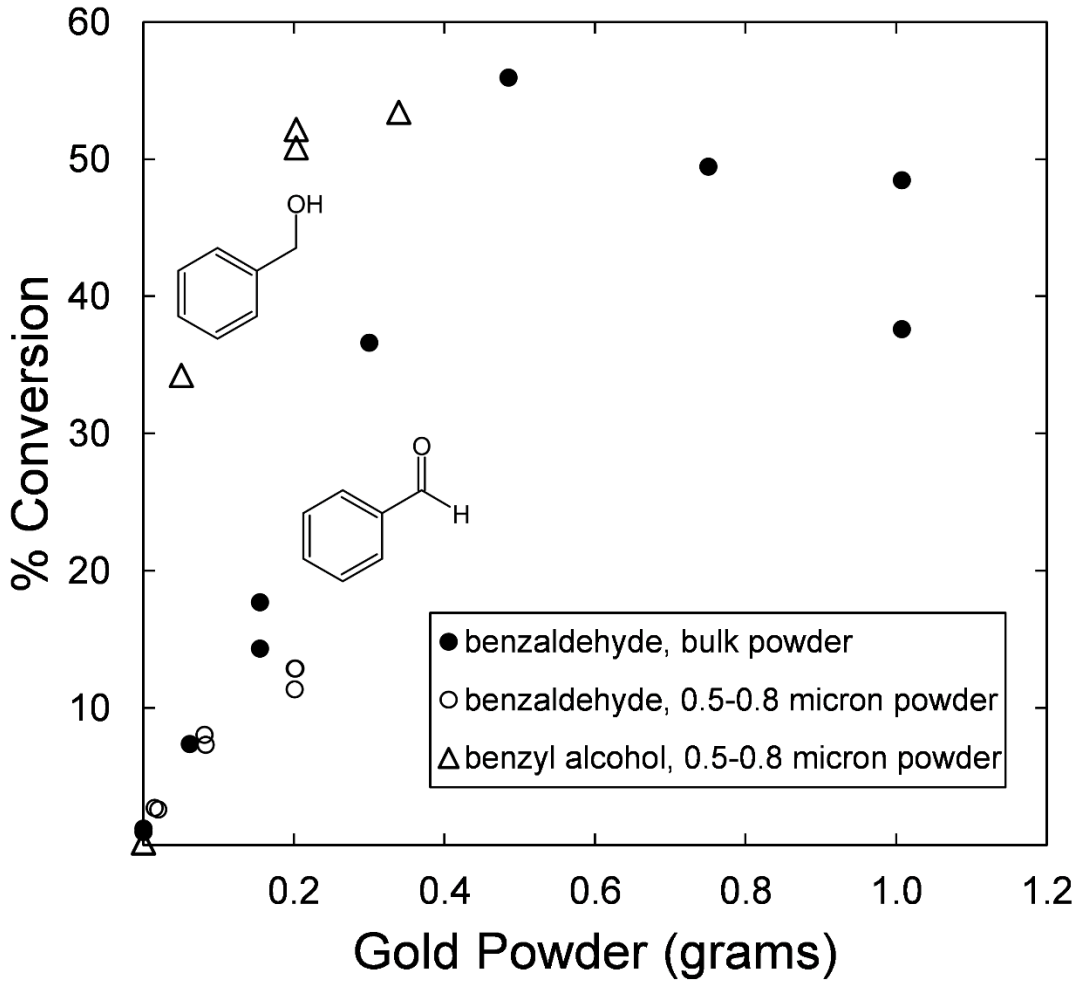

Figure 14. Conversion of benzaldehyde (circles) and benzyl alcohol (triangles) as a function of the mass of gold powder present. All experiments were conducted at 200 °C for a constant time of 2902 minutes. Open symbols indicate the 0.5-0.8 micron powder while filled symbols indicate the bulk powder.

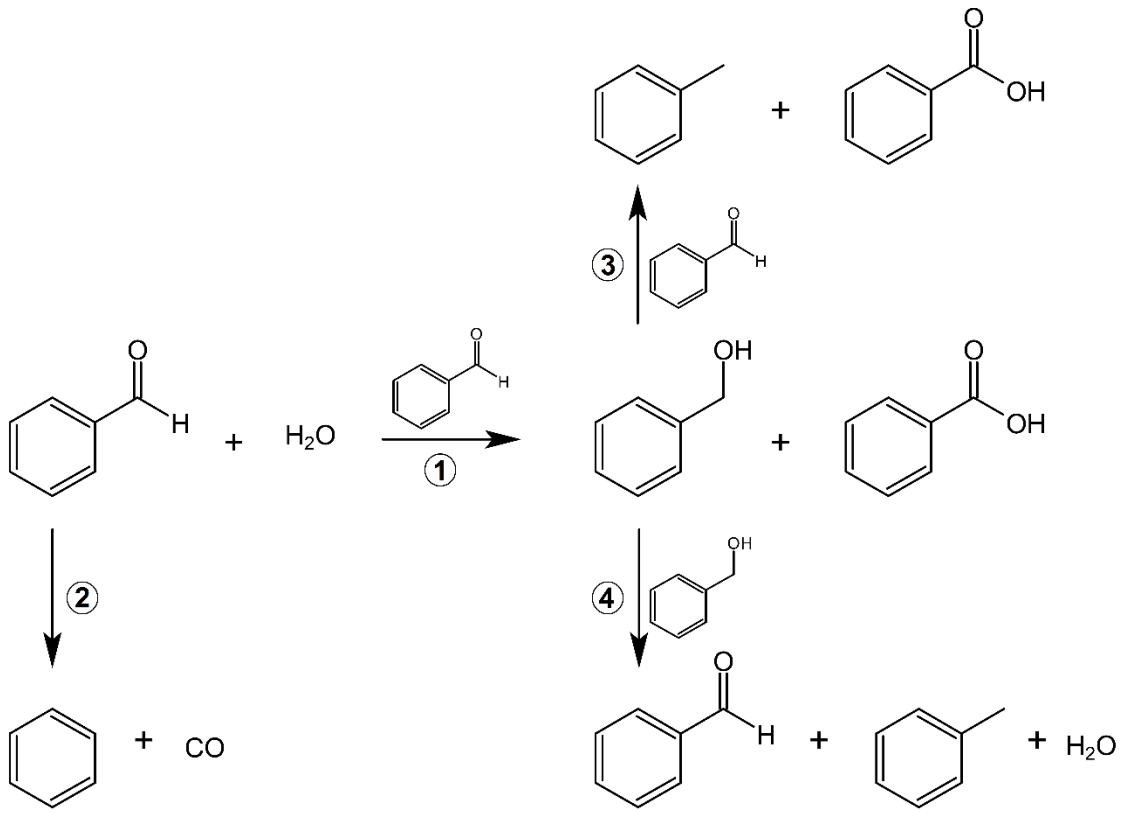

Figure 15. Reactions catalyzed by bulk gold in the benzaldehyde-benzyl alcohol system under hydrothermal conditions.

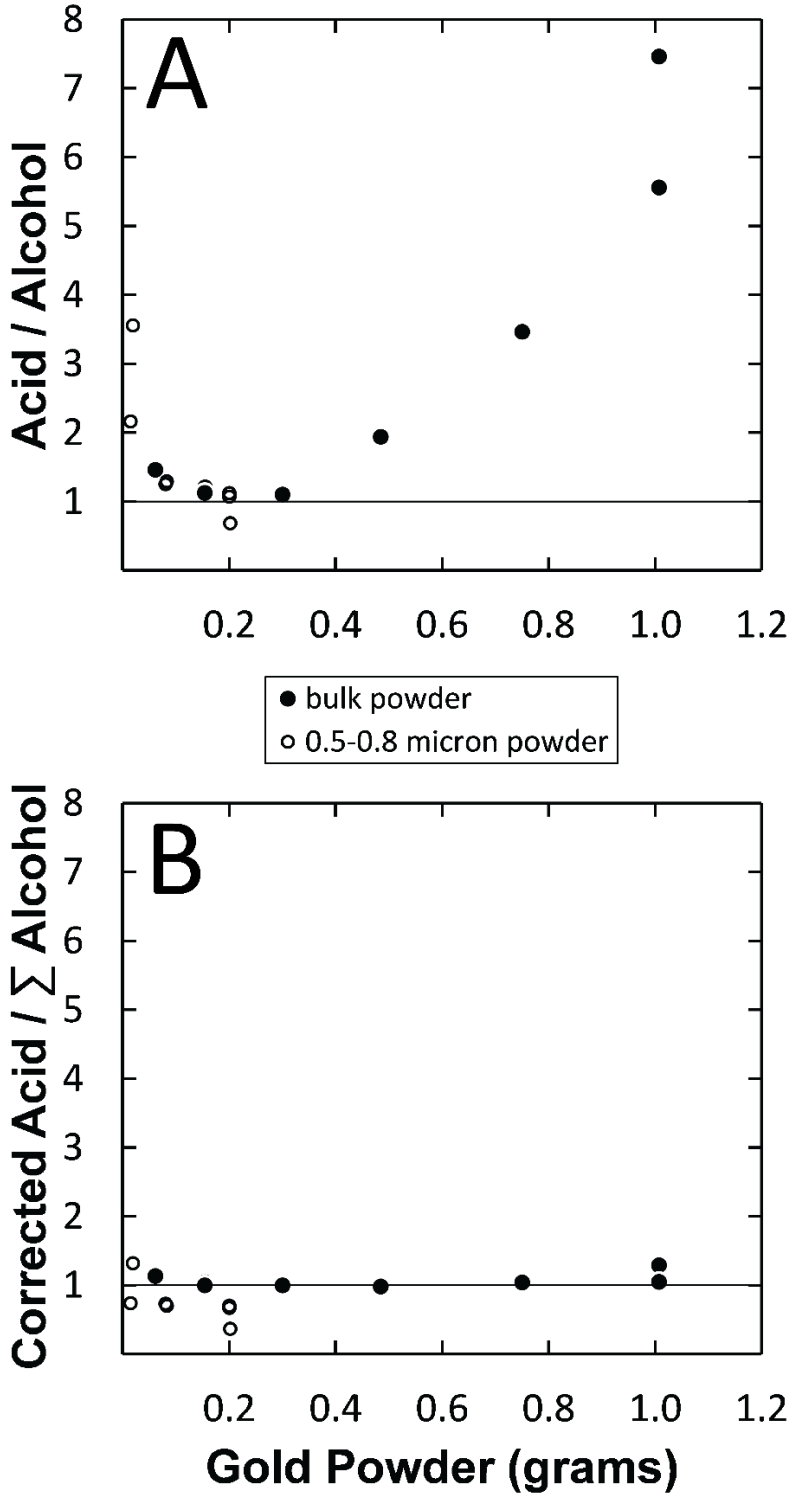

Figure 16. A) The ratio of benzoic acid to benzyl alcohol yield relative to the amount of bulk (filled circles) or 0.5-0.8 micron (open circles) gold powder present. B) The same ratios corrected to account for cross-disproportionation of the alcohol and uncatalyzed reactions.

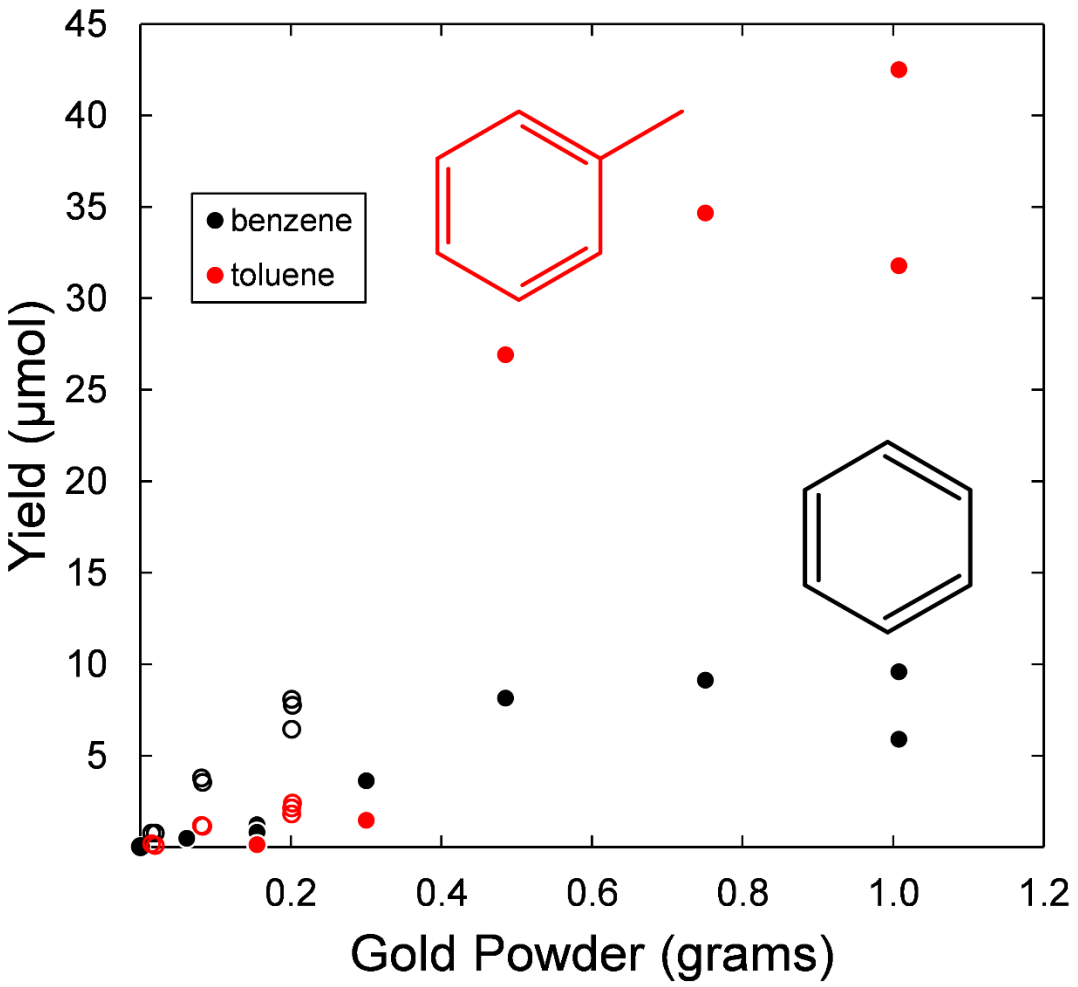

Figure 17. Yields of benzene (black circles) and toluene (red circles) in experiments starting with benzaldehyde in the presence of bulk (filled circles) or 0.5-0.8 micron (open circles) gold powder.

Table 5. Experimental details and product yields for experiments starting with benzaldehyde

powder grams	conversion %	mass balance %	benzaldehyde µmol	benzyl alcohol µmol	benzoic acid µmol	benzene µmol	toluene µmol
no powder, 100 millimolal							
0	0.92	108.44	432.33	0.25	3.72	0.04	<0.01[a]
0	1.16	110.77	440.57	0.26	4.86	0.04	<0.01
bulk powder, 100 millimolal							
0.0618[b]	7.37	103.97	387.51	12.32	18.02	0.50	<0.01
0.1547	17.70	102.36	338.98	33.82	38.11	0.82	0.15
0.1547	14.34	101.82	350.94	26.03	31.40	1.24	0.09
0.3004	36.62	101.84	259.74	68.95	75.99	3.64	1.48
0.4851	55.93	93.73	166.22	59.85	116.02	8.15	26.93
0.7505	49.45	91.42	185.95	30.94	107.13	9.14	34.68
1.0075	48.47	97.98	203.17	16.43	122.57	9.59	42.50
1.0076	37.60	91.44	229.58	15.35	85.32	5.90	31.79
0.5-0.8 micron powder, 100 millimolal							
0.0153	2.73	96.81	378.92	3.06	6.62	0.78	0.18
0.0197	2.60	91.48	358.54	1.91	6.80	0.78	0.10
0.0811	8.04	96.96	358.78	11.71	14.68	3.78	1.20
0.0829	7.31	94.94	354.10	10.14	13.10	3.54	1.14
0.2008	11.36	97.10	346.32	17.04	19.08	6.44	1.83
0.2008	12.87	96.44	338.11	19.16	20.55	8.10	2.15
0.2022	12.89	94.40	330.89	23.02	15.76	7.76	2.42
0.5-0.8 micron powder, 200 millimolal							
0.2009	8.75	97.60	716.76	27.34	26.04	12.89	2.43
0.2022	8.59	98.45	724.28	28.17	24.91	12.46	2.51
no powder, 200 millimolal							
0	1.36	99.54	790.18	0.86	10.04	0.05	<0.01
0	1.33	97.06	770.70	0.88	9.50	0.06	<0.01
0.5-0.8 micron powder, 100 millimolal, half time[c]							
0.0810	6.53	97.46	366.59	9.91	11.76	2.97	0.95
0.2032	11.96	96.62	342.30	18.10	20.17	6.10	2.14
0.2032	27.04	93.78	275.32	45.39	47.07	5.72	3.87

[a]below detection limits. [b]masses in italics refer to gold that had been previously used once. [c]1451 minutes; all other experiments were 2902 minutes.

lower conversions) indicating it is not a primary product of benzaldehyde. Therefore, toluene is proposed to be a product of benzyl alcohol.

The observed acid to alcohol ratios could be consistent with the Cannizzaro reaction if benzyl alcohol were being depleted via secondary reactions. At low yields of benzyl alcohol, the most likely source of toluene is a cross-disproportionation reaction (Figure 15, Reaction 3) which in solution likely occurs via a hemiacetal intermediate (Tsao *et al.,* 1992). To assess this hypothesis, the yield of toluene plus the yield of alcohol were compared with the yield of benzoic acid accounted for by the Cannizzaro reaction. In the absence of gold, benzaldehyde yielded small amounts of both benzyl alcohol and benzoic acid (Figure 18). The yield of benzyl alcohol increased by roughly a factor of 4 for a doubling of benzaldehyde concentration, suggesting it is produced via a second-order reaction, consistent with the Cannizzaro disproportionation. However, the yield of benzoic acid greatly exceeded that of the alcohol and more closely doubled for a doubling of concentration. These observations suggest most of the benzoic acid produced in the absence of gold arises by a first-order oxidative process, with either residual oxygen or water as oxidant, with minor amounts (equivalent to the corresponding yield of benzyl alcohol) arising via disproportionation, causing the concentration dependence of the benzoic acid yield to exceed a ratio of 2. Thus, the yield of benzoic acid in each experiment containing gold was corrected by subtracting this minor amount of benzoic acid derived independently of disproportionation. Furthermore, the yield of toluene in experiments with gold was subtracted from this corrected amount of benzoic acid, since the yield of toluene is stoichiometrically equal to the yield of benzoic acid attributed to the cross-disproportionation. After correction, the ratios of benzoic acid to benzyl alcohol in

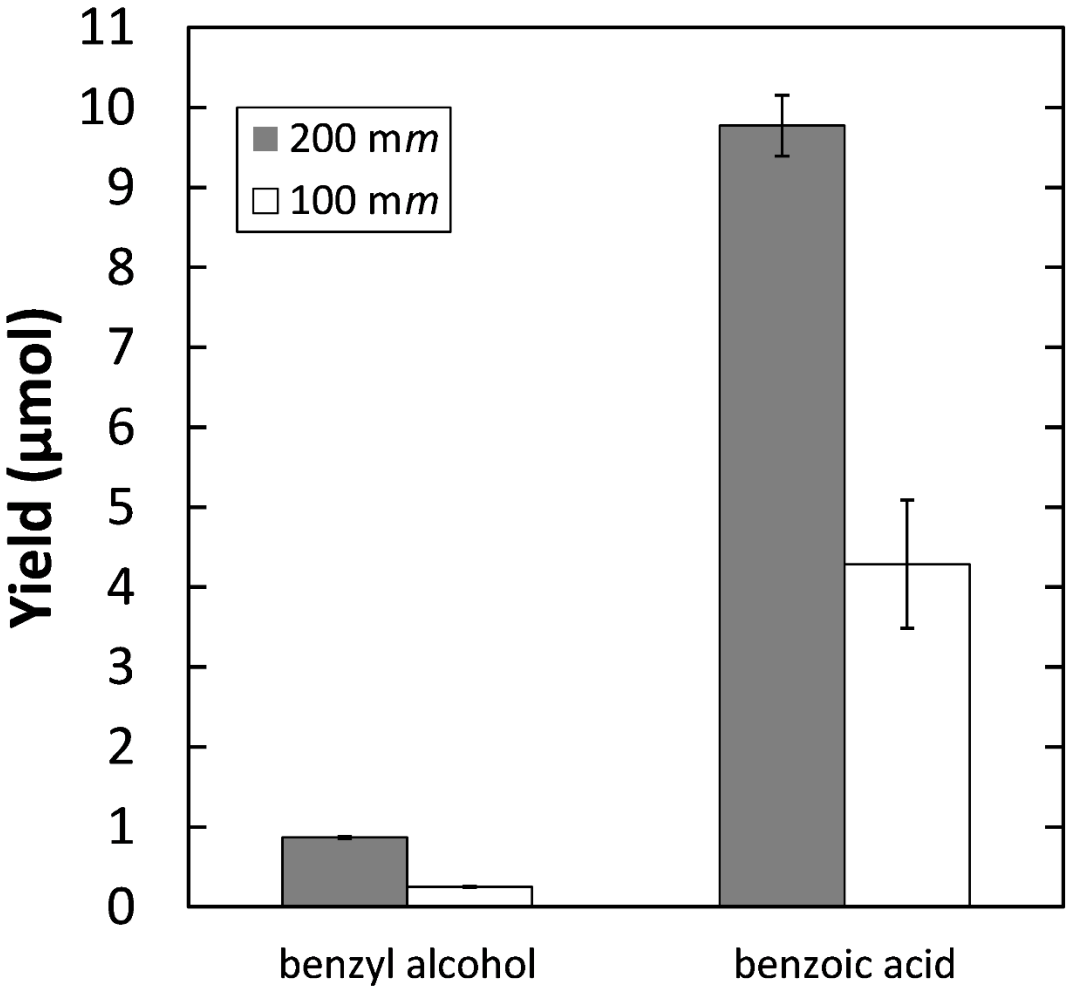

Figure 18. Yields of benzyl alcohol and benzoic acid in experiments without gold for 100 and 200 millimolal initial benzaldehyde concentrations.

experiments with gold are approximately 1 (Figure 16b) and confirm that gold is catalyzing the Cannizzaro reaction.

Cross-disproportionation accounts for the unequal yields of benzyl alcohol and benzoic acid and could account for deviations from linear behavior at higher loadings of gold, since more benzaldehyde would be consumed via cross-disproportionation at the expense of the Cannizzaro reaction. However, cross-disproportionation is unable to account for the apparent decrease in conversion at the highest gold loadings. Experiments were performed starting with benzyl alcohol to further explore its behavior under the experimental conditions. The alcohol was even more reactive in the presence of gold powder than was benzaldehyde (Figure 14). Toluene and benzaldehyde were the major products; other products included benzoic acid, benzene, benzyl ether, methyldiphenylmethanes (i.e., benzyltoluenes), diphenylmethane, and bibenzyl (Figure 19). Yields of all compounds are shown in Table 6. Benzene and benzoic acid putatively arise from benzaldehyde and exhibit increased yields with increasing gold. In contrast, the other products are likely derived via the alcohol and their production decreases with increasing amounts of gold, save for bibenzyl. This decrease, along with their very low yields, suggests that these products arise from reactions in the aqueous phase that are not gold-catalyzed, as higher gold loadings increase the amount of alcohol that reacts via a surface-catalyzed mechanism and decrease the rate of these uncatalyzed pathways. Benzyl ether arises from condensation of two equivalents of benzyl alcohol, while benzyl alcohol can also dehydrate to yield the stable benzyl cation, which can perform electrophilic aromatic substitution upon benzene or toluene to yield diphenylmethane and methyldiphenylmethanes, respectively. The yield of each methyldiphenylmethane isomer

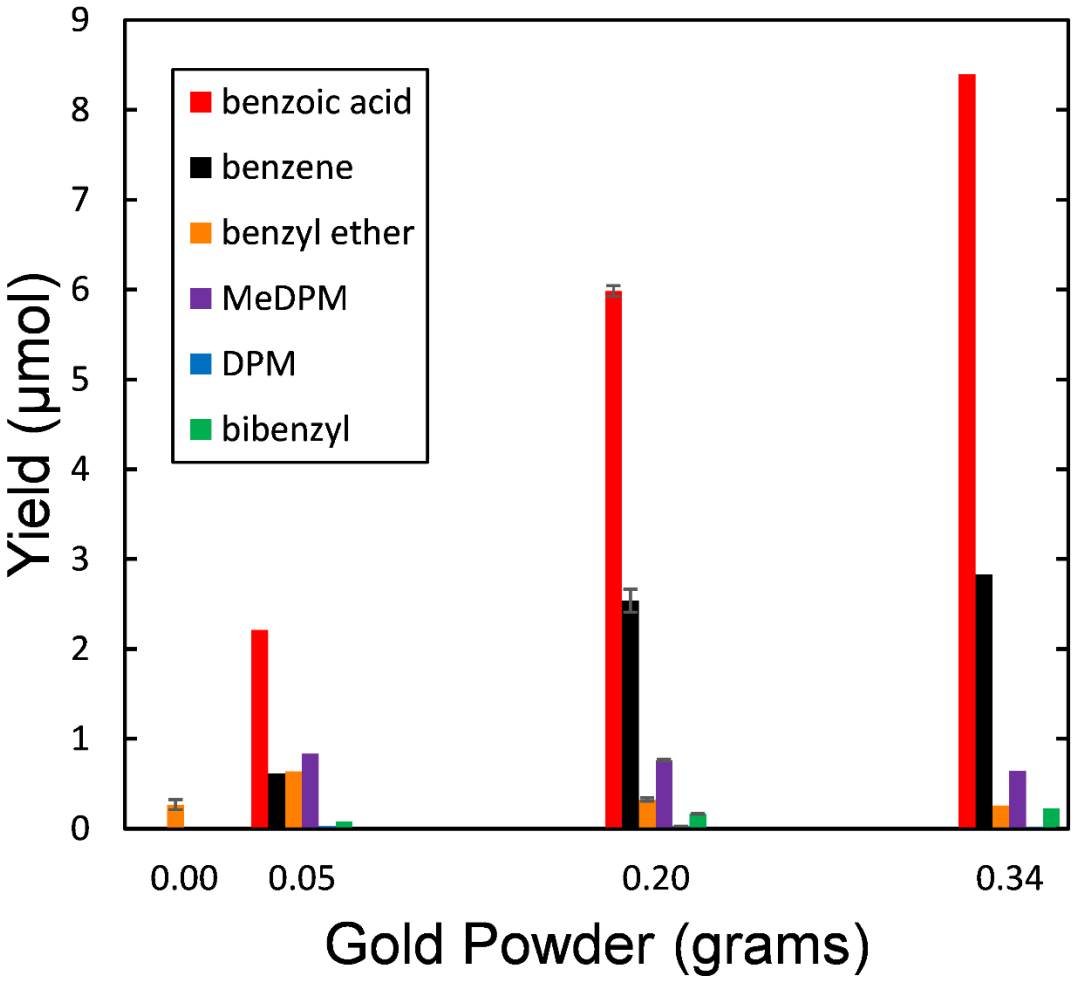

Figure 19. Yields of minor products in experiments starting with benzyl alcohol and 0.5-0.8 micron gold. Uncertainties are the standard deviation of duplicate experiments, which were completed only with no gold and 0.2 grams of gold. Abbreviations: MeDPM, methyldiphenylmethane; DPM, diphenylmethane.

Table 6. Experimental details and product yields of experiments starting with benzyl alcohol (using 0.5-0.8 micron gold powder).

powder	conversion	mass balance	benzald-ehyde	benzyl alcohol	benzoic acid	benzene	toluene	benzyl ether	DPM[b]	4-MeDPM[c]	3-MeDPM	2-MeDPM	bibenzyl
grams	%	%	µmol	µmol	µmol	µmol	µmol	µmol	µmol	µmol	µmol	µmol	µmol
0	0.20	103.00	0.22	411.81	<0.01[a]	<0.01	<0.01	0.31	<0.01	<0.01	<0.01	<0.01	<0.01
0	0.16	103.55	0.21	414.21	<0.01	<0.01	<0.01	0.23	<0.01	<0.01	<0.01	<0.01	<0.01
0.0505	34.25	100.07	68.17	263.61	2.21	0.61	63.18	0.64	0.029	0.38	0.11	0.34	0.08
0.2030	52.22	94.63	85.39	181.16	5.94	2.63	101.49	0.31	0.028	0.34	0.11	0.31	0.17
0.2031	50.86	95.99	85.08	188.97	6.03	2.45	99.47	0.34	0.028	0.35	0.11	0.32	0.16
0.3391	53.46	93.43	84.72	174.20	8.40	2.83	101.88	0.26	0.025	0.29	0.09	0.26	0.22

[a]below detection limits. [b]diphenylmethane. [c]methyldiphenylmethane.

(Figure 20) is consistent with *ortho/para* direction expected for a methyl substituent, with the yield of the *ortho*-isomer being slightly inferior to that of the *para*-isomer most likely due to steric effects. Bibenzyl, most likely, is formed either through a gold-catalyzed reaction of benzyl alcohol or from toluene, more of which is available at higher gold loadings.

The production of benzaldehyde and toluene suggests the disproportionation of benzyl alcohol, which has been observed on nanoparticulate gold powder on silica, titania, and other supports (Meenakshisundaram *et al.,* 2010; Fang *et al.,* 2011; Chen *et al.,* 2014) (Figure 15, Reaction 4). Analogous to the experiments starting with benzaldehyde, the ratio of benzaldehyde to toluene deviated from unity due to the reactivity of benzaldehyde in the presence of gold. Assuming that cross-disproportionation is the dominant mechanism for consuming benzaldehyde at low gold loadings, the total benzaldehyde (benzaldehyde + benzoic acid + benzene + diphenylmethane) was compared to the toluene derived from benzyl alcohol disproportionation (toluene + methyldiphenylmethanes – benzoic acid). Benzaldehyde was further corrected by subtracting the amount of benzaldehyde observed in the absence of gold, since due to the absence of toluene, this seems to be produced by oxidation of benzyl alcohol, again analogous to the situation when beginning with benzaldehyde. The ratios of corrected benzaldehyde to corrected toluene are closer to unity than the uncorrected ratios, except for the experiment with the lowest amount of gold (Figure 21).

Disproportionation of benzyl alcohol provides a mechanism for the reformation of benzaldehyde, which causes the decrease in net conversion of benzaldehyde at the highest gold loadings (Figure 14). Thus, in reactions commencing with benzaldehyde, as gold is

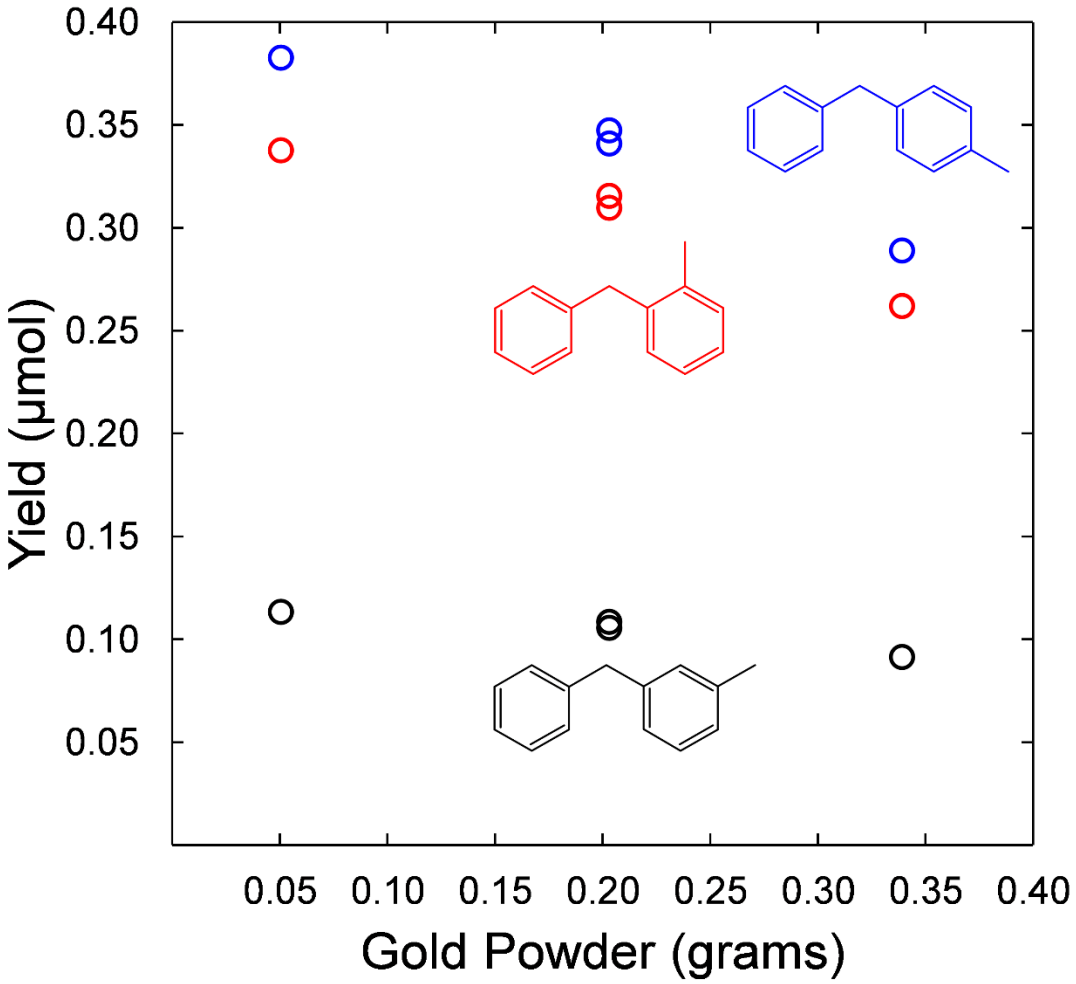

Figure 20. Yields of each isomer of methyldiphenylmethane as a function of the amount of 0.5-0.8 micron gold powder present.

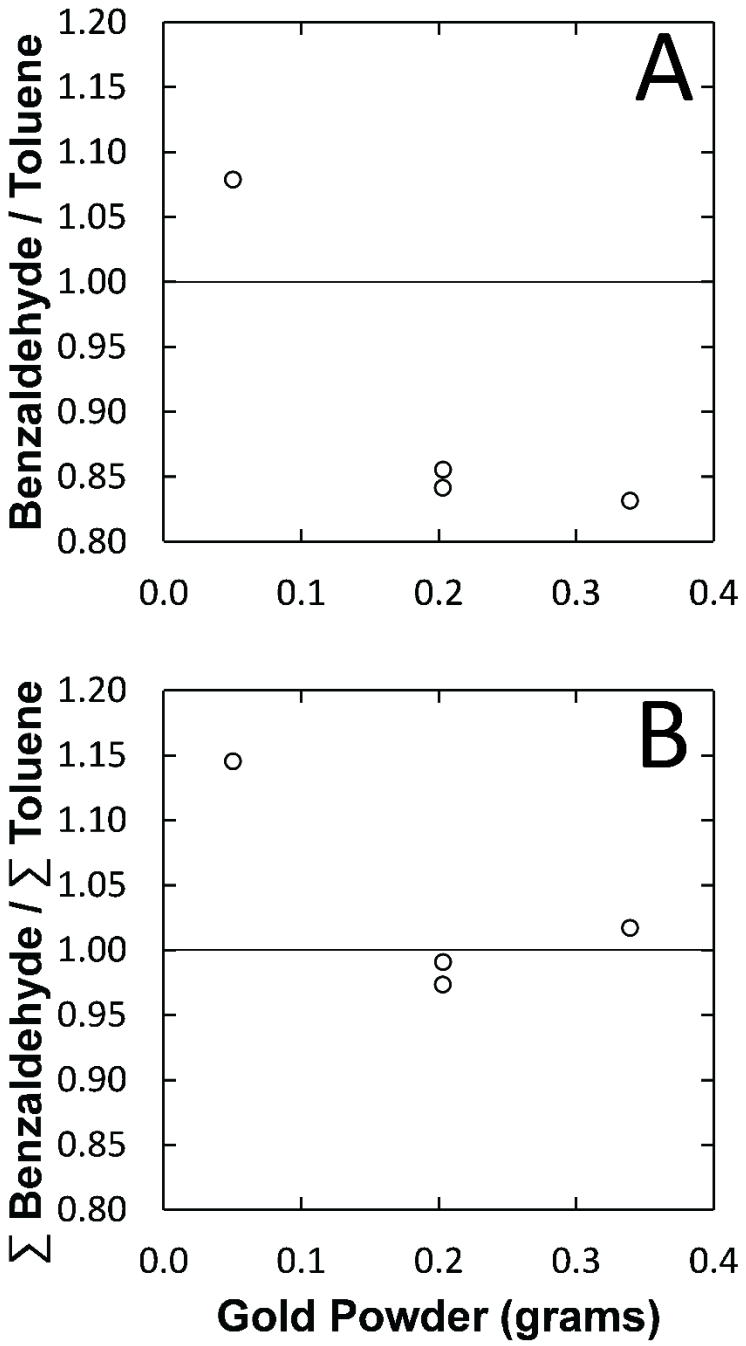

Figure 21. A) Ratios of benzaldehyde to toluene in experiments starting with benzyl alcohol relative to the amount of 0.5-0.8 micron gold powder present. B) The same ratios corrected for consumption of benzaldehyde and toluene by secondary reactions and by subtracting the small amount of benzaldehyde derived in the absence of gold.

increased the system transitions from cross-disproportionation to alcohol disproportionation as the dominant secondary reaction. With respect to the ratio of acid to alcohol, either reaction serves to correct the observed ratios to those commensurate with the Cannizzaro reaction (Figure 22) but it is not possible to directly quantify the contribution of each reaction. The total yields of the Cannizzaro reaction (benzyl alcohol + benzoic acid) for the bulk powder experiments for corrections assuming each type of secondary reaction are shown in Figure 23. The two corrections are indistinguishable at low gold loadings, but deviate at higher loadings where the yield of toluene becomes significant. The transition seems to occur around 0.5 grams of gold, resulting in an overall trend where, at the highest gold loadings, additional gold becomes less and less effective at increasing the rate of the Cannizzaro reaction. This deviation from linear behavior, still present after correction for secondary reactions, may be explained by competitive inhibition of benzaldehyde on the gold surface. At the highest gold loadings, net conversion is near 50% and other compounds likely compete with benzaldehyde for interaction with the active loci of the gold.

Though the surface area of the bulk powder was insufficient for its measurement, the surface area of the 0.5-0.8 micron gold was determined via Brunauer-Emmett-Teller adsorption of nitrogen to be 0.73 m^2/g, which agrees well with the 0.75 m^2/g reported for this powder by Ketchie and colleagues (Ketchie *et al.*, 2007). The total surface area in each experiment with this powder was thereby calculated and converted to the number of surface gold atoms using 0.0875 nm^2 as an estimate of the surface area of a gold atom (Ketchie *et al.*, 2007; Ertl *et al.*, 2008). Turnover per experiment (2902 minutes) was then calculated by linear regression of the equivalents of benzaldehyde or benzyl alcohol converted versus

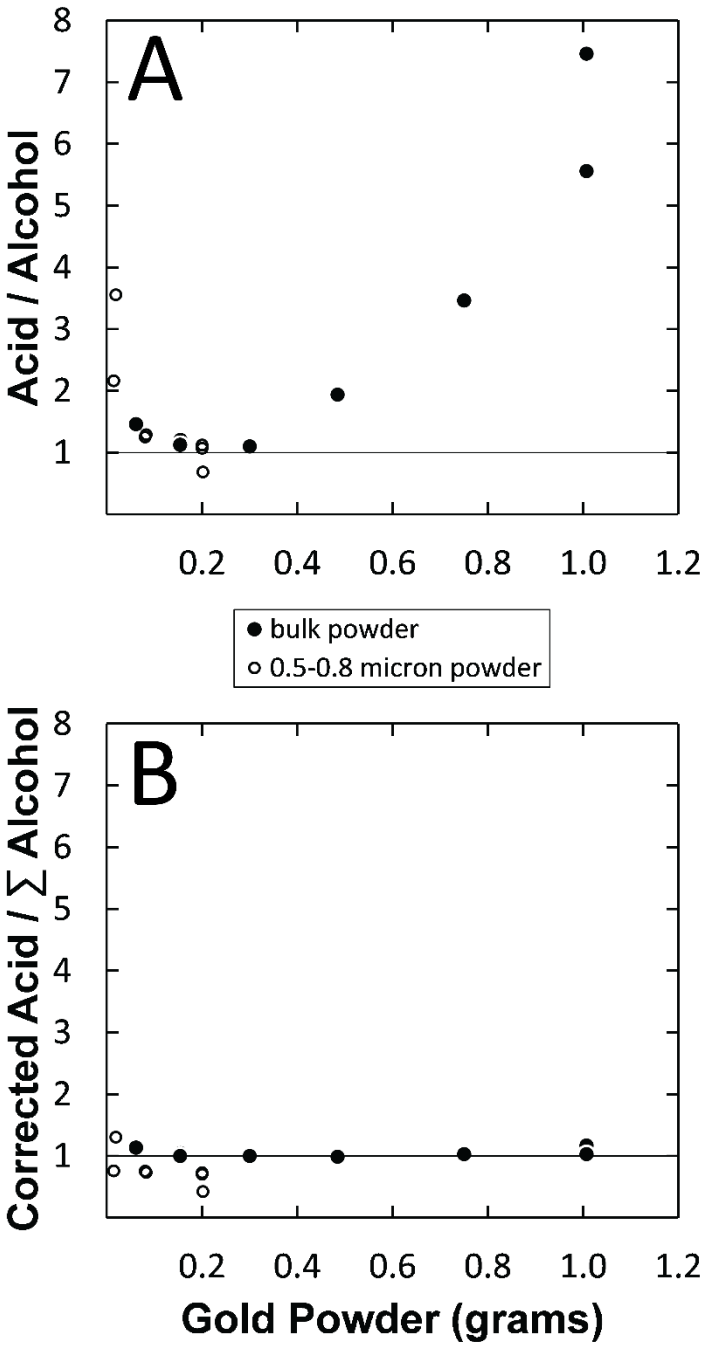

Figure 22. A) Ratio of benzoic acid to benzyl alcohol observed in experiments starting with benzaldehyde relative to the amount of bulk (filled circles) or 0.5-0.8 micron (open circles) gold powder present. B) The same ratios corrected by assuming benzyl alcohol disproportionation is the source of toluene (i.e., total alcohol = benzyl alcohol + 2 * toluene) and also corrected for the small amount of benzoic acid putatively obtained via oxidation.

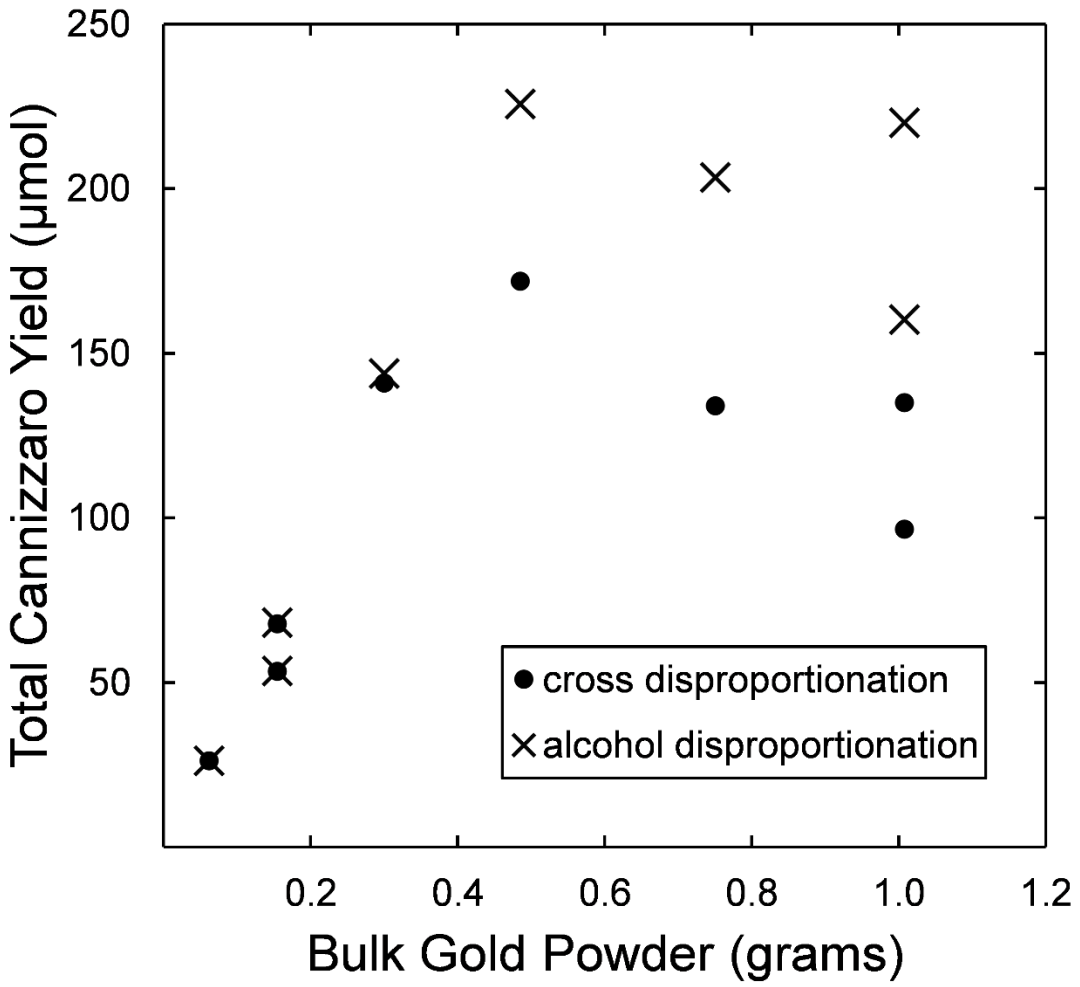

Figure 23. Total yield of the Cannizzaro reaction (benzoic acid + benzyl alcohol) in experiments with bulk gold powder corrected to account for cross disproportionation (circles) and alcohol disproportionation (crosses) reactions.

the number of surface gold atoms (Figure 24), resulting in turnover frequencies (TOFs) of 0.00013 s^{-1} and 0.0011 s^{-1} for benzaldehyde and benzyl alcohol, respectively. Only the lowest gold loading was used for benzyl alcohol as these data have the smallest contribution from other reactions; benzaldehyde exhibits a more linear trend and only the highest gold loading was omitted. The TOF for benzyl alcohol is about 3 orders of magnitude lower than for aqueous glycerol oxidation using the same powder (Ketchie *et al.,* 2007) or for benzyl alcohol oxidation using supported nano powders in organic solvent (Chen *et al.,* 2014). Benzyl alcohol oxidation in the absence of O_2 is still over an order of magnitude faster on supported gold than the TOF observed in this study (Chen *et al.,* 2014).

While gold-catalyzed benzaldehyde and benzyl alcohol disproportionation may be inherently slower than oxidations, the low observed TOFs are probably best attributed to coagulation of the 0.5-0.8 micron powder. SEM images of this powder prior to use showed some particles smaller than 0.5 microns, though there was no strong evidence for particles in excess of ~1 micron (Figure 25a). Prior to each experiment, the vessels were vortexed to create a suspension, but at the end of the experiment the gold existed as a cohesive sheet. This coagulated gold could be broken up during the extraction process, but SEM images of this used powder showed particles greatly in excess of 0.8 microns (Figure 25b). It appears that the original particles had fused; indeed, this used powder was reminiscent of the bulk powder (Appendix B). No such effect was noted when this gold was employed at 60 °C in the presence of water (Ketchie *et al.,* 2007) so it is likely a consequence, at least in part, of the higher temperature used in this study. As such, coagulation would decrease the surface area available for catalysis and the measured surface areas would only be available during the earliest stages of the experiment.

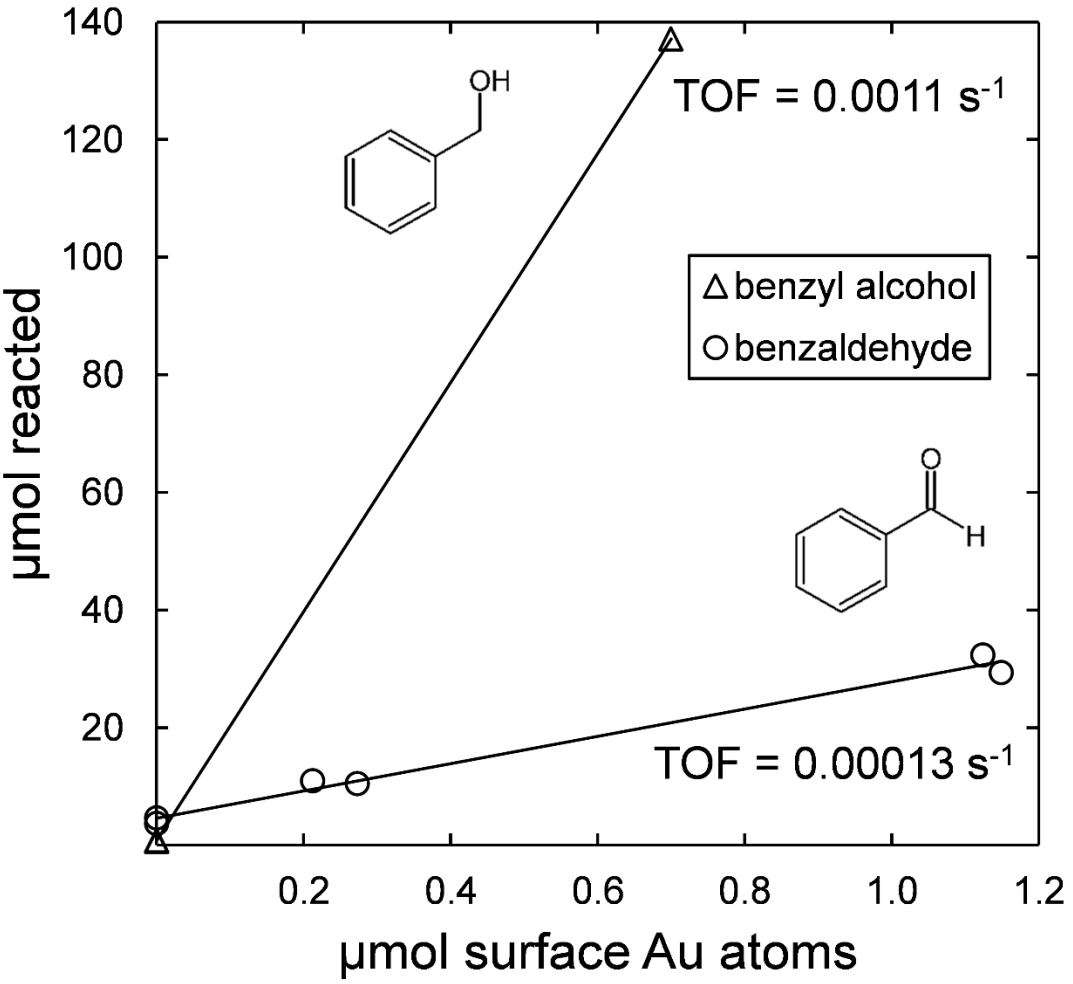

Figure 24. Total benzaldehyde (circles) or benzyl alcohol (triangles) consumed versus the number of surface gold atoms. Regression leads to turnover frequencies calculated using the total reaction time (2902 minutes).

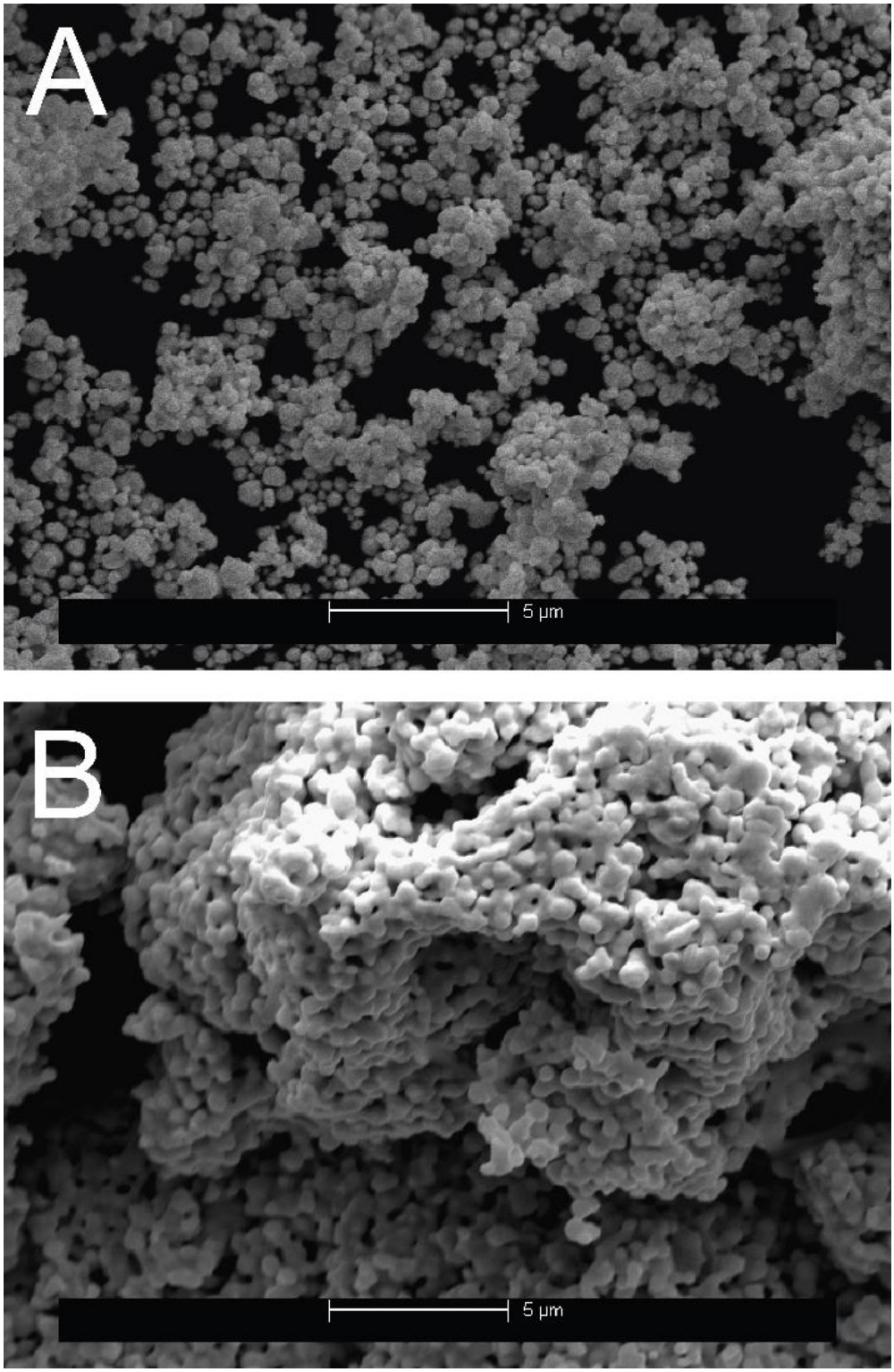

Figure 25. A) 0.5-0.8 micron powder after processing but prior to use in an experiment. B) 0.5-0.8 micron powder recovered from an experiment with benzaldehyde (200 °C, 2902 minutes).

To evaluate this hypothesis, several experiments were conducted with benzaldehyde for half the normal time (1451 minutes). Most of these experiments exhibited conversions on par with those observed for the normal time (2902 minutes) at the same gold loading, indicating that nearly all the conversion occurs in the first half of the experiment, likely even in the first hours of the experiment before gold coagulation has become significant (Figure 26). The conversion of one such half-time experiment greatly exceeded that of other experiments, even those conducted for the usual 2902 minutes. The origin of this anomalous result is unknown, as the gold in this experiment macroscopically appeared coagulated like the others. Presumably due to its larger particle size and heterogeneity, the bulk powder did not coagulate and no obvious differences were observed in SEM images of used and unused bulk powders (Appendix B). Indeed, the bulk powder was recovered, washed, and reused for some experiments, though reuse of this gold more than once exhibited a noticeable yet irreproducible decrease in catalytic ability (results not shown). The reasons for this loss of catalytic performance is unclear, though disproportionate loss of the smallest particles from the bulk gold powder would decrease its specific surface area, leading to decreased conversions for a given mass of gold. Alternatively, it has been suggested benzoic acid is capable of poisoning gold-based catalysts (Abad *et al.,* 2008; Klitgaard *et al.,* 2008; Skupien *et al.,* 2014).

A slight enhancement in the yields of benzyl alcohol and benzoic acid was observed upon a doubling of the starting concentration of benzaldehyde, which indicates a role for aqueous species in the rate-determining step (Figure 27). However, no apparent concentration dependence exists for toluene. This lack of concentration dependence may indicate the rate-determining step leading to toluene formation solely involves surface-

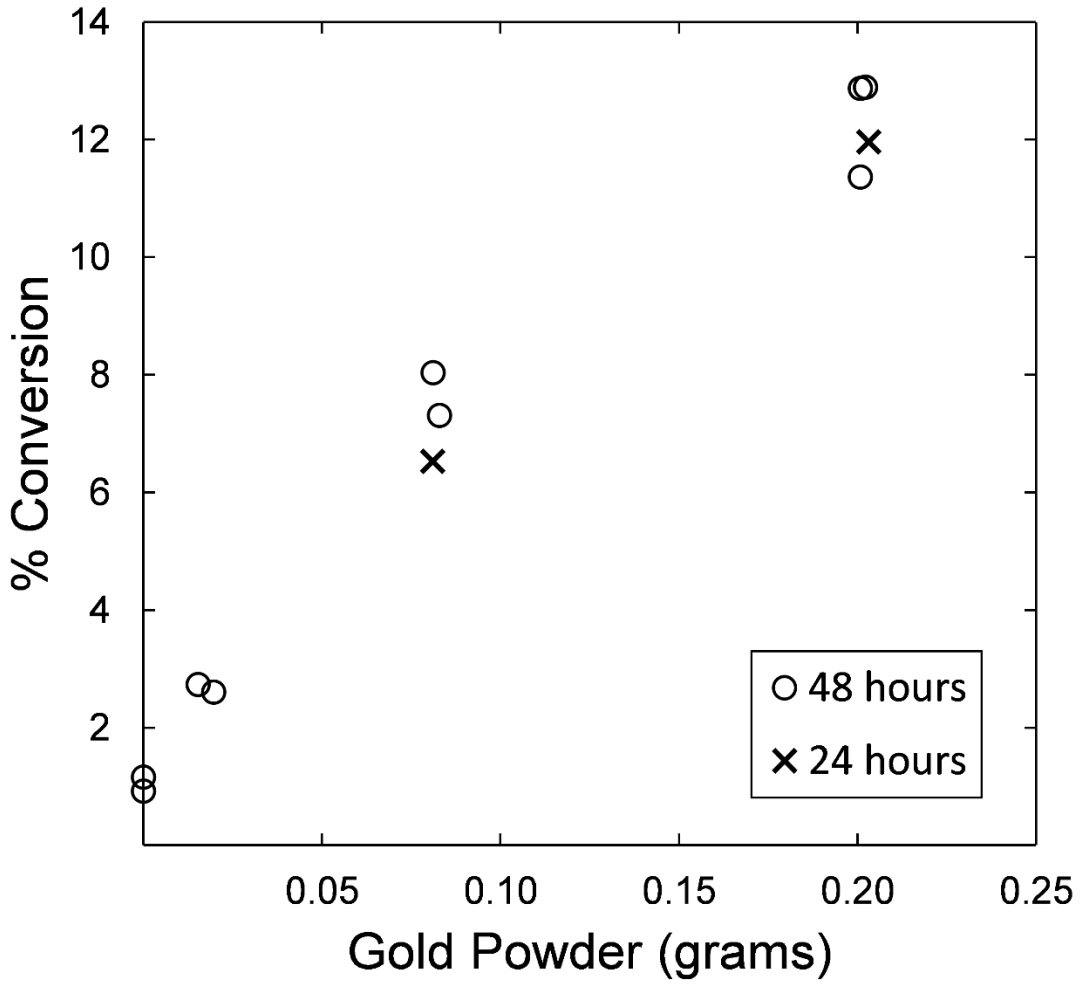

Figure 26. Conversion of benzaldehyde in experiments with 0.5-0.8 micron gold powder for full-time (2902 minutes) and half-time (1451 minutes) experiments.

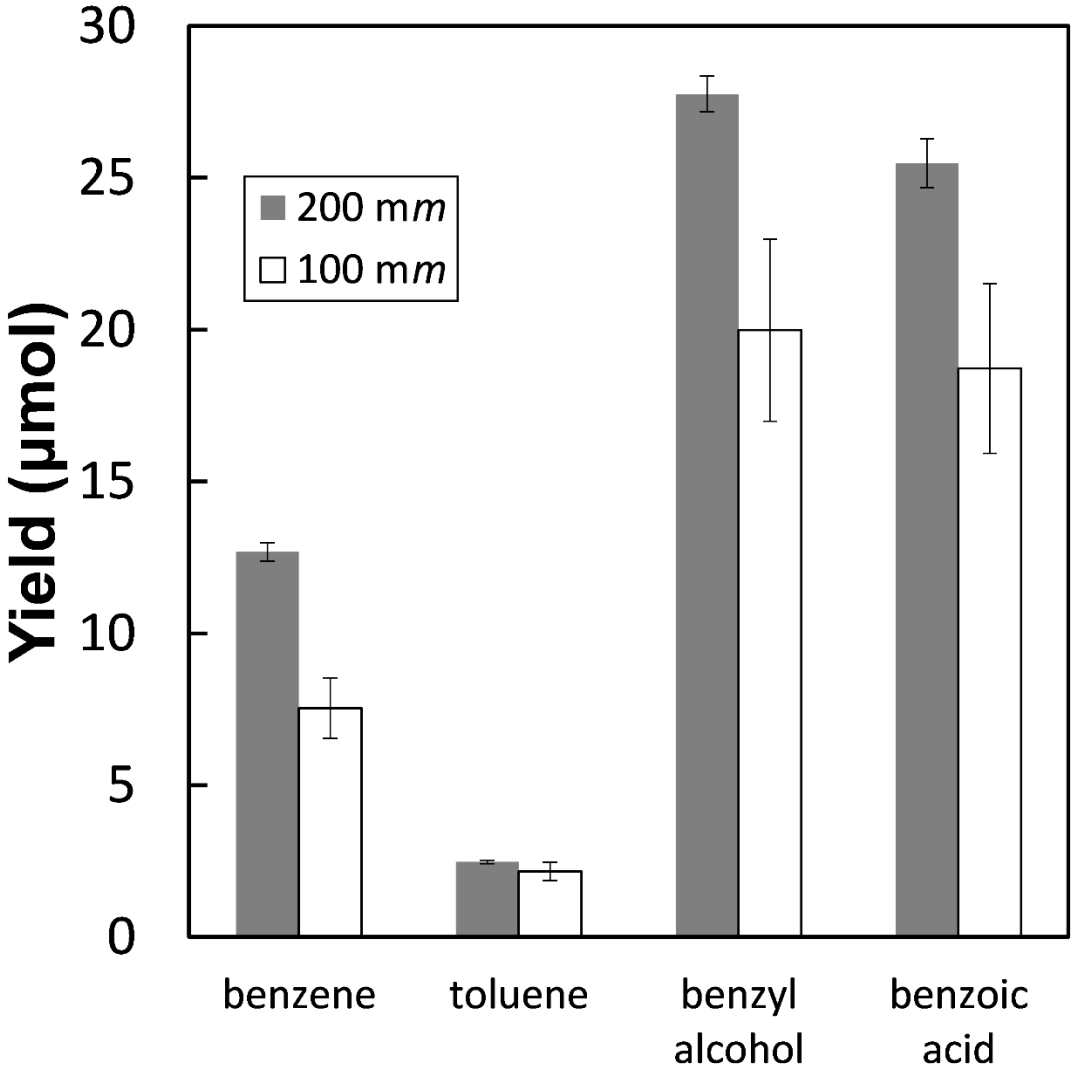

Figure 27. Yields of major products in experiments with approximately 200 mg of 0.5-0.8 micron gold for 100 and 200 millimolal starting benzaldehyde concentrations. Results are the mean and standard deviation of replicate experiments.

bound species. Alternatively, the increased yield of benzyl alcohol at the higher benzaldehyde concentration, which would be expected to lead to increased toluene production, may be offset by benzyl alcohol interacting less with the gold surface due to competition with benzaldehyde. In contrast to toluene, benzene exhibited a concentration dependence similar to benzyl alcohol and benzoic acid, again suggesting its rate-determining step involves an aqueous species. In solution, decarbonylation proceeds via protonation of the *ipso*-carbon (Schubert and Zahler, 1954), but its mechanism in the presence of gold is unclear.

Observations of disproportionations of both benzaldehyde and benzyl alcohol suggest gold is capable of catalyzing hydride transfer, which is putatively the rate-determining step for both reactions. Indeed, substituent effects for gold-catalyzed benzyl alcohol oxidation indicate a positively charged transition state at the α-carbon (Abad *et al.,* 2008; Fristrup *et al.,* 2008; Chen *et al.,* 2014) and abstraction of a hydrogen from this carbon has been invoked as rate-determining (Abad *et al.,* 2008; Conte *et al.,* 2009; Shang and Liu, 2011; Shylesh *et al.,* 2015). Direct evidence for bonding of hydrogen to gold was obtained via spin-trapping with electroparamagnetic resonance spectroscopy (Conte *et al.,* 2009) and calculations show this is feasible on pure gold (Shang and Liu, 2011). Under oxic conditions, molecular oxygen serves to regenerate the active gold surface by oxidizing gold-bound hydride (Abad *et al.,* 2008; Conte *et al.,* 2009; Shang and Liu, 2011) and also participates in the regeneration of gold-affiliated hydroxide when base is present (Zope *et al.,* 2010; Shang and Liu, 2011), which facilitates formation of alkoxide intermediates (Zhu *et al.,* 2008b; Shang and Liu, 2011; Ferraz *et al.,* 2016). Oxidation of benzyl alcohol via dehydrogenation in the absence of oxygen has also been studied on gold catalysts with

basic supports, such as hydrotalcite (Mitsudome *et al.,* 2009; Fang *et al.,* 2010; Fang *et al.,* 2011; Chen *et al.,* 2014; Shylesh *et al.,* 2015). In the absence of oxygen or base, disproportionation becomes the favored mechanism for gold-bound hydride. In the current system, the hydrate of benzaldehyde (i.e., the geminal diol) may also serve as a hydride donor, as hydrates have been suggested to interact with gold in a manner similar to other alcohols (Zope *et al.,* 2010; Shang and Liu, 2011). Gold is apparently a better hydride acceptor than benzaldehyde, thus increasing the rate of the rate-determining step compared to the reaction in the absence of gold. Nevertheless, infrared spectral data suggest that benzyl alcohol initially interacts with gold without covalent bonding during disproportionation, at least to some extent (Nowicka *et al.,* 2013). An additional carbonyl band was present at an especially low wavenumber (1655 cm^{-1}) indicative of donation of electron density to gold, though its origin is uncertain (Nowicka *et al.,* 2013). Thus, an aspect of the surface-catalyzed mechanism may be simply that the rate enhancement is derived from the locally higher concentrations of hydride donors and acceptors on the gold surface relative to those in solution, regardless of how these molecules bond or interact with the surface.

3.4 Conclusions

Catalysis of the Cannizzaro disproportionation reaction, as well as the disproportionation of benzyl alcohol and decarbonylation of benzaldehyde by bulk gold powder, offers novel insights into the catalytic abilities of gold. Catalysis occurs in the absence of acids, bases, or any other reagents. The low measured turnover frequencies could be substantially improved by use of gold with an inert support to prevent coagulation, which would also offer a substantial improvement in atom economy relative to bulk gold.

Appreciable rates are likely attainable at lower temperatures than those employed in this study, which also may mitigate coagulation. Nonetheless, within the realm of hydrothermal experiments that are traditionally performed in gold vessels for their perceived inertness, the reactivities of organic compounds in water alone presently observed at modest temperature and time may give pause to researchers seeking to mitigate container effects.

3.5 Acknowledgments

This work was supported by funding from the National Science Foundation (grants OCE-0826588 and OCE-1357243). SEM imaging was completed by Kristin Johnson using the facilities of the LeRoy Eyring Center for Solid State Science. Production of the silica tubes was completed by Christine Roeger of the ASU glassblowing facility. BET analyses were completed with the assistance of the Goldwater Environmental Laboratory. This work benefited greatly from many helpful discussions over the course of this project amongst the hydrothermal organic geochemistry group at ASU.

IV. KINETICS AND CHEMISTRY OF ALDEHYDES UNDER HYDROTHERMAL CONDITIONS

4.1 Introduction

In sedimentary basins, organic carbon represents as much as 25% of the carbon present, which collectively is roughly 4 orders of magnitude more organic carbon than is present in the biosphere (Falkowski *et al.,* 2000). There exists great interest in understanding the reaction pathways that lead to the complex mixture of organic compounds present in such systems, yet the mechanisms of these reactions remain poorly characterized. Spurred by evidence for metastable equilibrium states amongst certain organic compounds in natural systems (Helgeson *et al.,* 1993; Shock *et al.,* 2013), metastability was experimentally demonstrated between ethane and ethene (Seewald, 1994). Additional experiments demonstrated alkanes could lead to the production of carboxylic acids (Seewald, 2001), which are among the most abundant organic compounds in natural systems (Willey *et al.,* 1975; Carothers and Kharaka, 1978; Lang *et al.,* 2010).

A key intermediate in the proposed transformation of alkanes to carboxylic acids is the ketone, which was proposed to undergo C-C cleavage reactions adjacent to the carbonyl to yield two carboxylic acids (Seewald, 2001). However, experiments with dibenzylketone conducted in water only failed to yield any carboxylic acids (Yang *et al.,* 2012), suggesting that the C-C bond breaking step indicated by Seewald (2001) is mineral catalyzed by the mineral buffers present in those experiments, or that the carboxylic acids arose via some unknown pathway. Ketones are invoked because they result from the dehydrogenation of secondary alcohols, the production of which is favored via Markovnikov hydration of alkenes due to the higher stability of the secondary carbocation intermediates involved.

Nevertheless, evidence from a different experimental system demonstrated that all possible (i.e., both Markovnikov and *anti*-Markovnikov) alcohols were detectable from a starting alkane or alkene (Shipp *et al.*, 2013). These observations suggest that aldehydes, arising from primary alcohols, could also be produced from alkanes and alkenes under hydrothermal conditions.

Aldehydes are important constituents in hydrothermal settings (Schulte and Shock, 1993). They have been identified in diverse samples, ranging from volcanic gases (Tassi *et al.*, 2015) to meteorites (Monroe and Pizzarello, 2011; Elsila *et al.*, 2012). In the context of meteorites, aldehydes are commonly invoked as intermediates in the abiotic synthesis of amino acids via a Strecker mechanism (Schulte and Shock, 1993; Monroe and Pizzarello, 2011). Under hydrothermal conditions, aldehydes are thought to undergo disproportionation, a bimolecular reaction where two aldehyde molecules yield the corresponding alcohol and carboxylic acid, as has been investigated with the common aldehydes formaldehyde (Tsujino *et al.*, 1999; Watanabe *et al.*, 2003; Morooka *et al.*, 2005; Morooka *et al.*, 2007; Akgul and Kruse, 2013) and acetaldehyde (Nagai *et al.*, 2003; Nagai *et al.*, 2004b; Nagai *et al.*, 2005; Morooka *et al.*, 2008).

The mechanism for the disproportion reaction, which is reminiscent of the classic base-catalyzed Cannizzaro reaction of benzaldehyde (Cannizzaro, 1853), involves hydration of the aldehyde followed by rate-determining hydride transfer from the hydrate to another aldehyde, as shown in Figure 28 (Swain *et al.*, 1979). The mechanism dictates equal yields of carboxylic acid and alcohol and their derived products. Experimental evidence for the reaction under hydrothermal conditions is somewhat inconsistent. Katritzky and co-workers (1990a) reacted benzaldehyde at 250 °C in water for 5 days, yet

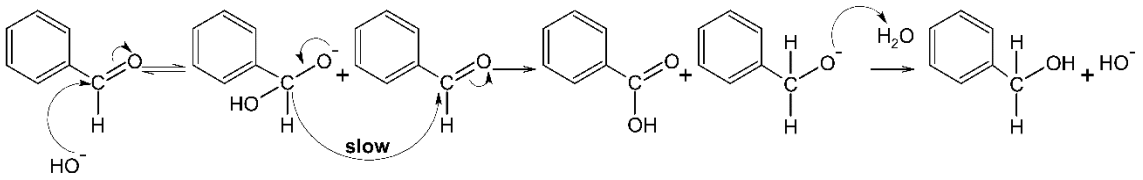

Figure 28. Traditional mechanism of the Cannizzaro reaction under basic conditions.

observed far more benzoic acid than benzyl alcohol. Tsao and others (1992) similarly observed an acid:alcohol ratio greater than unity under supercritical conditions and claimed that cross-disproportionation of benzaldehyde with benzyl alcohol led to toluene and consumption of some of the alcohol produced. In contrast, Funazukuri and colleagues (1997) studied benzaldehyde in supercritical water yet did not detect benzoic acid at all, while Nagai *et al.* (2004a) observed more benzyl alcohol than benzoic acid. In that study, the presence of formic acid was invoked to react with benzaldehyde to yield benzyl alcohol in addition to that derived from the Cannizzaro reaction (Nagai *et al.*, 2004a). Ikushima and others (2001) studied the kinetics of the reaction under supercritical conditions *in situ* via spectroscopic observation of benzyl alcohol, but did not quantify benzoic acid. Here, the hydrothermal chemistry of benzaldehyde was experimentally investigated from 250 °C to 350 °C with the goal of carefully identifying and quantifying both primary and secondary products of benzaldehyde to elucidate reaction pathways that lead to unequal yields of benzyl alcohol and benzoic acid. The role of pH was also investigated to explore the mechanism of benzaldehyde disproportionation under hydrothermal conditions and to offer additional evidence for the proposed reaction scheme as well as its effect on the kinetics.

4.2 Materials and Methods

4.2.1 Materials

Anthracene (99+%), benzaldehyde (redistilled, 99.5%), benzene (99.9%), benzoic acid (99.5%), benzophenone (99%), benzyl alcohol (99.8%), benzyl benzoate (99%), benzyl ether (99%), bibenzyl (99%), biphenyl (99.5%), decane (99%), 1,4-dibenzylbenzene, 9,10-dihydroanthracene (97%), diphenylmethane (99%), diphenylmethanol (99%), fluorene (98%), 9-fluorenone (98%), phenylacetic acid (99%),

phenylacetophenone (97%), 2-phenylbenzaldehyde (96%), 3-phenylbenzaldehyde (96%), 4-phenylbenzaldehyde (99%), cis-stilbene (96%), trans-stilbene (96%), and toluene (99.9%) were all obtained from Sigma-Aldrich (St. Louis, MO, USA) and used as received. 2-benzylbenzaldehyde and 3-benzylbenzaldehyde were obtained at 95% purity from Aldlab Chemicals (Woburn, MA, USA) and used as received, while 4-benzylbenzaldehyde (97%) as well as 4-benzylbiphenyl (98+%) were obtained from Alfa Aesar (Ward Hill, MA, USA) and used as received. 2-methyldiphenylmethane (Synquest Laboratories, Alachua, FL, USA) and 4-methyldiphenylmethane (Matrix Scientific, Columbia, SC, USA) were each obtained at 98% purity, while 3-methyldiphenylmethane (AKScientific, Union City, CA, USA) was obtained at 97% purity; all were used as received. 2-benzylbenzyl alcohol and 3-benzylbenzyl alcohol (95%) were obtained from Aldlab Chemicals, whereas 4-benzylbenzyl alcohol (98%) was obtained from Glycopep Chemicals (Chicago, IL, USA). Dichloromethane (99.9%) was obtained from Fisher Scientific (Pittsburg, PA, USA) and used as received. Deionized water was obtained from a Barnstead Diamond water purification system fed with locally produced reverse osmosis water to yield a final resistivity of 18.2 MΩ•cm.

4.2.2 Experimental Procedures

All experiments were conducted in autoclaves prepared from clear fused silica tubing, synthesized using natural quartz and obtained commercially (GM Associates, Oakland, CA, USA or Technical Glass Products, Painesville, OH, USA). Most experiments were conducted in tubing with a 6 mm inner diameter and 12 mm outer diameter; the tubing was cut into ~25 cm lengths and one end was sealed using a glass-blowing lathe, after which the tubes were annealed. Organic reagents that are liquids were then added into the

bottom of the tube dropwise via syringe; in the case of benzoic acid, aliquots of benzoic acid were individually weighed and then added to the tubes. Most experiments with benzaldehyde had 26.0 µL added resulting in final concentrations of ~0.1 molal; half this volume was added for ~0.05 molal experiments. Immediately after the addition of organics, 2.50 mL of deionized water that had been degassed via argon bubbling for at least 1 hour was added via syringe. The tube was then attached to a vacuum line equipped with a liquid nitrogen trap and subjected to 2 freeze-pump-thaw cycles for degassing via submersion in liquid nitrogen. The tube was then flame sealed with a hydrogen-oxygen torch to a final length of 14 cm for experiments at 250 °C and 300 °C, while a longer length (16 cm) was necessary at 350 °C to allow for the expansion of the solution. The estimated variability in the final length is ± 5 mm. The tubes were then maintained at -20 °C until use. Tubes for ~0.2 molal experiments were prepared similarly except that tubing with an inner diameter of 2 mm and an outer diameter of 6 mm was used. Benzaldehyde (6.0 µL) was added via a 10 µL syringe into the pointed end of a stainless steel luer needle (20 gauge, 10" length) and then flushed into the tube with 300 µL of deionized water that had been argon degassed for at least 1 hour via a 500 µL luer-tip syringe. The freeze-pump-thaw technique was not employed with this size tubing due to strong cohesion of the fluid in the narrow tubes, which leads to loss of fluid during degassing.

Tubes were thawed and placed in a preheated muffle furnace (Fisher Isotemp) set to yield the desired temperature as monitored via thermocouple probes in the center of the furnace. For experiments at 250 °C, galvanized iron pipes (~2 cm inner diameter, ~21 cm length) were preheated in the center of the furnace and the tubes were placed horizontally in the pipes for the duration of the experiment as secondary containment, as previously

described (Yang *et al.*, 2015). Experiments conducted at higher temperatures (save for the NMR experiment, *vide infra*) required external pressure to prevent tube failure. For experiments with 6 mm by 12 mm tubes, vessels were constructed from Swagelok tubing (3/4" outer diameter, 10" length) and capped with Swagelok fittings. Water (10 mL) was added to the vessels along with the experimental tube such that the pressure inside the vessel and inside the experimental tube would both be approximately equal to the saturation vapor pressure for water at the experimental temperature. For experiments with 2 mm by 6 mm tubes (i.e., ~0.2 molal experiments), vessels constructed with 1/2" outer diameter Swagelok stainless steel tubing were used and the amount of water added as a source of external pressure was 3.5 mL. Once loaded and sealed, the vessels were placed horizontally in the center of the preheated muffle furnace. While there was inevitably a heating lag time, the beginning of each experiment is considered to be the time when the vessels are inserted into the furnace. To end the experiment, the pipes or vessels were removed at temperature and quenched by running under tap water for several minutes, which was sufficient to bring the tubes to ambient temperature. Tubes were then generally immediately frozen at -20 °C until analysis.

4.2.3 Analytical Procedures

Experimental tubes were allowed to thaw and scored above the liquid level using a glass cutter and broken open. For 6 mm by 12 mm tubes, the contents were poured into 20 mL amber vials containing an amount of sodium chloride sufficient to yield a saturated aqueous solution (~0.9 g) to improve extraction efficiencies. Dichloromethane (5.00 mL) containing 9.23 mM decane (internal standard) was used to extract organics, with a portion of the dichloromethane solution added to the longest part of the experimental tube for

rinsing, whereupon it was then added to the 20 mL vial. The vial was then capped with a Teflon-lined septum and vigorously shaken for 45 s and allowed to stand for several minutes until phase separation had occurred. The shaking and standing sequence was repeated twice. A portion of the organic layer was transferred via Pasteur pipet to 2 mL amber autosampler vials with Teflon-lined caps. For 2 mm by 6 mm experimental tubes, the same procedures were generally followed, except 4 mL silanized clear vials were used containing ~0.11 g of sodium chloride. Due to capillary action, the contents could not be poured into the vial, so while inverted in the vial, the experimental tube was scored and broken open at the opposite end of the initial break. The contents were then pushed into the vial via a Pasteur pipet bulb, and then the tube was flushed with the dichloromethane solution (3.00 mL). Once all liquids were collected in the vial, the same extraction procedure described for the 6 mm by 12 mm tubes was completed.

The dichloromethane extracts were then analyzed by gas chromatography-flame ionization detection on either a Bruker Scion 456 or a Varian CP-3800 gas chromatograph. Both instruments were equipped with a Varian CP-8400 autosampler. All samples were injected at least 3 times at an injection volume of 1 µL. The injector (CP-1177) was held isothermal at 275 °C and a split ratio of 15 was used. The carrier gas was helium at a constant flow of 1.5 mL/minute through a capillary column (Supelco 5% phenyl, 95% polydimethylsiloxane, 30 m length by 0.25 mm diameter, 0.25 µm film thickness). The column oven was initially 40 °C but upon injection was increased to 140 °C over 10 minutes then raised to 300 °C over 32 minutes, after which it was held at 300 °C for 8 minutes. The flame ionization detector temperature was held isothermal at 300 °C. Each sample was subjected to at least 3 replicate injections; relative standard deviation was

generally less than 5%, though relative standard deviation for analytes of low abundance were more typically 5-15% and occasionally higher. These analytical uncertainties are considered negligible when compared to the overall experimental variability.

Identification of analytes was in most cases completed by comparing their retention times with those of authentic samples of each compound. Sample spikes were completed with certain compounds on selected samples in order to distinguish closely eluting compounds. The only analytes not assigned on this basis were the 1,2- and 1,3-isomers of dibenzylbenzene. The assignment of these analytes was based on their retention times relative to the 1,4-isomer and their relative abundance in the 3-ring region of the chromatogram, particularly in the experiments starting with benzene combined with benzyl alcohol, which are putative reactants eventually leading to the dibenzylbenzene isomers. Assignment of each analyte peak to a specific isomer was not possible.

For quantification, the mean of the ratios of the peak areas of each analyte relative to the peak area of the internal standard for each injection were converted to millimolar concentrations (as dichloromethane solutions) using response factors that were previously determined via calibration curves constructed with at least 4 solutions of known amounts of authentic samples of each analyte and 9.23 mM decane. In the case of isomers, calibration curves were obtained with a selected isomer and its response factor was used for the other isomers. The isomers used for this purpose were 4-methyldiphenylmethane, 4-phenylbenzaldehyde, 3-benzylbenzaldehyde, 2-benzylbenzyl alcohol, and 1,4-dibenzylbenzene. Unidentified analytes were classified as 2-ring, 3-ring, or 4-ring compounds on the basis of their retention times and estimates of the concentrations of 2-ring and 3-ring compounds were made using the response factors of diphenylmethane and

1,4-dibenzylbenzene, respectively. To estimate the abundances of 4-ring compounds, a response factor was obtained by extrapolation of an exponential fit of the response factors of benzene, diphenylmethane, and 1,4-dibenzylbenzene relative to the number of benzene-bonded benzyl groups they contain (Figure 29).

The concentrations of each analyte were then used to calculate total yields of each compound in each experiment. Mass balance was calculated on the basis of phenyl rings, comparing the total equivalents of phenyl rings added to each experiment to the total number of phenyl rings quantified upon analysis, thereby assuming these aromatic rings are inert under the experimental conditions. Anthracene, though it contains 3 aromatic rings, was considered to represent only 2 rings for the purposes of mass balance, since it is putatively derived from dihydroanthracene, which itself represents only 2 rings, presumably being formed from 2 benzyl alcohol molecules. Percent conversion is then calculated as the total mole percent of compounds measured that are not the starting reactant(s).

4.2.4 ^{13}C-NMR Study

2 µL of benzaldehyde-carbonyl-^{13}C (99 atom %, Sigma-Aldrich) was injected via a 10 µL syringe into the pointed end of a stainless steel luer needle (20 gauge, 10" length) and then flushed into a 7" heavy wall precision quartz electron paramagnetic resonance (EPR) sample tube (4.97 mm outer diameter, 2.16 mm inner diameter, Wilmad-Labglass, Vineland, NJ) by pushing via a 500 µL luer tip syringe 400 µL of deionized H_2O that had been argon degassed for approximately one hour. An additional experimental tube was similarly prepared using D_2O (Cambridge Isotopes, Cambridge, MA, USA). The EPR tube

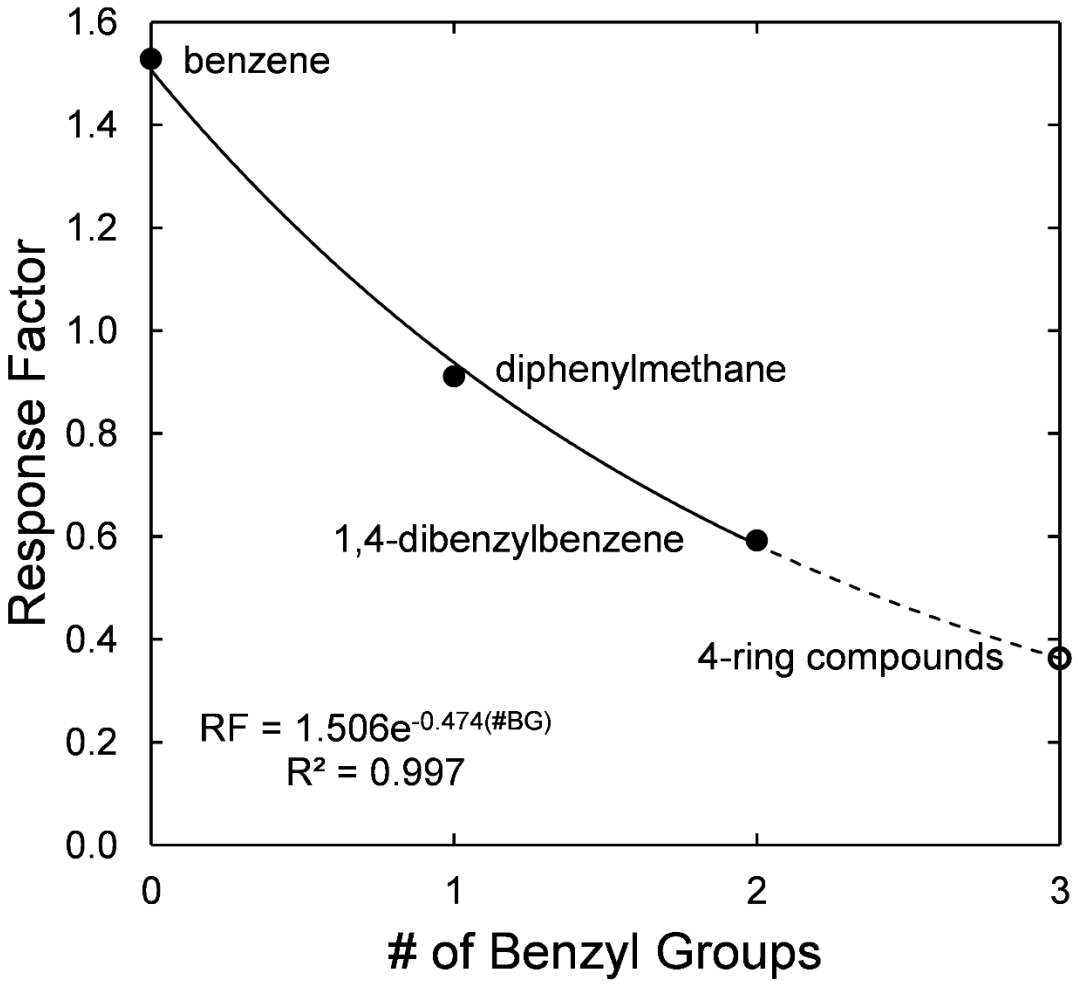

Figure 29. Response factors of benzene, diphenylmethane, and 1,4-dibenzylbenzene versus the number of benzene-bonded benzyl groups they contain (solid circles) fit to an exponential function. The extrapolated value for an analogous compound containing 3 benzyl groups (i.e., 4 aromatic rings) is depicted as an open circle.

had a ~5 cm sacrificial glass extension annealed to the open end of the tube to facilitate flame sealing the tube to a length (~15 cm) sufficient to accept the spinner of the NMR probe at the proper height. NMR spectra were collected on a 400 MHz Bruker Avance III spectrometer (Billerica, MA, USA) with a 5 mm Bruker bbfo Z-gradient solutions probe for ^{1}H-^{13}C observation and inverse-gated proton decoupling (waltz16 decoupling) at 25 °C. The sample was shimmed using a previously saved manual shimming file and 256 scans with a 30 degree excitation pulse, an acquisition time of 1.7 seconds, a relaxation delay of 45 seconds, and a scan width of 20-200 ppm were averaged. A variable relaxation delay array experiment, performed on a sample containing 20 mM benzoic acid-carboxyl-^{13}C (Cambridge Isotopes), demonstrated a 45 second relaxation delay was adequate to achieve nearly quantitative recovery of the carboxyl ^{13}C signal after each pulse, which is expected to have the longest longitudinal relaxation (T_1) time of the organic analytes (Figure 30). Free induction decays were Fourier transformed, integrated, and the concentrations of each analyte (benzaldehyde, benzoic acid, benzyl alcohol, and carbon dioxide) were calculated by normalizing the total integrations of each spectrum to the moles of ^{13}C initially added to the tube, 0.0194 mol (corresponding to ~0.05 molal). After initial (time = 0) NMR observation, the tube was heated horizontally in the preheated muffle furnace containing galvanized iron pipes as described above. Two pipes were used to create a symmetrical thermal environment inside the muffle furnace; the experimental tube was placed in the pipe just to the right of center. For each time point, the pipe was quenched as described above, NMR spectra were collected, and the tube was either returned to the preheated muffle furnace or frozen at -20 °C until the experiment was resumed.

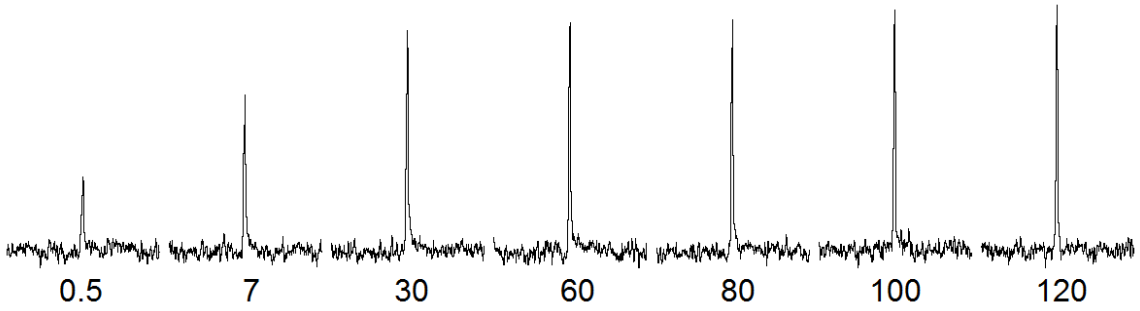

Figure 30. The singlet for benzoic acid-carboxyl-13C as a function of relaxation delay (labelled in seconds).

Some of the $^{13}CO_2$, as well as other labelled volatiles, such as ^{13}CO, are present in the headspace during analysis of the experiment. This ^{13}C is not accounted for in the integrations, which introduces some error in the normalization of the integrations to the total amount of ^{13}C, but this is considered more equitable when compared to the alternative approach of assuming the integration normalization is constant (i.e., external calibration). Furthermore, quantitative recovery of the $^{13}CO_2$ signal may not have been achieved due to its extreme T_1 relaxation time of 50 seconds (Seravalli and Ragsdale, 2008).

4.2.5 Benzoic Acid Decarboxylation Experiments

The rate constant for the decarboxylation reaction was determined using different methods at 300 °C and 350 °C. Experiments at 350 °C (~0.1 molal) were conducted in 6 mm by 12 mm silica tubes as described above. At 300 °C, experiments were conducted in gold capsules (5 mm outer diameter, 0.127 mm wall thickness, ~37.5 mm length) as previously described (Yang *et al.,* 2012). Neither fused silica nor gold are thought to catalyze decarboxylation to any significant extent (Bell *et al.,* 1994). Individually weighed aliquots of benzoic acid (~200 µmol) followed by deionized water that had been argon degassed (200 µL) were added to the capsule, the headspace was briefly flushed with ultra-high purity argon (~2 minutes), and the capsule was welded shut while submerged in a methanol:water (1:1) slurry that was chilled using liquid nitrogen. To conduct the experiment, the capsules were placed into a 51 cm long cylindrical cold-seal pressure vessel (Williams *et al.,* 2001) and pressurized to ~100 MPa with water. The vessel was heated in a preheated clamshell reactor furnace and allowed to reach 300 ± 2 °C, as monitored via a thermocouple probe inside the pressure vessel. Typically ~2 hours were required to nearly reach the desired temperature, during which water was periodically

released to maintain the pressure near 100 MPa. Several more hours were required for the system to equilibrate at the final temperature. Due to this heating lag time, for kinetics purposes the beginning of the experiment was considered to be 2 hours after heating commenced. To conclude each experiment, the pressure vessel was removed from the furnace and quenched in a room-temperature water bath while maintaining pressure by pumping water into the vessel. For analysis, the capsules were solvent-rinsed, punctured with a knife while immersed in 3.0 mL of dichloromethane containing 30 mM phenylacetic acid (internal standard) and then the vials were capped and vigorously shaken. An aliquot of the organic layer was removed and subjected to gas chromatography analysis as described above, using separate calibration curves constructed with phenylacetic acid as the internal standard.

4.2.6 Effects of pH

Several phosphate solutions were prepared and used in lieu of deionized water for a subset of experiments at 300 °C to evaluate the effect of pH. Some experiments were conducted in ~0.1 molal phosphoric acid, while others were conducted in solutions buffered near the pK_a values for the first and second dissociations of phosphoric acid. The pH and speciation of these solutions under the experimental conditions (300 °C, 8.58 MPa) were evaluated using the EQ3 aqueous speciation code (Wolery and Jarek, 2003), which uses an extended Debye-Hückel equation and the revised Helgeson-Kirkham-Flowers equation of state (Shock *et al.*, 1989; Shock *et al.*, 1997). A phosphoric acid stock solution was prepared by diluting 3.39 mL of 85% phosphoric acid (Sigma-Aldrich) with deionized water to a final volume of 50.00 mL in a volumetric flask, resulting in a ~1 molal solution. For the pKa1 solution, 305.60 mg of monobasic sodium phosphate monohydrate was

dissolved in deionized water in a volumetric flask along with 0.285 mL of the phosphoric acid stock solution. This solution was diluted to 25.00 mL with deionized water. The pKa2 solution was prepared by combining 65.41 mg of monobasic sodium phosphate monohydrate and 360.84 mg of dibasic sodium phosphate dihydrate in a volumetric flask, dissolving in deionized water, and diluting to 25.00 mL. Both solutions were ~0.1 molal in total phosphate. The pKa1 solution was calculated to have a pH of 3.019 at 25 °C and a pH of 4.257 at 300 °C, though there is uncertainty in these pH values owing to the uncertainty of the concentration of the phosphoric acid solution. The pKa2 solution was calculated to have a pH of 7.394 at 25 °C and 8.936 at 300 °C. These pH values at 300 °C are equal to the pK_a values for the first and second dissociations of phosphoric acid, where the buffering capacity is at its maximum.

The *in situ* pH of experiments at 300 °C were estimated at the end of the experiment using the EQ3 code taking into account the production of acidic products. Specifically, the yield of benzoic acid was included in the speciation model using the thermodynamic parameters reported by Shock (1995) as was carbon dioxide, using available thermodynamic data for aqueous carbon dioxide (Plyasunov and Shock, 2001) and bicarbonate/carbonate (Shock *et al.,* 1997). The yield of carbon dioxide was assumed to equal the yield of benzene and the aqueous fraction was estimated by calculating the amount of headspace present under the experimental conditions, based on the density and vapor pressure of pure water and approximation of the vessel as a cylinder, and partitioning the total carbon dioxide using the Henry's law constant at 300 °C reported by Majer and colleagues (Majer *et al.*, 2008).

4.2.7 Kinetic Modeling

Reaction pathways inferred from the product suites were applied to a kinetic model to extract rate constants for individual reactions and assess how well the proposed reaction scheme fit the time-dependent data. The selected reactions were combined with the time-dependent data for benzaldehyde and other compounds in 0.1 molal benzaldehyde experiments at 300 °C and 350 °C in a kinetic model using the Copasi software package, version 4.15, Build 95 (Hoops *et al.*, 2006). The data were fit numerically using the Levenberg-Marquardt algorithm. The longest (453 hours) experiments at 300 °C and the two longest (84 and 113 hours) experiments at 350 °C were not included in the fitting to avoid complications from unidentified products and the possibility of organic-rich phases.

4.3 Results and Discussion

4.3.1 Kinetics of Benzaldehyde Decomposition

Experiments beginning with solutions of benzaldehyde were conducted for varying times at 250, 300, and 350 °C, which are depicted as second-order kinetic plots in Figures 31-33, respectively. In all cases, least-squares regression of the data as second-order was superior to either first- or zero-order, though the differences between first- and second-order were not significant due to the low extents of conversion. At 250 °C, conversion of 0.1 molal solutions were very low, reaching only 3.6% conversion after over 400 hours of reaction. At 300 °C, conversion of 0.1 molal solutions reached nearly 35% conversion on similar time scales. Time-dependent data were also obtained at 300 °C for 0.05 molal ^{13}C-benzaldehyde solutions via ^{13}C-NMR which yielded a very similar slope (i.e., rate constant) to that for the 0.1 molal data, demonstrating the second-order behavior of benzaldehyde, since this concentration dependence cannot be explained via a first-order treatment. The

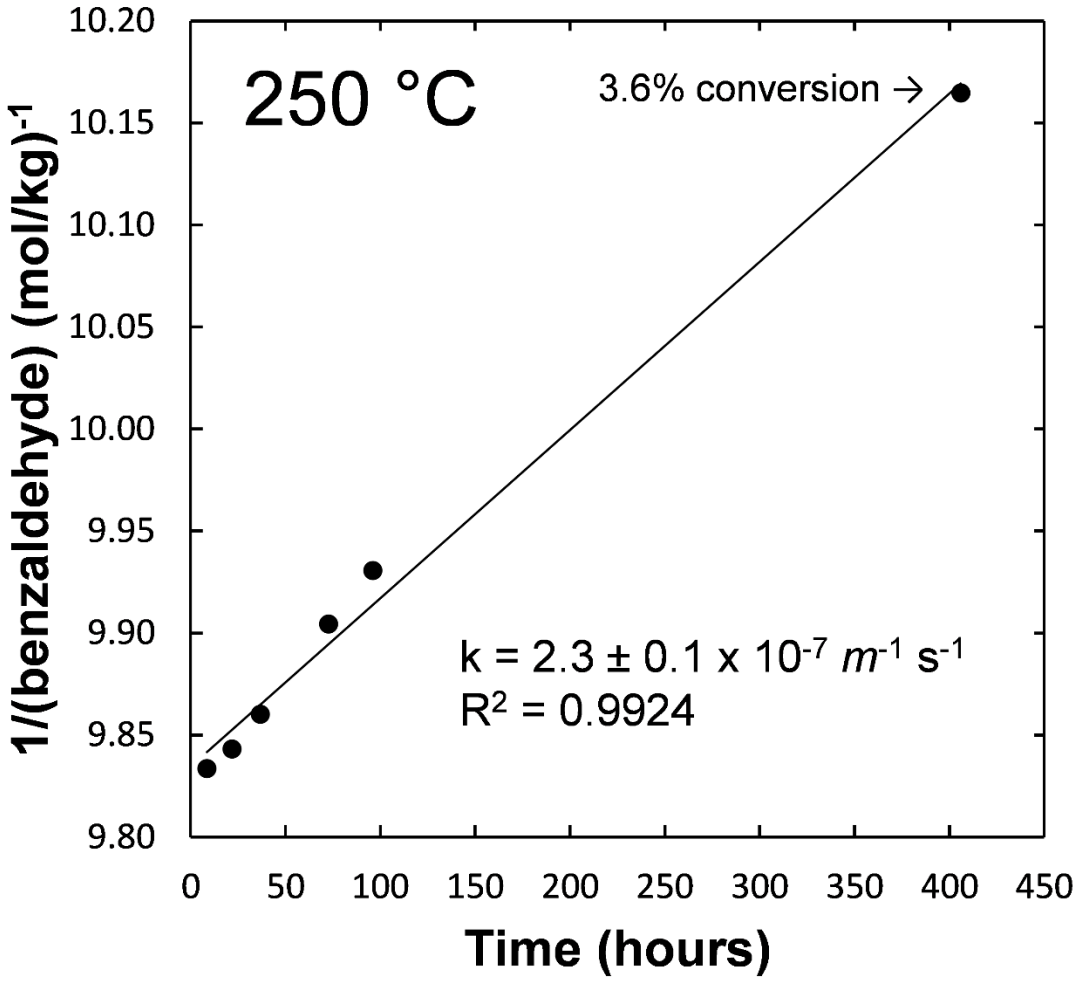

Figure 31. The inverse of the benzaldehyde concentration versus time for experiments conducted at 250 °C. The rate constant, coefficient of regression, and percent conversion achieved at the longest reaction time are indicated.

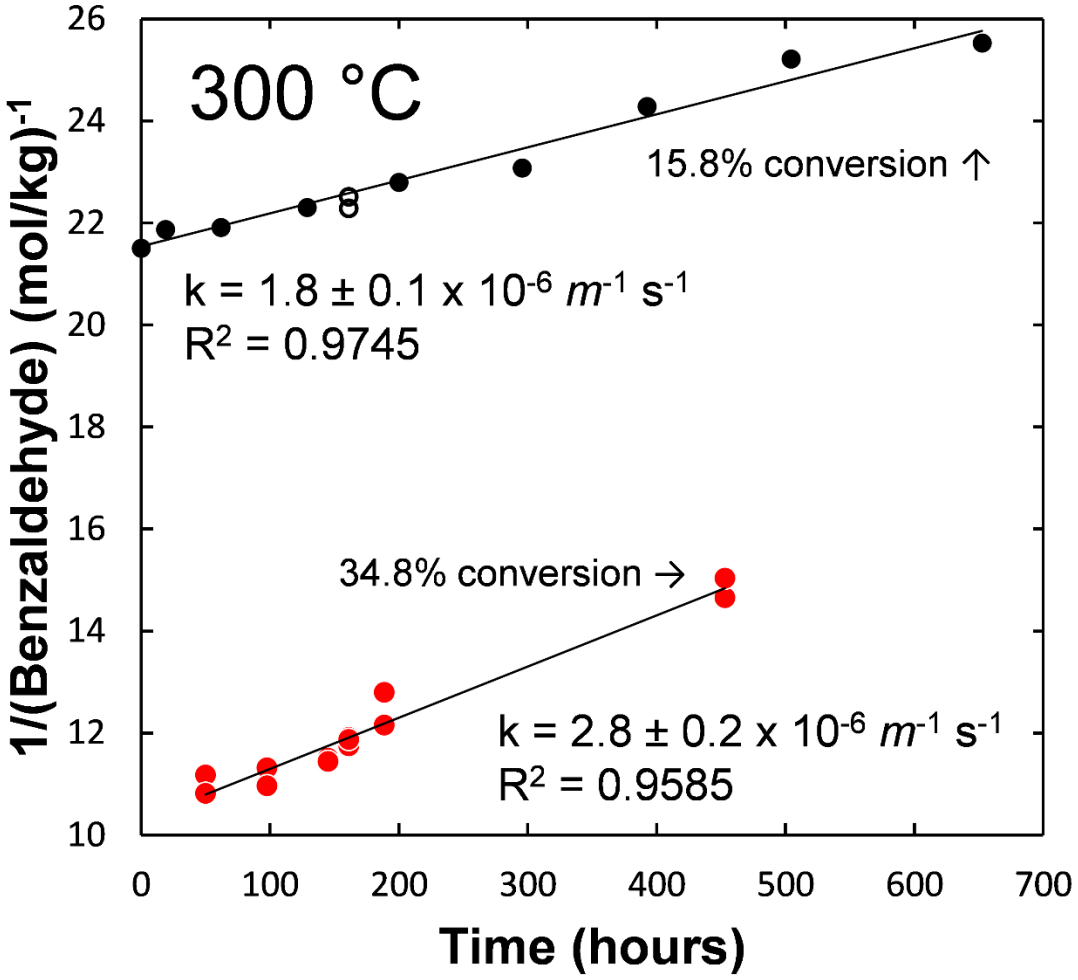

Figure 32. The inverse of the benzaldehyde concentration versus time for experiments conducted at 300 °C for 0.05 molal (black circles) and 0.1 molal (red circles) starting benzaldehyde concentrations. Open black circles indicated data derived from GC-FID analysis, whereas the other data at 0.05 molal concentration were obtained from ^{13}C-NMR. The rate constants, coefficients of regression, and percent conversions achieved at the longest reaction times are indicated.

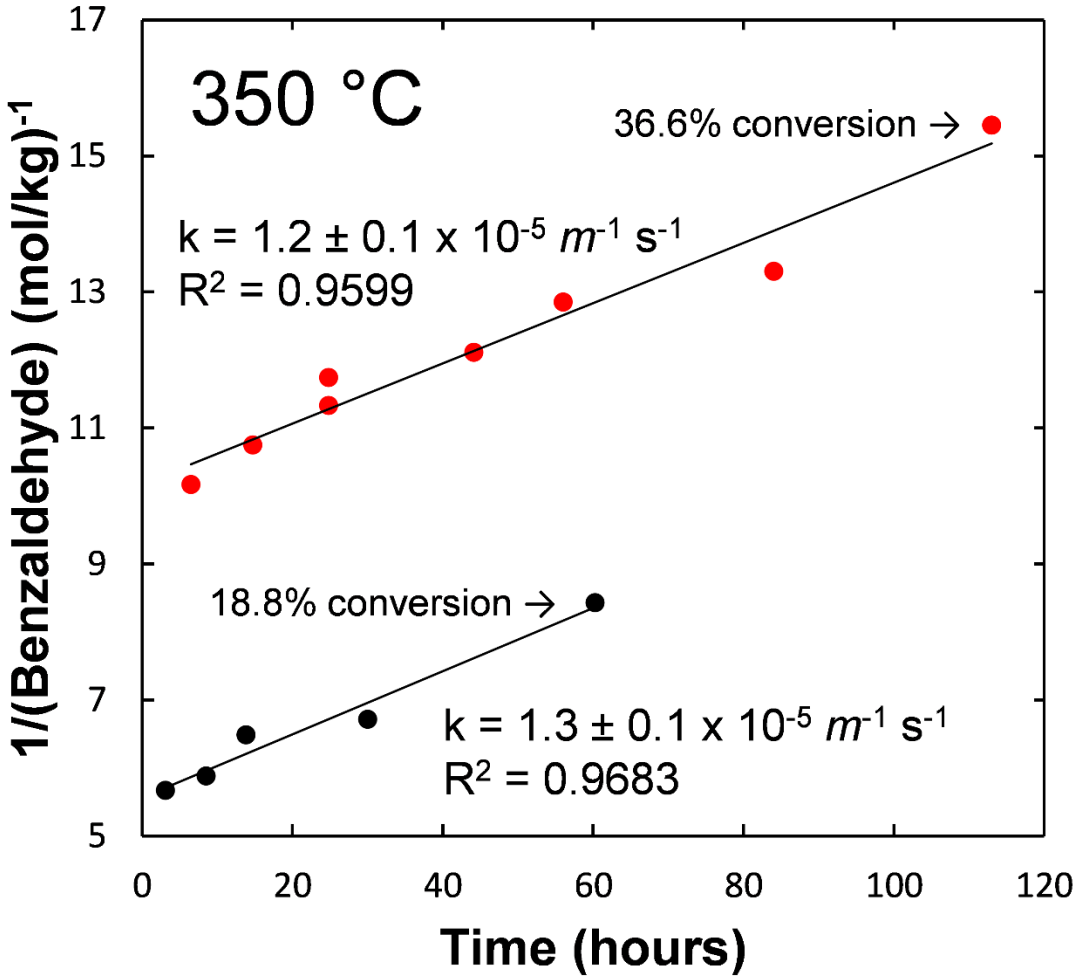

Figure 33. The inverse of the benzaldehyde concentration versus time for experiments conducted at 350 °C for 0.1 molal (red circles) and 0.2 molal (black circles) starting benzaldehyde concentrations. The rate constants, coefficients of regression, and percent conversions achieved at the longest reaction times are indicated.

concentration dependence is even more evident at 350 °C for 0.1 and 0.2 molal concentrations. The concentration dependence may be expressed as the reaction order according to the Noyes equation (Moore and Pearson, 1981):

$$n = 1 + \frac{\log t'_{1/2} - \log t_{1/2}}{\log a - \log a'}$$

where and a and a' and $t_{1/2}$ and $t'_{1/2}$ are two different starting concentrations of reactant and the half-lives at those concentrations, respectively, and n is the reaction order. At 300 °C the order is 1.8, whereas at 350 °C the order is 2.0. The deviation from pure second-order at 300 °C is possibly attributed to the larger uncertainties associated with the NMR data, or contribution from a first-order process that is a more significant contributor to benzaldehyde decay at 300 °C than 350 °C.

The observation of benzaldehyde isotopically labelled at the carbonyl carbon enabled confirmation of the benzaldehyde kinetics in a single experimental vessel without requiring liquid-liquid extraction for analysis. The kinetic isotope effect for the labelled benzaldehyde is considered negligible relative to unlabeled benzaldehyde, as there is only a ~1 amu difference in molecular mass. Initially present were singlets for the carbonyl carbons of benzaldehyde (~196 ppm) and benzoic acid (~170 ppm), which is present in the benzaldehyde due to oxidation, which is difficult to prevent in the small volume of labelled benzaldehyde. After periods of heating, two other signals appeared in the spectrum. A singlet at ~63 ppm was detectable after 200 hours representing the benzylic carbon of benzyl alcohol (Figure 34). Another singlet at ~126 ppm appeared earlier, at 129 hours, which is consistent with carbon dioxide (Abbott *et al.*, 1982). The presence of carbon dioxide suggests that benzene is being produced, which itself is below detection because it

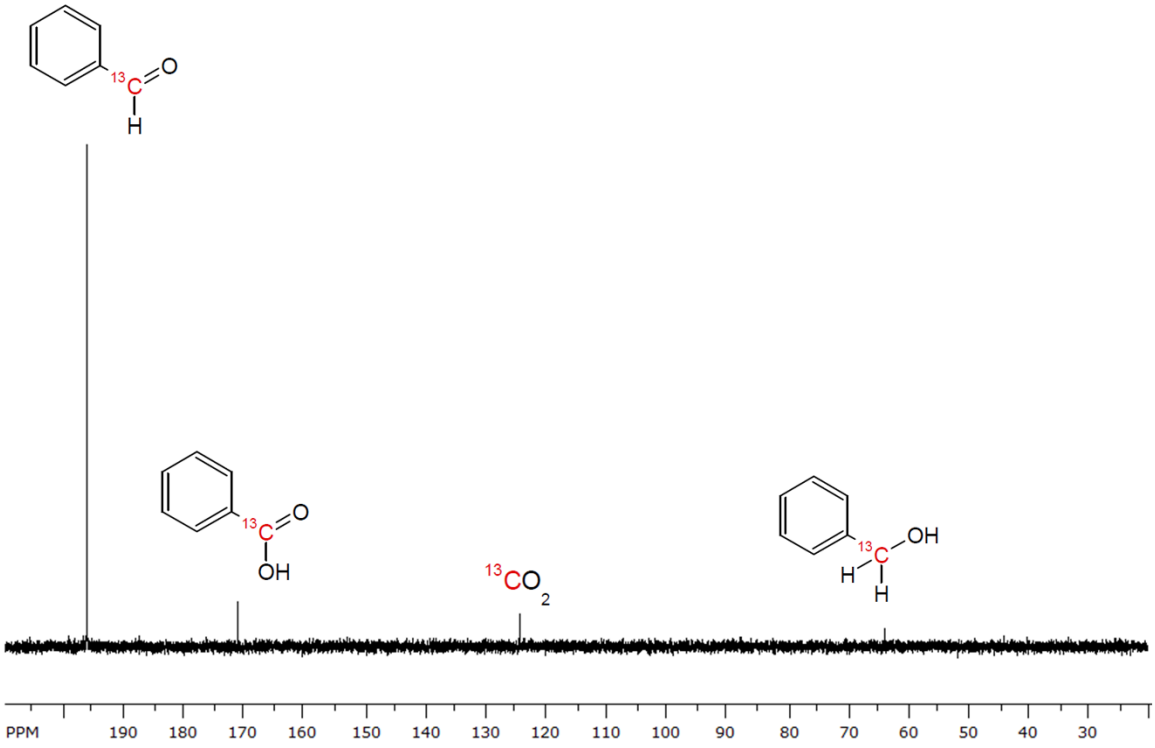

Figure 34. ^{13}C-NMR spectrum of the benzaldehyde experiment after 200 total hours of heating. Singlets are labelled with their putative structures with the ^{13}C atoms indicated in red.

is not expected to contain any of the ^{13}C label. Benzene and carbon dioxide could arise directly via decarboxylation of benzoic acid, or via decarbonylation of benzaldehyde followed by oxidation of the resulting carbon monoxide via the water-gas shift reaction, which happens readily under the experimental conditions (Seewald *et al.,* 2006; Picou *et al.,* 2014).

Study of benzaldehyde via NMR also offered insight into the reactivity of specific bonds of benzaldehyde. Benzaldehyde-carbonyl-^{13}C in D_2O initially appears identical to the analogous spectrum in H_2O, yielding a singlet for the carbonyl carbon of benzaldehyde. After 14.5 hours at 300 °C, however, the benzaldehyde resonance had become a triplet with 1:1:1 intensity and a coupling constant of 27 Hz, as shown in Figure 35. This splitting pattern is unequivocally due to ^{13}C-D splitting, demonstrating that the formyl hydrogen of benzaldehyde had nearly completely exchanged with D_2O. While the mechanism for this exchange is unknown, the rapid exchange demonstrates to kinetic lability of the aldehyde C-H bond in hydrothermal conditions.

The rates of benzaldehyde decomposition at the three temperatures are plotted on an Arrhenius plot in Figure 36. The present data yield an activation energy for benzaldehyde decomposition of 108 kJ mol^{-1} and a pre-exponential factor of 1.5 x 10^4 m^{-1} s^{-1}. An estimated rate constant extracted from a single experiment for 5 days at 250 °C (Katritzky *et al.,* 1990a) was slightly larger than that observed at that temperature in the present study. The data trend well with rates obtained in supercritical water reported by Tsao and others (Tsao *et al.,* 1992) though the activation energy and pre-exponential factor are significantly larger above the critical point. An estimated rate constant derived from data obtained at 400 °C from other work (Nagai *et al.,* 2004a) agrees well with the data of

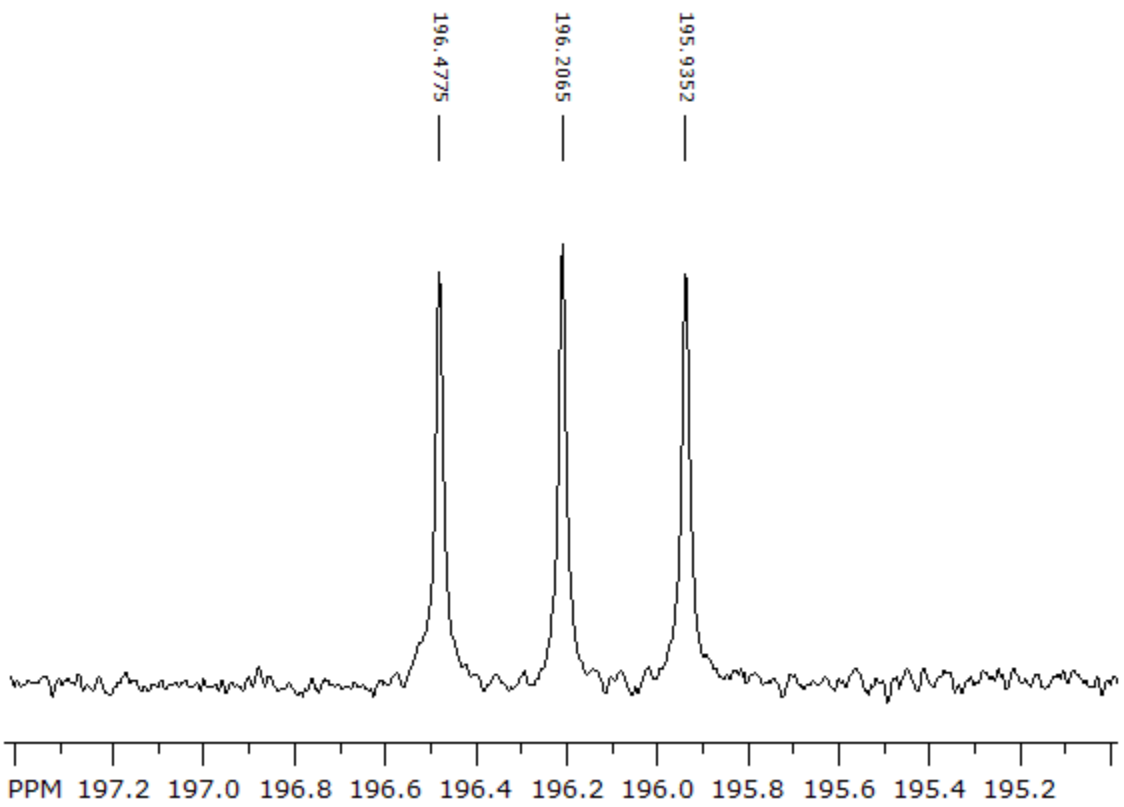

Figure 35. Partial ^{13}C-NMR spectrum of 0.05 molal benzaldehyde-carbonyl-^{13}C after 14.5 hours at 300 °C in D_2O.

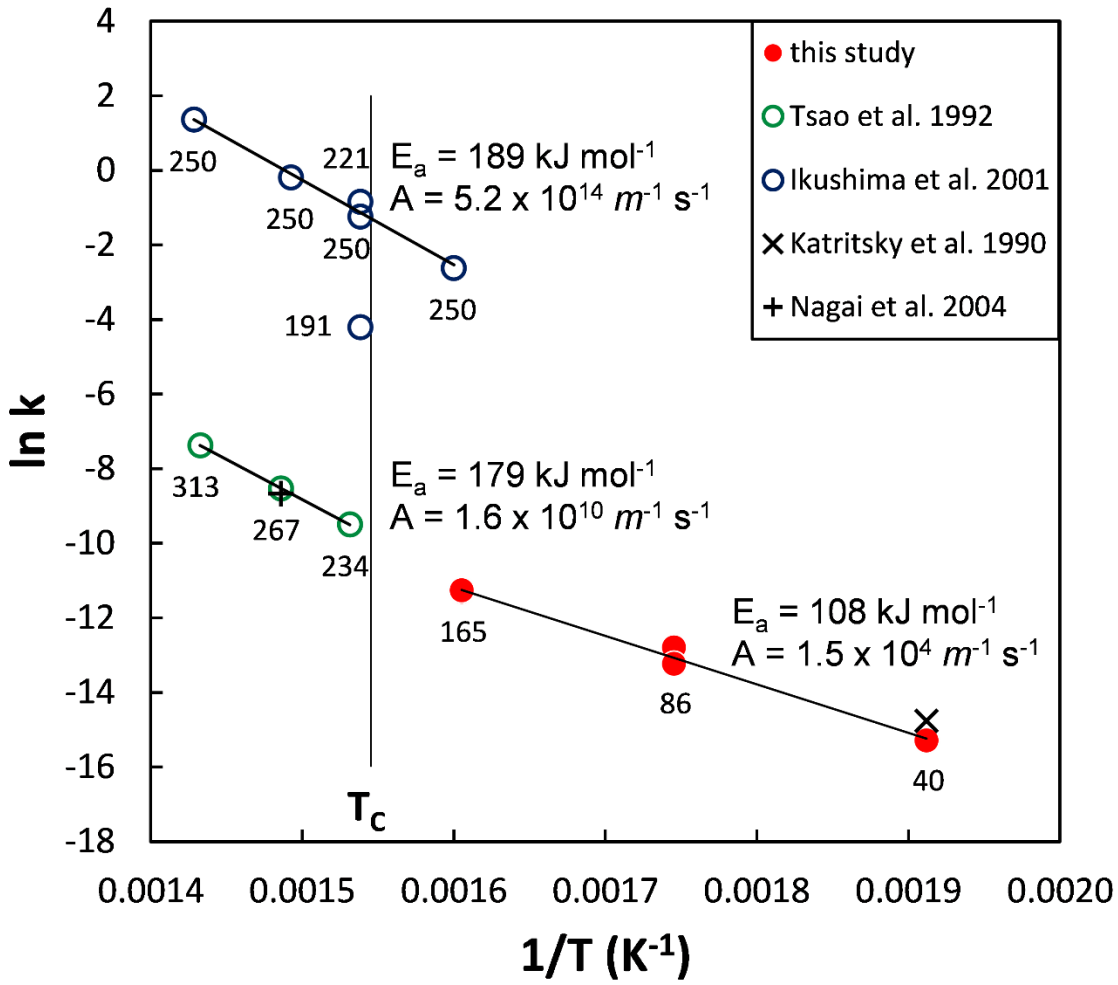

Figure 36. Arrhenius plot for benzaldehyde. The activation energies and pre-exponential factors for each data set (circles) are given. Black symbols indicate rates obtained from individual experiments and are not included in any of the regressions. Numbers below each point indicate the pressure of the experiments in bars. The critical point of water is indicated as a vertical line.

Tsao *et al.* (1992). There exist numerous examples of changes in activation energy at or near the critical point of water for aqueous reactions of organic compounds, which is thought to arise due to ionic pathways being favored in subcritical conditions while radical and other mechanisms that do not lead to charged intermediates are more strongly favored in supercritical conditions (Krammer and Vogel, 2000; Taylor *et al.*, 2001; Buhler *et al.*, 2002).

In contrast, the rates reported by Ikushima and colleagues (Ikushima *et al.*, 2001) greatly exceed those from the present study and the rest of the literature. Though similar activation energies were obtained in the supercritical region, the pre-exponential factor exceeds that of the other data by over 4 orders of magnitude. The reason for this extreme difference is not clear. The rates measured by Ikushima were obtained by quantifying the production of benzyl alcohol *in situ* in a flow reactor with a residence time of 6 minutes via its C-O stretching band in the infrared region (Ikushima *et al.*, 2001). It's possible that spectral features not present during calibration at lower temperatures affected the quantification or that there is an unappreciated temperature dependence for the molar absorptivity of this infrared absorption. There is also likely a difference in density normalization between the two studies, where the rates of Ikushima *et al.* (2001) are relative to concentrations at the experimental temperatures, while all other data are expressed relative to concentrations at ambient conditions (in other words, in units of molality). This difference is unable to account for the differences of several orders of magnitude, however. Additionally, the rate of one experiment (397 °C, 19.1 MPa) was significantly lower than analogous experiments at the same temperature but higher pressures. This anomaly is likely due to the subcritical pressure of this experiment, where

water is expected to be present as steam. Since benzaldehyde decomposition involves water as a reactant, the rate is likely highly sensitive to the phase of the solution.

The rates were also subjected to fitting with the Eyring equation as shown in Figure 37, which predictably appears quite similar to the Arrhenius plot. Most notable are the entropies of activation. Unlike the other data, the rate constants obtained from Ikushima and colleagues (2001) yield a positive entropy of activation. A positive activation entropy is inconsistent with a second-order reaction, where a negative entropy change is expected for the transition state as two molecules yield a single intermediate at the rate-limiting step. This result offers further evidence that the rates reported by Ikushima and others (2001) are anomalous.

4.3.2 Product Suites of Benzaldehyde Experiments

While the primary products benzoic acid and benzyl alcohol were detected via ^{13}C-NMR, as well as the production of benzene in an indirect manner, liquid-liquid extraction followed by GC-FID analysis offers an opportunity for a more thorough investigation of the suite of organic compounds produced in experiments starting with aqueous solutions of benzaldehyde. Comprehensive elucidation of secondary reactions in these experiments is essential because while production of benzyl alcohol and benzoic acid is suggestive of the Cannizzaro disproportionation reaction, disproportionation of benzaldehyde is not consistent with the unequal yields of benzoic acid to benzyl alcohol observed here via ^{13}C-NMR and in previous studies. At 250 °C, only the alcohol, acid, and benzene were detected at the low conversions obtained (Table 7). At 300 °C, however, 27 distinct products were identified, with numerous unidentified peaks evident at the longest reaction times (Table 8). Most of the same products were detected in experiments at 350 °C (Tables 9 and 10).

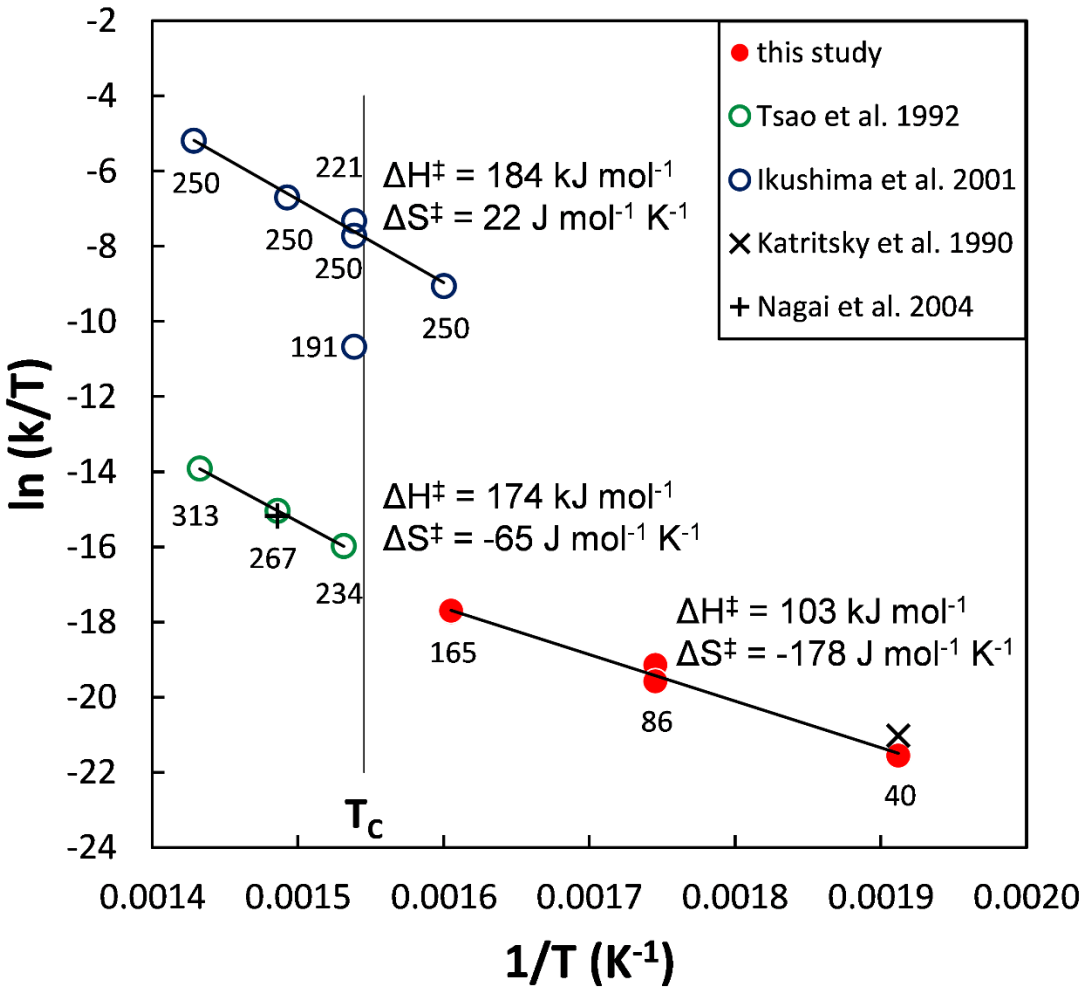

Figure 37. Eyring plot for benzaldehyde. The enthalpies and entropies of activation for each data set (circles) are given. Black symbols indicate rates obtained from individual experiments and are not included in any of the regressions. Numbers below each point indicate the pressure of the experiments in bars. The critical point of water is indicated as a vertical line.

Table 7. Yields (in μmol) of compounds in 0.1 molal benzaldehyde experiments at 250 °C.

time (hours)	**8.6**	**21.9$\overline{3}$**	**36.8$\overline{3}$**	**72.8$\overline{3}$**	**96.01$\overline{6}$**	**406**
benzaldehyde	254.232	253.982	253.543	252.410	251.745	245.951
benzene	<0.01	<0.01	<0.01	<0.01	<0.01	0.209
benzyl alcohol	0.213	0.325	0.544	1.105	1.446	4.998
benzoic acid	0.533	0.867	1.087	1.658	1.983	4.015
% conversion	0.37	0.47	0.64	1.08	1.34	3.61
% mass balance	100.17	92.72	94.95	94.15	93.09	101.00

Table 8. Yields (in µmol) of compounds in 0.1 molal benzaldehyde experiments at 300 °C. Blank entries are <0.005 µmol.

time (hours)	**50**	**50**	**97.6**	**97.6**	**145.1**	**145.1**	**161**	**161**	**161**	**188.5**	**188.5**	**453**	**453**
benzaldehyde	223.673	231.097	220.820	227.898	217.222	218.480	209.813	212.701	210.571	195.307	205.623	170.596	166.225
benzene	0.470	0.402	1.114	0.848	1.853	1.491	2.732	1.963	2.297	1.991	2.319	8.823	7.716
toluene	0.005	0.006	0.024	0.018	0.049	0.046	0.156	0.093	0.138	0.116	0.095	4.031	3.439
benzyl alcohol	3.796	3.955	6.756	7.141	8.656	8.990	10.235	8.571	8.382	10.662	10.156	2.510	2.852
benzoic acid	6.762	5.379	8.974	8.377	11.481	10.000	12.991	11.179	11.769	14.046	14.746	21.358	21.555
biphenyl					0.005	0.005	0.012	0.008	0.008	0.009	0.009	0.089	0.079
diphenylmethane	0.010	0.009	0.056	0.051	0.166	0.137	0.426	0.250	0.272	0.269	0.385	1.965	1.951
bibenzyl												0.031	0.032
3-methyldiphenylmethane							0.007	0.004	0.005		0.007	0.246	0.231
2-methyldiphenylmethane							0.015	0.009	0.012	0.014	0.009	0.459	0.425
4-methyldiphenylmethane					0.011	0.009	0.047	0.032	0.038	0.025	0.031	0.681	0.644
fluorene					0.005	0.005	0.009	0.006	0.007		0.010	0.070	0.062
benzophenone			0.010	0.010	0.017	0.018	0.037	0.025	0.025	0.028	0.033	0.217	0.193
9,10-dihydroanthracene	0.009	0.008	0.054	0.058	0.131	0.126	0.223	0.191	0.172	0.119	0.169		
3-phenylbenzaldehyde			0.007	0.006	0.011	0.010	0.020	0.015	0.015	0.014	0.018	0.136	0.128
trans-stilbene												0.014	0.012
4-phenylbenzaldehyde	0.006	0.008	0.019	0.019	0.034	0.032	0.078	0.054	0.054	0.054	0.073	0.412	0.379
phenylacetophenone							0.010	0.008				0.021	0.007
9-fluorenone			0.008	0.008	0.014	0.013	0.024	0.020	0.019	0.018	0.021	0.135	0.114
3-benzylbenzaldehyde	0.018	0.017	0.079	0.083	0.195	0.179	0.453	0.365	0.352	0.218	0.301	0.583	0.592
4-benzylbenzaldehyde	0.005	0.005	0.033	0.037	0.105	0.101	0.292	0.199	0.188	0.140	0.192	0.324	0.335
anthracene	0.005	0.005	0.015	0.016	0.024	0.024	0.038	0.029	0.030	0.029	0.028	0.069	0.068
3-benzylbenzyl alcohol			0.015	0.016	0.045	0.043	0.028	0.060	0.053				
4-benzylbenzyl alcohol			0.021	0.023	0.054	0.052	0.017	0.060	0.052				
dibenzylbenzene-1					0.006	0.005	0.030	0.016	0.017	0.013	0.022	0.192	0.188
dibenzylbenzene-2					0.005	0.004	0.022	0.012	0.013	0.010	0.019	0.137	0.129
4-benzylbiphenyl												0.023	0.019
1,4-dibenzylbenzene					0.010	0.008	0.047	0.026	0.027	0.019	0.033	0.291	0.283
2-ring unknown	0.005	0.006	0.016	0.015	0.064	0.059	0.077	0.059	0.055	0.081	0.116	0.330	0.303
3-ring unknown			0.016	0.020	0.099	0.090	0.302	0.222	0.223	0.149	0.206	0.826	0.710
4-ring unknown							0.062	0.024	0.027	0.012	0.013	0.396	0.330
% conversion	4.749	4.090	7.375	6.990	10.009	9.327	12.942	10.710	11.085	13.112	13.106	24.123	23.815
% mass balance	91.805	94.201	93.203	95.793	94.369	94.202	94.447	93.354	92.809	88.089	92.735	88.109	85.505
% unknown	0.004	0.005	0.032	0.035	0.166	0.152	0.513	0.344	0.348	0.258	0.353	1.834	1.584

Table 9. Yields (in μmol) of compounds in 0.1 molal benzaldehyde experiments at 350 °C. Blank entries are <0.005 μmol.

time (hours)	**6.5**	**14.7**	**24.8**	**24.8**	**24.8**	**44.1**	**56**	**84**	**113**
benzaldehyde	245.962	232.552	220.587	207.418	212.937	206.396	194.544	187.904	161.784
benzene	0.610	1.791	4.593	5.108	3.663	6.940	10.422	15.535	15.876
toluene	0.006	0.015	0.022	0.017	0.026	0.071	0.200	0.186	0.864
benzyl alcohol	1.791	4.075	6.124	6.222	6.061	10.580	12.243	15.991	7.351
benzoic acid	2.125	3.644	5.228	2.280	4.242	6.025	6.720	3.937	6.437
biphenyl	0.018	0.051	0.084	0.082	0.097	0.198	0.293	0.441	0.806
diphenylmethane	0.009	0.043	0.179	0.177	0.157	0.693	1.999	2.665	7.144
bibenzyl									0.010
3-methyldiphenylmethane							0.007	0.007	0.126
2-methyldiphenylmethane							0.029	0.022	0.253
4-methyldiphenylmethane							0.061	0.038	0.410
fluorene			0.016	0.015	0.015	0.028	0.045	0.046	0.113
benzophenone	0.034	0.098	0.147	0.139	0.167	0.315	0.489	0.610	1.102
9,10-dihydroanthracene			0.033	0.026	0.031	0.149	0.311	0.336	0.118
3-phenylbenzaldehyde	0.029	0.079	0.116	0.114	0.134	0.247	0.345	0.434	0.706
trans-stilbene									0.022
4-phenylbenzaldehyde	0.109	0.303	0.451	0.422	0.511	0.918	1.336	1.651	2.675
phenylacetophenone			0.009	0.015		0.037	0.057	0.064	0.124
9-fluorenone	0.013	0.045	0.073	0.072	0.078	0.152	0.226	0.308	0.354
3-benzylbenzaldehyde		0.012	0.054	0.043	0.046	0.200	0.541	0.513	1.231
4-benzylbenzaldehyde			0.021	0.019	0.030	0.124	0.364	0.428	0.808
anthracene			0.014	0.012	0.015	0.043	0.092	0.109	0.204
dibenzylbenzene-1							0.130	0.148	0.904
dibenzylbenzene-2							0.093	0.104	0.671
1,4-dibenzylbenzene							0.176	0.193	1.241
2-ring unknown	0.016	0.031	0.052	0.062		0.051	0.144	0.067	0.416
3-ring unknown				0.003			0.181	0.163	0.987
4-ring unknown							0.007	0.000	0.584
% conversion	1.90	4.21	7.26	6.70	6.69	11.50	16.00	19.11	25.60
% mass balance	98.26	95.14	93.21	87.12	89.43	91.40	90.76	91.04	85.22
% unknown	0.01	0.02	0.04	0.05	0.00	0.04	0.34	0.24	2.40

Table 10. Yields (in μmol) of compounds in 0.2 molal benzaldehyde experiments at 350 °C. Blank entries are <0.005 μmol.

time (hours)	**3.1**	**8.5**	**13.8**	**30**	**60.25**
benzaldehyde	52.865	50.964	46.202	44.650	35.568
benzene	0.214	0.568	1.156	2.745	4.552
toluene	0.008		0.017	0.054	0.227
benzyl alcohol	0.492	1.112	1.757	3.184	2.991
benzoic acid	0.707	1.036	1.301	1.422	1.429
biphenyl	0.004	0.009	0.015	0.083	0.110
diphenylmethane		0.011	0.069	0.420	0.959
bibenzyl					0.010
3-methyldiphenylmethane					0.012
2-methyldiphenylmethane					0.027
4-methyldiphenylmethane					0.036
fluorene			0.003	0.010	0.011
benzophenone	0.007	0.016	0.029	0.123	0.143
9,10-dihydroanthracene			0.014	0.043	0.026
3-phenylbenzaldehyde	0.006	0.013	0.021	0.086	0.092
trans-stilbene					0.003
4-phenylbenzaldehyde	0.022	0.046	0.076	0.323	0.332
phenylacetophenone					0.013
9-fluorenone		0.006	0.014	0.055	0.057
3-benzylbenzaldehyde			0.023	0.073	0.128
4-benzylbenzaldehyde			0.012	0.058	0.109
anthracene			0.004	0.024	0.030
dibenzylbenzene-1				0.017	0.058
dibenzylbenzene-2				0.009	0.040
1,4-dibenzylbenzene				0.018	0.075
2-ring unknown	0.009	0.028	0.063	0.186	0.399
3-ring unknown			0.023	0.090	0.644
4-ring unknown				0.013	0.467
% conversion	2.75	5.44	9.56	16.81	29.89
% mass balance	92.32	91.53	86.75	91.15	86.15
% unknown	0.02	0.05	0.18	0.49	2.14

A putative reaction scheme leading to these products from the starting point of benzaldehyde is depicted in Figure 38. With the exception of benzene, which is derived from some combination of benzaldehyde (Reaction 17) and benzoic acid (Reaction 2), many of the other reactions involve benzyl alcohol. Benzyl alcohol is thought to undergo facile dehydration to yield the resonance-stabilized benzyl cation. Other alcohols are known to dehydrate readily under hydrothermal conditions, as predicted thermodynamically (Shock, 1993), where the involvement of hydronium ions derived from the dissociation of water in the mechanism is typically invoked (Xu *et al.*, 1997; Antal *et al.*, 1998; Akiya and Savage, 2001; Xu and Qu, 2013). The formation of benzyl cations can lead to benzylation of aromatic compounds present in the experiment via electrophilic aromatic substitution (EAS), as observed and alluded to in previous work (Katritzky *et al.*, 1990a). The most abundant secondary product, diphenylmethane (DPM), is formed in this manner (Reaction 3). Support for DPM being formed from benzyl alcohol and benzene comes from experiments beginning with 0.05 molal benzyl alcohol along with 0.05 molal benzene (Table 11) where the yield of DPM is drastically enhanced over experiments with 0.1 molal benzaldehyde for the same reaction time. The poor mass balance of these experiments is most likely attributed to loss of benzene during the freeze-pump-thaw degassing of the experiments during their preparation.

Benzyl cations derived from benzyl alcohol can react with benzaldehyde (Reaction 4), toluene (Reaction 7), or benzyl alcohol (Reaction 8) to yield isomers of benzylbenzaldehyde, methyldiphenylmethane, and benzylbenzyl alcohol, respectively. The regioselectivity of these reactions are generally consistent with EAS. The formyl group of benzaldehyde is a *meta*-directing substituent and accordingly 3-benzylbenzaldehyde is

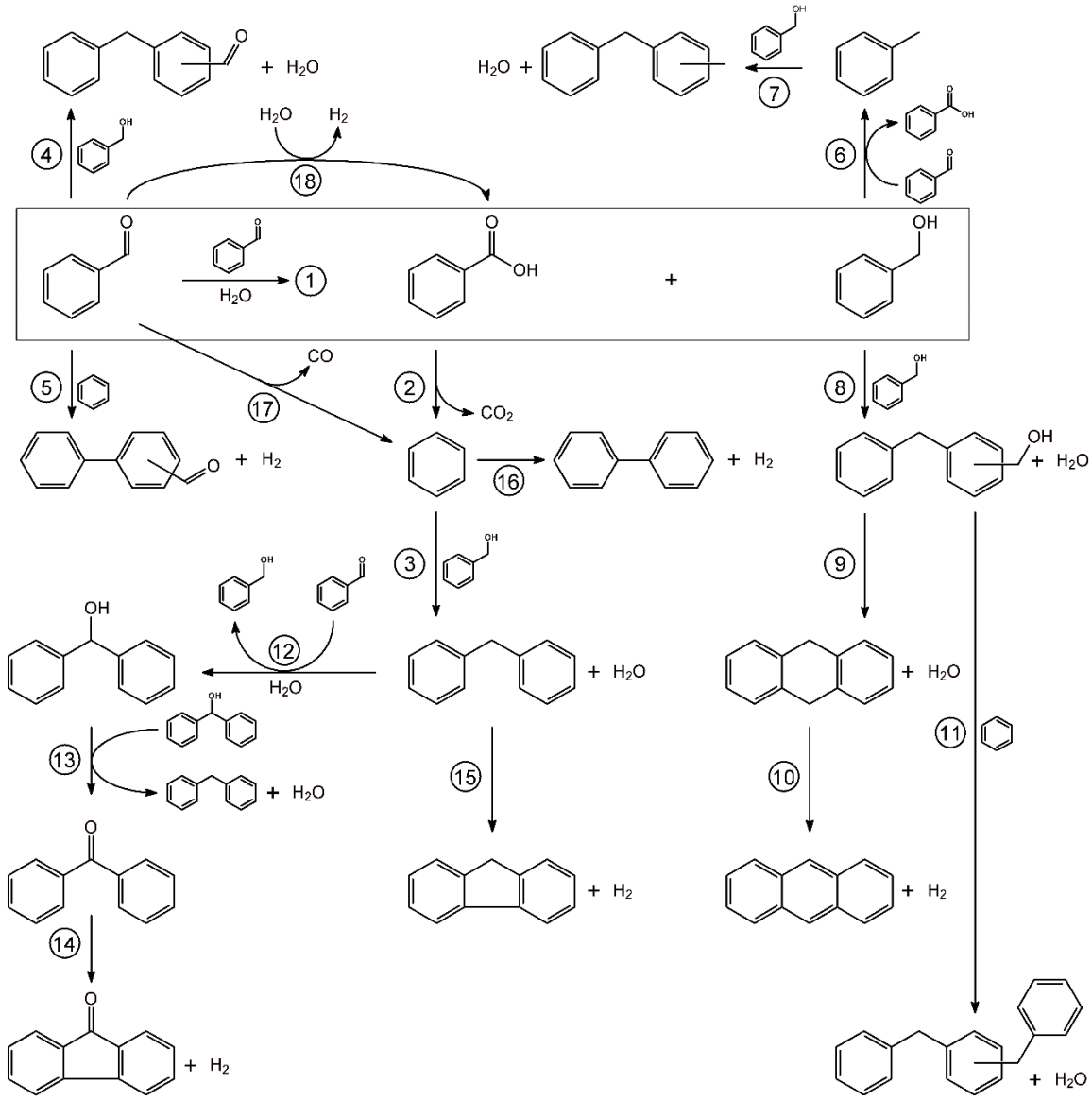

Figure 38. Proposed reaction pathways for compounds observed in benzaldehyde experiments. Reactions are numbered and referenced in the text. The disproportionation reaction of benzaldehyde is outlined in the box.

Table 11. Yields of compounds (in µmol) in miscellaneous experiments for 24.8 hours at 350 °C. Experiments with two reactants listed began with approximately 0.05 molal of each compound. Blank entries are <0.005 µmol. Abbreviations are as follows: B-ol, benzyl alcohol; Bene, benzene; Bald, benzaldehyde; DPM, diphenylmethane; B-acid, benzoic acid; DPMol, diphenylmethanol.

	B-ol Bene	B-ol Bene	Bald Bene	Bald Bene	Bald Bene 0.1 m H_3PO_4	Bald DPM	Bald B-acid	DPMol
benzaldehyde	2.738	2.512	111.188	112.413	111.291	105.671	115.861	0.091
benzene	62.841	53.379	76.031	79.975	85.856	3.395	31.147	0.340
toluene	1.497	0.988	0.020	0.026	0.030	0.110	0.016	0.010
benzyl alcohol	14.499	22.795	0.091	0.094	0.041	0.298	1.100	0.141
benzoic acid			4.523	5.240	5.035	1.824	78.432	0.016
biphenyl			0.043	0.051	0.060	0.058	0.032	
diphenylmethane	14.398	10.491	2.228	2.306	2.795	85.394	0.424	8.992
bibenzyl	0.018							
3-methyldiphenylmethane	0.139	0.083				0.048		
2-methyldiphenylmethane	0.192	0.118				0.019		
4-methyldiphenylmethane	0.646	0.470			0.004	0.038		
fluorene			0.015	0.014	0.036	0.070		0.375
benzophenone			0.019	0.021	0.025	3.081	0.020	8.978
diphenylmethanol				0.002				115.392
9,10-dihydroanthracene	1.348	1.334				0.030	0.007	0.010
3-phenylbenzaldehyde			0.013	0.017	0.017	0.060	0.017	
4-phenylbenzaldehyde			0.045	0.054	0.060	0.236	0.063	
phenylacetophenone						0.012	0.006	
9-fluorenone	0.008	0.016				0.016	0.014	0.011
3-benzylbenzaldehyde	0.090	0.072	0.030	0.033	0.037	0.019	0.019	0.018
4-benzylbenzaldehyde	0.084	0.072	0.005	0.006	0.007	0.006		
anthracene	0.117	0.076	0.010	0.011	0.014	0.013	0.006	
3-benzylbenzyl alcohol	0.465	0.693						
4-benzylbenzyl alcohol	0.231	0.384						
dibenzylbenzene-1	1.429	0.978	0.022	0.024	0.026	1.492		
dibenzylbenzene-2	1.270	0.880	0.021	0.023	0.033	1.037		
4-benzylbiphenyl	0.019	0.011				0.065		
1,4-dibenzylbenzene	2.343	1.662	0.035	0.037	0.047	1.729	0.005	
2-ring unknown	0.036	0.055	0.014	0.011	0.045	0.139	0.069	0.039
3-ring unknown	2.605	2.330	0.013	0.015	0.026	0.209	0.005	0.012
4-ring unknown	3.742	2.951				0.309		0.576
% conversion	50.12	44.31	4.95	5.28	5.60	9.24	14.76	14.70
% mass balance	62.28	54.95	78.47	80.91	83.20	80.87	90.21	99.08
% unknown	9.18	7.59	0.03	0.03	0.07	0.57	0.06	0.88

the most abundant isomer. Nonetheless, significant amounts of 4-benzylbenzaldehyde are also produced, yet no 2-benzylbenzaldehyde was detected in any experiment. These results suggest that regioselectivity in EAS reactions may be less sensitive at higher temperatures and that formation of 2-benzylbenzaldehyde is strongly sterically hindered, possibly due to unfavorable interactions between the benzyl cation and the partially positive charge of the formyl carbon atom. The yields of methyldiphenylmethane isomers also support an EAS mechanism, as the methyl group of toluene is a weakly *ortho/para*-directing substituent and 2-methyldiphenylmethane and 4-methyldiphenylmethane are produced in greater yields than 3-methyldiphenylmethane. Steric effects influence the formation of 2-methyldiphenylmethane, as its yield should be comparable to that of the *para*-isomer (4-methyldiphenylmethane) but is instead more intermediate to the other two isomers.

Benzylbenzyl alcohols were only detected in certain experiments at 300 °C, which is likely due to the high reactivity of benzylbenzyl alcohol. The $–CH_2OH$ substituent of benzyl alcohol is weakly *meta*-directing, yet the yield 3-benzylbenzyl alcohol was generally comparable to that of 4-benzylbenzyl alcohol when observed. 2-benzylbenzyl alcohol was never detected *per se*, yet this isomer is believed to be the precursor to 9,10-dihydroanthracene (DHA), which is obtained via an intramolecular EAS reaction (Reaction 9) as previously suggested (Katritzky *et al.*, 1990a). The yields of DHA, combined with its fully aromatic analogue, anthracene, exceeded the combined yields of 3-benzylbenzyl alcohol and 4-benzyl benzyl alcohol, which is at odds with an EAS mechanism. However, 3-benzylbenzyl alcohol and 4-benzylbenzyl alcohol react in further reactions to yield 3-ring and larger unknown structures in reactions where 2-benzylbenzyl alcohol may be more sterically affected than the other isomers. Indeed, benzylbenzyl alcohol isomers are

proposed to react with benzene to yield dibenzylbenzene (Reaction 11) where the *para*-isomer is most abundant. Overall, the regioselectivity of the formation of benzylbenzyl alcohol is not as clear as it is for other benzylation reactions.

Benzene is also proposed to act as an electrophile upon protonation leading to the formation of phenylbenzaldehydes (Reaction 5) and biphenyl (Reaction 16). However, 4-phenylbenzaldehyde was always produced in greater yield than 3-phenylbenzaldehyde, which is inconsistent with EAS for a formyl substituent. 2-phenylbenzaldehyde was only detected with added acid and at much lower abundances than the other isomers, again suggesting an unfavorable charge-dipole interaction for the reaction at the *ortho*-position. It's possible that reactivity of phenylbenzaldehyde could affect the observed abundances, though no products expected from such reactions were identified. Alternatively, a different mechanism could be operating in addition to or in lieu of EAS. Though the bond dissociation energies for phenyl C-H bonds (112.9 kcal/mol) are quite large (Blanksby and Ellison, 2003) it's possible that homolytic cleavage of these bonds could be involved in the formation of biphenyl and/or phenylbenzaldehyde, especially at 350 °C. Experiments beginning with 0.05 molal benzaldehyde combined with 0.05 molal benzene produced less phenylbenzaldehyde than in 0.1 molal benzaldehyde experiments for the same time (Table 11) which does not support the proposed reaction and instead suggests that benzaldehyde, perhaps via homolytic bond cleavage and subsequent radical coupling, is itself the precursor to phenylbenzaldehydes. Additionally, the presence of phosphoric acid in such an experiment (Table 11) did not noticeably enhance the yield of phenylbenzaldehydes or biphenyl, which would be expected if protonated benzene were acting as an electrophile. Yet, if benzaldehyde radicals were forming, coupling would be expected to produce some

bibenzaldehydes, which were not identified. Yields of biphenyl in experiments beginning with benzene were lower than experiments beginning with benzaldehyde, or in some cases absent, raising doubt that benzene is involved in biphenyl production. Additional experiments probing the mechanism of the production of biphenyl and phenylbenzaldehyde would allow stronger conclusions regarding their formation.

The formation of toluene is proposed to arise via a cross-disproportionation reaction between benzaldehyde and benzyl alcohol (Reaction 6), which has been previously proposed in other experimental studies (Katritzky *et al.*, 1990a; Tsao *et al.*, 1992). Nucleophilic attack of the benzyl alcohol oxygen upon the carbonyl carbon of benzaldehyde leads to a hemiacetal intermediate, which may then undergo intramolecular hydride transfer in a rate-limiting step, analogous to the Cannizzaro mechanism. It's also possible that toluene may arise via a reduction pathway, which is supported by the strong induction period observed for toluene, such that the yield of toluene is dramatically higher at the longest reaction times. One possible reductive scheme involves benzyl cations being reduced to toluene via hydride transfer from an appropriate hydride donor, though there is little independent evidence available to support such a mechanism. Molecular hydrogen, expected as a product of several reactions, could also serve as a reducing agent, particularly at longer reaction times, yet the presence of a headspace allowed most of the hydrogen to be present outside of the solution, which would have hampered the rates of such reactions.

Evidence for the origin of benzophenone via consecutive disproportionation reactions is offered in Table 11. The yield of benzophenone was greatly enhanced in an experiment beginning with 0.05 molal benzaldehyde and 0.05 molal DPM, indicating that DPM is involved in the formation benzophenone. DPM is an excellent hydride donor,

owing to the resonance stabilization of the resulting carbocation. The resulting carbocation would readily be hydrated by water to yield diphenylmethanol via Reaction 12. In the proposed reaction, hydride is donated to benzaldehyde to yield benzyl alcohol, though in the present system other hydride acceptors are possible, including hydronium, which would formally be an oxidation of DPM rather than a disproportionation. While diphenylmethanol was typically not detected, it is known to disproportionate rapidly to yield equal amounts of DPM and benzophenone in supercritical water (Hatano *et al.,* 2002). This disproportionation (Reaction 13) was confirmed under the present conditions (Table 11) with equal yields of DPM and benzophenone.

A variety of minor products were also detected that apparently arise via dehydrogenation reactions, including anthracene, 9-fluorenone, and fluorene (Reactions 10, 14, and 15, respectively). In the case of fluorene and 9-fluorenone, this results in formation of a planar molecule via formation of a C-C bond, whereas the formation of anthracene results in an additional aromatic ring. The mechanism of dehydrogenation is unclear, and may be different in each case. Since a concerted mechanism involving homolytic or heterolytic C-H bond cleavage on two separate rings simultaneously seems strongly kinetically inhibited, a step-wise ionic mechanism for C-C bond formation is more plausible. One hydrogen may leave as hydride, reacting with hydronium ions to yield molecular hydrogen and a phenyl cation. Alternatively, hydride could be donated to another hydride acceptor, such as benzaldehyde. Intramolecular electrophilic attack of the phenyl cation would result in formation of the C-C bond and formation of another carbocation on the other ring, which would rapidly reform the aromatic system upon removal of a proton by water. In the case of anthracene, while a step-wise homolytic

mechanism is conceivable due to resonance, again a step-wise ionic mechanism seems more likely.

4.3.3 pH Dependence of Product Distributions

The pH of a subset of experiments was controlled by the addition of phosphoric acid or phosphate-buffered solutions to yield additional evidence for the reactions proposed above and to offer insights into the role of pH on such reactions in natural settings. The calculated pH for experiments at 300 °C both with and without buffers are depicted versus reaction time in Figure 39. In the high pH buffered experiments, the pH at the experimental conditions is initially near 9, but the high conversion of these experiments causes the buffer to become overwhelmed and reach a final *in situ* pH near 7, which is still well above neutrality. The buffered experiments at lower pH have lower conversions and the pH changes negligibly over the course of the experiment. Unbuffered experiments begin near the pH of pure water at 300 °C (~5.65) but rapidly become acidified to pH ~4 due to the production of acidic compounds. The pH then slowly continues to decline as conversion increases. Notably, the pH of the unbuffered experiments is close to that of the experiments buffered near the first pKa of phosphoric acid.

The yields of products in experiments conducted for 161 hours at 300 °C are shown as a function of starting pH in Figures 40-42 and tabulated in Table 12. At high pH, the yield of the primary products benzoic acid and benzyl alcohol are greatly enhanced relative to the other pH conditions, which is due to the disproportionation of benzaldehyde being catalyzed by hydroxide ions according to the traditional Cannizzaro mechanism (Swain *et al.,* 1979). Two yields of benzoic acid are shown in Figure 40. At the pH of the experiment, benzoic acid is speciated primarily as benzoate, which does not extract well into the organic

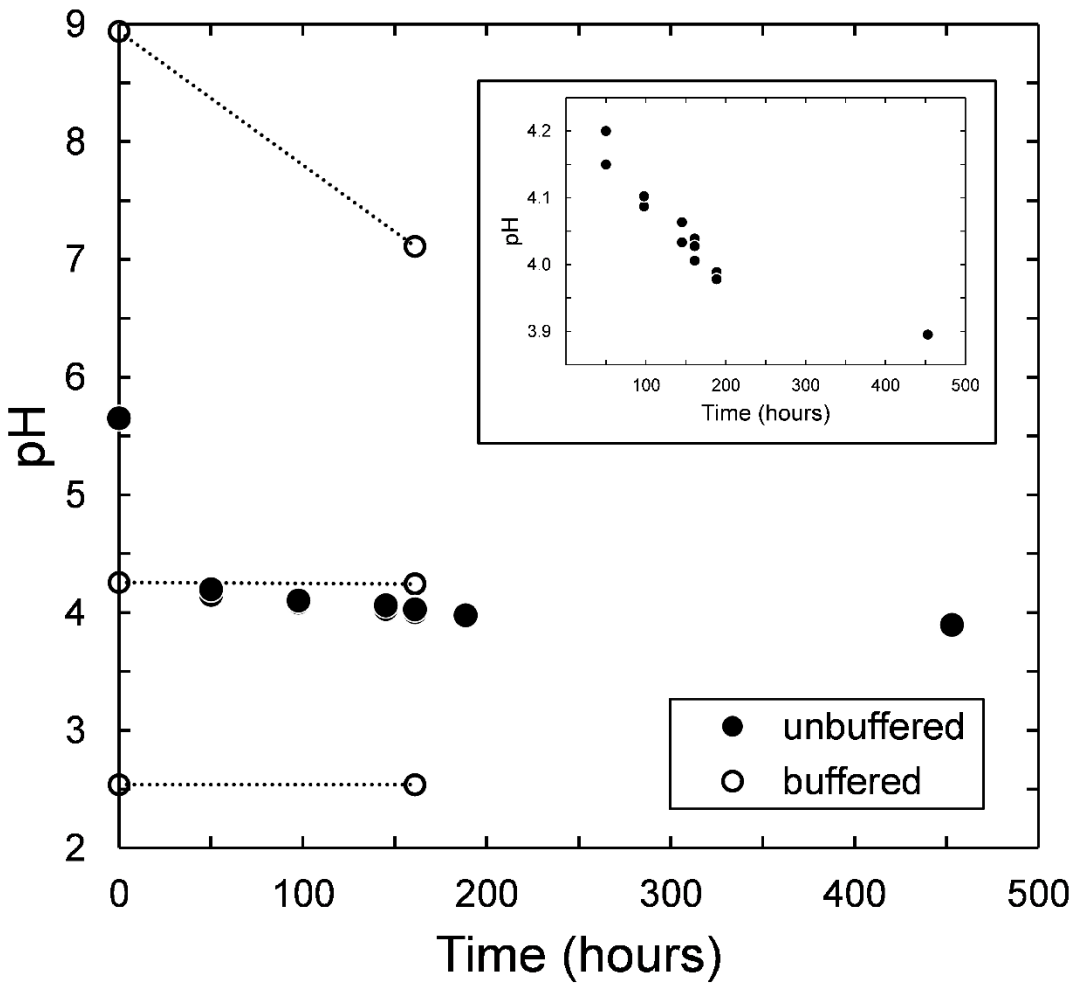

Figure 39. Calculated *in situ* pH as a function of time for benzaldehyde experiments at 300 °C. Experiments in pure water are shown as filled circles and are detailed in the inset. Buffered experiments (open circles) are connected with tie lines.

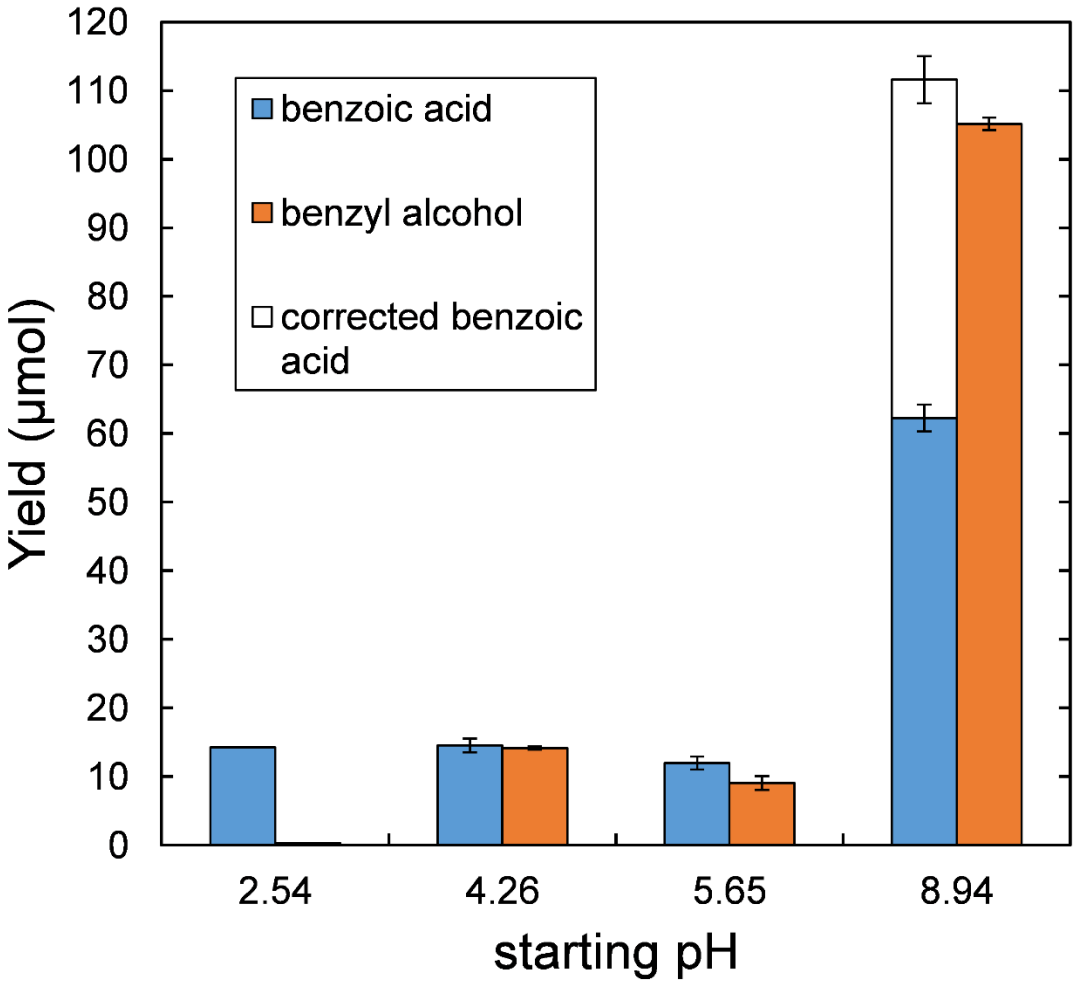

Figure 40. Yields of benzoic acid and benzyl alcohol in experiments starting with 0.1 molal benzaldehyde conducted for 161 hours at 300 °C as a function of starting pH. The yield of benzoic acid corrected for extraction efficiency at high pH is shown as an open bar, while the measured yield is shown in blue, as it is for other pH values. Error bars represent +/- one standard deviation of replicate experiments, except for the corrected yield of benzoic acid, which also propagates uncertainties associated with the assumptions of that correction.

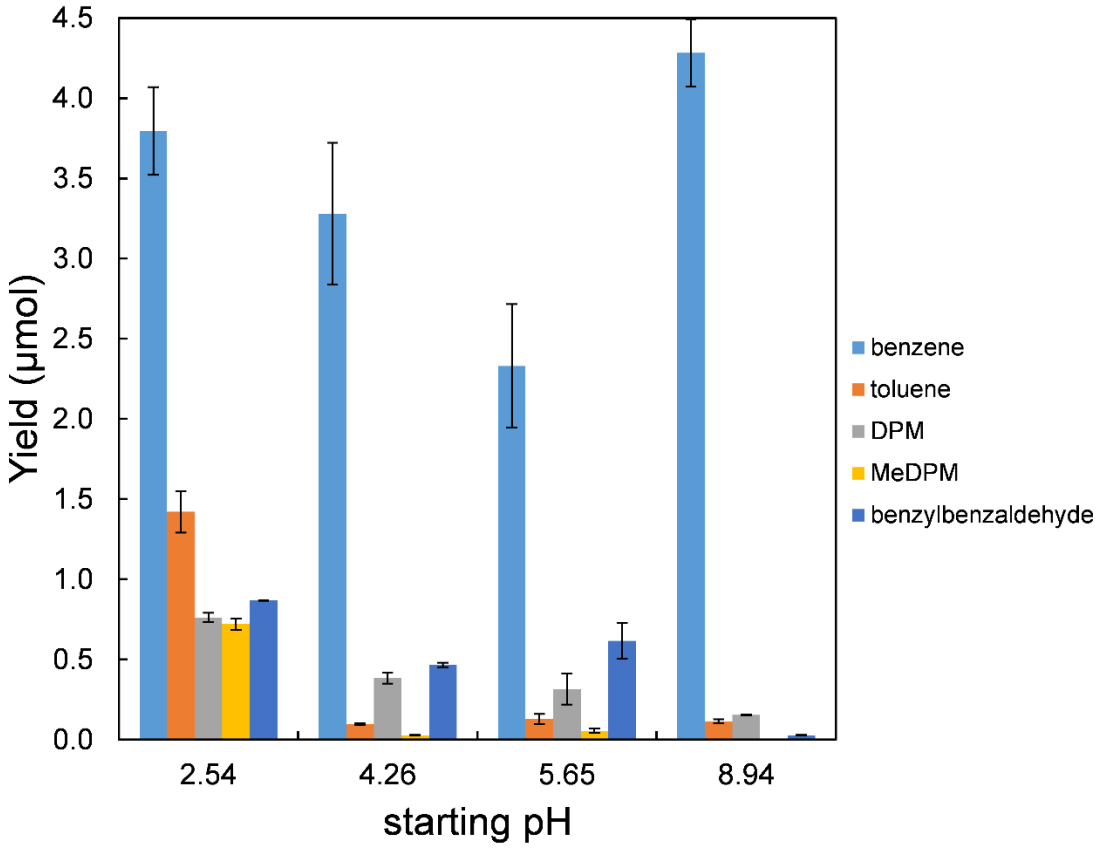

Figure 41. Yields of major products in experiments starting with 0.1 molal benzaldehyde conducted for 161 hours at 300 °C as a function of starting pH. Error bars represent +/- one standard deviation of replicate experiments.

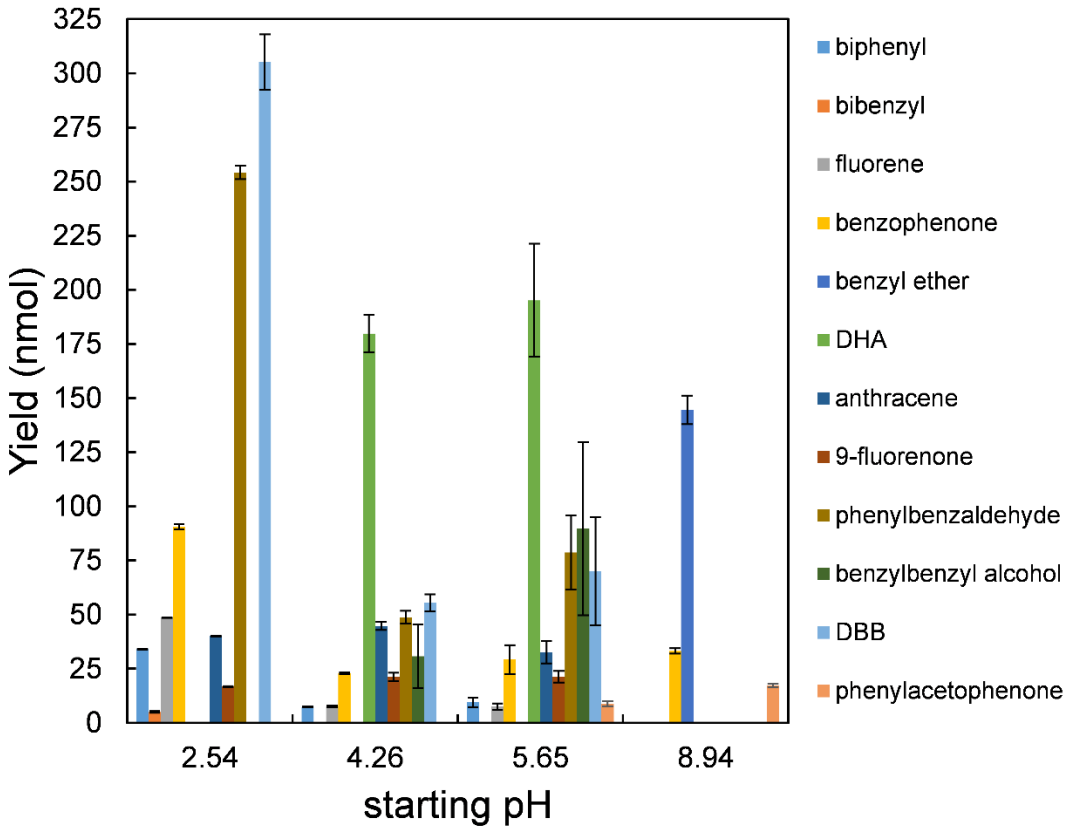

Figure 42. Yields of minor products in experiments starting with 0.1 molal benzaldehyde conducted for 161 hours at 300 °C as a function of starting pH. Error bars represent +/- one standard deviation of replicate experiments.

Table 12. Yields of compounds (in µmol) in benzaldehyde experiments for 161 hours at 300 °C with phosphate solutions or in water at 0.05 molal starting concentration. Blank entries are <0.005 µmol.

	0.1 molal H_3PO_4	**0.1 molal H_3PO_4**	**pKa1 buffer**	**pKa1 buffer**	**pKa2 buffer**	**pKa2 buffer**	**0.05 molal**	**0.05 molal**
benzaldehyde	203.569	203.500	211.802	208.723	23.485	23.515	112.173	111.038
benzene	3.988	3.601	2.968	3.592	4.134	4.430	0.943	1.180
toluene	1.513	1.329	0.092	0.101	0.107	0.123	0.009	0.012
benzyl alcohol	0.311	0.298	14.335	13.990	105.786	104.490	2.926	2.810
benzoic acid	14.265	14.326	13.830	15.247	63.655	60.896	3.614	4.233
biphenyl	0.034	0.034	0.007	0.007				
diphenylmethane	0.743	0.782	0.360	0.409	0.158	0.154	0.025	0.033
bibenzyl	0.005	0.005						
3-methyldiphenylmethane	0.162	0.176						
2-methyldiphenylmethane	0.215	0.231	0.005	0.005				
4-methyldiphenylmethane	0.319	0.338	0.023	0.024				
fluorene	0.049	0.049	0.008	0.007				
2-phenylbenzaldehyde	0.006	0.007						
benzophenone	0.090	0.091	0.023	0.023	0.034	0.032		
benzyl ether					0.149	0.140		
9,10-dihydroanthracene			0.186	0.174			0.022	0.023
3-phenylbenzaldehyde	0.058	0.058	0.013	0.012				
trans-stilbene								
4-phenylbenzaldehyde	0.189	0.192	0.038	0.034				0.006
phenylacetophenone					0.017	0.018		
9-fluorenone	0.017	0.017	0.023	0.020				
3-benzylbenzaldehyde	0.745	0.747	0.276	0.267	0.015	0.014	0.032	0.034
4-benzylbenzaldehyde	0.123	0.123	0.201	0.190	0.015	0.014	0.012	0.012
anthracene	0.040	0.040	0.043	0.046			0.007	0.008
3-benzylbenzyl alcohol			0.024	0.012				
4-benzylbenzyl alcohol			0.018	0.008				
dibenzylbenzene-1	0.077	0.081	0.016	0.018				
dibenzylbenzene-2	0.089	0.095	0.013	0.014				
4-benzylbiphenyl	0.006	0.006						
1,4-dibenzylbenzene	0.131	0.138	0.024	0.026				
2-ring unknown	0.043	0.050	0.076	0.071	0.126	0.116	0.006	0.006
3-ring unknown	0.637	0.649	0.158	0.154	0.006	0.005		
4-ring unknown	0.194	0.217	0.005	0.007				
% conversion	12.60	12.55	14.01	14.78	88.15	87.91	6.42	7.06
% mass balance	91.28	91.20	96.53	95.99	77.68	76.20	93.95	93.64
% unknown	1.09	1.14	0.25	0.25	0.11	0.11	0.01	0.01

layer during the liquid-liquid extraction step, causing poor mass balance and a yield of benzoic acid significantly less than that of benzyl alcohol. If the assumption is made that deviation from typical mass balances in these experiments is caused solely by the poor recovery of benzoic acid, the benzoic acid may be corrected by increasing the observed yield to achieve an appropriate mass balance. This correction results in a corrected benzoic acid yield quite close to the observed yield of benzyl alcohol.

The yields of benzoic acid and benzyl alcohol at lower pH values are roughly 10% of that achieved under basic conditions and do not significantly vary with pH (Figure 40). The yields are quite similar between unbuffered experiments and those buffered at the first pKa of phosphoric acid (4.26). The yield of benzoic acid is indistinguishable between starting pH values of 2.54 and 4.26, while the yield of benzyl alcohol is strongly inhibited at the lower pH. This pH dependence suggests that the total yield of benzaldehyde disproportionation is equal at these two pH values, but benzyl alcohol is much more rapidly depleted in acid-catalyzed reactions at the lower pH. This pH dependence rules out the possibility that benzaldehyde disproportionation may be acid-catalyzed via a mechanism where the hydrate of benzaldehyde is formed via protonation of the carbonyl by hydronium ions. This result is consistent with the theory of microscopic reversibility which in this case dictates that the equilibrium of hydrate formation cannot be affected by the presence of an acid catalyst. Even more importantly, nearly identical yields of benzaldehyde disproportionation spanning more than 3 pH units indicates that hydroxide ions are not involved in the formation of the hydrate in this pH regime and instead that water acts as the nucleophile in hydrate formation, as shown in Figure 43, which is very similar to the more familiar hydroxide mechanism. Water acting as a nucleophile (i.e., Lewis base) is an

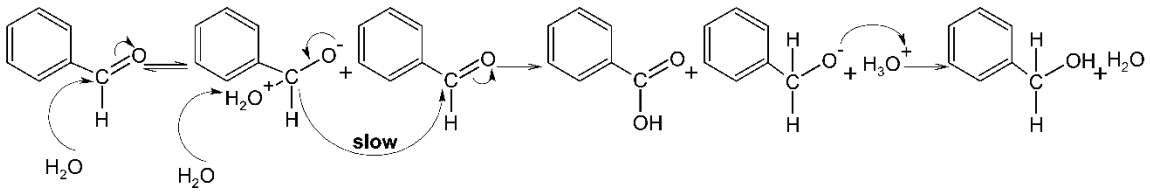

Figure 43. Mechanism of benzaldehyde disproportionation with water acting as the nucleophile.

example of general acid-base catalysis that has been postulated for other reactions in superheated water, in contrast to specific acid-base catalysis afforded by the greater dissociation of water at elevated temperatures (Hunter and Savage, 2004).

The yields of secondary reactions in benzaldehyde experiments are also affected by pH. The yield of toluene (Figure 41) is significantly enhanced at the lowest pH, though the reason for this enhancement is not completely clear. Acid catalysis of hemiacetal formation cannot affect the equilibrium concentration of hemiacetal for the same reasons benzaldehyde hydrate formation is unaffected by acid. One hypothesis is the greater toluene yield is due to greater reduction of benzyl cations, the concentration of which is enhanced by lower pH. The greater abundance of benzyl cations is also observed in the enhanced yields of DPM, methyldiphenylmethanes, and benzylbenzaldehydes. Conversely, the yields of these compounds under basic conditions is significantly retarded due to the absence of specific catalysis by hydronium ions.

The pH dependence of minor products is shown in Figure 42. Only benzophenone, benzyl ether, and phenylacetophenone were observed at the highest pH, whereas the other products are derived directly or indirectly via an acid-catalyzed EAS mechanism and are inhibited by basic conditions. Benzyl ether was only observed under basic conditions which is most likely due to the significantly greater concentrations of benzyl alcohol present in these experiments. Benzophenone is unaffected by high pH, but its yield is slightly enhanced under the most acidic conditions due to more facile protonation of diphenylmethanol, which increases the rate of the rate-limiting nucleophilic hydride transfer where water is the leaving group. Benzylbenzyl alcohol was only detected at intermediate starting pH. Like other benzylation reactions, its formation is inhibited by

high pH. Its absence at low pH is the result of its reactivity under acidic conditions, which leads to the significantly enhanced yield of dibenzylbenzene. Benzylbenzyl alcohol also is the precursor to 9,10-dihydroanthracene, which similarly was only detected at intermediate pH. Under acidic conditions its dehydrogenation to anthracene is putatively enhanced, yet this does not result in an increased yield of anthracene. Apparently, a decrease in pH directs more benzylbenzyl alcohol toward intermolecular benzylation, resulting in dibenzylbenzene and other large compounds, at the expense of the intramolecular benzylation pathway. Phenylbenzaldehyde and biphenyl yields are strongly enhanced by low pH and inhibited by basic conditions, in support of the hypothesized EAS mechanism yet in conflict with the lack of a pH dependence observed in experiments beginning with benzaldehyde in the presence of benzene discussed above. The dehydrogenation product fluorene shows the expected dependence on pH, being absent at high pH and enhanced at the lowest pH studied, while its analogue 9-fluorenone is similarly absent under basic conditions but its production is not affected by the addition of acid.

4.3.4 Kinetic Model for the Benzaldehyde System

As portrayed above, experiments starting with aqueous solutions of benzaldehyde are clouded in the complexity of secondary reactions. In order to evaluate the kinetics of benzaldehyde itself, the time dependence of many of the products were numerically fitted to rate constants for the reactions in the proposed reaction scheme (Figure 38) using freely available software at 300 °C and 350 °C. Only experiments with 16% conversion or less were used in the model in order to avoid complications of the production of unknown products that becomes significant at long reaction times, thereby adhering to the method of initial rates. The rate constants are given in Table 13, numbered according to the reactions

Table 13. Estimated rate constants[a] for reactions in the kinetic model at 300 °C and 350 °C.

# in Figure 37	k at 300 °C	k at 350 °C	units	type
1	1.87E-06	7.72E-06	m^{-1} s^{-1}	disproportionation
2	4.48E-07	1.02E-05	s^{-1}	decarboxylation
3	4.13E-04	1.29E-03	m^{-1} s^{-1}	EAS[b] (benzylation)
4	3.31E-06	1.21E-05	m^{-1} s^{-1}	EAS (benzylation)
5	3.01E-06	4.36E-05	m^{-1} s^{-1}	phenylation
6	9.76E-07	4.09E-06	m^{-1} s^{-1}	disproportionation
7	1.06E-03	4.01E-03	m^{-1} s^{-1}	EAS (benzylation)
8	7.69E-05	3.18E-04	m^{-1} s^{-1}	EAS (benzylation)
9	1.71E-05	3.91E-03	m^{-1} s^{-1}	EAS (benzylation)
10	1.11E-06	4.59E-06	s^{-1}	dehydrogenation
11	7.97E-03	1.62E+00	m^{-1} s^{-1}	EAS (benzylation)
14	4.89E-06	9.82E-06	s^{-1}	dehydrogenation
15	1.90E-07	4.84E-07	s^{-1}	dehydrogenation
16	5.19E-05	3.91E-03	m^{-1} s^{-1}	phenylation
17	5.41E-09	1.37E-07	s^{-1}	decarbonylation
18	2.45E-08	*< 2.45E-08*	s^{-1}	oxidation

[a]rate constants do not include water and assume its concentration does not change.[b]electrophilic aromatic substitution.

in Figure 38. Rate constants for Reactions 12 and 13 are not reported because the model fitted an aggregate rate constant for the two reactions combined. Importantly, the rate constants at 350 °C are greater than those for the same reaction at 300 °C, obeying statistical mechanics and other kinetic theory. The only exception is reaction 18, the oxidation of benzaldehyde by water. This reaction has the smallest rate constant at 300 °C but was smaller than plausible constraints at 350 °C. This result suggests that oxidation of benzaldehyde is a minor, if not absent, process. At 300 °C, the model may have benefited from the inclusion of this reaction to account for the slight amount of oxidation of benzaldehyde due to oxygen contamination, yet at 350 °C where conversions are higher it likely had no effect on the numerical fitting.

Generally, the magnitudes of the rate constants are consistent with the proposed reactions. As indicated above, an important reaction pathway is the depletion of benzyl alcohol in electrophilic aromatic substitution reactions. At both temperatures, the rate constants follow the expected trend with respect to the inductive effects of the ring substituents involved, such that the rate constants follow the trend $k7 > k3 > k8 >> k4$. The formyl group of benzaldehyde is strongly deactivating toward EAS and thus the rate constant for Reaction 4 is approximately two orders of magnitude less than that for EAS involving benzene (Reaction 3). That significant yields of benzylbenzaldehydes were observed is a consequence of the large abundance of benzaldehyde relative to other substrates for benzylation. The $–CH_2OH$ substituent of benzyl alcohol is only slightly deactivating and Reaction 8 yields a rate constant only slightly lower than that for the analogous reaction with benzene. The methyl substituent of toluene is instead weakly activating and the rate constant for Reaction 7 is somewhat larger than that for Reaction 3.

Similarly, the rate constant for Reaction 11 is greater than that for Reaction 3 because the benzyl substituent of benzylbenzyl alcohol affords somewhat enhanced stability of the resulting electrophilic carbocation compared to benzyl alcohol. The rate constant at 350 °C is likely anomalously high because there is no concentration data for benzylbenzyl alcohol at this temperature to constrain the fitting of this reaction. Nevertheless, the concentrations of benzylbenzyl alcohol predicted by the model at 350 °C are below the detection limits of the GC analysis, consistent with isomers of benzylbenzyl alcohol not being observed in experiments at that temperature. The rate constants for phenylbenzaldehyde and biphenyl production offer additional insight into these reactions, as they are the most mechanistically inconclusive. For an EAS mechanism, the rate constant for formation of phenylbenzaldehyde should be noticeably less than that for biphenyl. This expectation holds true at both temperatures, supporting the tentative assignment of an EAS mechanism to these compounds in spite of conflicting lines of evidence.

An important aspect of the model is the relative rates of decarbonylation and decarboxylation reactions to yield benzene. Decarbonylation of aromatic aldehydes is thought to proceed via protonation of the *ipso*-carbon (Schubert and Zahler, 1954). Decarboxylation of carboxylic acids has been studied with a variety of acids, where the mechanism is likely quite dependent on structure (Palmer and Drummond, 1986; Li and Brill, 2003; McCollom and Seewald, 2003; Fu *et al.*, 2009; Glein, 2012). The model demonstrates that most of the benzene may be accounted for via decarboxylation of benzoic acid, as the decarboxylation rate constant is approximately two orders of magnitude larger than that of decarbonylation at both temperatures. Because decarboxylation is the only major reaction pathway expected for benzoic acid, an opportunity exists to independently

evaluate the strength of the model by experimentally evaluating decarboxylation rate constants of benzoic acid. Time courses for benzoic acid decomposition and the resulting first-order rate constants at 300 °C and 350 °C are shown in Figure 44 and tabulated in Table 14. In previous work, benzoic acid showed negligible conversion for 5 days at 250 °C (Katritzky *et al.,* 1990a) or for 1 hour at 350 °C (Dunn *et al.*, 2003). The rate determined at 300 °C is less than that extracted from experiments in the presence of minerals (McCollom *et al.,* 2001), suggesting that decarboxylation may be subject to mineral catalysis. The measured rate constants exceed those determined in the kinetic model by factors of ~2.5 (300 °C) and ~3.5 (350 °C). This suggests that the model may be overly favoring the decarbonylation pathway and that more of the benzene may be accounted for via decarboxylation. Nevertheless, attempts to fit benzene yields in the benzaldehyde model with the experimentally measured decarboxylation rate constants yielded an excess of benzene, even when decarbonylation was removed from the model. Thus, these discrepancies are the result of relatively large uncertainties that arise in a kinetic model with 17 independent variables. Decarboxylation does appear to be the major pathway to yield benzene in the benzaldehyde system.

The goodness of fit of the model to the time-dependent yields of compounds it includes are depicted in Figures 45 and 46 for 300 °C and 350 °C, respectively. The model fits the major products benzyl alcohol, benzoic acid, and benzene quite well at both temperatures, suggesting that the suite of reactions included in the model are reflective of pathways that lead to the non-unity ratios of benzoic acid to benzyl alcohol. Many of the minor products are also fit well with the model, yet there are notable discrepancies in some. Products of dehydrogenation reactions, such as fluorene, fluorenone, and anthracene have

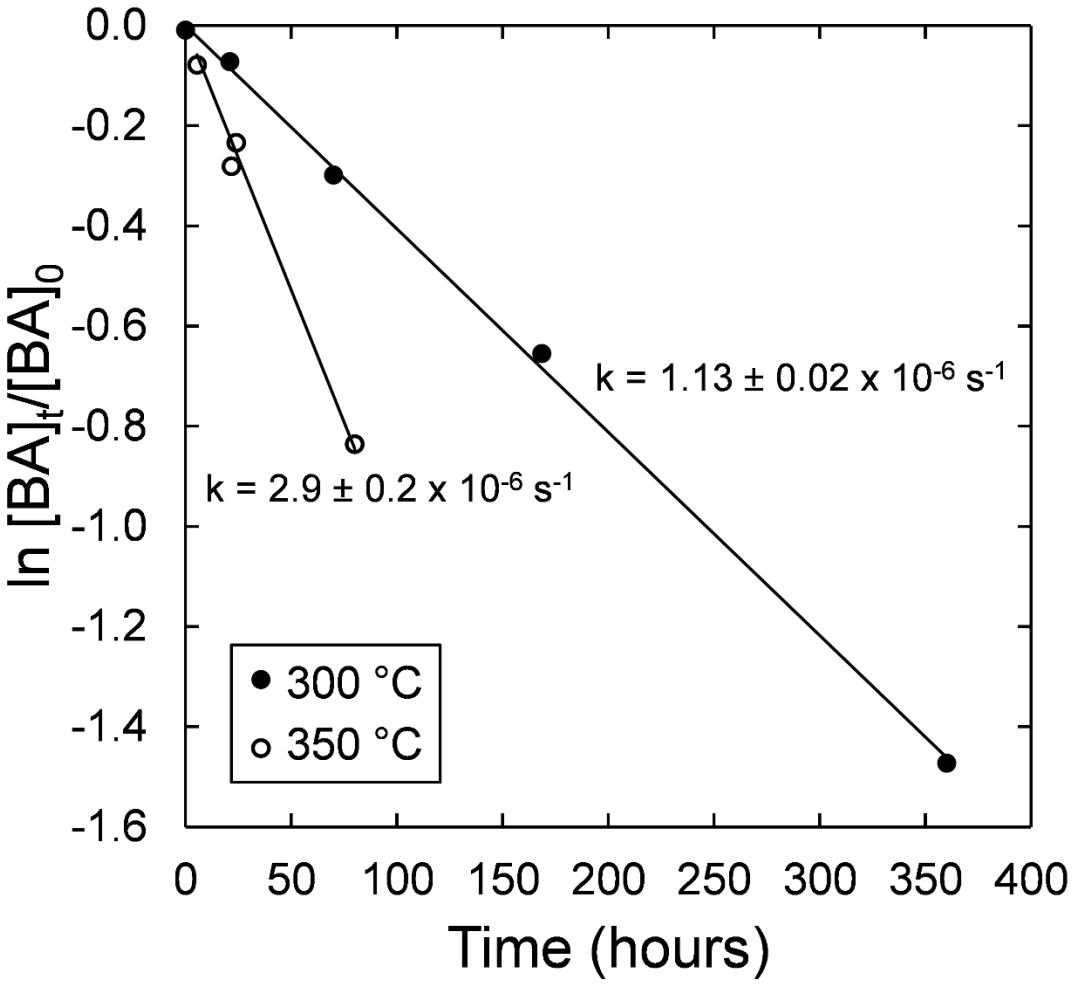

Figure 44. The natural logarithm of the ratio of measured benzoic acid concentration to initial benzoic acid concentration as a function of time for experiments at 300 °C (filled circles) and 350 °C (open circles). Rate constants derived from linear regression are reported with their uncertainties, which is the uncertainty of the slope of the best-fit line. Measured benzoic acid concentrations are based on analyses of benzene, the yield of which is assumed to equal the amount of benzoic acid consumed. Traces of biphenyl were also detected and assumed to represent the yield of two equivalents of benzene for the purposes of the kinetic analysis.

Table 14. Starting amounts and yields (in μmol) in benzoic acid experiments at 300 °C and 350 °C. Blank entries are less than 0.010 μmol.

time (hours)	benzoic acid (initial)	benzoic acid (measured)	benzene	biphenyl
300 °C				
0	205	205	1.82	
21	198	186	13.7	
70	213	156	55	
168.5	209	107	100.4	
360	203	40.1	156	0.22
350 °C				
5.5	247.789	229.526	18.768	0.006
21.8	246.233	165.974	60.351	0.014
24	247.625	149.337	51.563	0.010
80	245.578	51.493	139.063	0.032

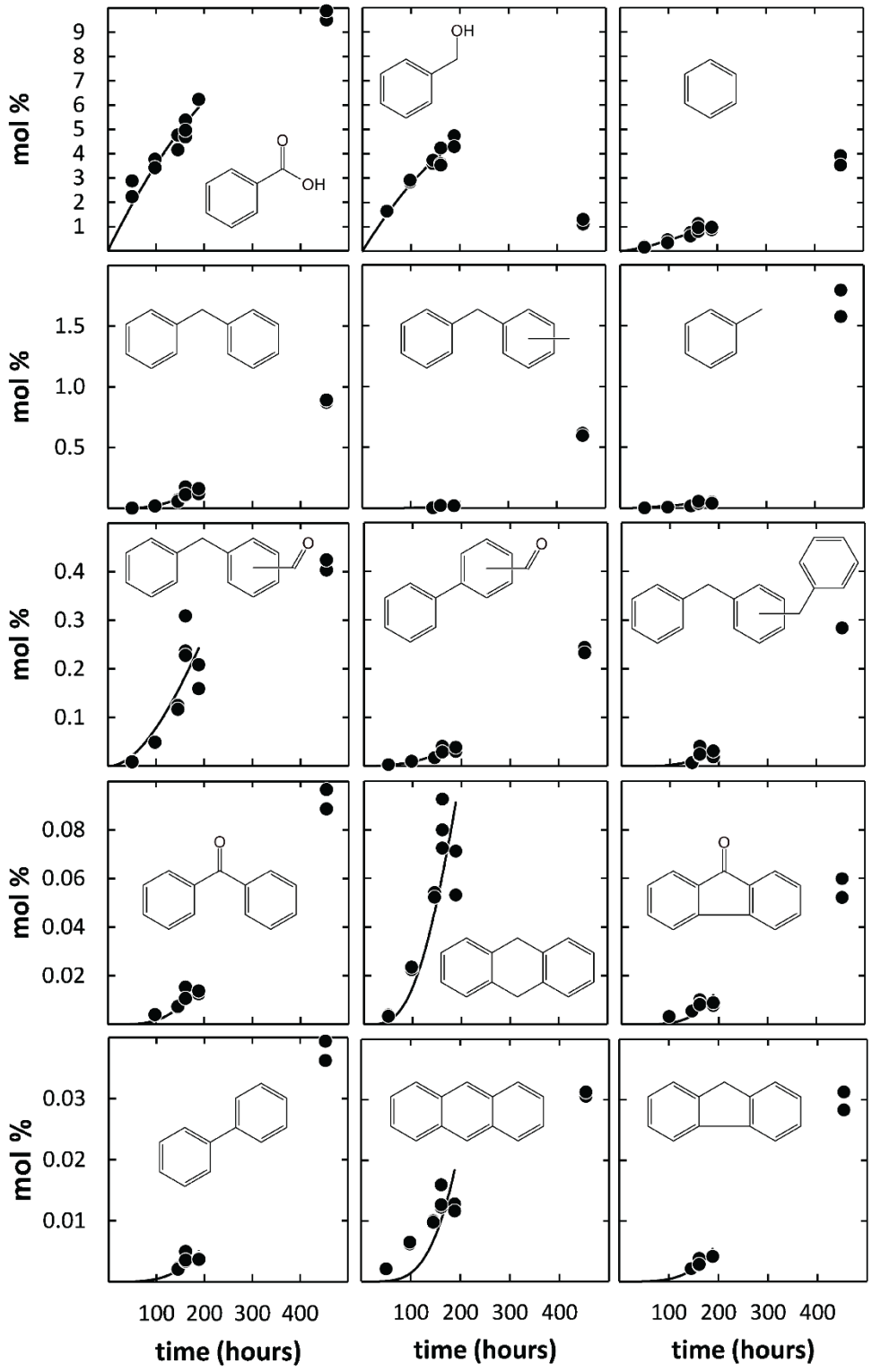

Figure 45. Yields (expressed as mol %) of selected products of 0.1 molal benzaldehyde experiments at 300 °C as a function of time. Curves represent the time dependence of product yields based on the kinetic model.

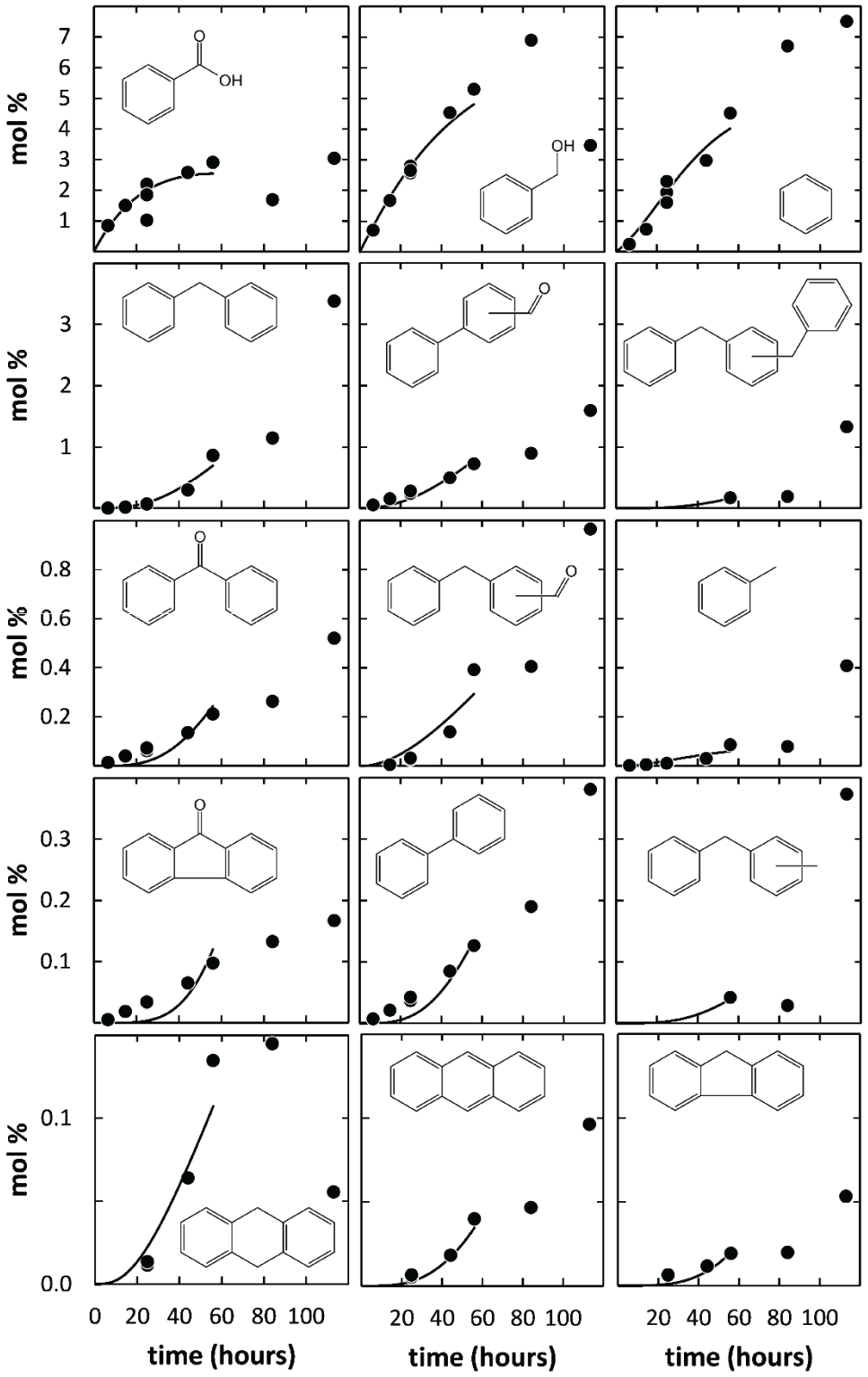

Figure 46. Yields (expressed as mol %) of selected products of 0.1 molal benzaldehyde experiments at 350 °C as a function of time. Curves represent the time dependence of product yields based on the kinetic model.

modeled time dependencies that exhibit an induction period not supported by the analytical data. One possibility for this discrepancy is that these reactions may be reversible. Reversibility would allow the forward reaction to possess a relatively large rate constant to account for the appearance of the dehydrogenation products at early times, yet not build up to significant concentrations due to the reverse reaction. Allowing these reactions to be reversible in the model, however, did not noticeably alter the goodness of fit to the data for these compounds. Though the reactions are written in terms of molecular hydrogen, mechanistically this is likely an oversimplification that may not allow the model to adequately represent these reactions. In any case, these compounds are far less abundant than the major products and therefore have a negligible effect on their fit.

The rate constants for reaction 1, the disproportionation of benzaldehyde, are among the smallest of all the reactions considered. This observation is not surprising, as the relative rates of the secondary reactions allow for a great deal of complexity to be reached even before benzaldehyde has come close to its first half-life. Complexity at low conversions of initial reactants is a common occurrence in hydrothermal experiments (Yang *et al.*, 2012; Shipp *et al.*, 2013). While reaction 1 may be rate-limiting, the appearance of other products opens new pathways to benzaldehyde degradation, which can be seen in comparison to k_{obs} on an Arrhenius plot (Figure 47), where k_{obs} is the rate constant obtained solely from benzaldehyde regression. The two rate constants are assumed to be equal at 250 °C because there is insufficient data at this temperature to determine k_1. The rate constant for disproportionation possesses a slightly smaller activation energy and a much smaller pre-exponential factor than k_{obs}. In reality, k_1 is an aggregate rate constant:

$$k_1 = K_{hydrate} * k_{HT}$$

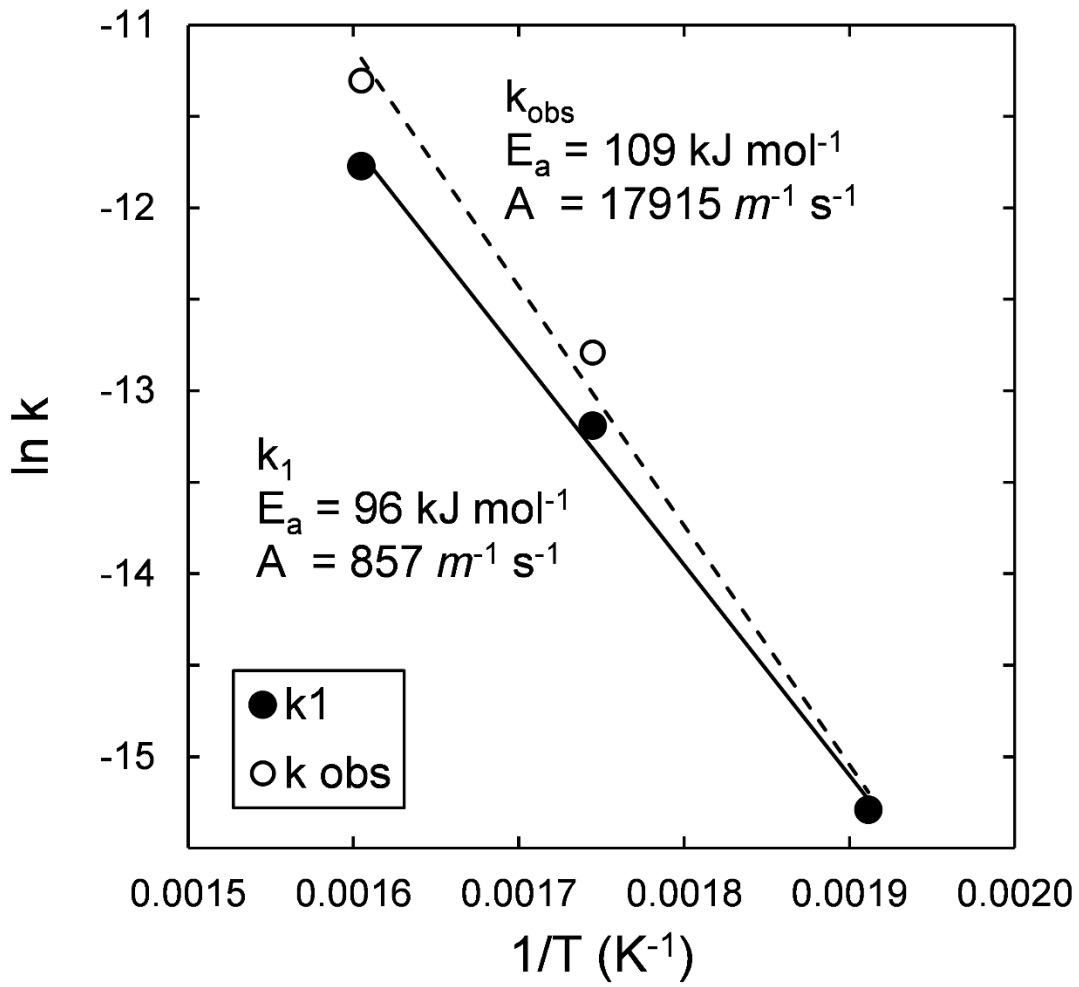

Figure 47. Arrhenius plot comparing the rate constants for the disproportionation reaction of benzaldehyde obtained via kinetic modeling (filled circles; solid regression line) with the observed rate constants for benzaldehyde decomposition (open circles; dashed regression line). Activation energies and pre-exponential factors obtained by regression are indicated.

where $K_{hydrate}$ is the equilibrium constant for formation of the hydrate of benzaldehyde and k_{HT} is the rate constant of the rate-limiting hydride transfer step between the hydrate and another benzaldehyde molecule. While the rate constant for the rate-limiting step should increase with increasing temperature, increasing temperature disfavors hydrate formation, though it has not been investigated in the temperature regime presently considered (Kurz, 1967; Pocker and Dickerson, 1969; Matubayasi *et al.*, 2007; Nakazawa and Takahashi, 1999). This situation could potentially lead to non-linear Arrhenius behavior, yet there is no strong evidence of this over the temperature range studied here, given the uncertainties in the rate constants. In comparison with k_{obs}, k_1 and its Arrhenius parameters offer a more useful depiction of the kinetics of benzaldehyde itself, as a portion of benzaldehyde decomposition in experiments is due to secondary reactions.

4.3.5 Implications for Natural Systems

The experiments depicted here have allowed for new light to be shed on the behavior of benzaldehyde under hydrothermal conditions and its kinetics, yet also allow for insights regarding aldehydes in natural systems. Particularly illuminating is the time-dependence of the hydrogen and oxygen contents of the benzaldehyde system as shown in Figure 48. At 300 °C, both hydrogen and oxygen are increasingly incorporated into the organics present in the experiment, except at the longest reaction time, where oxygen begins to decrease while hydrogen continues to increase. This addition of hydrogen and oxygen is reflective of water reacting with benzaldehyde. At 350 °C, oxygen content initially increases but quickly begins to decrease to levels well below the initial oxygen content of the benzaldehyde, whereas hydrogen increases. This loss of oxygen, even via reaction with water, combined with a steady increase in the H:C ratio, is reminiscent of the

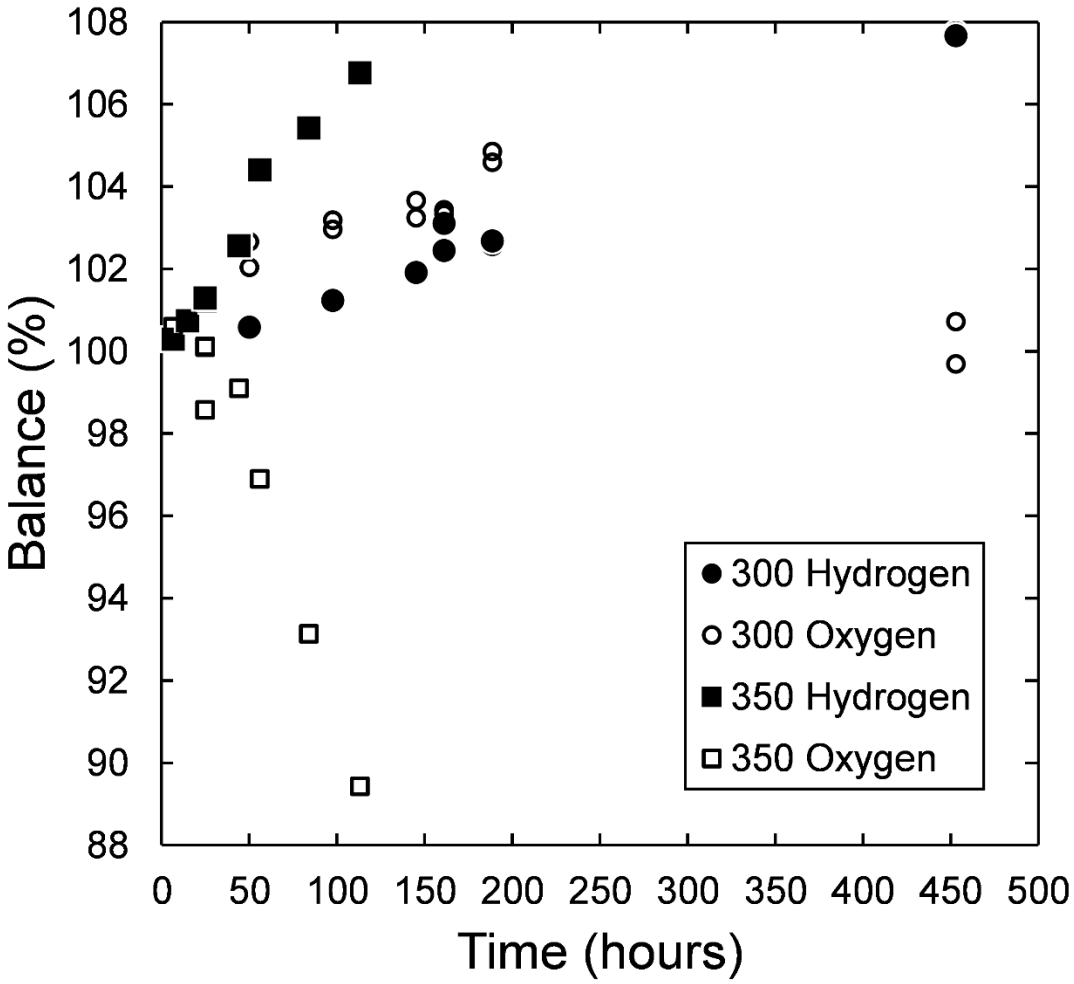

Figure 48. Percent mole abundance of hydrogen (filled symbols) and oxygen (open symbols) in quantified organic compounds as a function of reaction time for 0.1 molal benzaldehyde experiments relative to the number of moles present in benzaldehyde at the beginning of each experiment. Experiments at 300 °C (circles) and 350 °C (squares) are both shown.

evolution of petroleum, which pushes the system toward the composition of methane. While poly-aromatic structures also are formed, these represent in most cases coupling of existing aromatic rings, where there is no increase in aromaticity. The only exception is the formation of anthracene from two equivalents of benzyl alcohol. Thus, on geologic time scales, aldehydes may act as reactive, oxygenated intermediates that lead to carboxylic acids, connecting them with hydrocarbons via decarboxylation.

It is worthwhile to consider to what extent the hydrothermal chemistry of benzaldehyde is reflective of aldehydes in general. Benzaldehyde lacks α-hydrogens that most aldehydes possess, which precludes any chemistry via enol intermediates, such as the Aldol condensation. Nevertheless, unless other reaction pathways kinetically inhibit it, most aldehydes should be capable of the disproportionation reaction, which is likely the major mechanism for the formation of carboxylic acids from aldehydes. Indeed, an analogue of benzaldehyde containing α-hydrogens, phenylacetaldehyde, underwent both disproportionation and Aldol reactions (Katritzky *et al.*, 1990b). Being a bimolecular reaction, however, means that the high concentrations of a single reactant present in experiments may not reflect the situation in nature, which contains a plethora of compounds each at individually minute concentrations. Instead, cross-disproportionations may be more common, where hydride donors donate hydride to any suitable hydride acceptor. There are hints of this behavior in benzaldehyde experiments, for example where the formation of toluene becomes more and more favorable at longer reaction times as more benzyl alcohol is formed and the organic mixture becomes more complex.

The complexity of benzaldehyde experiments, especially at long reaction times, is due to the capabilities of the alcohol formed, benzyl alcohol. Being benzylic, benzyl

alcohol forms an anomalously stable carbocation upon dehydration, which allows for the abundance of benzylation reactions observed, which are the primary mode of C-C bond formation in these experiments. The alcohol of other aldehydes would lack this capability, but for an aldehyde possessing α-hydrogens the resulting alcohol could form the alkene, opening other reaction pathways. Additionally, as with disproportionation, benzylation is a bimolecular reaction that is favored in experiments with large concentrations of amenable reactants. These would likely be significantly retarded in nature, yet on geologic time scales, could still be a significant process when benzylic alcohols are present.

4.4 Conclusions

The present study offers novel insights into the chemistry of benzaldehyde under hydrothermal conditions. The concentration dependence on the rate confirmed overall second-order kinetics, yet inconsistent ratios of benzoic acid to benzyl alcohol raised doubt regarding the primary mechanism of benzaldehyde decomposition. Kinetic modeling of secondary reactions was able to explain the observed trends in benzoic acid and benzyl alcohol, confirming the validity of the Cannizzaro disproportionation reaction. Experiments with varied pH demonstrate that while the reaction is catalyzed by hydroxide ions under basic conditions, below neutrality water acts as the nucleophile for hydrate formation and its rate is not enhanced by acidic conditions. Arrhenius parameters were obtained over the temperature range 250-350 °C that differ from those derived from data in the supercritical region, meaning the present parameters are more useful for extrapolation of the rate of aldehyde decomposition to temperatures of geologic relevance, such as those found in sedimentary basins.

It is likely that disproportionation is a reaction pathway of most aldehydes under hydrothermal conditions. While their formation is less favorable than ketones, on geologic time scales aldehydes may be formed from alkanes and alkenes via *anti*-Markovnikov hydration to primary alcohols and subsequent dehydrogenation. While ketone C-C bond cleavage may be a pathway leading to carboxylic acids in nature, particularly if naturally catalyzed by mineral surfaces, aldehyde disproportionation could be an equally or more important pathway resulting in the formation of carboxylic acids.

4.5 Acknowledgements

Funding for this study was provided by the National Science Foundation (grants OCE-0826588 and OCE-1357243). Production of the silica tubes was performed by Christine Roeger of the ASU glassblowing facility. Brian Cherry and Steve Davidowski of the ASU Magnetic Resonance Research Center provided crucial assistance with the NMR study. Christopher Glein completed the benzoic acid decarboxylation experiments at 300 °C to complement those at 350 °C performed in this study. This work benefited greatly from many discussions with other members of the hydrothermal organic chemistry (HOG) group at ASU, in particular Christiana Bockisch, Christopher Glein, Kristin Johnson, Kirtland Robinson, Jessie Shipp, and Ziming Yang.

V. FUTURE WORK

Biomolecular and geochemical analysis of YNP hot springs in the pH range of ~3-6 have painted a dynamic picture of these hot springs and the microbial communities that inhabit them. Meteoric water supply is hypothesized to be an important control on hot spring conditions and is thought to vary on seasonal and other time scales. Thus, future work should focus on the temporal study of selected hot springs with sampling on a monthly basis. In order to more clearly evaluate the activity of *Cyanidiales* and cyanobacteria, sequencing of ribosomal RNA genes from mRNA rather than genomic DNA should be attempted. These results will indicate under what conditions *Cyanidiales* are active in these systems that also contain cyanobacteria. Analysis of RNA will also be able to unequivocally demonstrate simultaneous activity of both *Cyanidiales* and cyanobacteria if it were to occur. It is also of interest to look for and study similar hot springs in other parts of YNP and beyond to see how the transition between eukaryal and bacterial phototrophs plays out in a geographically separate area. Intriguing locales to search for such hot springs include Hot Springs Basin in YNP and the thermal areas of New Zealand.

The gold catalysis results, while a compelling demonstration of catalysis, were hindered by the apparent coagulation of the 0.5-0.8 micron gold powder, which prevented the measurement of meaningful turnover frequencies. While the bulk powder did not seem to coagulate, its specific surface area was too small to determine via BET analysis. Future work could test other gold powders with particle sizes larger than 0.5-0.8 microns that may not coagulate yet still possess enough surface area for its determination. Turnover

frequencies on bulk gold are essential in order to compare the efficacy of bulk gold in comparison with other catalysts.

The observation that gold is able to effectively heterogeneously catalyze the Cannizzaro reaction, which is traditionally catalyzed homogenously in solution, suggests that the chemistry of benzaldehyde under hydrothermal conditions can be influenced by the presence of solid phases. While gold is unlikely to interact with organic carbon in most natural hydrothermal systems, minerals are ubiquitously present in such situations. Future efforts involving benzaldehyde should build on the comprehensive understanding of its behavior in water alone by systematically testing the effect of common mineral surfaces. Preliminary results involving minerals are depicted in Figure 49. All experiments were completed for 55 hours at 250 °C with 0.1 molal benzaldehyde and 2.45 m^2 of mineral, as determined via BET, using methods described in Chapter 4. Hematite (Fe_2O_3), sphalerite (ZnS), and corundum (Al_2O_3) all yield benzene, either by catalyzing decarbonylation or decarboxylation, the latter of which is somewhat more favorable due to the higher yields of benzoic acid in the presence of these minerals. Hematite and corundum enhance overall conversion but yield more benzoic acid than benzyl alcohol. The similarities in their effects are interesting because these minerals have identical crystal structures. Sphalerite seems to catalyze the cross-disproportionation of benzaldehyde and benzyl alcohol, which yields toluene and benzoic acid. Diphenylmethane is also produced in the presence of sphalerite under these conditions. Magnetite (Fe_3O_4), in contrast, does not overly affect disproportionation but does cause an increased yield of benzyl alcohol, possibly via reduction coupled to the oxidation of magnetite to hematite.

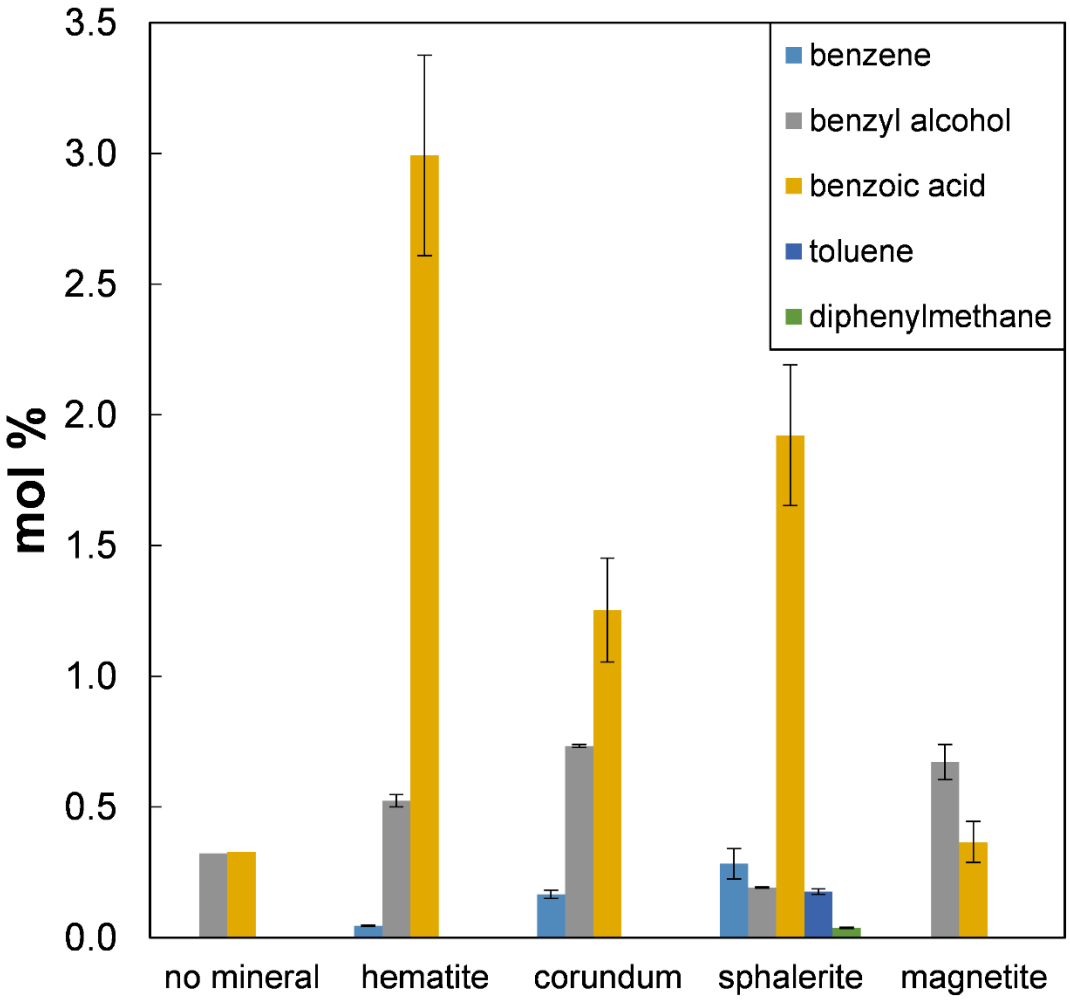

Figure 49. Yields of compounds (as mol %) in experiments with 0.1 molal benzaldehyde conducted at 250 °C for 55 hours in the presence of various mineral powders (total surface area of 2.45 m^2). An analogous experiment without any minerals is shown for comparison. Yields with minerals are shown as the mean of duplicate experiments with uncertainties of +/- one standard deviation.

The hypothesis that aldehydes could be an important intermediate in the production of carboxylic acids in natural systems warrants rigorous testing. Benzaldehyde is not robust for this purpose because of the unique reactivity of its alcohol and the lack of an analogous alkene. Phenylacetaldehyde is potentially an excellent candidate to test functional group interconversions involving aldehydes while directly building on existing knowledge involving benzaldehyde. First, secondary reactions should be categorized in comparison with those for benzaldehyde. New pathways are expected through mechanisms involving the α-hydrogens, while EAS reactions should be less significant compared to benzaldehyde. Second, it is essential to evaluate reversibility between functional groups. Based on an understanding of benzaldehyde, experiments commencing with phenylacetaldehyde should yield the corresponding alkane (ethylbenzene), alkene (styrene), alcohol (2-phenylethanol), and carboxylic acid (phenylacetic acid), yet reversibility amongst these functional groups should be evaluated by conducting experiments beginning with each to assess which of the other compounds can be obtained from each starting point, as has been done in other systems (e.g., Shipp *et al.*, 2013). The alkene, styrene, presents a potential challenge to this goal, however. Styrene may be quite reactive and thus not be observed in phenylacetaldehyde experiments; more importantly, styrene may tend toward polymerization under certain conditions, which is not conducive to the current analytical approaches. Styrene is also expected to yield 1-phenylethanol much more readily than 2-phenylethanol, which may obfuscate the interconversions through the aldehyde. Given these challenges, hydrocinnamaldehyde could be a more appropriate aldehyde to look for reversibility between all functional groups through an aldehyde intermediate.

REFERENCES

Abad A, Corma A, Garcia H (2008) Catalyst parameters determining activity and selectivity of supported gold nanoparticles for the aerobic oxidation of alcohols: The molecular reaction mechanism. *Chemistry: A European Journal*, **14**, 212-222.

Abbott TM, Buchanan GW, Kruus P, Lee KC (1982) Carbon-13 nuclear magnetic resonance and Raman investigations of aqueous carbon dioxide systems. *Canadian Journal of Chemistry*, **60**, 1000-1006.

Airs RL, Temperton B, Sambles C, Farnham G, Skill SK, Llewellyn CA (2014) Chlorophyll *f* and chlorophyll *d* are produced in the cyanobacterium *Chlorogloeopsis fritschii* when cultured under natural light and near-infrared radiation. *FEBS Letters*, **588**, 3770-3777.

Akgul G, Kruse A (2013) Hydrothermal disproportionation of formaldehyde at subcritical conditions. *Journal of Supercritical Fluids*, **73**, 43-50.

Akiya N, Savage PE (2001) Kinetics and mechanism of cyclohexanol dehydration in high-temperature water. *Industrial & Engineering Chemistry Research*, **40**, 1822-1831.

Akiya N, Savage PE (2002) Roles of water for chemical reactions in high-temperature water. *Chemical Reviews*, **102**, 2725-2750.

Allewalt JP, Bateson MM, Revsbech NP, Slack K, Ward DM (2006) Effect of temperature and light on growth of and photosynthesis by *Synechococcus* isolates typical of those predominating in the Octopus Spring microbial mat community of Yellowstone National Park. *Applied and Environmental Microbiology*, **72**, 544-550.

Amend JP, Shock EL (2001) Energetics of overall metabolic reactions of thermophilic and hyperthermophilic Archaea and Bacteria. *FEMS Microbiology Reviews*, **25**, 175-243.

Amenabar M, Urschel MR, Boyd ES (2015) "Metabolic and taxonomic diversification in continental magmatic hydrothermal systems," in *Microbial Evolution under Extreme Conditions*, ed. C. Bakermans. De Gruyter: Berlin, Germany, pp. 57-96.

An J, Bagnell L, Cablewski T, Strauss CR, Trainor RW (1997) Applications of high-temperature aqueous media for synthetic organic reactions. *Journal of Organic Chemistry*, **62**, 2505-2511.

Angelici RJ (2013) Bulk gold (non-nanogold) catalysis of aerobic oxidations of amines, isocyanides, carbon monoxide, and carbene precursors. *Catalysis Science & Technology*, **3**, 279-296.

Antal MJ, Carlsson M, Xu X, Anderson DGM (1998) Mechanism and kinetics of the acid-catalyzed dehydration of 1- and 2-propanol in hot compressed liquid water. *Industrial & Engineering Chemistry Research*, **37**, 3820-3829.

Archibald JM (2009) The puzzle of plastid evolution. *Current Biology*, **19**, R81-R88.

Ashby EC, Coleman D, Gamasa M (1987) Single-electron transfer in the Cannizzaro reaction. *Journal of Organic Chemistry*, **52**, 4079-4085.

Ball JW, McCleskey RB, Nordstrom DK, Holloway JM (2008) Water-chemistry data for selected springs, geysers, and streams in Yellowstone National Park, Wyoming, 2003-2005, U.S. Geological Survey Open-File Report 2006–1339, 137 p.

Ball JW, McCleskey RB, Nordstrom DK (2010) Water-chemistry data for selected springs, geysers, and streams in Yellowstone National Park, Wyoming, 2006–2008: U.S. Geological Survey Open-File Report 2010–1192, 109 p.

Bell JLS, Palmer DA, Barnes HL, Drummond SE (1994) Thermal decomposition of acetate. III. Catalysis by mineral surfaces. *Geochimica et Cosmochimica Acta*, **58**, 4155-4177.

Berg IA (2011) Ecological aspects of the distribution of different autotrophic CO_2 fixation pathways. *Applied and Environmental Microbiology*, **77**, 1925-1936.

Biller SJ, Berube PM, Lindell D, Chisholm SW (2015) *Prochlorococcus*: the structure and function of collective diversity. *Nature Reviews Microbiology*, **13**, 13-27.

Blankenship RE (2014) *Molecular mechanisms of photosynthesis.* 2nd ed. Blackwell Science, Oxford.

Blanksby SJ, Ellison GB (2003) Bond dissociation energies of organic molecules. *Accounts of Chemical Research*, **36**, 255-263.

Bond GC, Louis C, Thompson DT (2006) *Catalysis by Gold.* Imperial College Press, London.

Bond GC, Thompson DT (1999) Catalysis by gold. *Catalysis Reviews – Science and Engineering*, **41**, 319-388.

Boomer SM, Lodge DP, Dutton BE, Pierson B (2002) Molecular characterization of novel red green nonsulfur bacteria from five different hot spring communities in Yellowstone National Park. *Applied and Environmental Microbiology*, **68**, 346-355.

Boomer SM, Noll KL, Geesey GG, Dutton BE (2009) Formation of multilayered photosynthetic biofilms in an ermal spring in Yellowstone National Park, Wyoming. *Applied and Environmental Microbiology,* **75**, 2464-2475.

Boyd ES, Jackson RA, Encarnacion G, Zahn JA, Beard T, Leavitt WD, Pi Y, Zhang CL, Pearson A, Geesey GG (2007). Isolation, characterization, and ecology of sulfur-respiring *Crenarchaea* inhabiting acid-sulfate-chloride-containing geothermal springs in Yellowstone National Park. *Applied and Environmental Microbiology*, **73**, 6669-6677.

Boyd ES, Leavitt WD, Geesey GG (2009) CO_2 uptake and fixation by a thermoacidophilic microbial community attached to precipitated sulfur in a geothermal spring. *Applied and Environmental Microbiology*, **75**, 4289-4296.

Boyd ES, Hamilton TL, Spear JR, Lavin M, Peters JW (2010) [FeFe]-hydrogenase in Yellowstone National Park: evidence for dispersal limitation and phylogenetic niche conservatism. *The ISME Journal*, **4**, 1485-1495.

Boyd ES, Fecteau KM, Havig JR, Shock EL, Peters JW (2012) Modeling the habitat range of phototrophs in Yellowstone National Park: Toward the development of a comprehensive fitness landscape. *Frontiers in Microbiology*, **3**, 221.

Briggs BR, Brodie EL, Tom LM, Dong H, Jiang H, Huang Q, Wang S, Hou W, Wu G, Huang L, Hedlund BP, Zhang C, Dijkstra P, Hungate BA (2014) Seasonal patterns in microbial communities inhabiting the hot springs of Tengchong, Yunnan Province, China. *Environmental Microbiology*, **16**, 1579-1591.

Britton G (1995) "UV/Visible spectroscopy," in *Carotenoids Volume 1B: Spectroscopy*, eds. Britton G, Liaaen-Jensen S, Pfander H. Birkhäuser Verlag, Basel, pp. 13-62.

Brock TD (1967) Life at high temperatures. *Science,* **158**, 1012-1019.

Brock TD and Brock ML (1968) Measurement of steady-state growth rates of a thermophilic alga directly in nature. *Journal of Bacteriology,* **95**, 811-815.

Brock TD (1971) Bimodal distribution of pH values of thermal springs of the world. *Geological Society of America Bulletin*, **82**, 1393-1394.

Brock TD (1973) Lower pH limit for the existence of blue-green algae: Evolutionary and ecological implications. *Science,* **179**, 480-483.

Brock TD, Bauld J (1973) Ecological Studies of *Chloroflexis*, a gliding photosynthetic bacterium. *Archives of Microbiology*, **92**, 267-284.

Brock TD (1978) *Thermophilic Microorganisms and Life at High Temperatures*. Springer-Verlag, New York.

Brown PB, Wolfe GV (2006) Protist genetic diversity in the acidic hydrothermal environments of Lassen Volcanic National Park, USA. *Journal of Eukaryotic Microbiology*, **53**, 420-431.

Bryant DA, Costas AMG, Maresca JA, Chew AGM, Klatt CG, Bateson MM, Tallon LJ, Hostetler J, Nelson WC, Heidelberg JF, Ward DM (2007) *Candidatus* Chloracidobacterium thermophilum: an aerobic phototrophic acidobacterium. *Science*, **317**, 523-526.

Buhler W, Dinjus E, Ederer HJ, Kruse A, Mas C (2002) Ionic reactions and pyrolysis of glycerol as competing reaction pathways in near- and supercritical water. *Journal of Supercritical Fluids*, **22**, 37-53.

Cannizzaro S (1853) Alcohols corresponding to benzoic acid. *Justus Liebigs Annals of Chemistry*, **88**, 129-130.

Carothers WW, Kharaka YK (1978) Aliphatic acid anions in oil-field waters - implications for origin of natural gas. *American Association of Petroleum Geologists Bulletin*, **62**, 2441-2453.

Castenholz RW (1996) Endemism and biodiversity of thermophilic cyanobacteria. *Nova Hedwigia*, **112**, 33-47.

Chen J, Fang W, Zhang Q, Deng W, Wang Y (2014) A comparative study of size effects in the Au-catalyzed oxidative and non-oxidative dehydrogenation of benzyl alcohol. *Chemistry - An Asian Journal*, **9**, 2187-2196.

Chen M (2014) Chlorophyll modifications and their spectral extension in oxygenic photosynthesis. *Annual Review of Biochemistry*, **83**, 317-340.

Chung S (1982) Mechanism of the Cannizzaro reaction: possible involvement of radical intermediates. *Journal of the Chemical Society, Chemical Communications*, 480-481.

Conte M, Miyamura H, Kobayashi S, Chechik V (2009) Spin trapping of Au-H intermediate in the alcohol oxidation by supported and unsupported gold catalysts. *Journal of the American Chemical Society*, **131**, 7189-7196.

Cox A, Shock EL, Havig JR (2011) The transition to microbial photosynthesis in hydrothermal ecosystems. *Chemical Geology*, **280**, 344-351.

Criscuolo A, Gribaldo S (2011) Large-scale phylogenomic analyses indicate a deep origin of primary plastids with cyanobacteria. *Molecular Biology & Evolution*, **28**, 3019-3032.

Cunningham FX, Lee H, Gantt E (2007) Carotenoid biosynthesis in the primitive red alga *Cyanidioschyzon merolae*. *Eukaryotic Cell*, **6**, 533-545.

Dagan T, Roettger M, Stucken K, Landan G, Koch R, Major P, Gould SB, Goremykin VV, Rippka R, Tandeau de Marsac N, Gugger M, Lockhart PJ, Allen JF, Brune I, Maus I, Pühler A, Martin WF (2013) Genomes of stigonematalean cyanobacteria (subsection V) and the evolution of oxygenic photosynthesis from prokaryotes to plastids. *Genome Biology and Evolution*, **5**, 31-44.

Doemel, WN (1970) The physiological ecology of *Cyanidium caldarium*. Ph.D. thesis, Indiana University.

Doemel, WN, Brock TD (1970) The upper temperature limit of *Cyanidium caldarium*. *Archives of Microbiology*, **72**, 326-332.

Doemel WN, Brock TD (1971) The physiological ecology of *Cyanidium caldarium*. *Journal of General Microbiology*, **67**, 17-32.

Doering WE, Sotiriou-Leventis C, Roth WR (1995) Thermal interconversions among 15-*cis*-, 13-*cis*-, and *all-trans*-β-carotene: Kinetics, Arrhenius parameters, thermochemistry, and potential relevance to anticarcinogenicity of *all-trans*-β-carotene. *Journal of the American Chemical Society*, **117**, 2747-2757.

Dunn JB, Burns ML, Hunter SE, Savage PE (2003) Hydrothermal stability of aromatic carboxylic acids. *Journal of Supercritical Fluids*, **27**, 263-274.

Edgar RC, Haas BJ, Clemente JC, Quince C, Knight R (2011) UCHIME improves sensitivity and speed of chimera detection. *Bioinformatics*, **27**, 2194-2200.

Elsila JE, Charnley SB, Burton AS, Glavin DP, Dworkin JP (2012) Compound-specific carbon, nitrogen, and hydrogen isotopic ratios for amino acids in CM and CR chondrites and their use in evaluating potential formation pathways. *Meteoritics & Planetary Science*, **47**, 1517-1536.

Ertl G, Knozinger H, Schuth F, Weitkamp J (eds.) (2008) *Handbook of heterogeneous catalysis* Volume 2. 2nd ed. Wiley VCH, Weinheim.

Evans EH, Foulds I, Carr NG (1976) Environmental conditions and morphological variation in the blue-green alga *Chlorogloea fritschii*. *Journal of General Microbiology*, **92**, 147-155.

Evans EH, Britton G (1983) Relationship between growth conditions, cell morphology and carotenoid composition of the cyanobacterium *Chlorogloeopsis (Chlorogloea) fritschii*, and carotenoid compositions of photosystem 1 and photosystem 2 preparations. *Archives of Microbiology*, **135**, 284-286.

Falcón LI, Magallón S, Castillo A (2010) Dating the cyanobacterial ancestor of the chloroplast. *The ISME Journal*, **4**, 777-783.

Falkowski P, Scholes RJ, Boyle E, Canadell J, Canfield D, Elser J, Gruber N, Hibbard K, Higberg P, Linder S, Mackenzie FT, Moore, B, Pedersen T, Rosenthal Y, Seitzinger S, Smetacek V, Steffen W (2000) The global carbon cycle: A test of our knowledge of Earth as a system. *Science*, **290**, 291-296.

Fang W, Chen J, Zhang Q, Deng W, Wang Y (2011) Hydrotalcite-supported gold catalyst for the oxidant-free dehydrogenation of benzyl alcohol: Studies on support and gold size effects. *Chemistry: A European Journal*, **17**, 1247-1256.

Fang W, Zhang Q, Chen J, Deng W, Wang Y (2010) Gold nanoparticles on hydrotalcites as efficient catalysts for oxidant-free dehydrogenation of alcohols. *Chemical Communications*, **46**, 1547-1549.

Ferraz CP, Garcia MAS, Teixeira-Neto E, Rossi LM (2016) Oxidation of benzyl alcohol catalyzed by gold nanoparticles under alkaline conditions: Weak vs. strong bases. *RSC Advances*, **6**, 25279-25285.

Ferris MJ, Sheehan KB, Kühl M, Cooksey K, Wigglesworth-Cooksey B, Harvey R, Henson JM (2005) Algal species and light microenvironment in a low-pH, geothermal microbial mat community. *Applied and Environmental Microbiology,* **71**, 7164-7171.

Fournier RO (2005) "Geochemistry and dynamics of the Yellowstone National Park hydrothermal system," in *Geothermal Biology and Geochemistry in Yellowstone National Park,* eds WP Inskeep and TR McDermott. Montana State University, Bozeman, pp. 3-29.

Fristrup P, Johansen LB, Christensen CH (2008) Mechanistic investigation of the gold-catalyzed aerobic oxidation of alcohols. *Catalysis Letters*, **120**, 184-190.

Fu J, Savage PE, Lu X (2009) Hydrothermal decarboxylation of pentafluorobenzoic acid and quinolinic acid. *Industrial & Engineering Chemistry Research*, **48,** 10467-10471.

Funazukuri T, Serikawa RM, Yamaura K (1997) Rate of dibenzyl ether decomposition in supercritical water. *Fuel*, **76**, 865-870.

Gan F, Zhang S, Rockwell NC, Martin SS, Lagarias JC, Bryant DA (2014) Extensive remodeling of cyanobacterial photosynthetic apparatus in far-red light. *Science*, **345**, 1312-1317.

Garcia Costas AM, Tsukatani Y, Rijpstra WIC, Schouten S, Welander PV, Summons RE, Bryant DA (2012) Identification of the bacteriochlorophylls, carotenoids, lipids, quinones, and hopanoids of "*Candidatus* Chloracidobacterium thermophilum". *Journal of Biological Chemistry*, **194**, 1158-1168.

Gerloff-Elias A, Barua D, Mölich A, Spijkerman E (2006) Temperature- and pH-dependent accumulation of heat-shock proteins in the acidophilic green alga *Chlamydamonas acidophila*. *FEMS Microbiology Ecology*, **56**, 345-354.

Glein C (2012) Theoretical and experimental studies of cryogenic and hydrothermal organic geochemistry. Ph.D. thesis, Arizona State University.

Gould SB, Waller RF, McFadden GI (2008) Plastid Evolution. *Annual Review of Plant Biology*, **59**, 491-517.

Guo H, Al-Hunaiti A, Kemell M, Rautiainen S, Leskelae M, Repo T (2011) Gold catalysis outside nanoscale: Bulk gold catalyzes the aerobic oxidation of π-activated alcohols. *ChemCatChem*, **3**, 1872-1875.

Hamilton TL, Lange RK, Boyd ES, Peters JW (2011a) Biological nitrogen fixation in acidic high temperature geothermal springs in Yellowstone National Park, Wyoming. *Environmental Microbiology*, **13**, 2204-2215.

Hamilton TL, Boyd ES, Peters JW (2011b) Environmental constraints underpin the distribution and phylogenetic diversity of *nifH* in the Yellowstone geothermal complex. *Microbial Ecology*, **61**, 860-870.

Hamilton TL, Vogl K, Bryant DA, Boyd ES, Peters JW (2012) Environmental constraints defining the distribution, composition, and evolution of chlorophototrophs in thermal features of Yellowstone National Park. *Geobiology*, **10**, 236-249.

Hamilton TL, Peters JW, Skidmore ML, Boyd ES (2013) Molecular evidence for an active endogenous microbiome beneath glacial ice. *The ISME Journal*, **7**, 1402-1412.

Hao C, Zhang L, Wang L, Li S, Dong H (2012) Microbial community composition in acid mine drainage lake of Xiang Mountain sulfide mine in Anhui Province, China. *Geomicrobiology Journal*, **29**, 886-895.

Hatano B, Kadokawa J, Tagaya H (2002) Disproportionation of diarylmethanol derivatives by using supercritical water. *Tetrahedron Letters*, **43**, 5859-5861.

Haruta M (1997) Size- and support-dependency in the catalysis of gold. *Catalysis Today*, **36**, 153-166.

Havig JR, Raymond J, Meyer-Dombard DR, Zolotova N, Shock EL (2011) Merging isotopes and community genomics in a siliceous sinter-depositing hot spring. *Journal of Geophysical Research*, **116**, G01005.

Helgeson HC, Knox AM, Owens CE, Shock EL (1993) Petroleum, oil field waters, and authigenic mineral assemblages: Are they in metastable equilibrium in hydrocarbon reservoirs? *Geochimica et Cosmochimica Acta*, **57**, 3295-339.

Holloway JM, Nordstrom DK, Böhlke JK, McCleskey RB, Ball JW (2011) Ammonium in thermal waters of Yellowstone National Park: Processes affecting speciation and isotope fractionation. *Geochimica et Cosmochimica Acta*, **75**, 4611-4636.

Hoops S, Sahle S, Gauges R, Lee C, Pahle J, Simus N, Singhal M, Xu L, Mendes P, Kummer U (2006) COPASI - A COmplex PAthway SImulator. *Bioinformatics*, **22**, 3067-3074.

Hunter SE, Savage PE (2004) Recent advances in acid- and base-catalyzed organic synthesis in high-temperature liquid water. *Chemical Engineering Science*, **59**, 4903-4909.

Ikushima Y, Hatakeda K, Sato O, Yokoyama T, Arai M (2001) Structure and base catalysis of supercritical water in the noncatalytic benzaldehyde disproportionation using water at high temperatures and pressures. *Angewandte Chemie, International Edition*, **40**, 210-213.

Kallas T, Castenholz RW (1982) Internal pH and ATP-ADP Pools in the cyanobacterium *Synechococcus* sp. during exposure to growth-inhibiting low pH. *Journal of Bacteriology*, **149**, 229-236.

Katritzky AR, Balasubramanian M, Siskin M (1990a) Aqueous high-temperature chemistry of carbo- and heterocycles. 2. Monosubstituted benzenes: benzyl alcohol, benzaldehyde and benzoic acid. *Energy & Fuels*, **4**, 499-505.

Katritzky AR, Luxem FJ, Siskin M (1990b) Aqueous high-temperature chemistry of carbo- and heterocycles. 5. Monosubstituted benzenes with a two carbon atom side chain oxygenated at the β-position. *Energy & Fuels*, **4**, 514-517.

Katritzky AR, Allin SM, Siskin M (1996) Aquathermolysis: Reactions of organic compounds with superheated water. *Accounts of Chemical Research*, **29**, 399-406.

Katritzky AR, Nichols DA, Siskin M, Murugan R, Balasubramanian M (2001) Reactions in high-temperature aqueous media. *Chemical Reviews*, **101**, 837-892.

Ketchie WC, Fang Y, Wong MS, Murayama M, Davis RJ (2007) Influence of gold particle size on the aqueous-phase oxidation of carbon monoxide and glycerol. *Journal of Catalysis*, **250**, 94-101.

Kharaka YK, Thordsen JJ, White LD (2002) Isotope and chemical compositions of meteoric and thermal waters and snow from the greater Yellowstone National Park region. *U.S. Geological Survey Open-File Report* 02-194.

Klatt CG, Bryant DA, Ward DM (2007) Comparative genomics provides evidence for the 3-hydroxypropionate autotrophic pathway in filamentous anoxygenic phototrophic bacteria and in hot spring microbial mats. *Environmental Microbiology*, **9**, 2067-2078.

Klatt CG, Inskeep WP, Herrgard MJ, Jay ZJ, Rusch DB, Tringe SG, Parenteau MN, Ward DM, Boomer SM, Bryant DA, Miller SR (2013) Community structure and function of high-temperature chlorophototrophic microbial mats inhabiting diverse geothermal environments. *Frontiers in Microbiology*, **4**, 106.

Klitgaard SK, DeLa Riva AT, Helveg S, Werchmeister RM, Christensen CH (2008) Aerobic oxidation of alcohols over gold catalysts: Role of acid and base. *Catalysis Letters*, **126**, 213-217.

Klobukowski ER, Angelici RJ, Woo LK (2012a) Bulk gold-catalyzed oxidations of amines and benzyl alcohol using amine N-oxides as oxidants. *Catalysis Letters*, **142**, 161-167.

Klobukowski ER, Angelici RJ, Woo LK (2012b) Bulk gold-catalyzed reactions of isocyanides, amines, and amine N-oxides. *Organometallics*, **31**, 2785-2792.

Klobukowski ER, Mueller ML, Angelici RJ, Woo LK (2011) Conversions of cyclic amines to nylon precursor lactams using bulk gold and fumed silica catalysts. *ACS Catalysis*, **1**, 703-708.

Kobayashi M, Akiyama M, Kano H, Kise H (2006) "Spectroscopy and structure determination," in *Chlorophylls and Bacteriochlorophylls*, eds B Grimm, RJ Porra, W Rüdiger, and H Sheer. Springer, Dordrecht, pp. 79-94.

Krammer P, Vogel H (2000) Hydrolysis of esters in subcritical and supercritical water. *Journal of Supercritical Fluids*, **16**, 189-206.

Kruse A, Dinjus E (2007) Hot compressed water as reaction medium and reactant. *Journal of Supercritical Fluids*, **39**, 362-380.

Kruse A, Dahmen N (2015) Water - A magic solvent for biomass conversion. *Journal of Supercritical Fluids*, **96**, 36-45.

Kuhlmann B, Arnett EM, Siskin M (1994) Classical organic reactions in pure superheated water. *Journal of Organic Chemistry*, **59**, 3098-101.

Kurz JL (1967) Hydration of acetaldehyde. I. Equilibrium thermodynamic parameters. *Journal of the American Chemical Society*, **89**, 3524-3528.

Lacap DC, Barraquio W, Pointing SB (2007) Thermophilic microbial mats in a tropical geothermal location display pronounced seasonal changes but appear resilient to stochastic disturbance. *Environmental Microbiology*, **9**, 3065-3076.

Lang SQ, Butterfield DA, Schulte M, Kelley DS, Lilley MD (2010) Elevated concentrations of formate, acetate and dissolved organic carbon found at the Lost City hydrothermal field. *Geochimica et Cosmochimica Acta*, **74**, 941-952.

Lazar M, Angelici RJ (2006) Gold metal-catalyzed reactions of isocyanides with primary amines and oxygen: Analogies with reactions of isocyanides in transition metal complexes. *Journal of the American Chemical Society*, **128**, 10613-10620.

Lazar M, Zhu B, Angelici RJ (2007) Non-nanogold catalysis of reactions of isocyanides, secondary amines, and oxygen to give ureas. *Journal of Physical Chemistry C*, **111**, 4074-4076.

Lehr CR, Frank SD, Norris TB, D'Imperio S, Kalinin AV, Toplin JA, Castenholz RW, McDermott TR (2007) Cyanidia (Cyanidiales) population diversity and dynamics in an acid-sulfate-chloride spring in Yellowstone National Park. *Journal of Phycology*, **43**, 3-14.

Li J, Brill TB (2003) Spectroscopy of hydrothermal reactions 23: The effect of OH substitution on the rates and mechanisms of decarboxylation of benzoic acid. *Journal of Physical Chemistry A*, **107**, 2667-2673.

Loiacono ST, Meyer-Dombard DR, Havig JR, Poret-Peterson AT, Hartnett HE, Shock EL (2012) Evidence for high-temperature *in situ nifH* transcription in an alkaline hot spring of Lower Geyser Basin, Yellowstone National Park. *Environmental Microbiology*, **14**, 1272-1283.

Louda JW, Mongkhonsri P, Baker EW (2011) Chlorophyll degraded during senescence and death-III: 3-10 yr experiments, implications for ETIO series generation. *Organic Geochemistry*, **42**, 688-699.

Lowell C, Castenholz RW (2013) The lowering of external pH in confined environments by thermo-acidophilic algae (class: *Cyanidiophyceae*). *Environmental Microbiology Reports*, **5**, 660-664.

Macur RE, Langner HW, Kocar BD, Inskeep WP (2004) Linking geochemical processes with microbial community analysis: successional dynamics in an arsenic-rich, acid-sulphate-chloride geothermal spring. *Geobiology*, **2**, 163-177.

Macur RE, Jay ZJ, Taylor WP, Kozubal MA, Kocar BD, Inskeep WP (2013) Microbial community structure and sulfur biogeochemistry in mildly-acidic sulfidic geothermal springs in Yellowstone National Park. *Geobiology*, **11**, 86-99.

Madigan MT (1984) A novel photosynthetic purple bacterium isolated from a Yellowstone hot spring. *Science*, **225**, 313-315.

Madigan MT (1986) *Chromatium tepidum* sp. nov., a thermophilic photosynthetic bacterium of the family *Chromatiaceae*. *International Journal of Systematic Bacteriology*, **36**, 222-227.

Madigan MT (2003) Anoxygenic phototrophic bacteria from extreme environments. *Photosynthesis Research*, **76**, 157-171.

Majer V, Sedlbauer J, Bergin G (2008) Henry's law constant and related coefficients for aqueous hydrocarbons, CO_2 and H_2S over a wide range of temperature and pressure. *Fluid Phase Equilibria*, **272,** 65-74.

Matsuzaki M, Misumi O, Shin-i T, Maruyama S, Takahara M, Miyagishima S, Mori T, Nishida K, Yagisawa F, Nishida K, Yoshida Y, Nishimura Y, Nakao S, Kobayashi T, Momoyama Y, Higashiyama T, Minoda A, Sano M, Nomoto H, Oishi K, Hayashi H, Ohta F, Nishizaka S, Haga S, Miura S, Morishita T, Kabeya Y, Terasawa K, Suzuki Y, Ishii Y, Asakawa S, Takano H, Ohta N, Kuroiwa H, Tanaka K, Shimizu N, Sugano S, Sato N, Nozaki H, Ogasawara N, Kohara Y, Kuroiwa T (2004) Genome sequence of the ultrasmall unicellular red alga Cyanidioschyzon merolae 10D. *Nature*, **428,** 653-657.

Matubayasi N, Morooka S, Nakahara M, Takahashi H (2007) Chemical equilibrium of formaldehyde and methanediol in hot water: Free-energy analysis of the solvent effect. *Journal of Molecular Liquids*, **134**, 58-63.

Mazaki H, Watanabe T, Takahashi T (1992) Epimerization of chlorophyll derivatives. V. Effects of the central magnesium and ring substituents on the epimerization of chlorophyll derivatives. *Bulletin of the Chemical Society of Japan*, **65**, 3080-3087.

McCleskey RB, Chiu, RB, Nordstrom, DK, Campbell, KM, Roth, DA, Ball, JW, and Plowman, TI (2014) Water-chemistry data for selected springs, geysers, and streams in Yellowstone National Park, Wyoming, beginning 2009: doi:10.5066/F7M043FS.

McCollom TM, Seewald JS, Simoneit BRT (2001) Reactivity of monocyclic aromatic compounds under hydrothermal conditions. *Geochimica et Cosmochimica Acta*, **65**, 455-468.

McCollom TM, Seewald JS (2003) Experimental study of the hydrothermal reactivity of organic acids and acid anions: II. Acetic acid, acetate, and valeric acid. *Geochimica et Cosmochimica Acta*, **67**, 3645-3664.

McCollom TM, Seewald JS (2007) Abiotic synthesis of organic compounds in deep-sea hydrothermal environments. *Chemical Reviews*, **107**, 382-401.

Meenakshisundaram S, Nowicka E, Miedziak PJ, Brett GL, Jenkins RL, Dimitratos N, Taylor SH, Knight DW, Bethell D, Hutchings GJ (2010) Oxidation of alcohols using supported gold and gold-palladium nanoparticles. *Faraday Discussions*, **145**, 341-356.

Meyer-Dombard DR, Swingley W, Raymond J, Havig J, Shock EL, Summons RE (2011) Hydrothermal ecotones and streamer biofilm communities in the Lower Geyser Basin, Yellowstone National Park. *Environmental Microbiology*, **13**, 2216-2231.

Miller SR, Purugganan MD, Curtis SE (2006) Molecular population genetics and phenotypic diversification of two populations of the thermophilic cyanobacterium *Mastigocladus laminosus*. *Applied and Environmental Microbiology*, **72**, 2793-2800.

Miller SR, Williams C, Strong AL, Carvey D (2009) Ecological specialization in a spatially structured population of the thermophilic cyanobacterium *Mastigocladus laminosus*. *Applied and Environmental Microbiology*, **75**, 729-734.

Mitchell KR and Takacs-Vesbach CD (2008) A comparison of methods for total community DNA preservation and extraction from various thermal environments. *Journal of Industrial Microbiology & Biotechnology*, **35**, 1139-1147.

Monroe AA, Pizzarello S (2011) The soluble organic compounds of the Bells meteorite: Not a unique or unusual composition. *Geochimica et Cosmochimica Acta*, **75**, 7585-7595.

Mitsudome T, Noujima A, Mizugaki T, Jitsukawa K, Kaneda K (2009) Efficient aerobic oxidation of alcohols using a hydrotalcite-supported gold nanoparticle catalyst. *Advanced Synthesis & Catalysis*, **351**, 1890-1896.

Moore JW, Pearson RG (1981) *Kinetics and Mechanism.* John Wiley & Sons, New York.

Moreira D, Le Guyader H, Philippe H (2000) The origin of red algae and the evolution of chloroplasts. *Nature*, **405**, 69-72.

Morooka S, Wakai C, Matubayasi N, Nakahara M (2005) Hydrothermal carbon-carbon bond formation and disproportionations of C1 aldehydes: Formaldehyde and formic acid. *Journal of Physical Chemistry A*, **109**, 6610-6619.

Morooka S, Matubayasi N, Nakahara M (2007) Kinetic study on disproportionations of C1 aldehydes in supercritical water: Methanol from formaldehyde and formic Acid. *Journal of Physical Chemistry A*, **111**, 2697-2705.

Morooka S, Matubayasi N, Nakahara M (2008) Hydrothermal C-C bond formation and disproportionation of acetaldehyde with formic acid. *Journal of Physical Chemistry A*, **112**, 6950-6959.

Nagai Y, Wakai C, Matubayasi N, Nakahara M (2003) Noncatalytic Cannizzaro-type reaction of acetaldehyde in supercritical water. *Chemistry Letters*, **32**, 310-311.

Nagai Y, Matubayasi N, Nakahara M (2004a) Noncatalytic disproportionation and decarbonylation reactions of benzaldehyde in supercritical water. *Chemistry Letters*, **33**, 622-623.

Nagai Y, Morooka S, Matubayasi N, Nakahara M (2004b) Mechanisms and kinetics of acetaldehyde reaction in supercritical water: Noncatalytic disproportionation, condensation, and decarbonylation. *Journal of Physical Chemistry A*, **108**, 11635-11643.

Nagai Y, Matubayasi N, Nakahara M (2005) Mechanisms and kinetics of noncatalytic ether reaction in supercritical water. 1. Proton-transferred fragmentation of diethyl ether to acetaldehyde in competition with hydrolysis. *Journal of Physical Chemistry A*, **109**, 3550-3557.

Nakazawa Y, Takahashi F (1999) Thermodynamic and magnetic studies on the formation of gem-diol in an aldehyde-water mixture. *Bulletin of the Chemical Society of Japan*, **72**, 975-980.

Nordstrom DK, Ball JW, McCleskey RB (2005) "Ground water to surface water: chemistry of thermal outflows in Yellowstone National Park," in *Geothermal Biology and Geochemistry in Yellowstone National Park*, eds WP Inskeep and TR McDermott. Montana State University, Bozeman, pp. 143–162.

Nordstrom, DK, McCleskey RB, Ball JW (2009) Sulfur geochemistry of hydrothermal waters in Yellowstone National Park: IV acid-sulfate waters. *Applied Geochemistry*, **24**, 191-207.

Nowicka E, Hofmann JP, Parker SF, Sankar M, Lari GM, Kondrat SA, Knight DW, Bethell D, Weckhuysen BM, Hutchings GJ (2013) In situ spectroscopic investigation of oxidative dehydrogenation and disproportionation of benzyl alcohol. *Physical Chemistry Chemical Physics*, **15**, 12147-12155.

Ochoa de Alda JAG, Esteban R, Diago ML, Houmard J (2014) The plastid ancestor originated among one of the major cyanobacterial lineages. *Nature Communications*, **5**, 4937.

Palmer DA, Drummond SE (1986) Thermal decarboxylation of acetate. Part I. The kinetics and mechanism of reaction in aqueous solution. *Geochimica et Cosmochimica Acta*, **50**, 813-823.

Papke RT, Ramsing NB, Bateson MM, Ward DM (2003) Geographical isolation in hot spring cyanobacteria. *Environmental Microbiology*, **5**, 650-659.

Pennington, FC, Strain, HH, Svec WA, Katz JJ (1964) Preparation and properties of pyrochlorophyll *a*, methyl pyrochlorophyllide *a*, pyropheophytin *a*, and methyl pyropheophorbide *a* derived from chlorophyll by decarbomethoxylation. *Journal of the American Chemical Society*, **86**, 1418-1426.

Pfennig N (1974) *Rhodopseudomonas globiformis*, sp. n., a new species of the Rhodospirillaceae. *Archives of Microbiology*, **100**, 197-206.

Picou J, Stever M, Bouquet J, Wenzel J, Lee S (2014) Kinetics of the non-catalytic water gas shift reaction in supercritical water. *Energy Sources, Part A*, **36**, 2666-2672.

Pierson BK, Castenholz RW (1974) A Phototrophic gliding filamentous bacterium of hot springs, *Chloroflexus aurantiacus* gen. nov. and sp. nov. *Archives of Microbiology*, **100**, 5-24.

Plyasunov AV, Shock EL (2001) Correlation strategy for determining the parameters of the revised Helgeson-Kirkham-Flowers model for aqueous nonelectrolytes. *Geochimica et Cosmochimica Acta*, **65**, 3879-3900.

Pocker Y, Dickerson DG (1969) Hydration of propionaldehyde, isobutyraldehyde, and pivalaldehyde. Thermodynamic parameters, buffer catalysis and transition state characterization. *Journal of Physical Chemistry*, **73**, 4005-4012.

Rodriguez-Espeleta N, Brinkmann H, Burey SC, Roure B, Burger G, Löffelhardt W, Bohnert HJ, Philippe H, Lang BF (2005) Monophyly of primary photosynthetic eukaryotes: Green plants, red algae, and glaucophytes. *Current Biology*, **15**, 1325-1330.

Roeselers G, Norris TB, Castenholz RW, Rysgaard S, Glud RN, Kühl M, Muyzer G (2007) Diversity of phototrophic bacteria in microbial mats from Arctic hot springs (Greenland). *Environmental Microbiology*, **9**, 26-39.

Ross KA, Feazel LM, Robertson CE, Farthepure BZ, Wright KE, Turk-MacLeod RM, Chan MM, Held NL, Spear JR, Pace NR (2012) Phototrophic phylotypes dominate mesothermal microbial mats associated with hot springs in Yellowstone National Park. *Microbial Ecology*, **64**, 162-170.

Sander LC, Sharpless KE, Craft NE, Wise SA (1994) Development of engineered stationary phases for the separation of carotenoid isomers. *Analytical Chemistry*, **66**, 1667-1674.

Savage PE (1999) Organic chemical reactions in supercritical water. *Chemical Reviews*, **99**, 603-621.

Schliep M, Cavigliasso G, Quinnell RG, Stranger R, Larkum AWD (2013) Formyl group modification of chlorophyll *a*: A major evolutionary mechanism in oxygenic photosynthesis. *Plant, Cell, Environment*, **36**, 521-527.

Schloss PD, Westcott SL, Ryabin T, Hall JR, Hartmann M, Holister EB *et al.* (2009) Introducing Mothur: open-source, platform-independent, community-supported software for describing and comparing microbial communities. *Applied and Environmental Microbiology*, **75**, 7537:7541.

Schmidt K, Liaaen-Jensen S (1973) New keto-carotenoids from *Rhodopseudomonas globiformis*. *Acta Chemica Scandinavica*, **27**, 3040-3052.

Schubert WM, Zahler RE (1954) Aromatic electrophilic substitution by hydrogen. III. The mechanism of the acid-catalyzed decarboxylation of aromatic aldehydes. *Journal of the American Chemical Society*, **76**, 1-9.

Schubotz F, Meyer-Dombard DR, Bradley AS, Fredricks HF, Hinrichs K-U, Shock EL, Summons RE (2013) Spatial and temporal variability of biomarkers and microbial diversity reveal metabolic and community flexibility in streamer biofilm communities in the Lower Geyser Basin, Yellowstone National Park. *Geobiology*, **11**, 549-569.

Schulte MD, Shock EL (1993) Aldehydes in hydrothermal solution: Standard partial molal thermodynamic properties and relative stabilities at high temperatures and pressures. *Geochimica et Cosmochimica Acta*, **57**, 3835-3846.

Seewald JS (1994) Evidence for metastable equilibrium between hydrocarbons under hydrothermal conditions. *Nature*, **370**, 285-287.

Seewald JS (2001) Aqueous geochemistry of low molecular weight hydrocarbons at elevated temperatures and pressures: Constraints from mineral buffered laboratory experiments. *Geochimica et Cosmochimica Acta*, **65**, 1641-1664.

Seewald JS, Zolotov MY, McCollom T (2006) Experimental investigation of single carbon compounds under hydrothermal conditions. *Geochimica et Cosmochimica Acta*, **70**, 446-460.

Seravalli J, Ragsdale SW (2008) 13C NMR characterization of an exchange reaction between CO and CO_2 catalyzed by carbon monoxide dehydrogenase. *Biochemistry*, **47**, 6770-6781.

Shang C, Liu Z (2011) Origin and activity of gold nanoparticles as aerobic oxidation catalysts in aqueous solution. *Journal of the American Chemical Society*, **133**, 9938-9947.

Shipp J, Gould IR, Herckes P, Shock EL, Williams LB, Hartnett HE (2013) Organic functional group transformations in water at elevated temperature and pressure: Reversibility, reactivity, and mechanisms. *Geochimica et Cosmochimica Acta,* **104**, 194-209.

Shock EL, Helgeson HC, Sverjensky DA (1989) Calculation of the thermodynamic and transport properties of aqueous species at high pressures and temperatures: Standard partial molal properties of inorganic neutral species. *Geochimica et Cosmochimica Acta*, **53**, 2157-2183.

Shock EL (1993) Hydrothermal dehydration of aqueous organic compounds. *Geochimica et Cosmochimica Acta*, **57**, 3341-3349.

Shock EL (1995) Organic acids in hydrothermal solutions: Standard molal thermodynamic properties of carboxylic acids and estimates of dissociation constants at high temperatures and pressures. *American Journal of Science*, **295**, 496-580.

Shock EL, Sassani DC, Willis M, Sverjensky DA (1997) Inorganic species in geologic fluids: Correlations among standard molal thermodynamic properties of aqueous ions and hydroxide complexes. *Geochimica et Cosmochimica Acta*, **61**, 907-950.

Shock EL, Schulte MD (1998) Organic synthesis during fluid mixing in hydrothermal systems. *Journal of Geophysical Research*, **103,** 28513-28527.

Shock EL, Holland M, Meyer-Dombard D, Amend JP, Osburn GR, Fischer TP (2010) Quantifying inorganic sources of geochemical energy in hydrothermal ecosystems, Yellowstone National Park, USA. *Geochimica et Cosmochimica Acta*, **74**, 4005-4043.

Shock EL, Canovas P, Yang Z, Boyer G, Johnson K, Robinson K, Fecteau K, Windman T, Cox A (2013) Thermodynamics of organic transformations in hydrothermal fluids. *Reviews in Mineralogy and Geochemistry*, **76**, 311-350.

Shylesh S, Kim D, Ho CR, Johnson GR, Wu J, Bell AT (2015) Non-oxidative dehydrogenation pathways for the conversion of C2-C4 alcohols to carbonyl compounds. *ChemSusChem* **8**, 3959-3962.

Skorupa DJ, Reeb V, Castenholz RW, Bhattacharya D, McDermott TR (2013) Cyanidiales diversity in Yellowstone National Park. *Letters in Applied Microbiology,* **57**, 459-466.

Skupien E, Berger RJ, Santos VP, Gascon J, Makkee M, Kreutzer MT, Kooyman PJ, Moulijn JA, Kapteijn F (2014) Inhibition of a gold-based catalyst in benzyl alcohol oxidation: understanding and remediation. *Catalysts* **4**, 89-115.

Smith, MB (2013) *March's advanced organic chemistry: Reactions, mechanisms, and structure*. 7th Ed. John Wiley and Sons, Hoboken.

Sorokin C (1967) New high-temperature Chlorella. *Science,* **158**, 1204-1205.

Steinberg CEW, Schäfer H, Beisker W (1998) Do acid-tolerant cyanobacteria exist? *Acta Hydrochimica Hydrobiologica,* **26**, 13-19.

Stephen A, Hashmi K, Hutchings GJ (2006) Gold catalysis. *Angewandte Chemie, International Edition*, **45**, 7896-7936.

Sverjensky DA, Shock EL, Helgeson HC (1997) Prediction of the thermodynamic properties of aqueous metal complexes to 1000°C and 5 kb. *Geochimica et Cosmochimica Acta*, **61**, 1359-1412.

Swain CG, Powell AL, Sheppard WA, Morgan CR (1979) Mechanism of the Cannizzaro reaction. *Journal of the American Chemical Society,* **101**, 3576-3583.

Tank M and Bryant DA (2015) *Chloracidobacterium thermophilum* gen. nov., sp. nov.: An anoxygenic microaerophilic chlorophotoheterotrophic acidobacterium. *International Journal of Systematic and Evolutionary Microbiology,* **65**, 1426-1430.

Tansey MR, Brock TD (1972) The upper temperature limit for eukaryotic organisms. *Proceedings of the National Academy of Sciences of the United States of America*, **69**, 2426-2628.

Tassi F, Venturi S, Cabassi J, Capecchiacci F, Nisi B, Vaselli O (2015) Volatile organic compounds (VOCs) in soil gases from Solfatara crater (Campi Flegrei, southern Italy): Geogenic source(s) vs. biogeochemical processes. *Applied Geochemistry*, **56**, 37-49.

Taylor JD, Steinfeld JI, Tester JW (2001) Experimental measurement of the rate of methyl *tert*-butyl ether hydrolysis in sub- and supercritical water. *Industrial & Engineering Chemistry Research*, **40**, 67-74.

Toplin JA, Norris TB, Lehr CR, McDermott TR, Castenholz RW (2008) Biogeographic and phylogenetic diversity of thermoacidophilic Cyanidiales in Yellowstone National Park, Japan, and New Zealand. *Applied and Environmental Microbiology*, **74**, 2822-2833.

Tsao CC, Zhou Y, Liu X, Houser TJ (1992) Reactions of supercritical water with benzaldehyde, benzylidenebenzylamine, benzyl alcohol, and benzoic acid. *Journal of Supercritical Fluids*, **5**, 107-13.

Tsujino Y, Wakai C, Matubayashi N, Nakahara M (1999) Noncatalytic Cannizzaro-type reaction of formaldehyde in hot water. *Chemistry Letters*, 287-288.

Tsukatani Y, Romberger SP, Golbeck JH, Bryant DA (2012) Isolation and characterization of the homodimeric type-I reaction center complex from *Candidatus* Chloracidobacterium thermophilum, an aerobic chlorophototroph. *The Journal of Biological Chemistry*, **287**, 5720-5732.

Urbieta MS, González-Toril E, Bazán AA, Giaveno MA, Donati E (2015) Comparison of the microbial communities of hot springs waters and the microbial biofilms in the acidic geothermal area of Copahue (Neuquén, Argentina). *Extremophiles*, **19**, 437-450.

van Breemen RB, Dong L, Pajkovic ND (2012) Atmospheric pressure chemical ionization tandem mass spectrometry of carotenoids. *International Journal of Mass Spectrometry*, **312**, 163-172.

van der Meer MTJ, Schouten S, Bateson MM, Nübel U, Wieland A, Kühl M, de Leeuw JW, Damsté JSS, Ward DM (2005) Diel variations in carbon metabolism by green nonsulfur-like bacteria in alkaline silicieous hot spring microbial mats from Yellowstone National Park. *Applied and Environmental Microbiology*, **71**, 3978-3986.

van der Meer MTJ, Klatt CG, Wood J, Bryant DA, Bateson MM, Lammerts L, Schouten S, Damsté JSS, Madigan MT, Ward DM (2010) Cultivation and genomic, nutritional, and lipid biomarker characterization of *Roseiflexus* strains closely related to predominant *in situ* populations inhabiting Yellowstone hot spring microbial mats. *Journal of Bacteriology*, **192**, 3033-3042.

Wang S, Dong H, Hou W, Jiang H, Huang Q, Briggs BR, Huang L (2014) Greater temporal changes of sediment microbial community than its waterborne counterpart in Tengchong hot springs, Yunnan Province, China. *Scientific Reports*, **4**, 7479.

Wang Q, Garrity GM, Tiedje JM, Cole JR (2007) Naïve Bayesian classifier for rapid assignment of rRNA sequences into the new bacterial taxonomy. *Applied and Environmental Microbiology*, **73**, 5261-5267.

Watanabe M, Osada M, Inomata H, Arai K, Kruse A (2003) Acidity and basicity of metal oxide catalysts for formaldehyde reaction in supercritical water at 673 K. *Applied Catalysis A*, **245**, 333-341.

Willey LM, Kharaka YK, Presser TS, Rapp JB, Barnes I (1975) Short chain aliphatic acid anions in oil field waters and their contribution to the measured alkalinity. *Geochimica et Cosmochimica Acta* **39**, 1707-1711.

Williams LB, Hervig RL, Holloway JR, Hutcheon I (2001) Boron isotope geochemistry during diagenesis. Part I. Experimental determination of fractionation during illitization of smectite. *Geochimica et Cosmochimica Acta*, **65**, 1769-1782.

Wolery TW and Jarek RL (2003) Software User's Manual EQ3/6, Version 8.0. U.S. Department of Energy, Office of Civilian Radioactive Waste Management, Office of Repository Development, Software Document Number 10813-UM-8.0-00, 376 pages.

Xu X, Antal MJ, Anderson DGM (1997) Mechanism and temperature-dependent kinetics of the dehydration of *tert*-butyl alcohol in hot compressed liquid water. *Industrial & Engineering Chemistry Research*, **36**, 23-41.

Xu Z, Qu J (2013) Hot water-promoted SN1 solvolysis reactions of allylic and benzylic alcohols. *Chemistry – A European Journal*, **19**, 314-323.

Yang Z, Gould IR, Williams LB, Hartnett HE, Shock EL (2012) The central role of ketones in reversible and irreversible hydrothermal organic functional group transformations. *Geochimica et Cosmochimica Acta*, **98**, 48-65.

Yang Z, Lorance ED, Bockisch C, Williams LB, Hartnett HE, Shock EL, Gould IR (2014) Hydrothermal photochemistry as a mechanistic tool in organic geochemistry: The chemistry of dibenzyl ketone. *Journal of Organic Chemistry*, **79**, 7861-7871.

Yang Z, Hartnett HE, Shock EL, Gould IR (2015) Organic oxidations using geomimicry. *Journal of Organic Chemistry*, **80**, 12159-12165.

Zehr JP, Jenkins BD, Short SM, Steward GF (2003) Nitrogenase gene diversity and microbial community structure: a cross-system comparison. *Environmental Microbiology*, **5**, 539-554.

Zenvirth D, Volokita M, Kaplan A (1985) Photosynthesis and inorganic carbon accumulation in the acidophilic alga *Cyanidioschyzon merolae*. *Plant Physiology*, **77**, 237-239.

Zhou Y, Angelici RJ, Woo LK (2010) Bulk gold-catalyzed reactions of diazoalkanes with amines and O_2 to give enamines. *Catalysis Letters*, **137**, 8-15.

Zhou Y, Trewyn BG, Angelici RJ, Woo LK (2009) Catalytic reactions of carbene precursors on bulk gold metal. *Journal of the American Chemical Society*, **131**, 11734-11743.

Zhu B, Angelici RJ (2007) Non-nanogold catalyzed aerobic oxidation of secondary amines to imines. *Chemical Communications*, 2157-2159.

Zhu B, Angelici RJ (2006) Non-nanogold catalysis of carbon monoxide oxidative amination. *Journal of the American Chemical Society*, **128**, 14460-14461.

Zhu B, Lazar M, Trewyn BG, Angelici RJ (2008a) Aerobic oxidation of amines to imines catalyzed by bulk gold powder and by alumina-supported gold. *Journal of Catalysis*, **260**, 1-6.

Zhu J, Figueiredo JL, Faria JL (2008b) Au/activated-carbon catalysts for selective oxidation of alcohols with molecular oxygen under atmospheric pressure: Role of basicity. *Catalysis Communications*, **9**, 2395-2397.

Zope BN, Hibbitts DD, Neurock M, Davis RJ (2010) Reactivity of the gold/water interface during selective oxidation catalysis. *Science*, **330**, 74-78.

APPENDIX A

ABUNDANCE DATA, SAMPLE CHROMATOGRAMS, AND SPECTRA OF PIGMENT ANALYSES

Table A1. Semi-quantitative abundance data for chlorophyll *a* and its derivatives.[a]

Assignment	chl. *a*	chl. *a*'	phe. *a*	phe. *a*'	phe. *a* allomer	pyrophe. *a*	phede. *a*
Peak number[b]	B2	B3	B6	B5	B4	B7	B1
Soret band (nm)	431	432	409	409	409	410	408
Q_y band (nm)	665	665	666	666	666	666	665
molecular ion (m/z)	893.4	893.5	871.5	871.5	887.5	813.5	593.2
FF1	nd[c]	nd	20674	2898	3872	10418	28521
IG1	30452	396	1214	174	231	157	6180
IG2	62118	2475	1766	325	nd	572	3328
IG3	90981	1707	35160	5301	5152	586	2388
RN1-2011	12749	144	528	65	817	1894	nd
RN1-2012	93304	1479	2747	515	2494	286	nd
RN2	100392	3310	33731	6256	22130	15701	3863
RN3	223066	2857	14790	2512	9688	5654	nd
RS1	144631	4956	9389	2041	3534	3000	4786
RS2	41007	1158	7702	1435	5461	3388	nd
RS3	73171	1806	16080	2516	15697	3344	2303
RS4	83014	980	3615	385	1265	172	nd
RS5-2011	73321	1193	7088	1303	1259	1288	3115
RS5-2012	nd	nd	446	199	307	999	nd

[a]data from observation at 665 nm. [b]figure A1. [c]not detected.

Table A2. Semi-quantitative abundance data for major carotenoids.[a]

assignment	β-carotene	β-crypto-xanthin	zea-xanthin	echinenone	cantha-xanthin	13-Z-β-carotene	9-Z-β-carotene
peak number[b]	A5	not shown[c]	A1	A3	A2	A4	A6
absorbance maxima (nm)	452, 478	452, 478	451, 477	465	477	338, 444, 470	448, 474
% III/II	22	28	31	undefined[d]	undefined[d]	4	25
molecular ion (m/z)	537.4	553.4	569.5	551.4	565.4	537.4	537.4
FF1	4457	nd[e]	7468	nd	nd	nd	1646
IG1	4371	1263	15303	nd	nd	621	1353
IG2	9709	3226	43092	nd	nd	1704	2986
IG3	12971	nd	11147	9416	3857	1774	3540
RN1-2011	4683	nd	990	1668	384	nd	1421
RN1-2012	21792	nd	8497	8198	2711	3464	5803
RN2	25869	nd	9258	21075	5877	nd	9186
RN3	52709	nd	13335	15340	4993	nd	14022
RS1	119548	nd	27570	9347	2336	26504	44259
RS2	6530	nd	2329	2404	424	nd	2236
RS3	7704	nd	3675	8885	17671	1037	2580
RS4	10565	nd	4573	4073	593	1433	3149
RS5-2011	17659	nd	5357	7845	1618	1856	4395
RS5-2012	398	nd	394	408	nd	nd	208

[a]data from observation at 475 nm. [b]figure A1. [c]not shown in Figure A1; retention time is 54 minutes. [d]only one absorbance maximum, so value undefined. [e]not detected.

Table A3. Semi-quantitative abundance data for other chlorophylls and their derivatives.[a]

Assignment	bacterio-chlorophyll *a*	bacterio-pheophytin *a*	chloro-phyllide *b*	pheophytin *b*	pheophytin *b* allomer	chlorophyll *d*	pyro-pheophytin *d*
Retention time (min.)	16	32	18	61	53	24	71
soret band (nm)	365	359	436	436	435	443	424
Q_y band (nm)	761	746	652	653	652	697	692
molecular ion (m/z)	bdl[b]	889.6	628.5	885.6	901.4	895.7	815.5
FF1	nd	416	nd	1774	310	nd	nd
IG1	nd	nd	166	338	nd	nd	nd
IG2	nd	nd	339	231	nd	nd	nd
IG3	nd	nd	nd	nd	nd	nd	nd
RN1-2011	nd	nd	nd	nd	nd	160	nd
RN1-2012	nd	nd	nd	nd	nd	nd	nd
RN2	nd	nd	nd	nd	nd	1207	nd
RN3	nd	nd	nd	nd	nd	nd	464
RS1	152	986	nd	nd	nd	36	nd
RS2	nd	1265	nd	nd	nd	nd	631
RS3	nd	nd	nd	nd	nd	nd	nd
RS4	385	nd	nd	nd	nd	nd	nd
RS5-2011	nd	nd	nd	nd	nd	nd	nd
RS5-2012	nd	nd	nd	nd	nd	nd	nd

[a]data from observation at 360 nm. [b]signal to noise in mass spectrum too low; assignment made from absorbance spectrum and comparison of the retention time to that of the bchl *a* peak in a pigment extract of *R. sphaeroides*. [c]not detected.

Table A4. Quantitative abundances for selected pigments expressed as µmol/g N.

	chlorophyll a	β-carotene	zeaxanthin[a]	β-cryptoxanthin[a]
FF1	nd[b]	2.2	3.5	nd
IG1	16.7	2.2	7.2	0.6
IG2	34.0	4.8	20.2	1.6
IG3	49.7	6.4	5.2	nd
RN1-2011	7.0	2.3	0.5	nd
RN1-2012	51.0	10.8	4.0	nd
RN2	54.9	12.8	4.3	nd
RN3	122.0	26.2	6.2	nd
RS1	79.1	59.3	12.9	nd
RS2	22.4	3.2	1.1	nd
RS3	40.0	3.8	1.7	nd
RS4	45.4	5.2	2.1	nd
RS5-2011	40.1	8.8	2.5	nd
RS5-2012	nd	0.2	0.2	nd

[a]quantified using the response factor for β-carotene and not corrected for slight differences in molar absorptivity. [b]not detected.

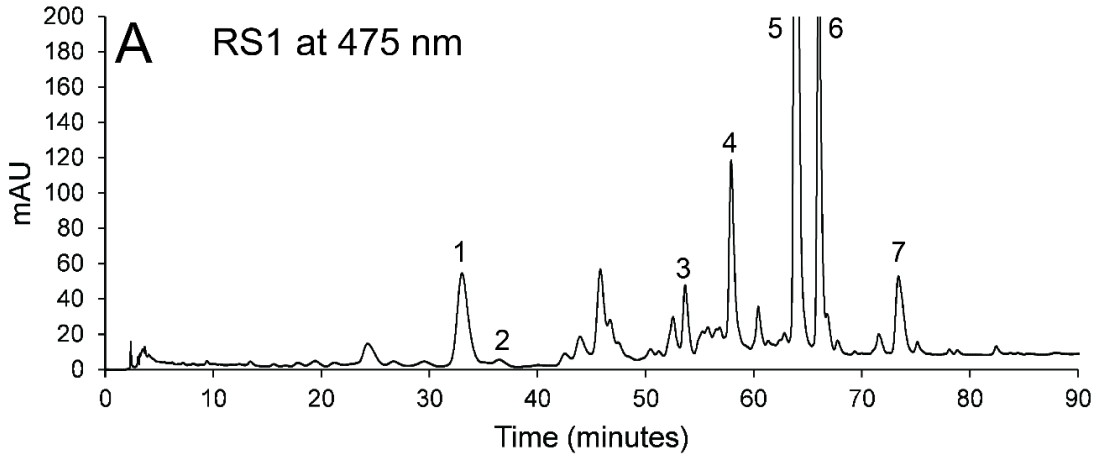
A
RS1 at 475 nm
mAU
Time (minutes)
1
2
3
4
5
6
7

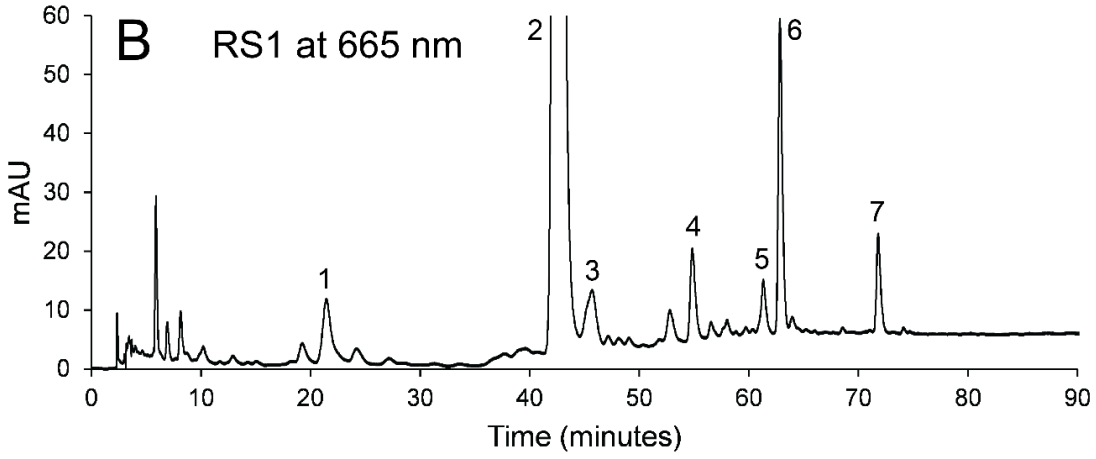
B
RS1 at 665 nm
mAU
Time (minutes)
1
2
3
4
5
6
7

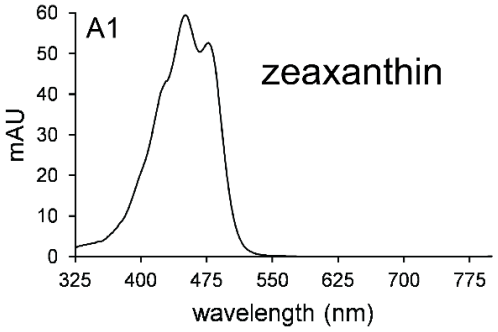
A1
zeaxanthin
mAU
wavelength (nm)

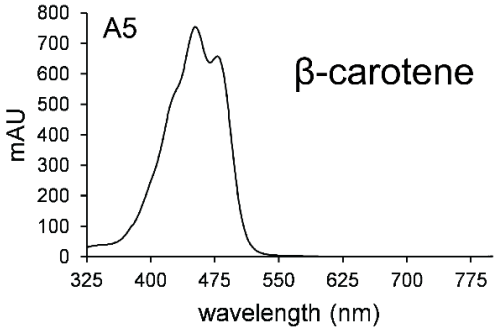
A5
β-carotene
mAU
wavelength (nm)

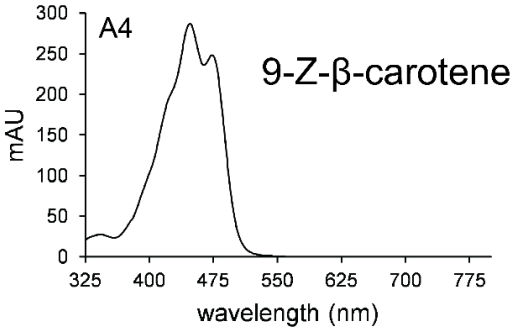
A4
9-Z-β-carotene
mAU
wavelength (nm)

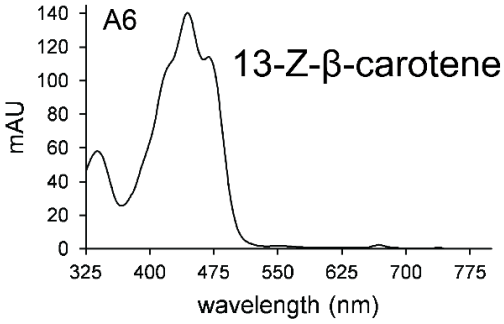
A6
13-Z-β-carotene
mAU
wavelength (nm)

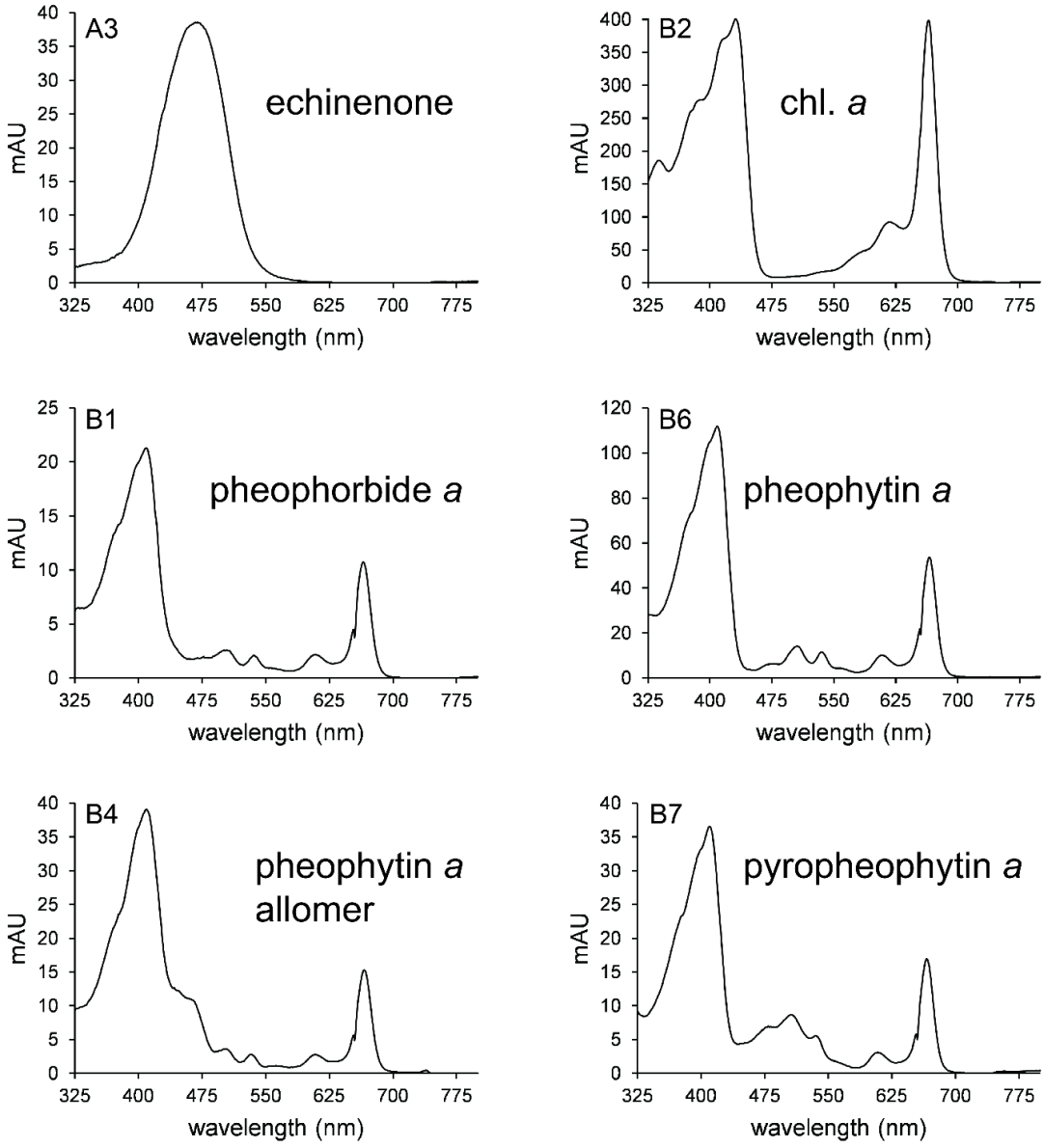

Figure A1. Typical chromatograms recorded at 475 nm (A) and 665 nm (B) with major peaks numbered (sample RS1 shown) as well as baseline-corrected diode array spectra for selected major pigments. The chromatogram and peak number are indicated in the upper left of each spectrum. Peak A7 is hypothesized to be lycopene (spectrum and data not shown).

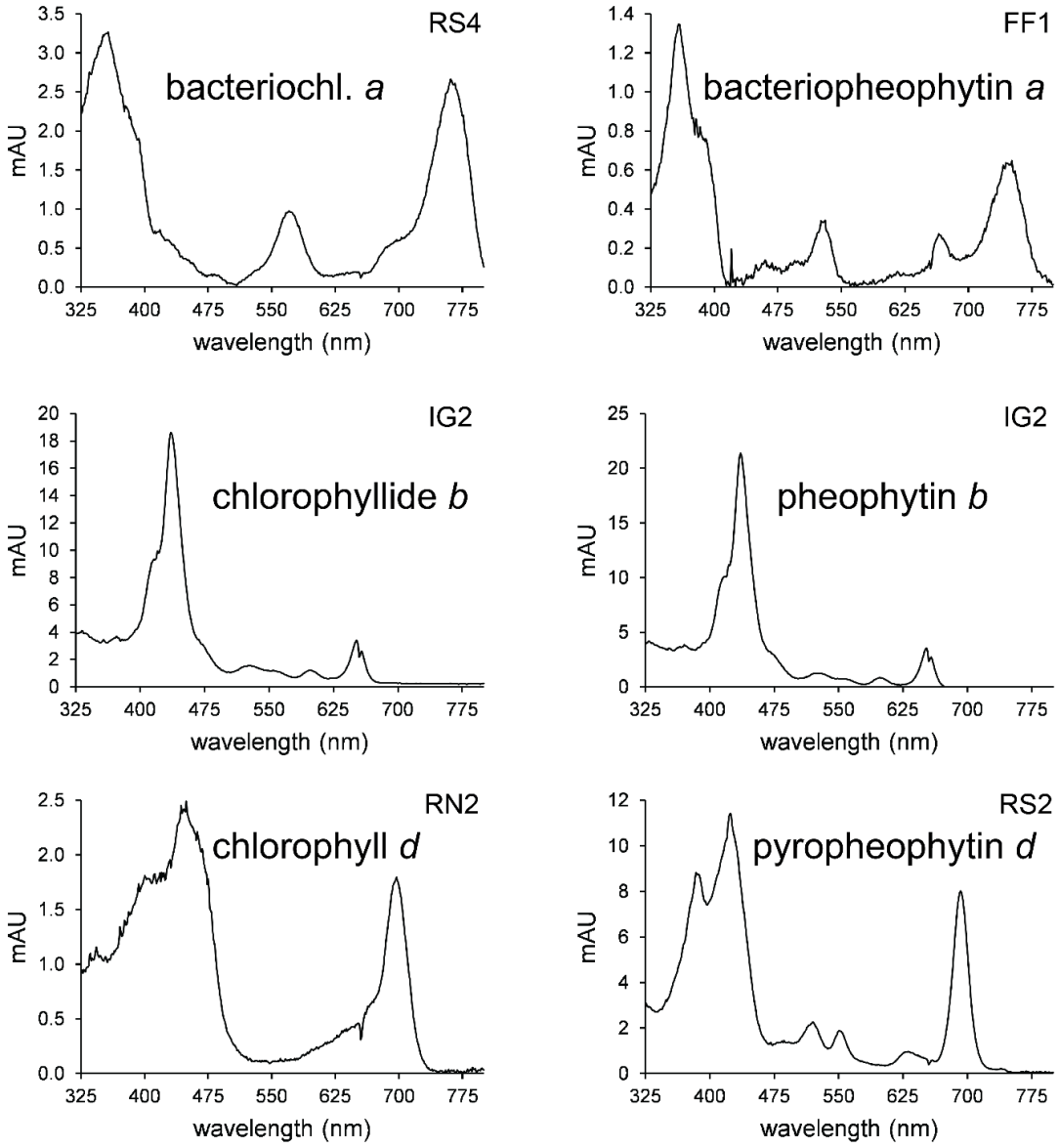

Figure A2. Baseline-corrected diode-array spectra of other chlorophylls. The sample from which each spectrum arises is indicated in the upper right corner.

APPENDIX B

SCANNING ELECTRON MICROGRAPHS OF NEW AND USED GOLD POWDERS

SEM of new 0.5-0.8 micron powder

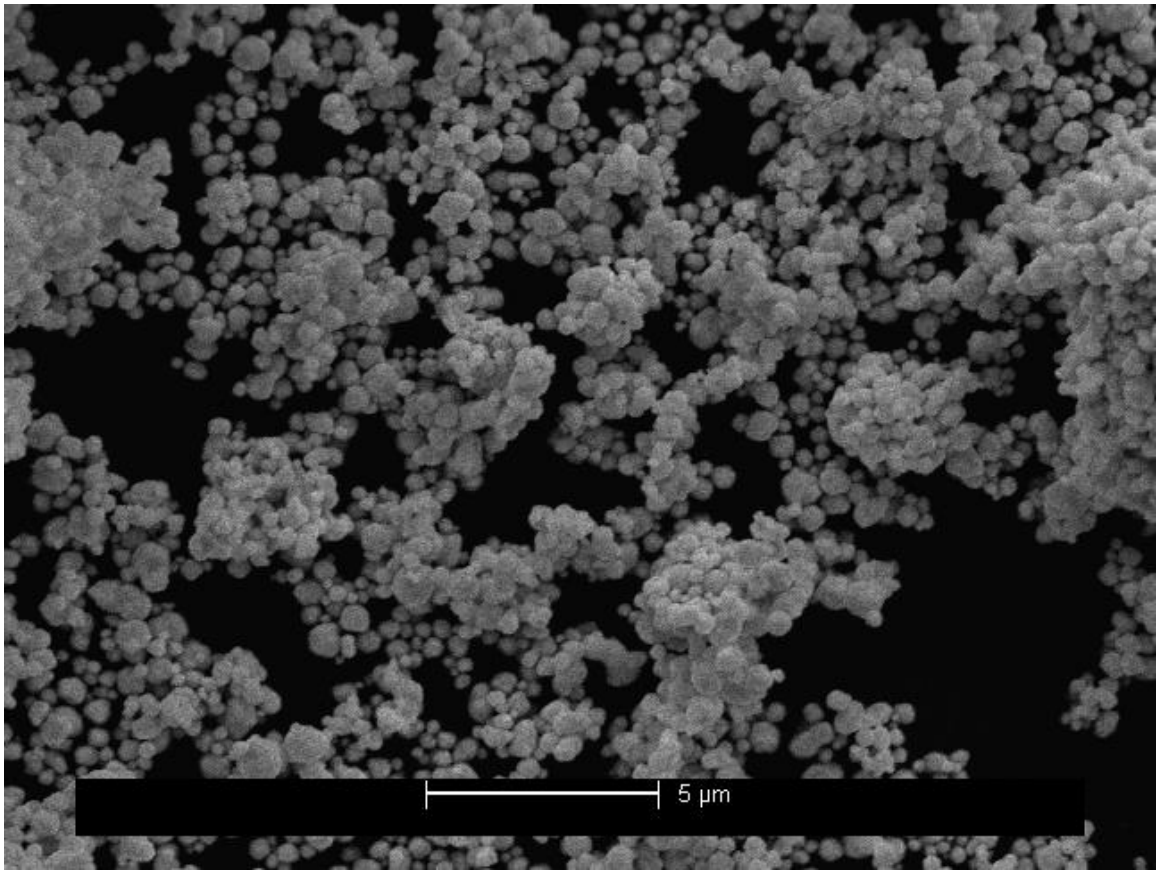

Figure B1. New 0.5-0.8 micron gold powder.

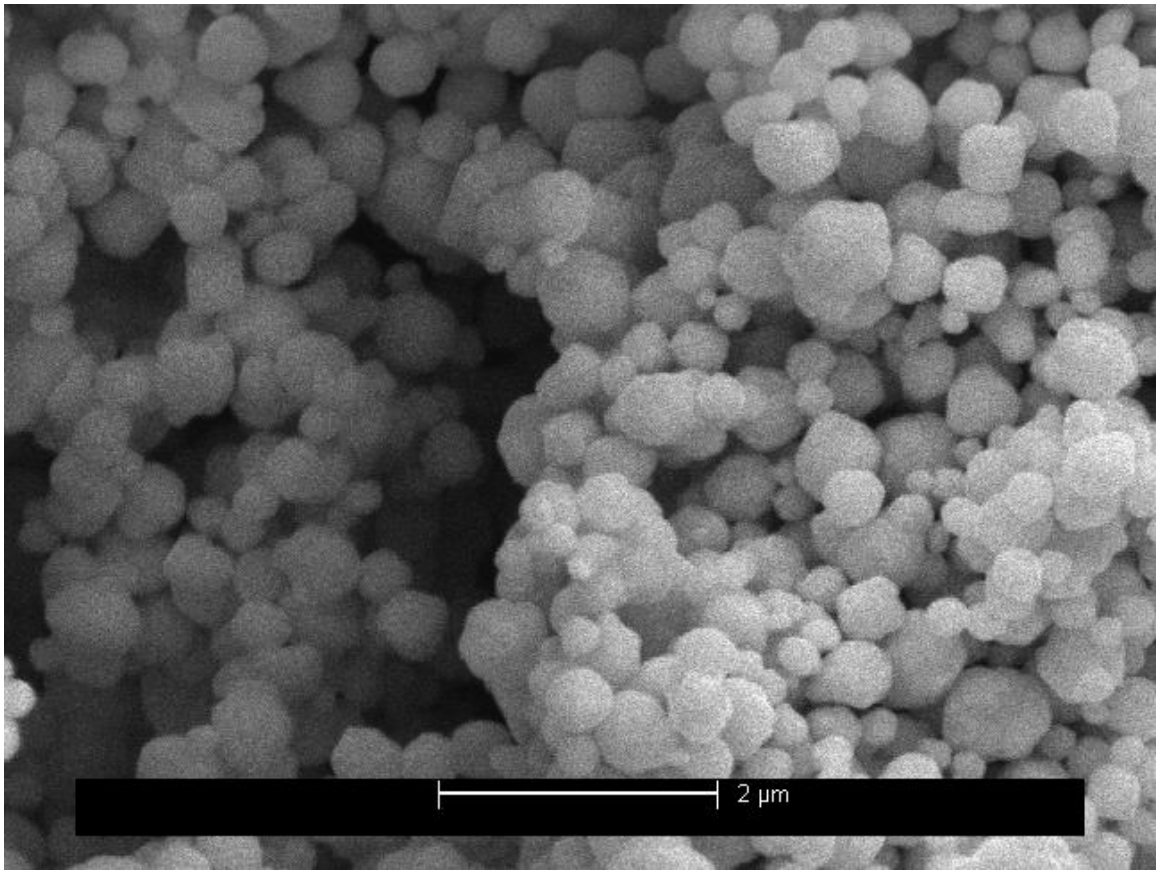

Figure B2. New 0.5-0.8 micron gold powder.

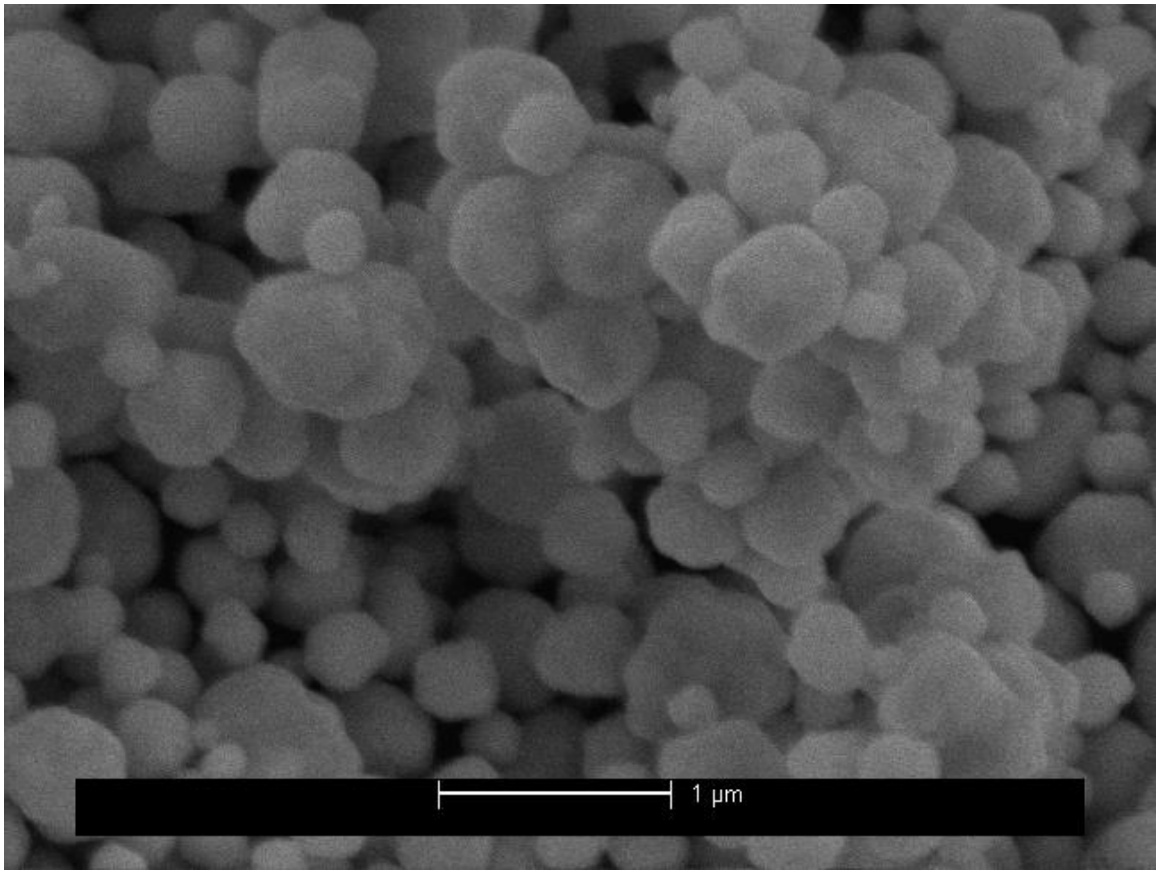

Figure B3. New 0.5-0.8 micron gold powder.

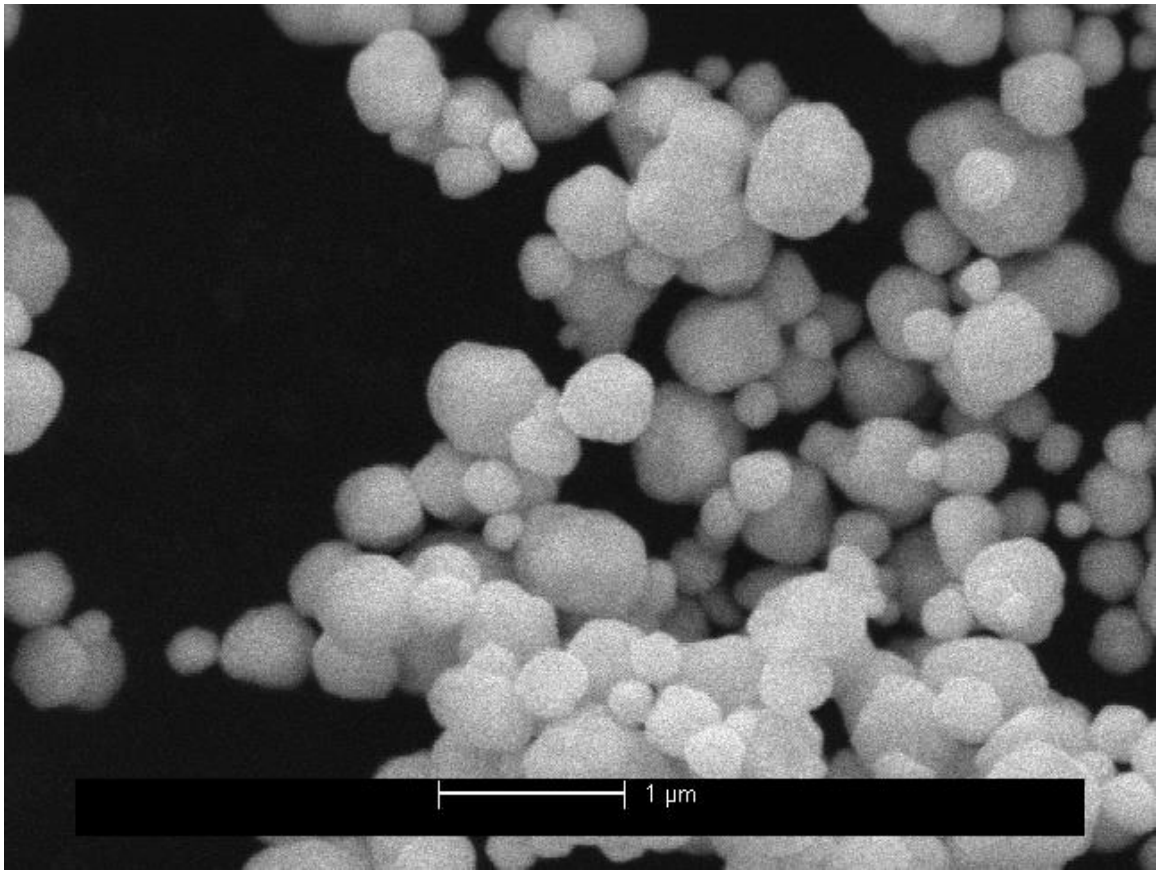

Figure B4. New 0.5-0.8 micron gold powder.

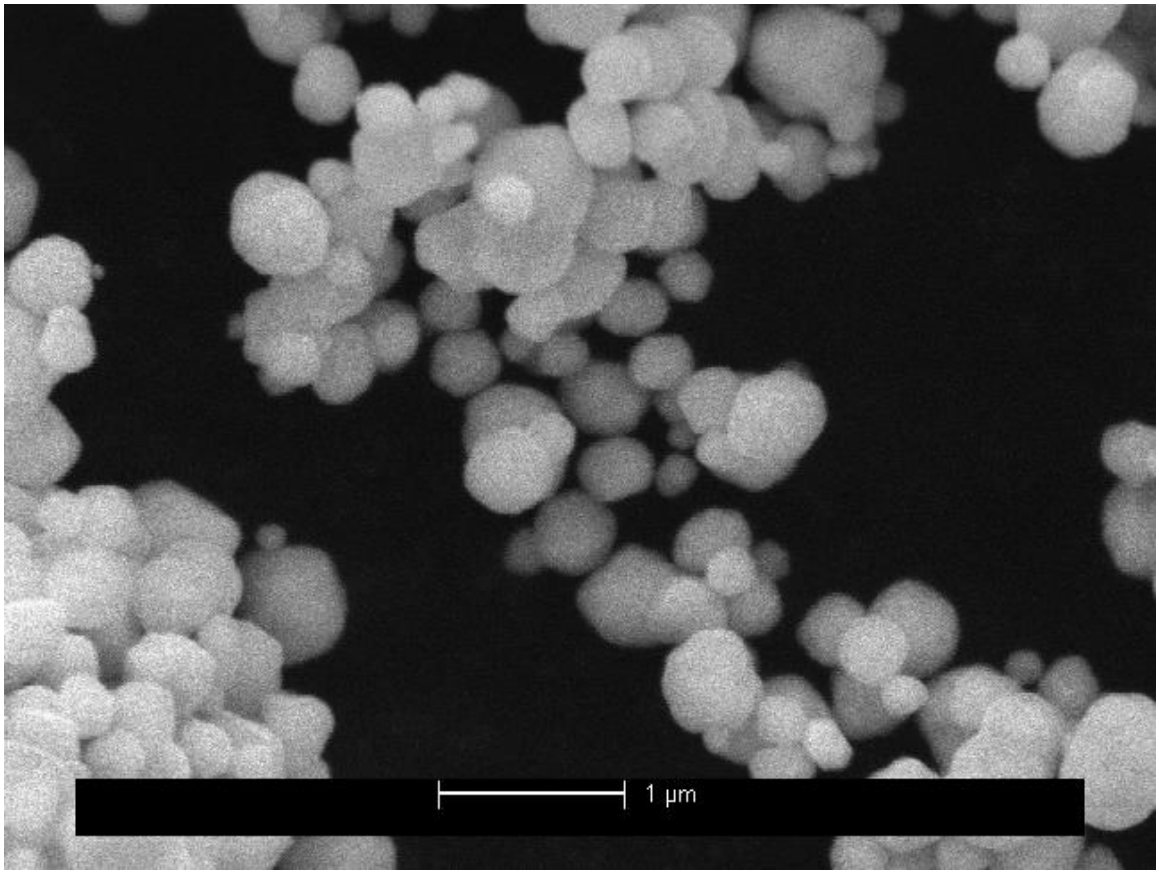

Figure B5. New 0.5-0.8 micron gold powder.

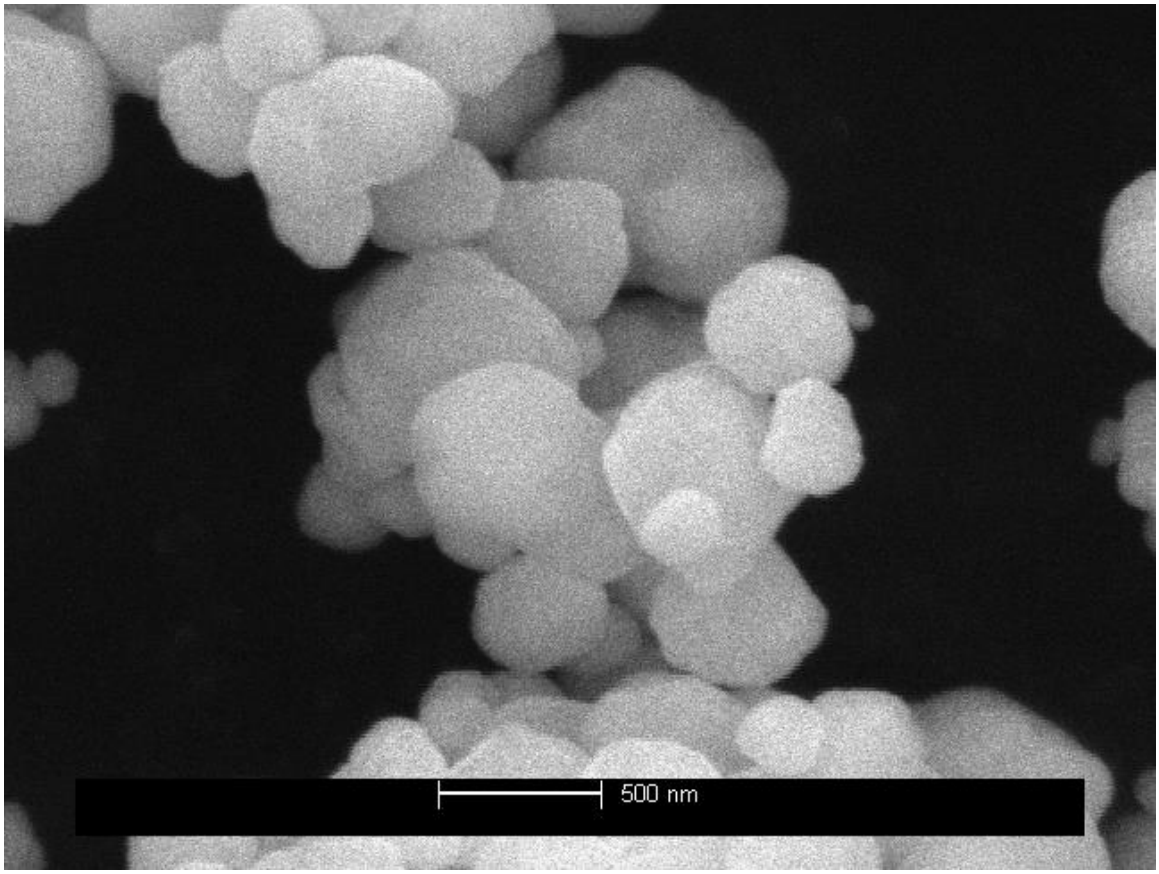

Figure B6. New 0.5-0.8 micron gold powder.

SEM of used 0.5-0.8 micron powder

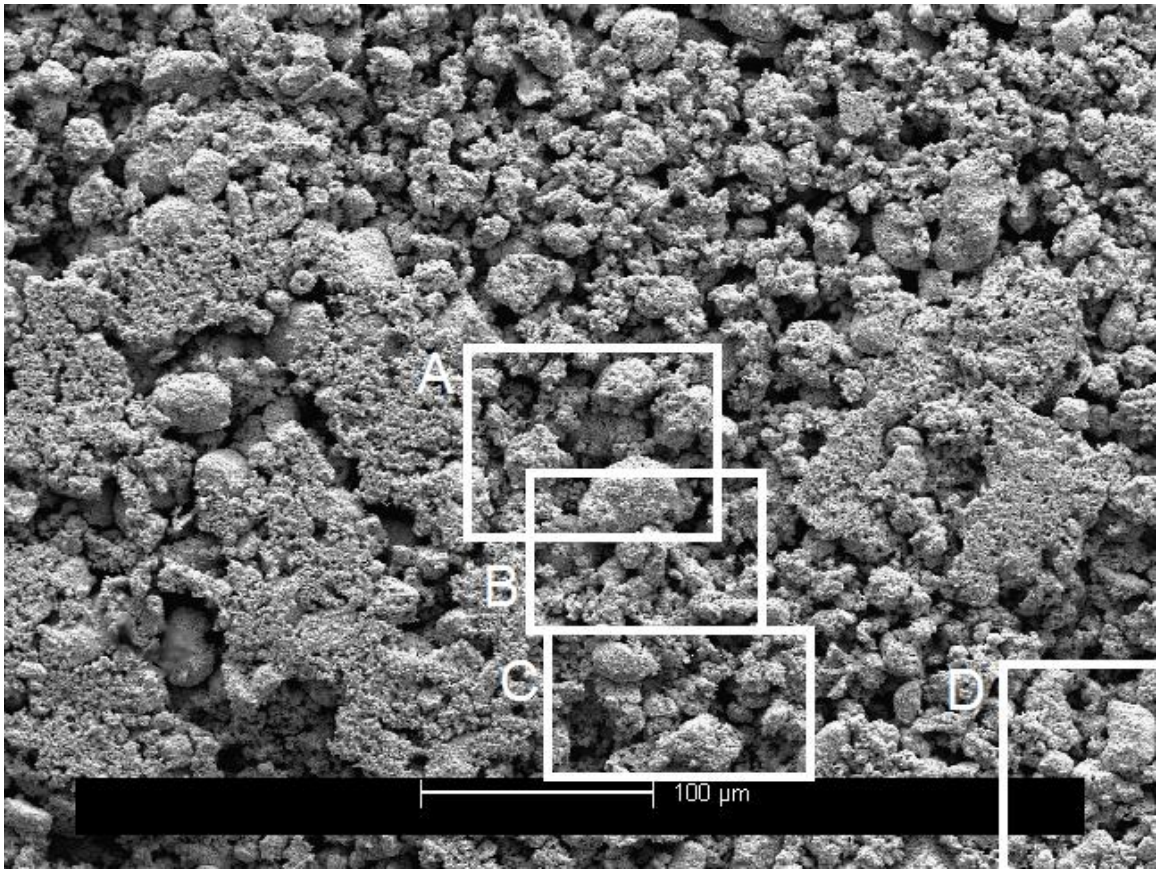

Figure B7. Used 0.5-0.8 micron gold powder (broad view with regions indicated).

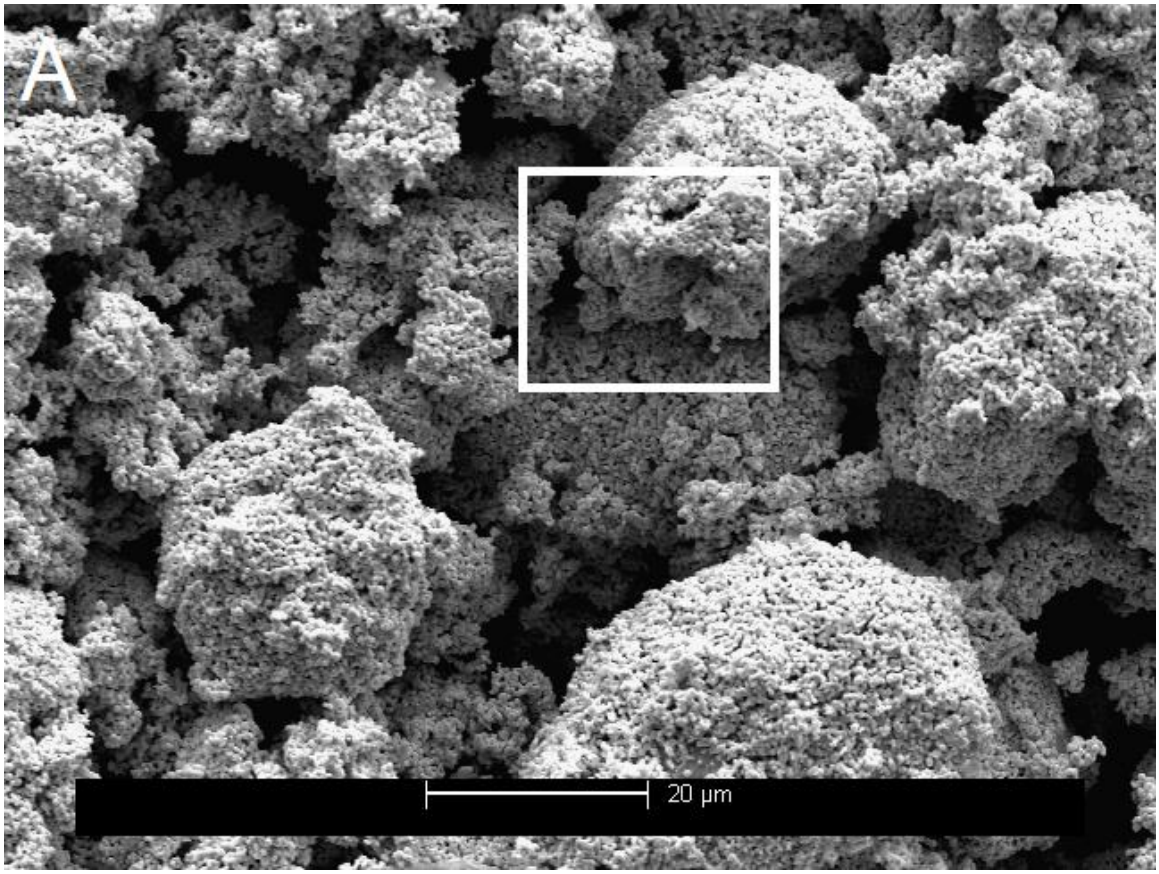

Figure B8. Used 0.5-0.8 micron gold powder (region A).

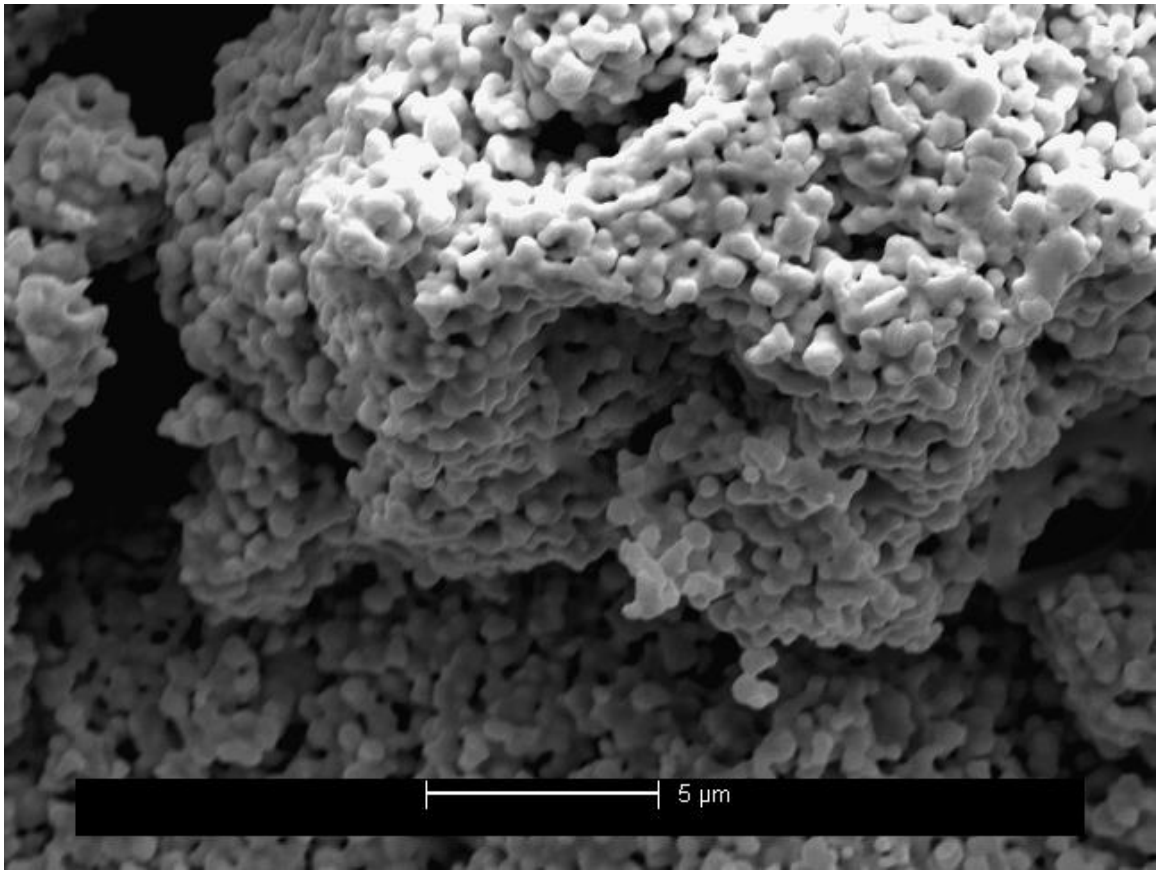

Figure B9. Used 0.5-0.8 micron gold powder (region A; boxed area in Figure B8).

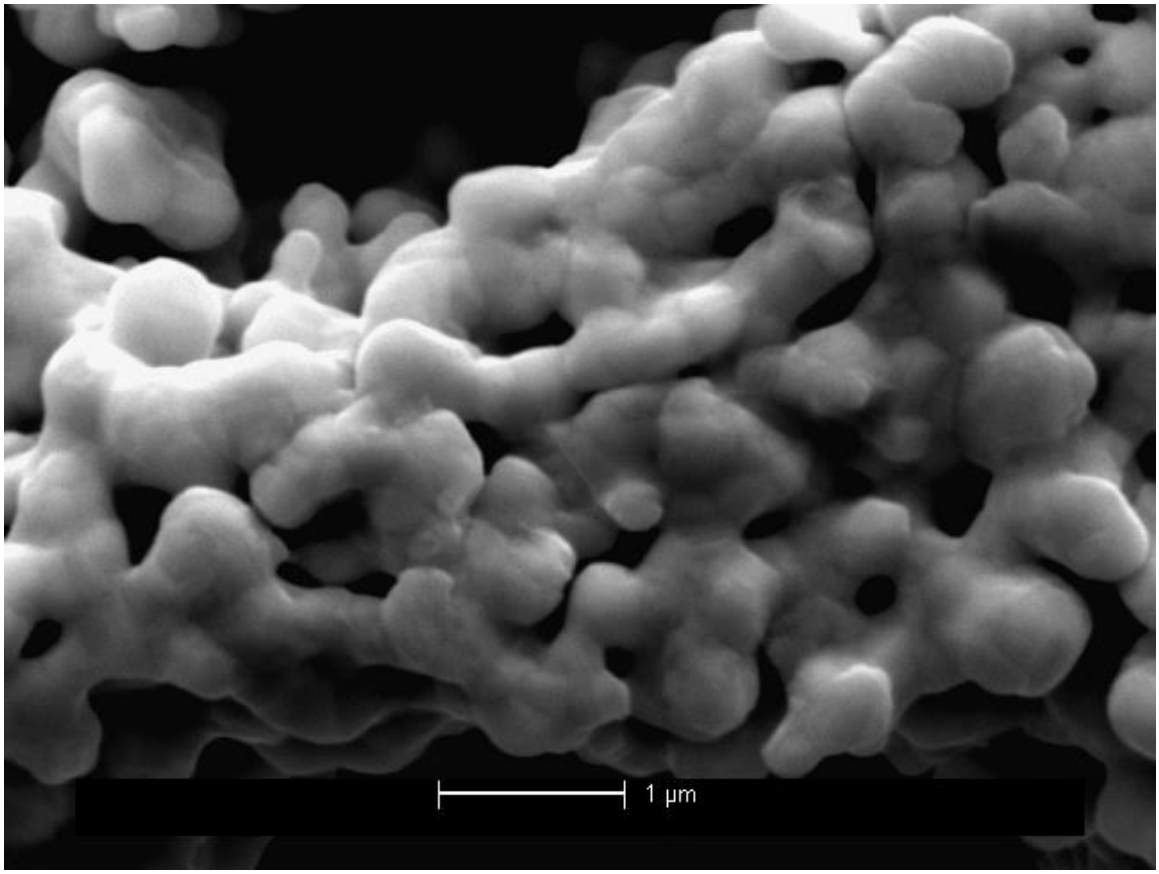

Figure B10. Used 0.5-0.8 micron gold powder (region A; zoomed in).

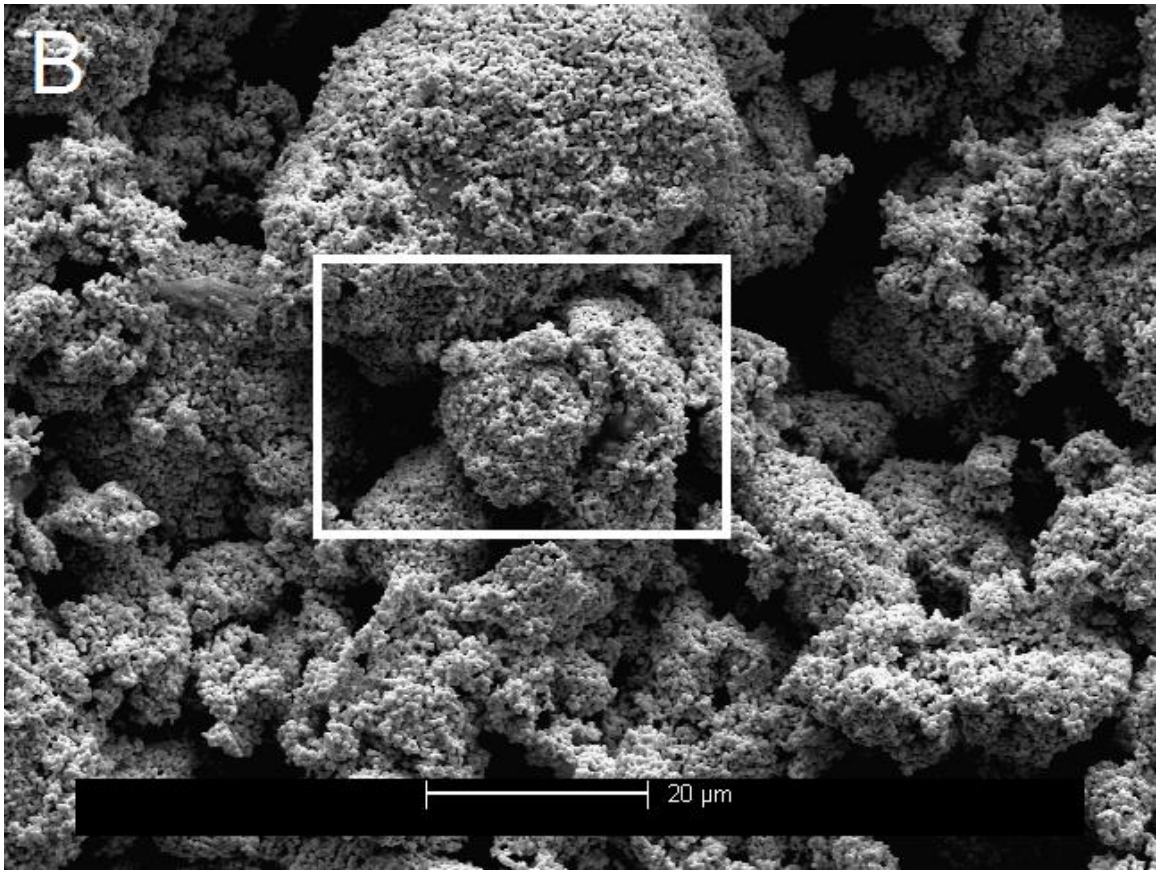

Figure B11. Used 0.5-0.8 micron gold powder (region B).

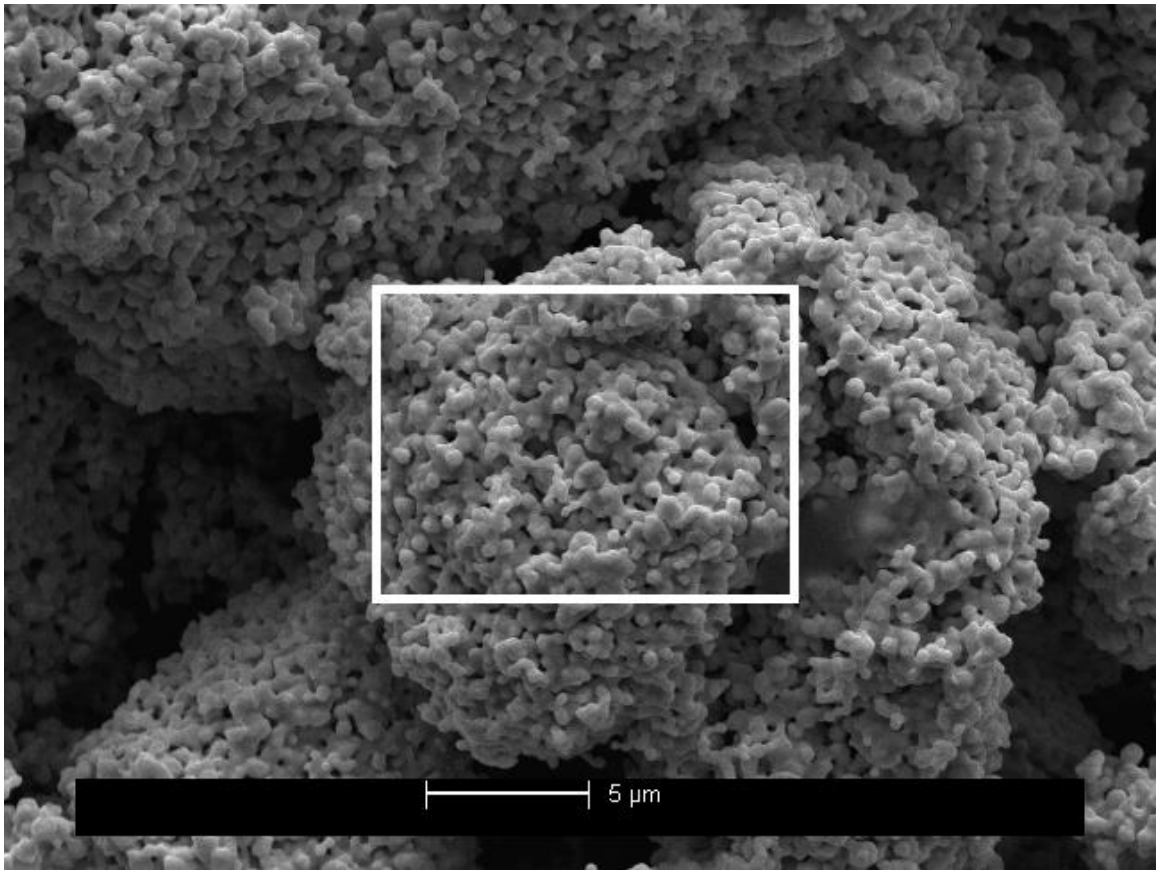

Figure B12. Used 0.5-0.8 micron gold powder (region B; boxed area in Figure B11).

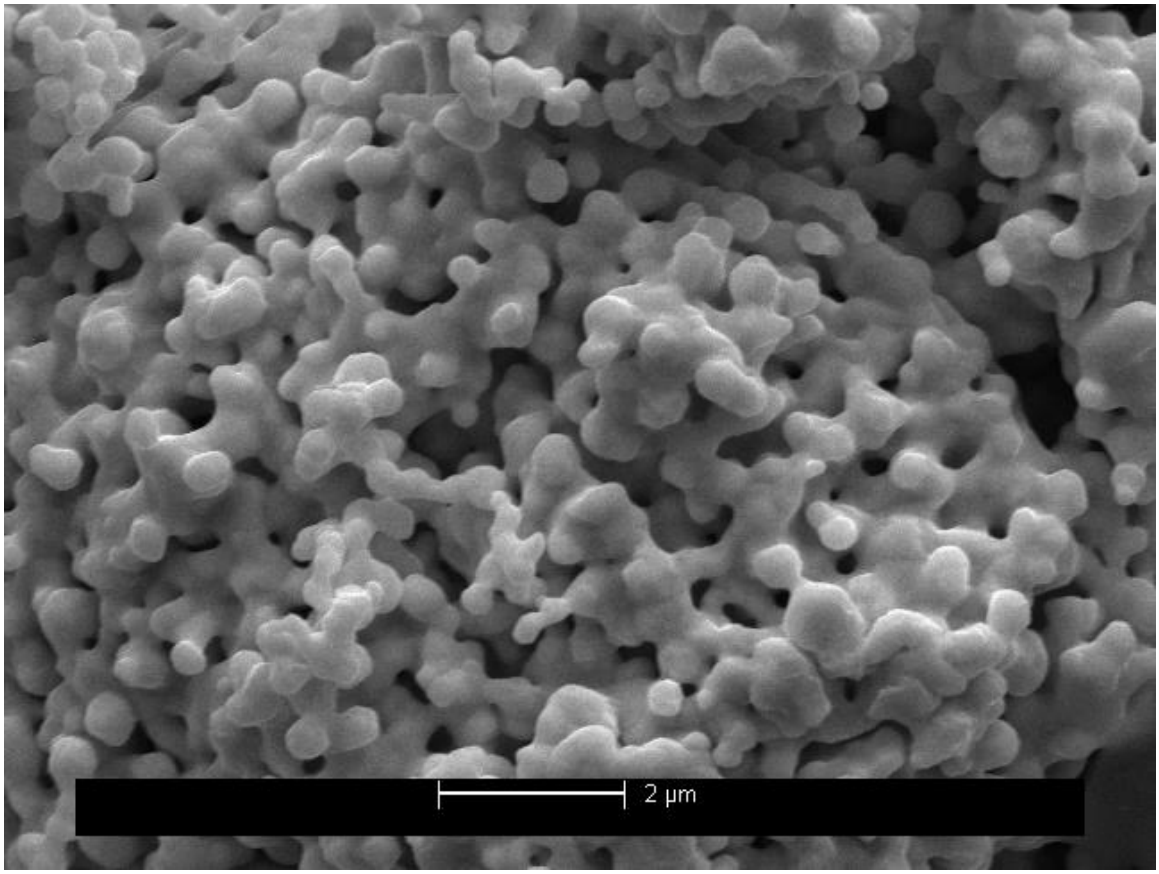

Figure B13. Used 0.5-0.8 micron gold powder (region B; boxed area in Figure B12).

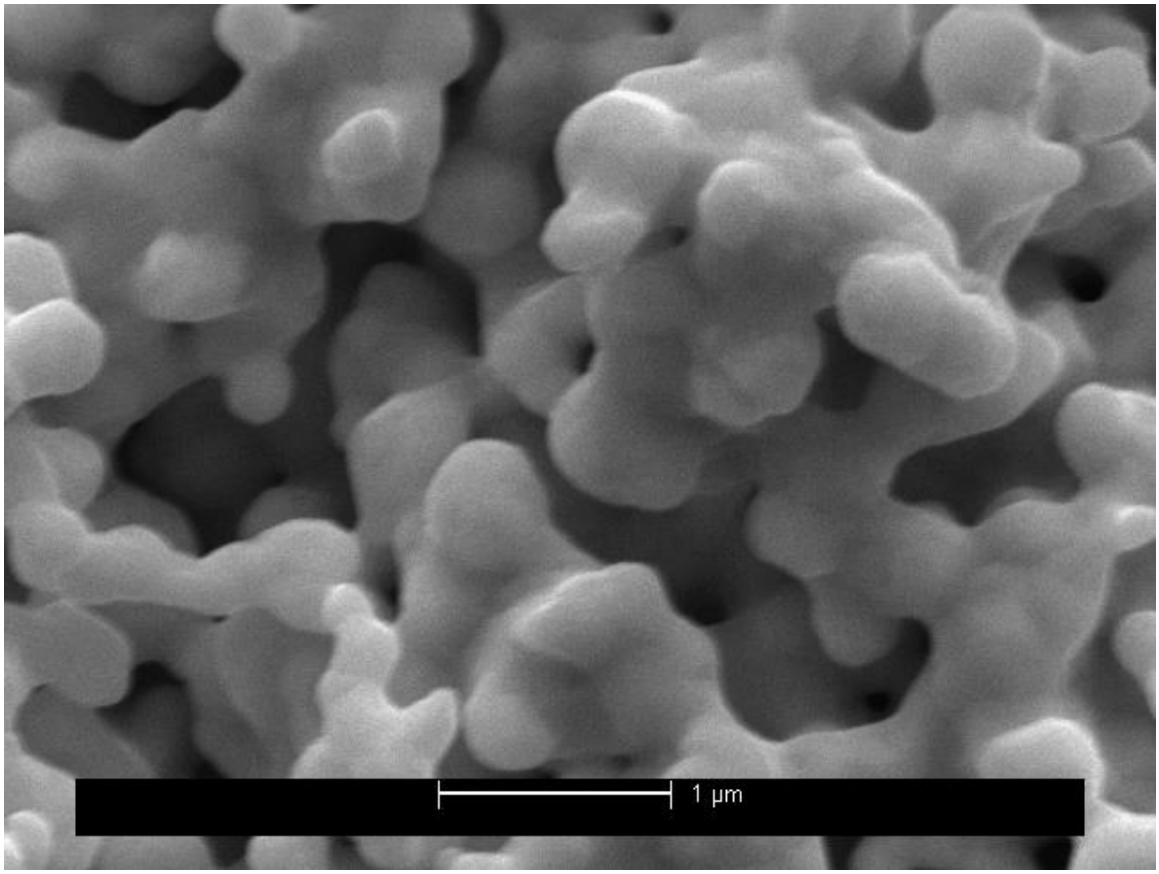

Figure B14. Used 0.5-0.8 micron gold powder (region B; zoomed in).

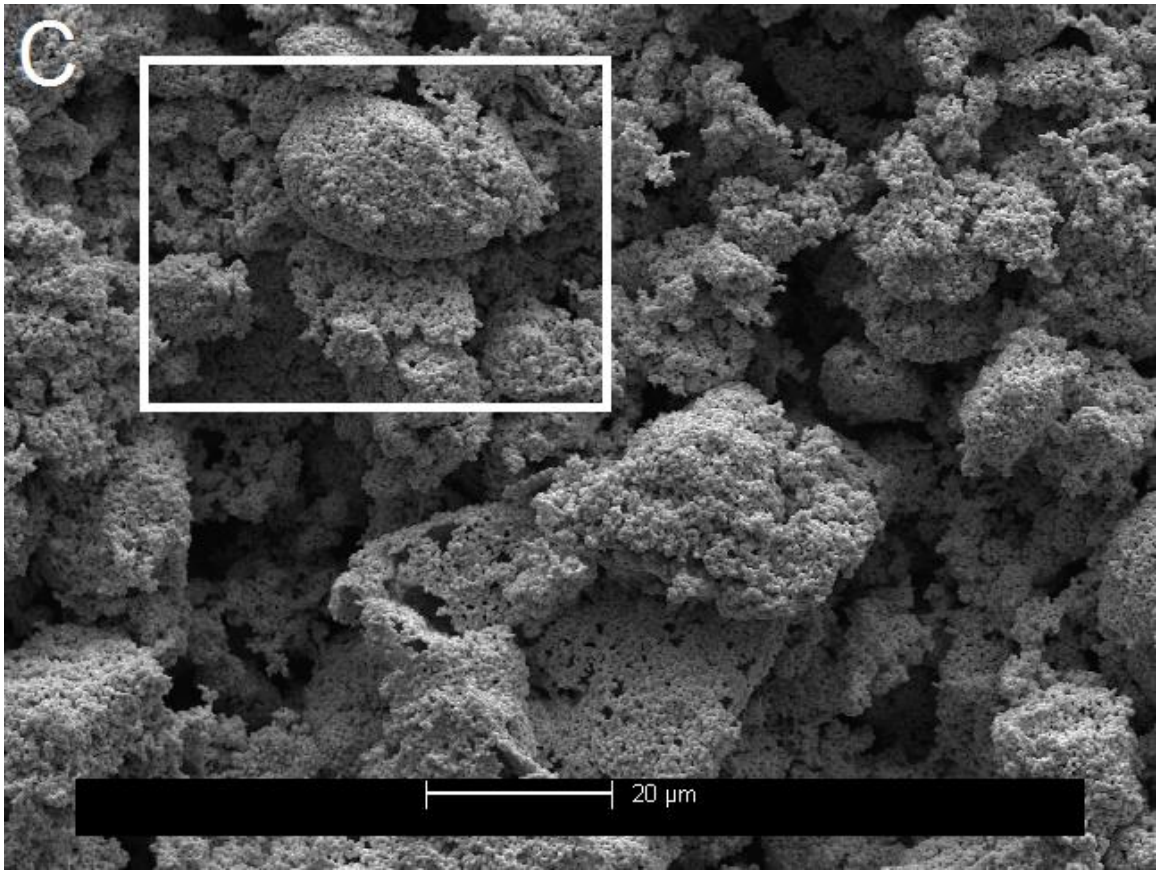

Figure B15. Used 0.5-0.8 micron gold powder (region C).

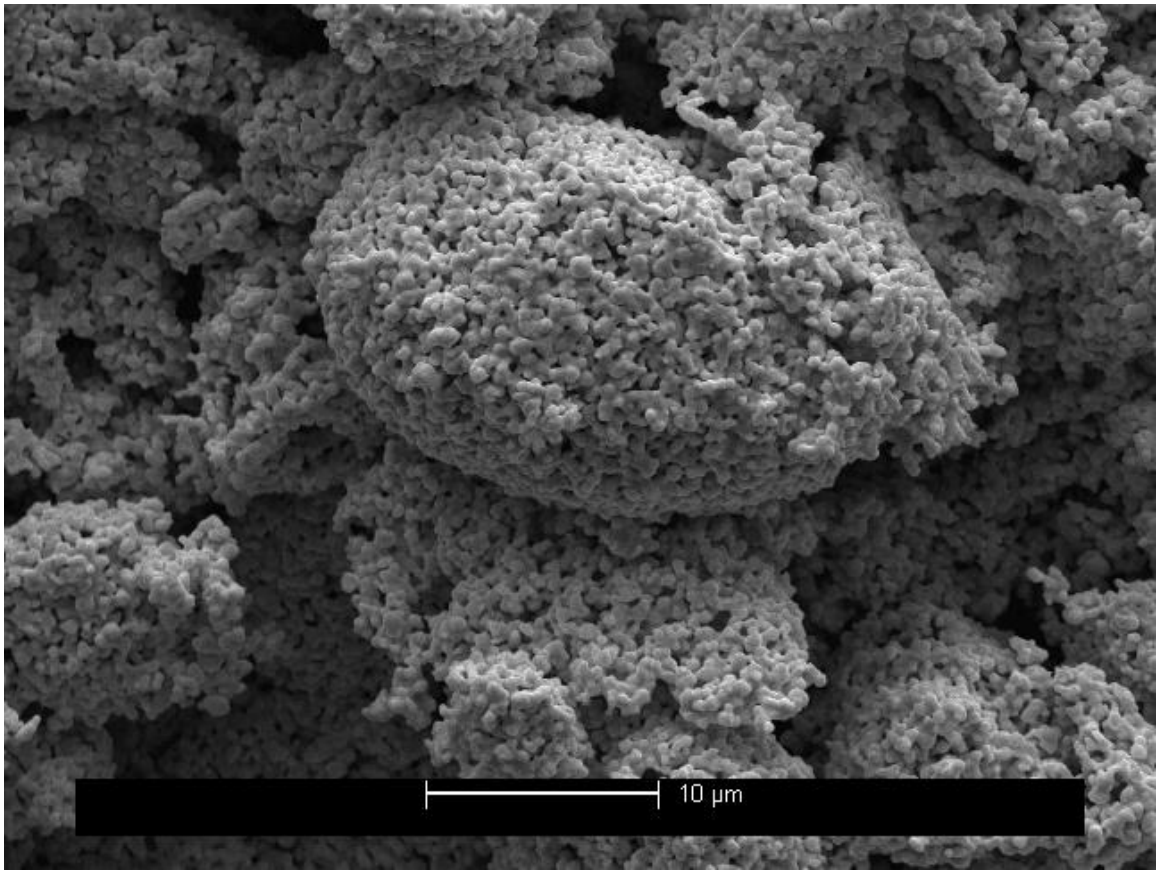

Figure B16. Used 0.5-0.8 micron gold powder (region C; boxed area in Figure B15).

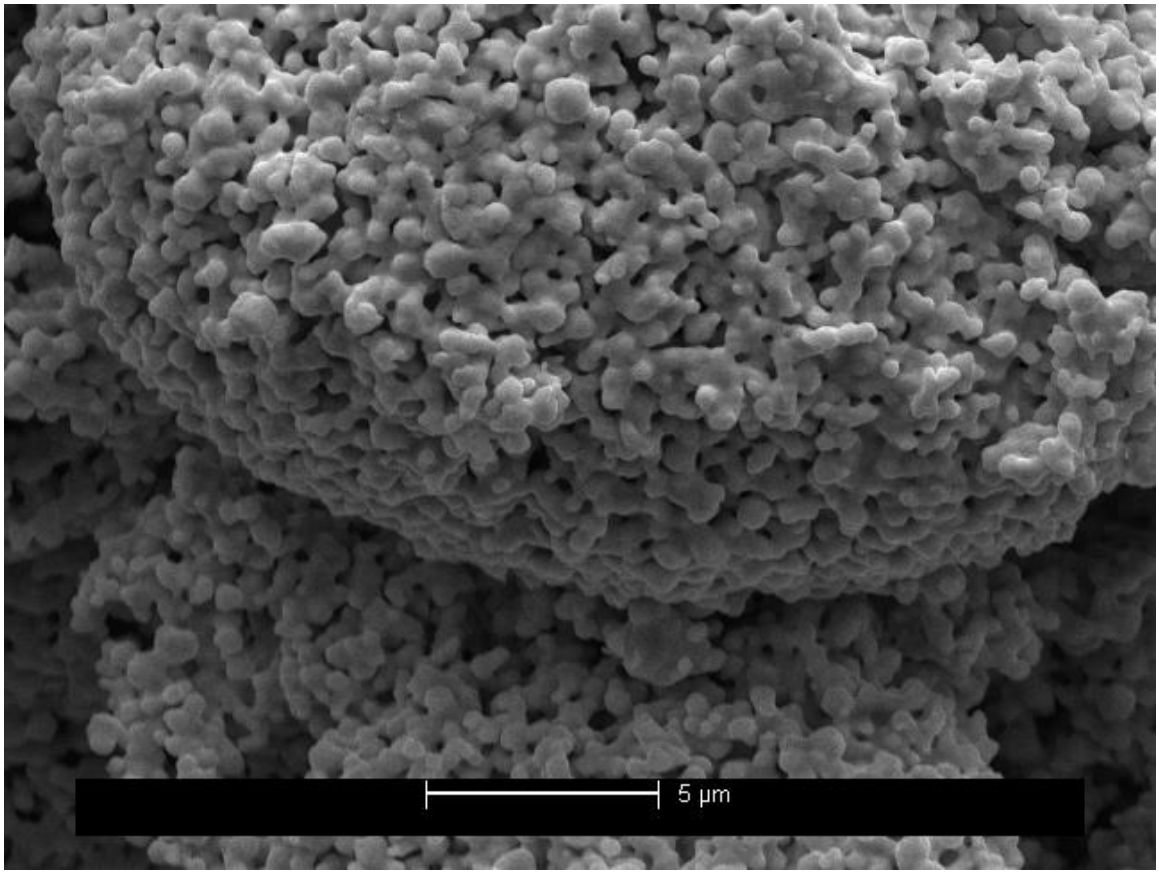

Figure B17. Used 0.5-0.8 micron gold powder (region C; zoomed in).

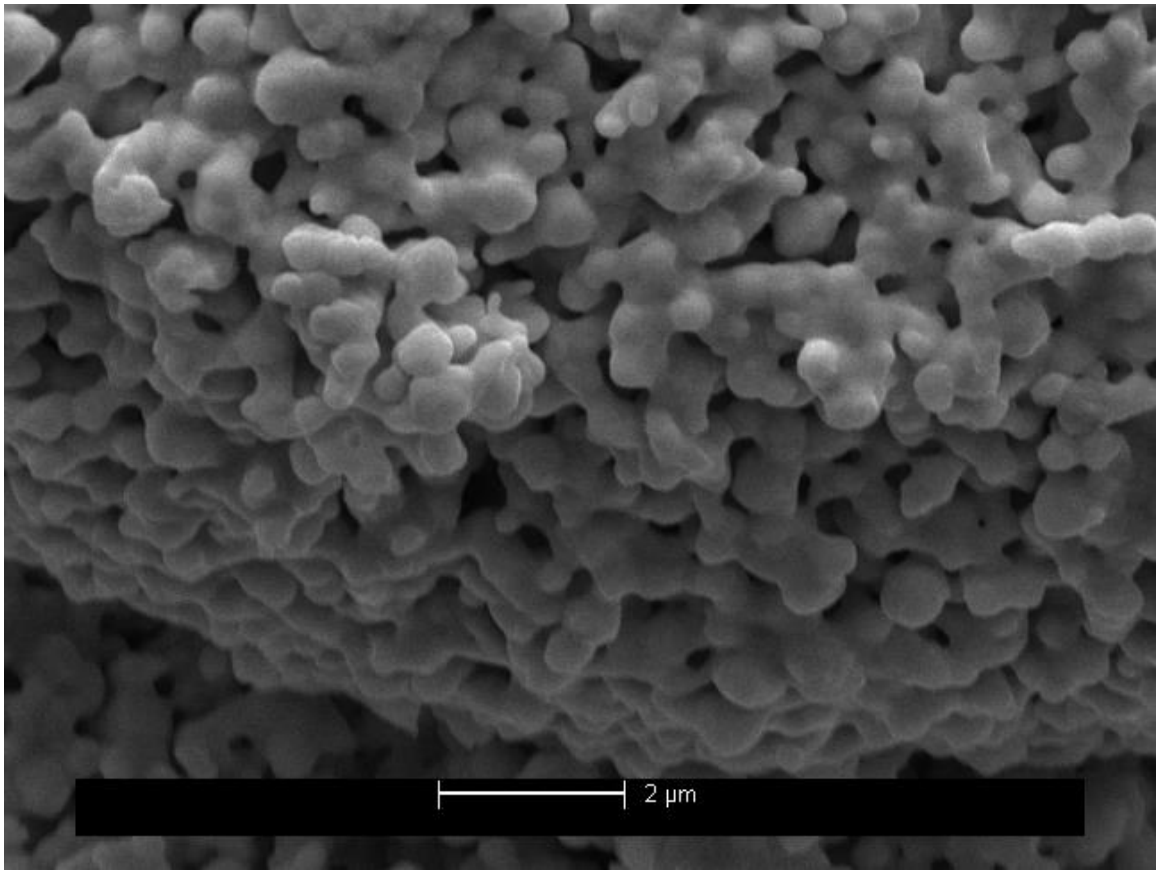

Figure B18. Used 0.5-0.8 micron gold powder (region C; zoomed in).

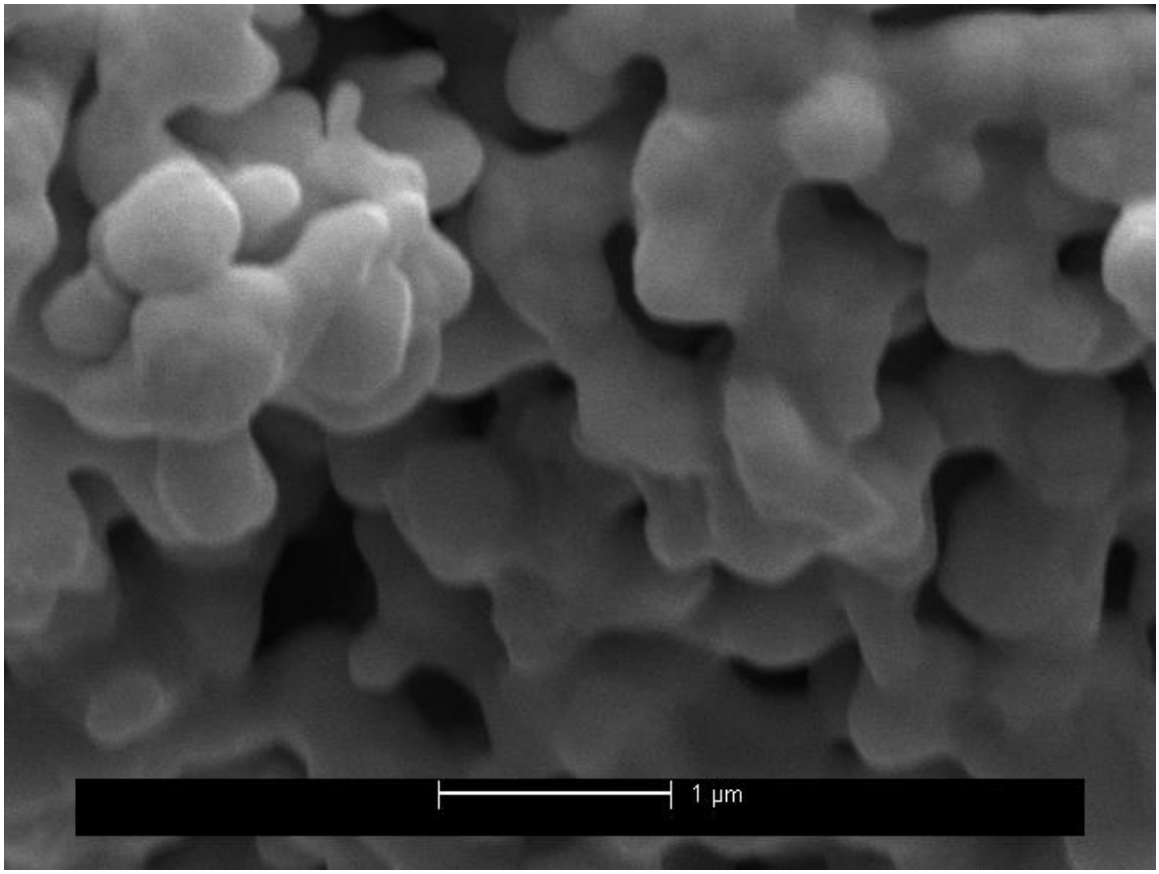

Figure B19. Used 0.5-0.8 micron gold powder (region C; zoomed in).

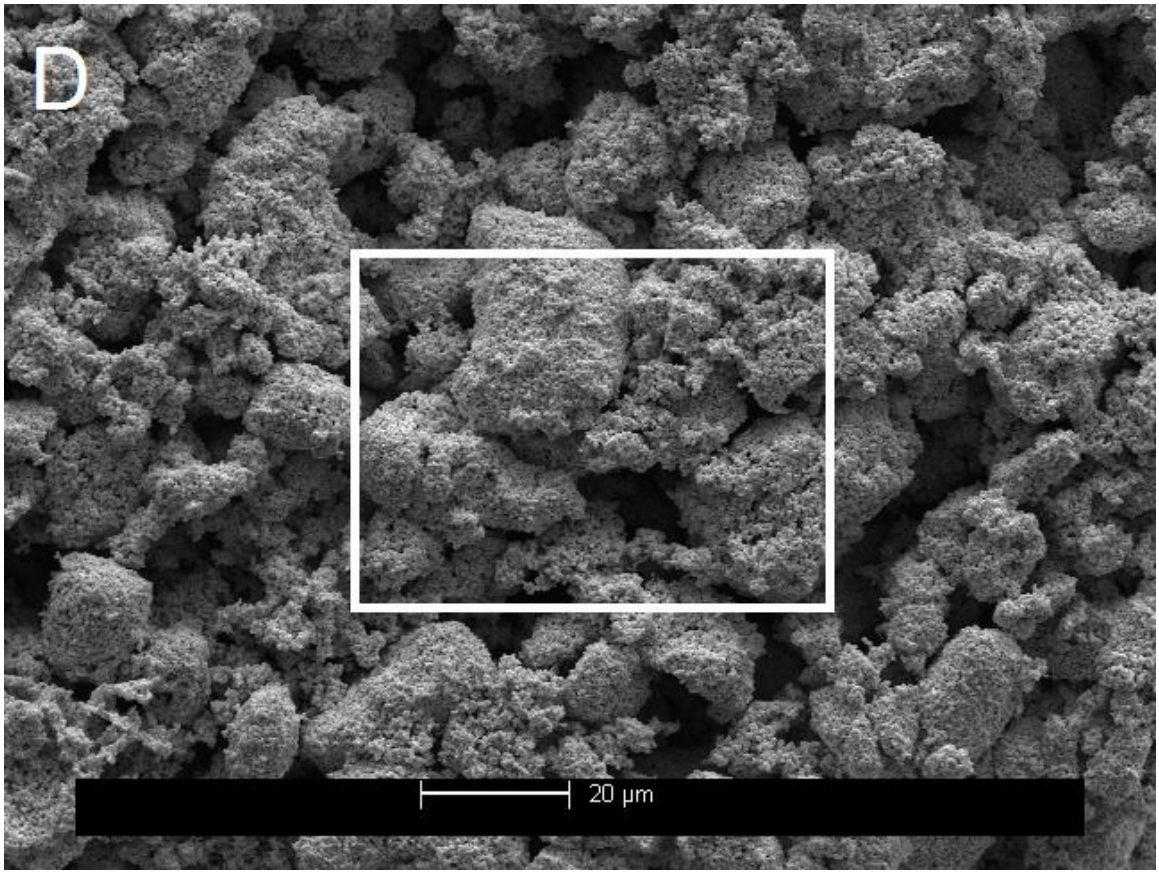

Figure B20. Used 0.5-0.8 micron gold powder (region D).

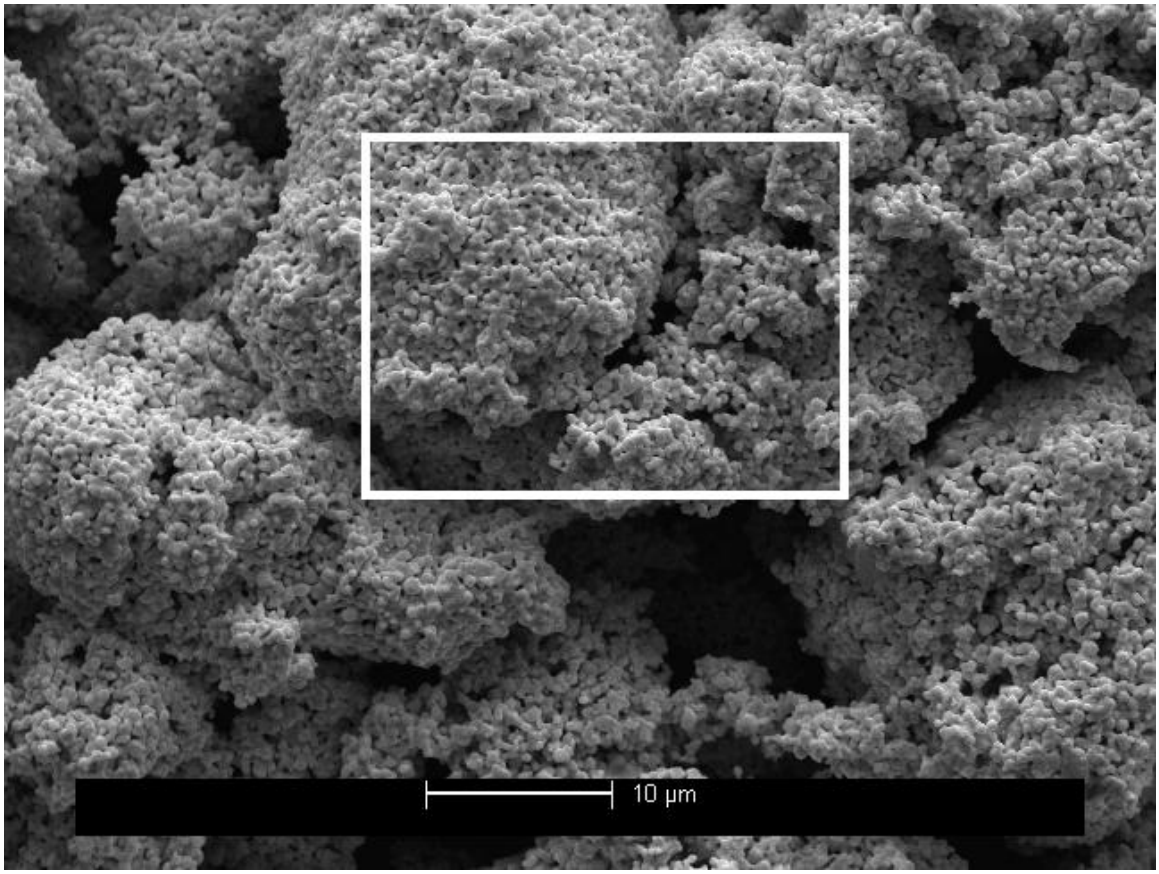

Figure B21. Used 0.5-0.8 micron gold powder (region D; boxed area in Figure B20).

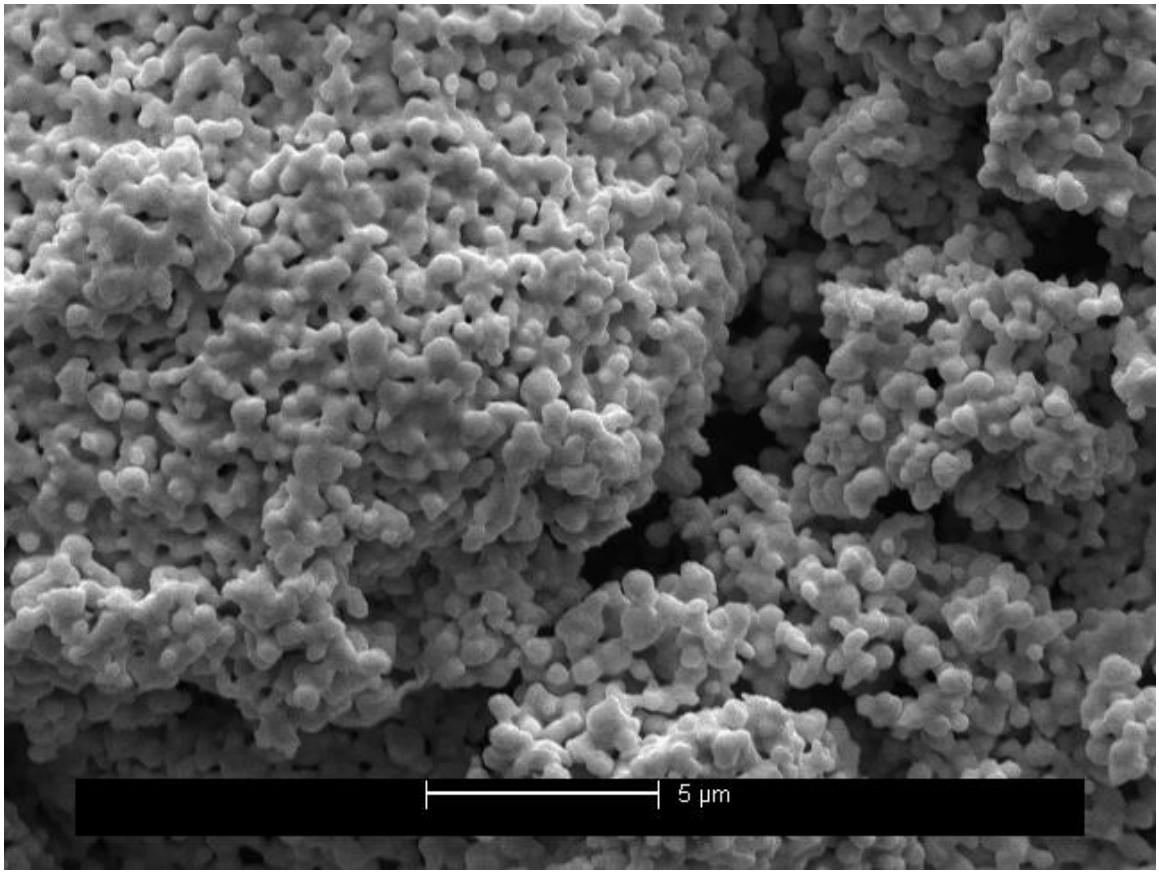

Figure B22. Used 0.5-0.8 micron gold powder (region D; boxed area in Figure B21).

SEM of new bulk gold

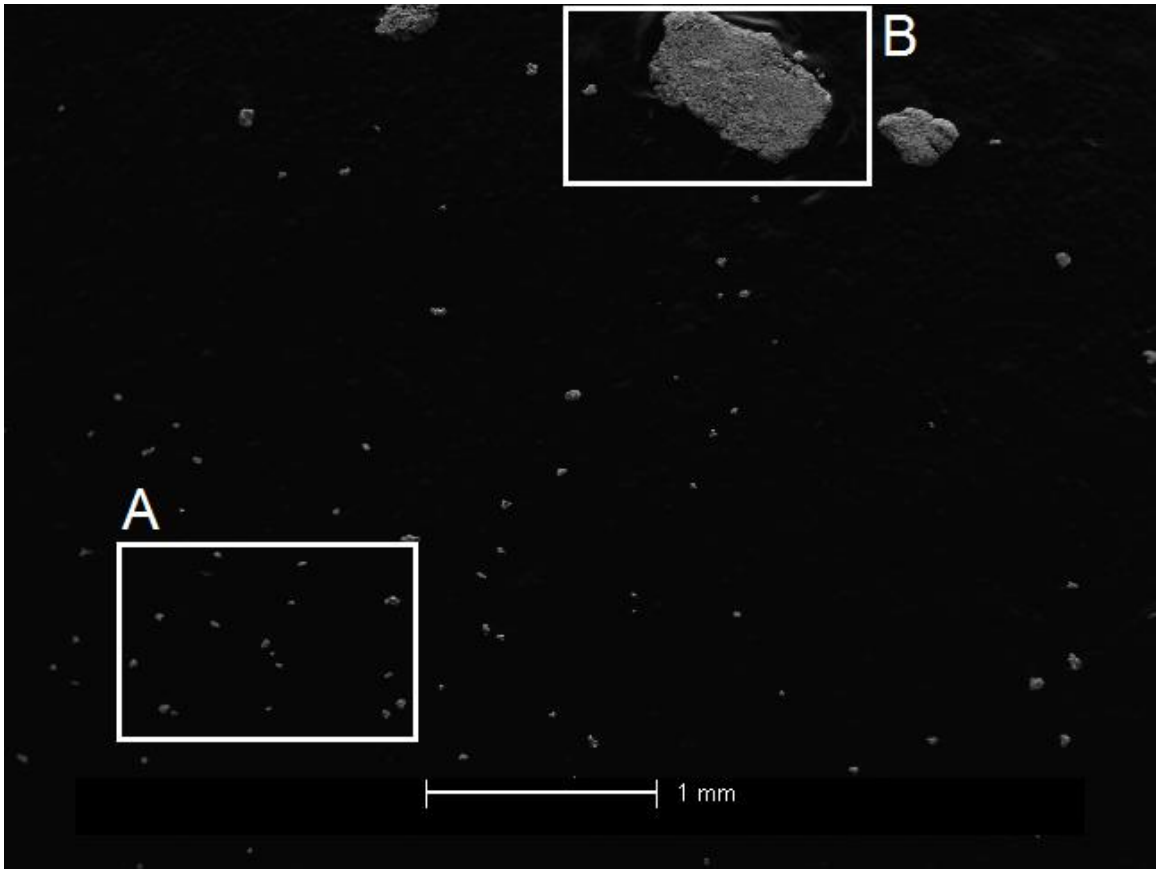

Figure B23. New bulk gold powder (broad view with regions indicated).

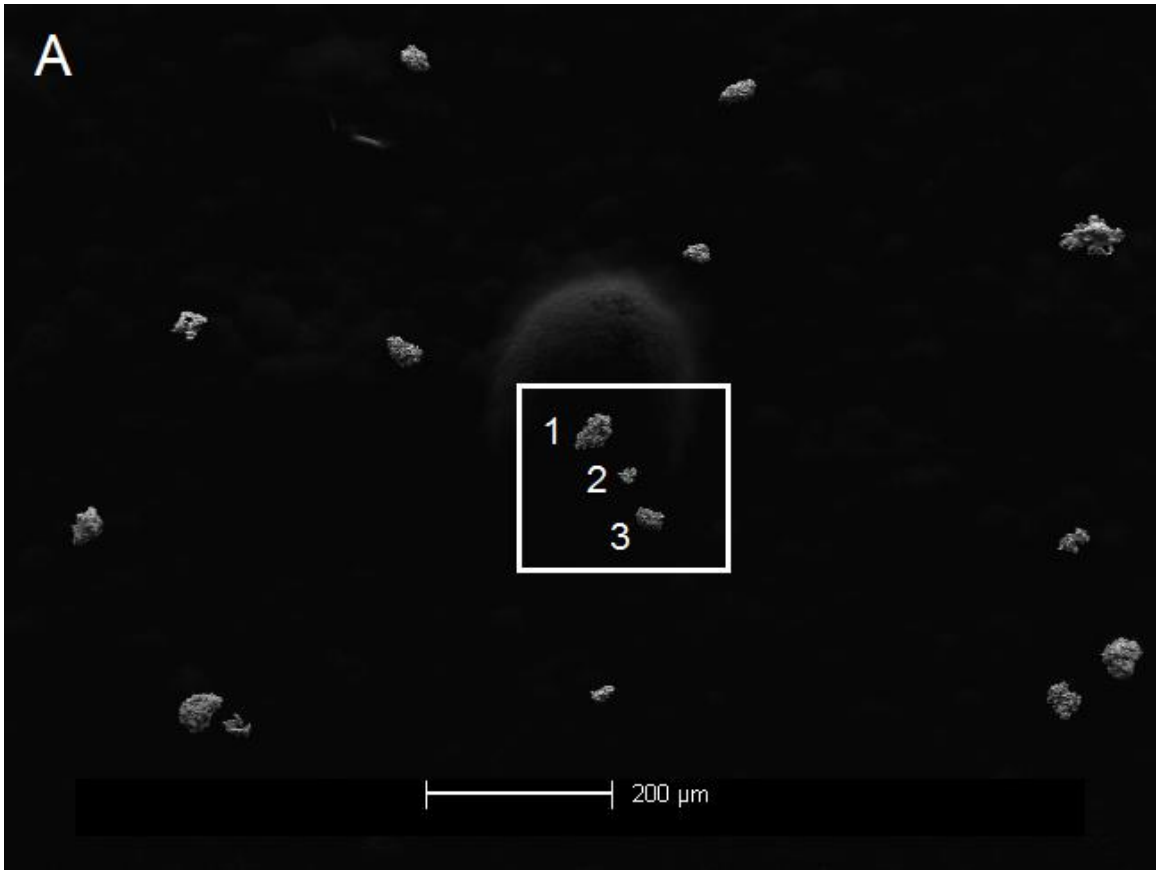

Figure B24. New bulk gold powder (region A).

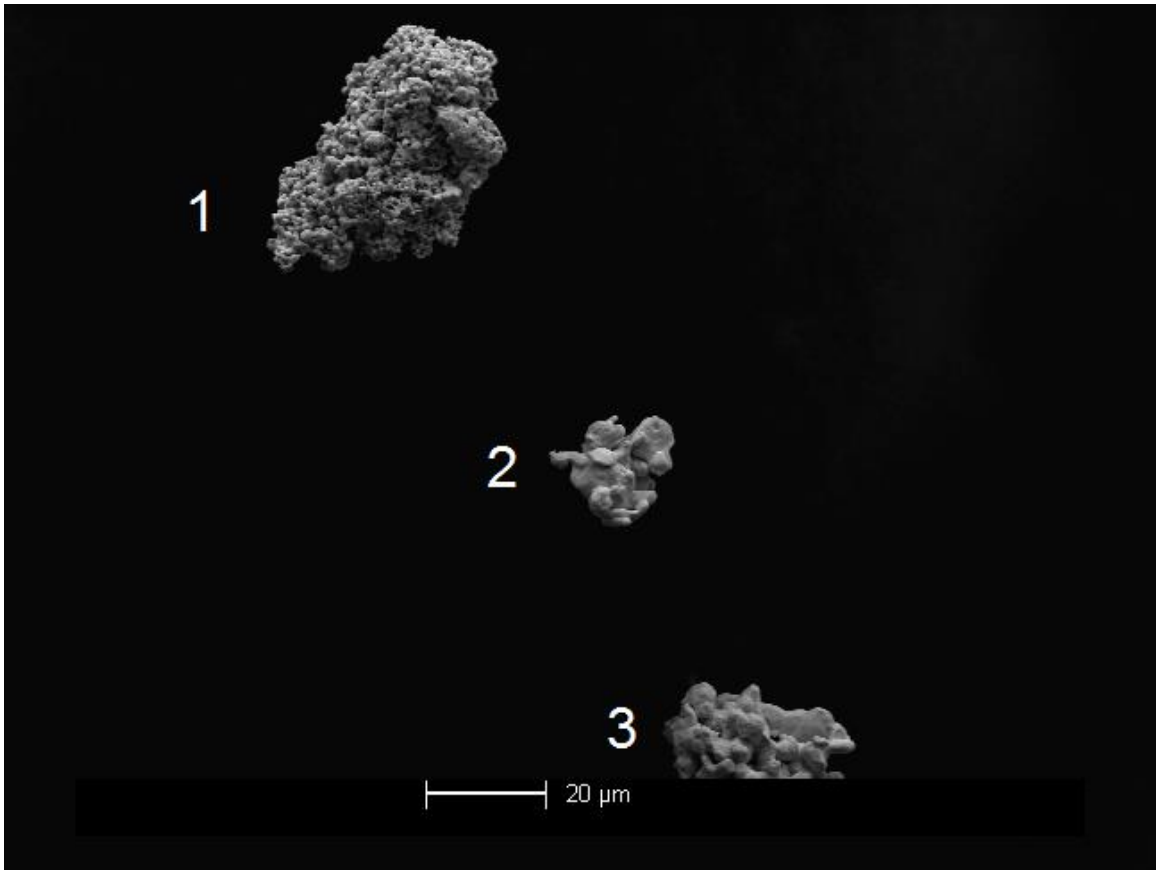

Figure B25. New bulk gold powder (region A; boxed area in Figure B24).

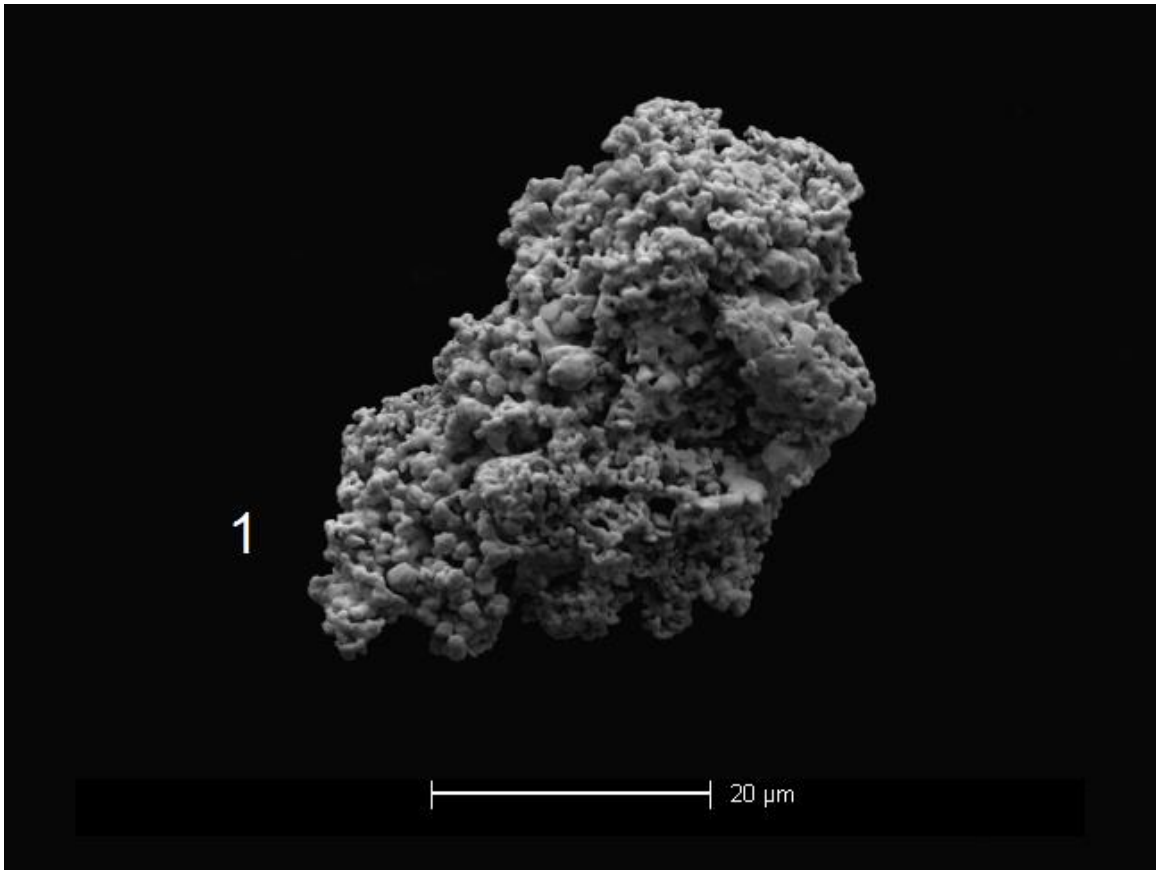

Figure B26. New bulk gold powder (region A; particle 1).

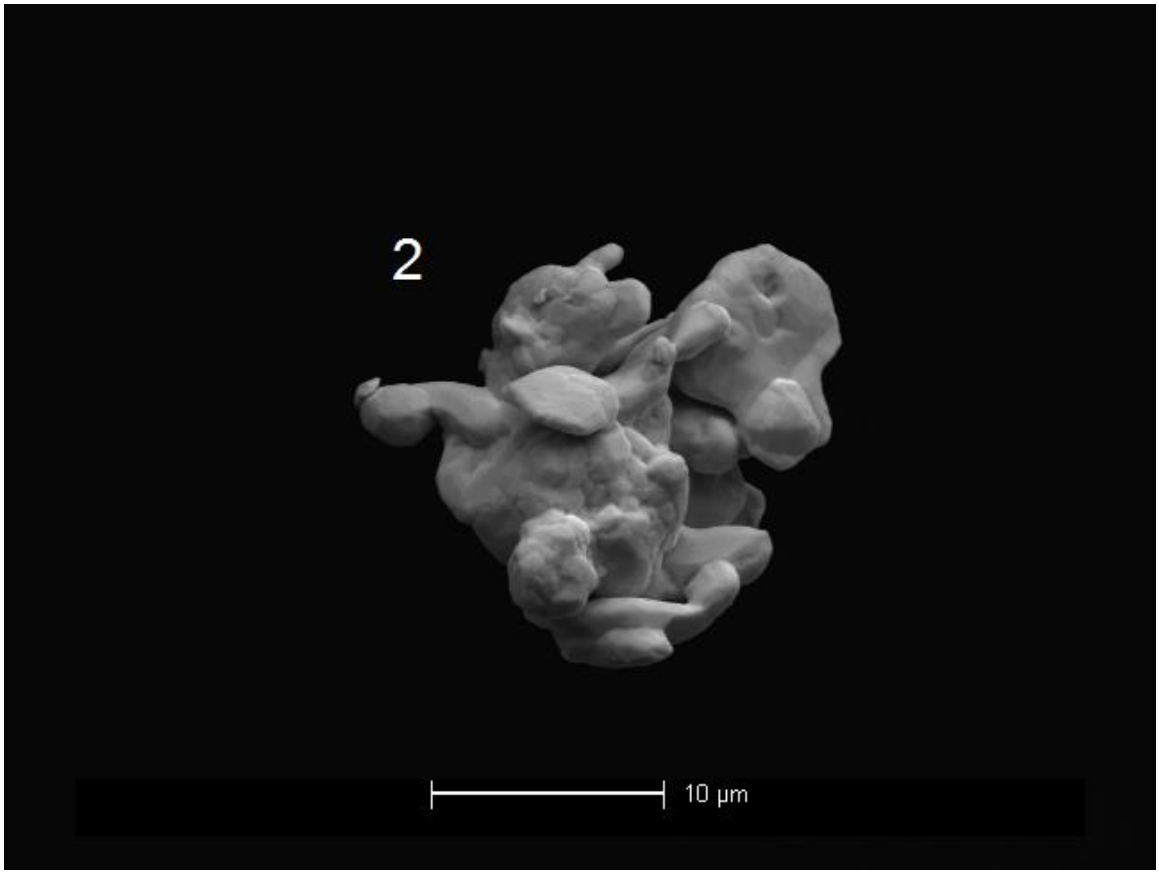

Figure B27. New bulk gold powder (region A; particle 2).

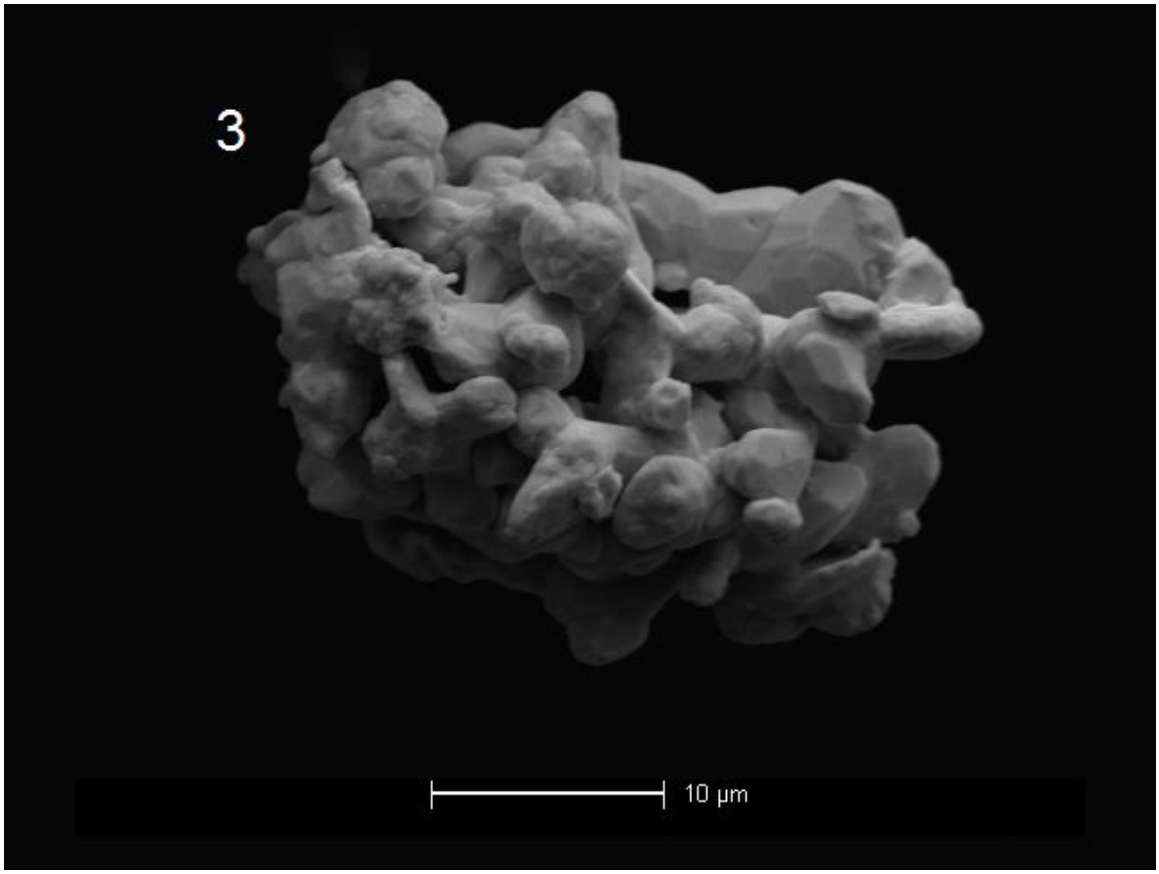

Figure B28. New bulk gold powder (region A; particle 3).

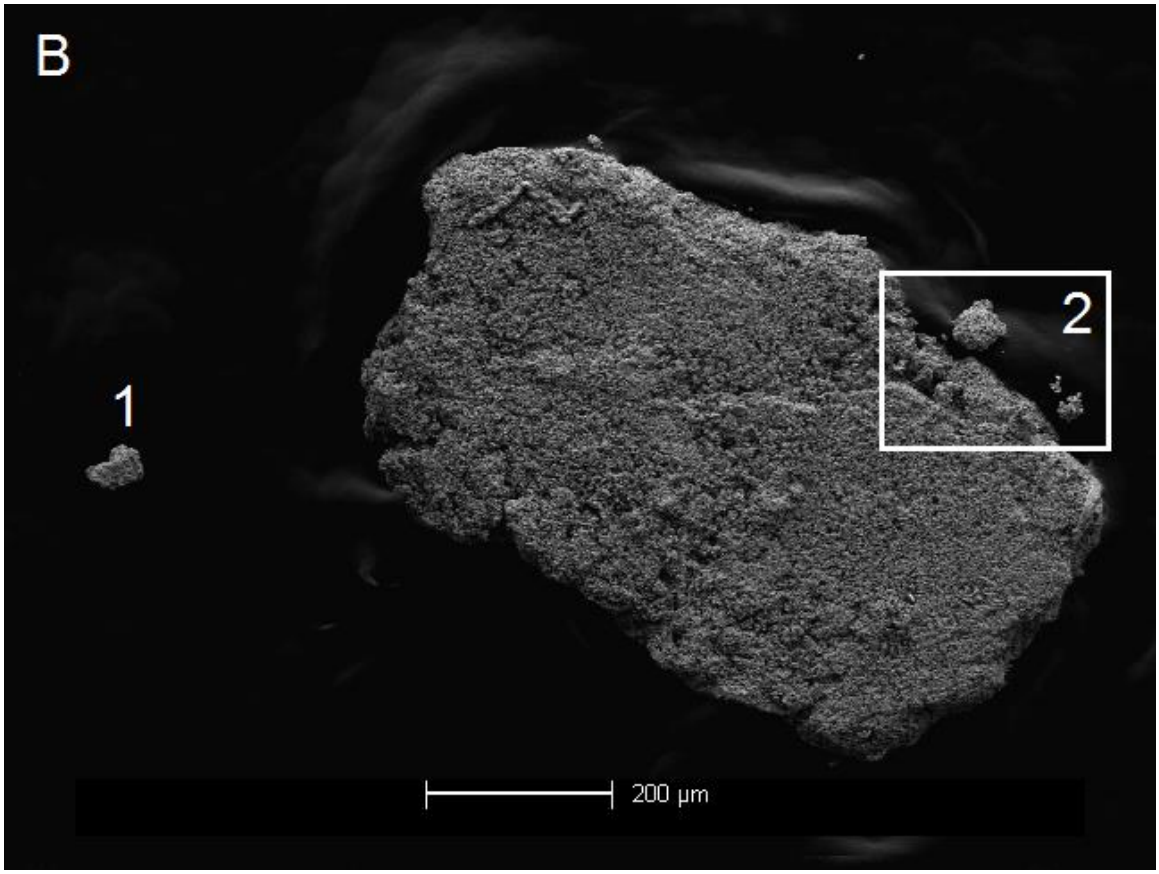

Figure B29. New bulk gold powder (region B).

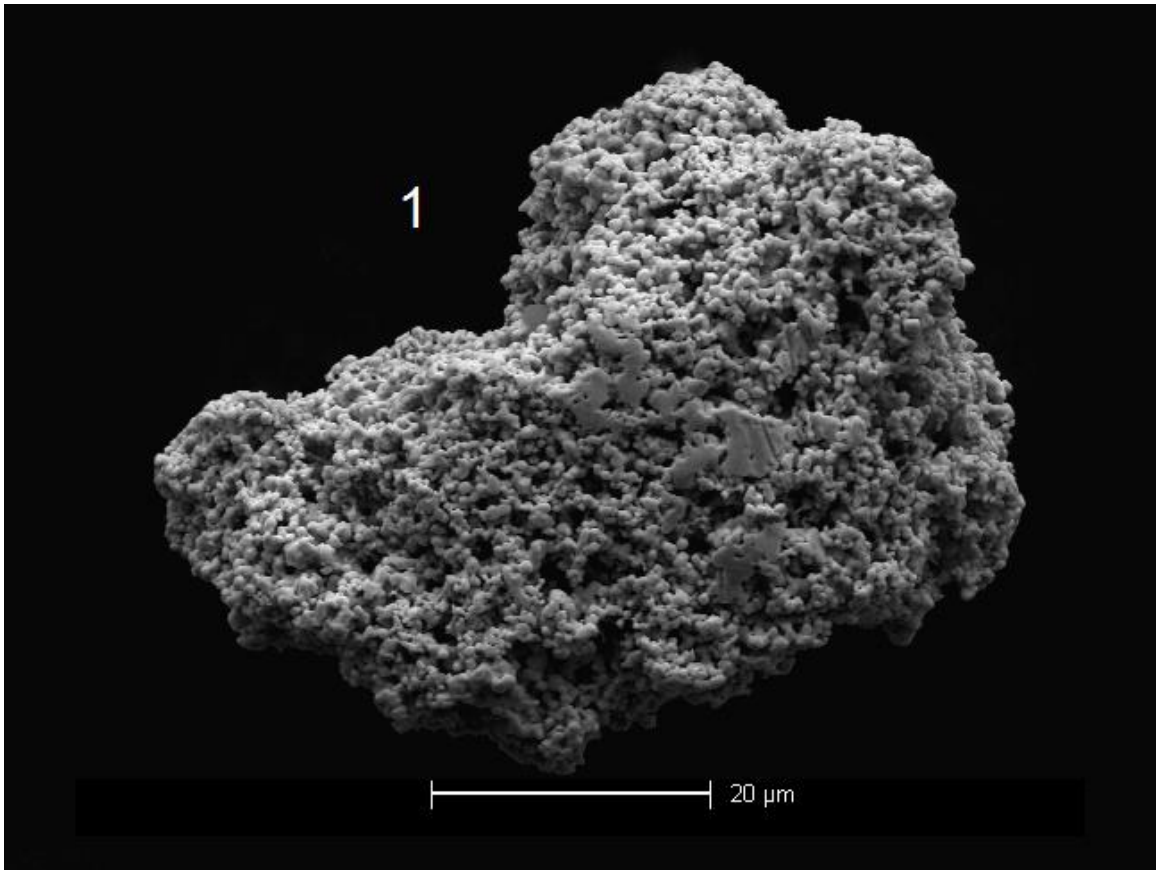

Figure B30. New bulk gold powder (region B; particle 1).

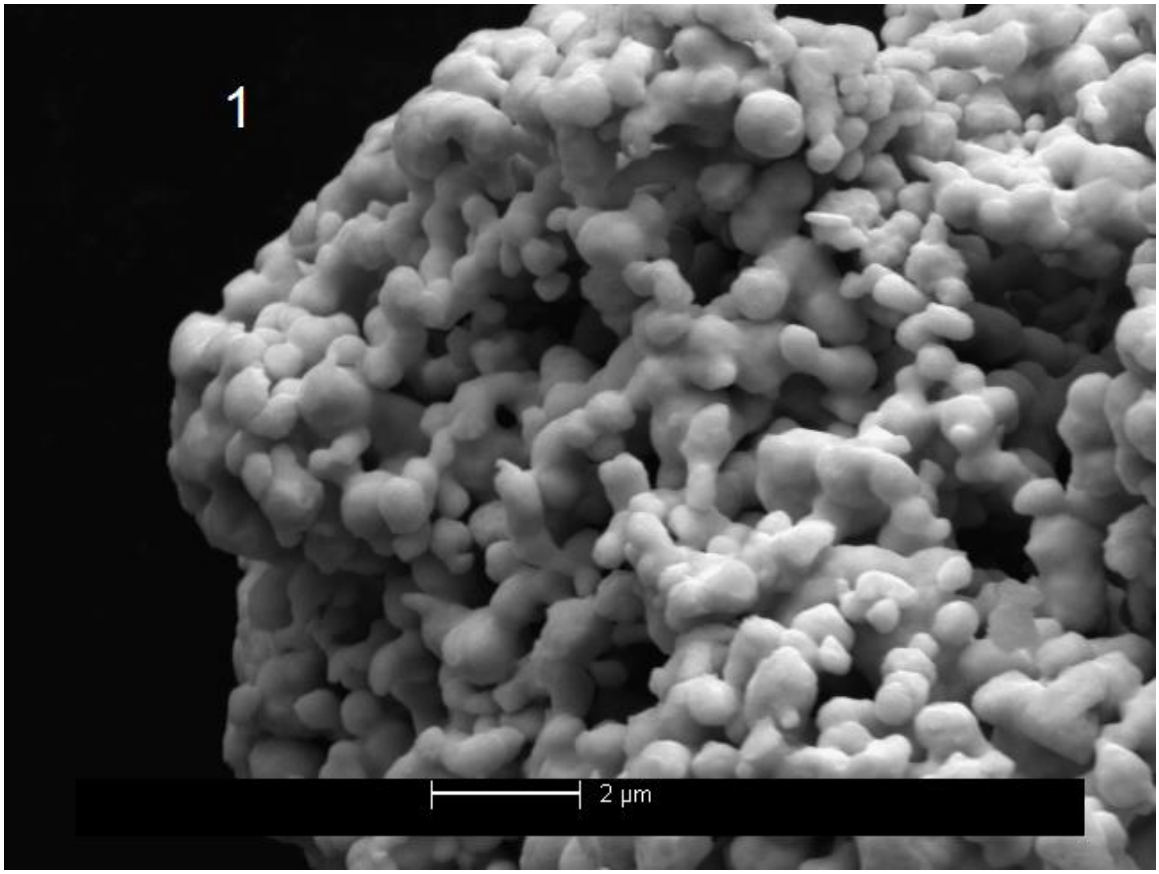

Figure B31. New bulk gold powder (region B; particle 1, zoomed in).

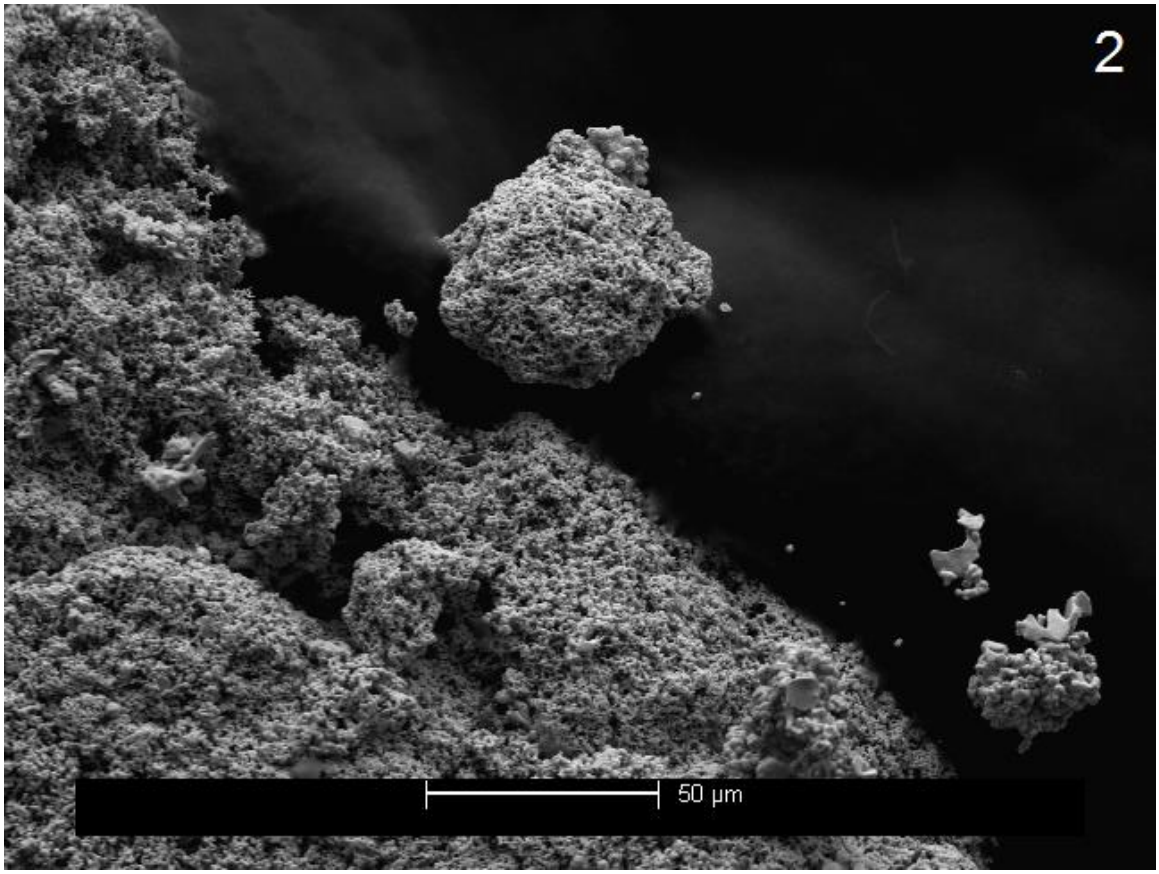

Figure B32. New bulk gold powder (region B; area 2).

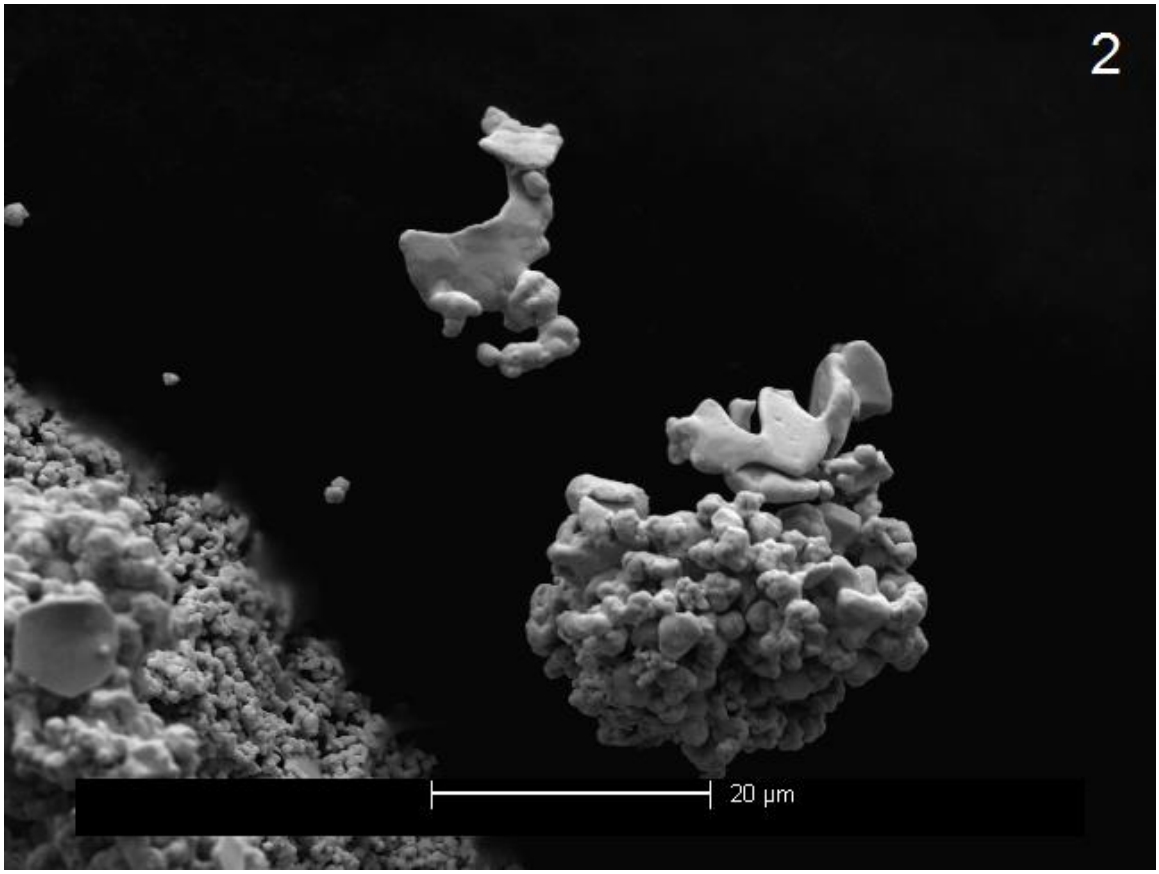

Figure B33. New bulk gold powder (region B; area 2, zoomed in).

SEM of used bulk gold

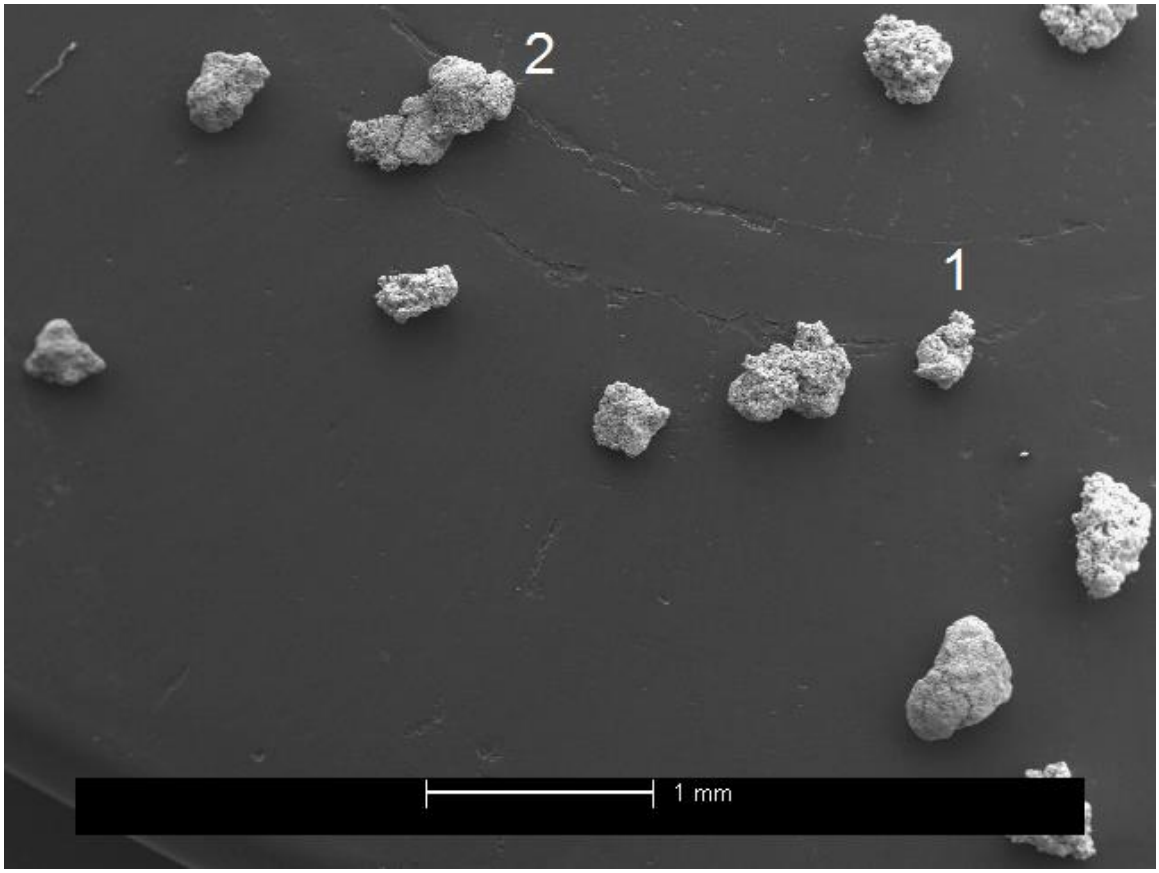

Figure B34. Used bulk gold powder (broad view with selected particles indicated).

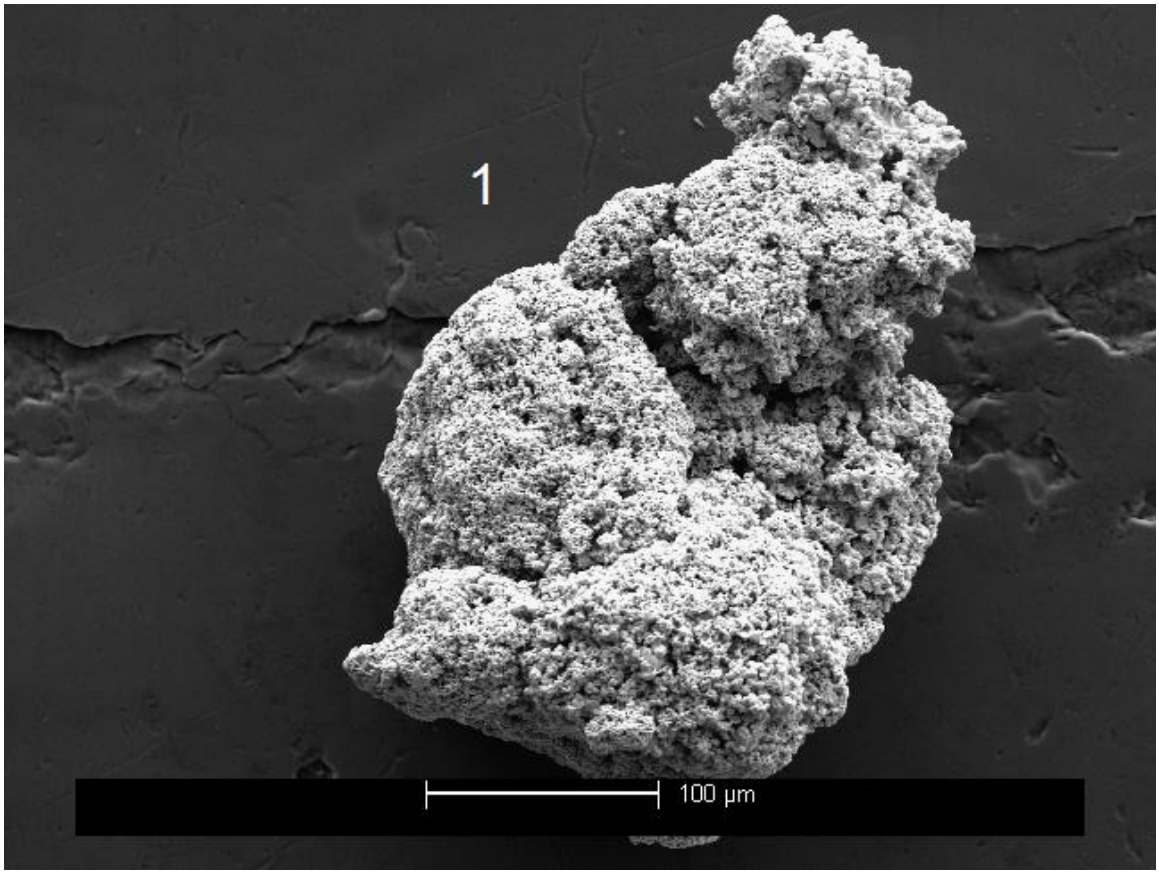

Figure B35. Used bulk gold powder (particle 1 in Figure B34).

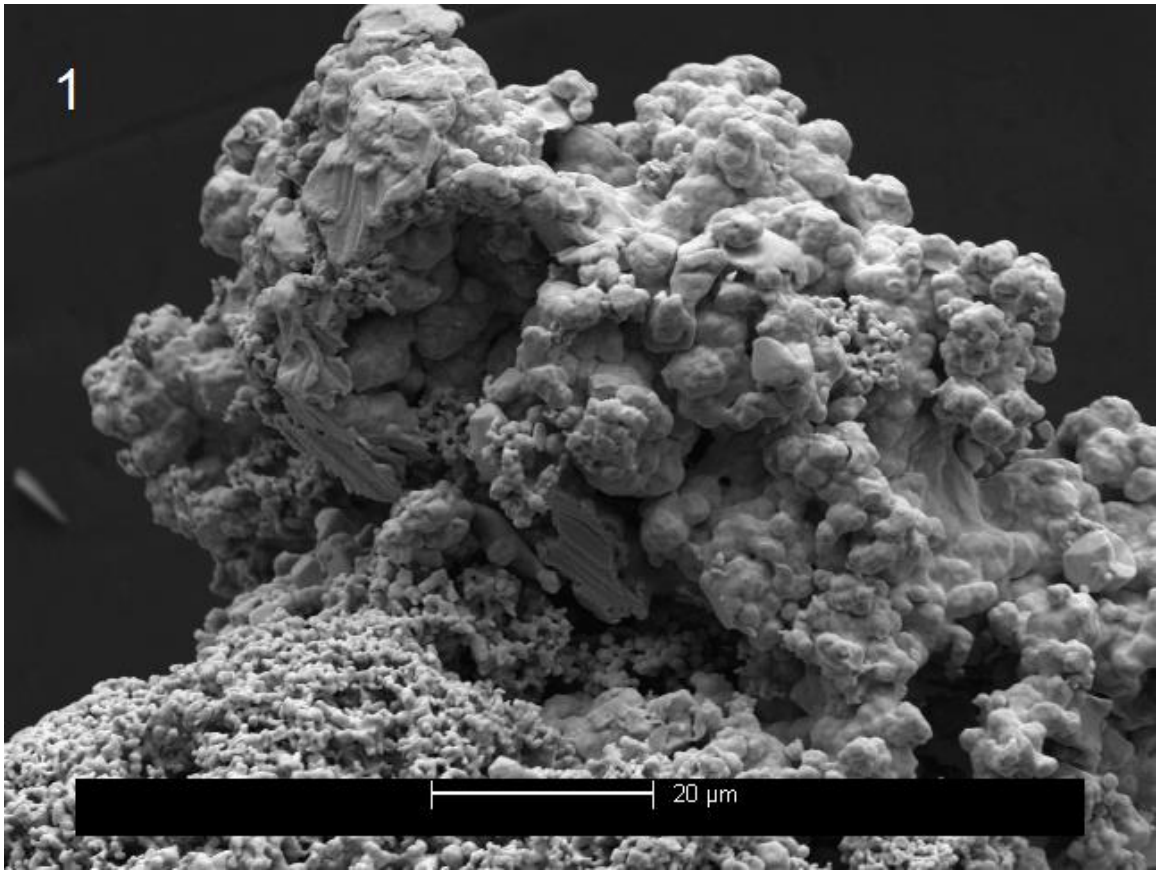

Figure B36. Used bulk gold powder (particle 1 in Figure B34, zoomed in).

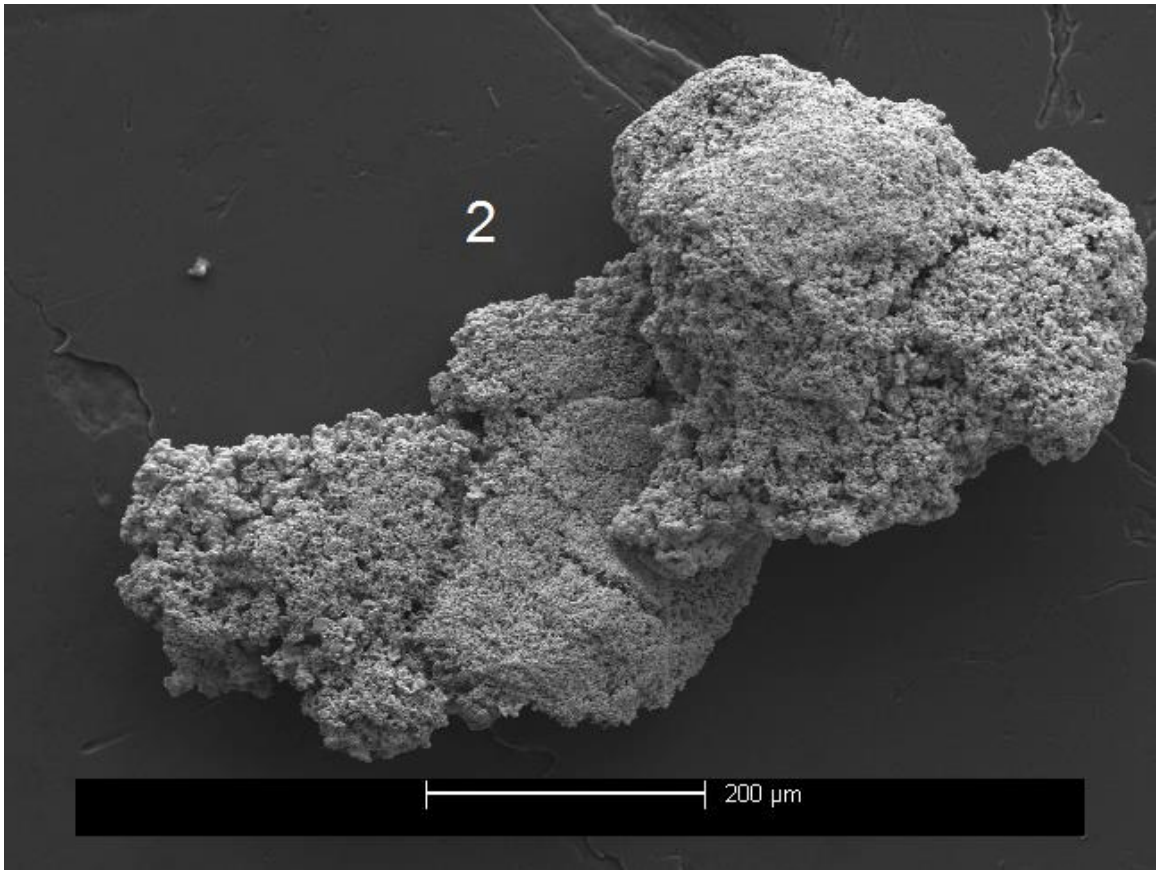

Figure B37. Used bulk gold powder (particle 2 in Figure B34).

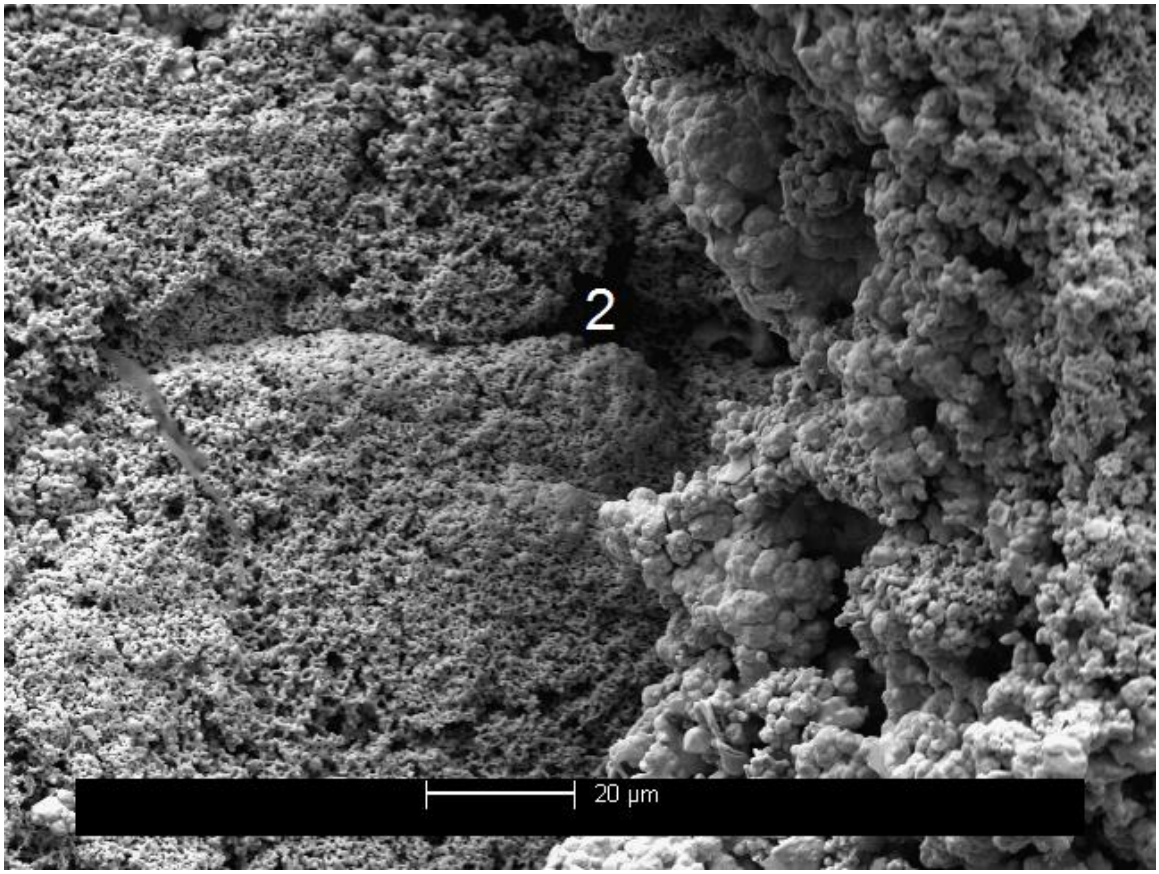

Figure B38. Used bulk gold powder (particle 2 in Figure B34, zoomed in).

APPENDIX C

SAMPLE CHROMATOGRAM FROM BENZALDEHYDE EXPERIMENTS

(300 °C, 453 HOURS)

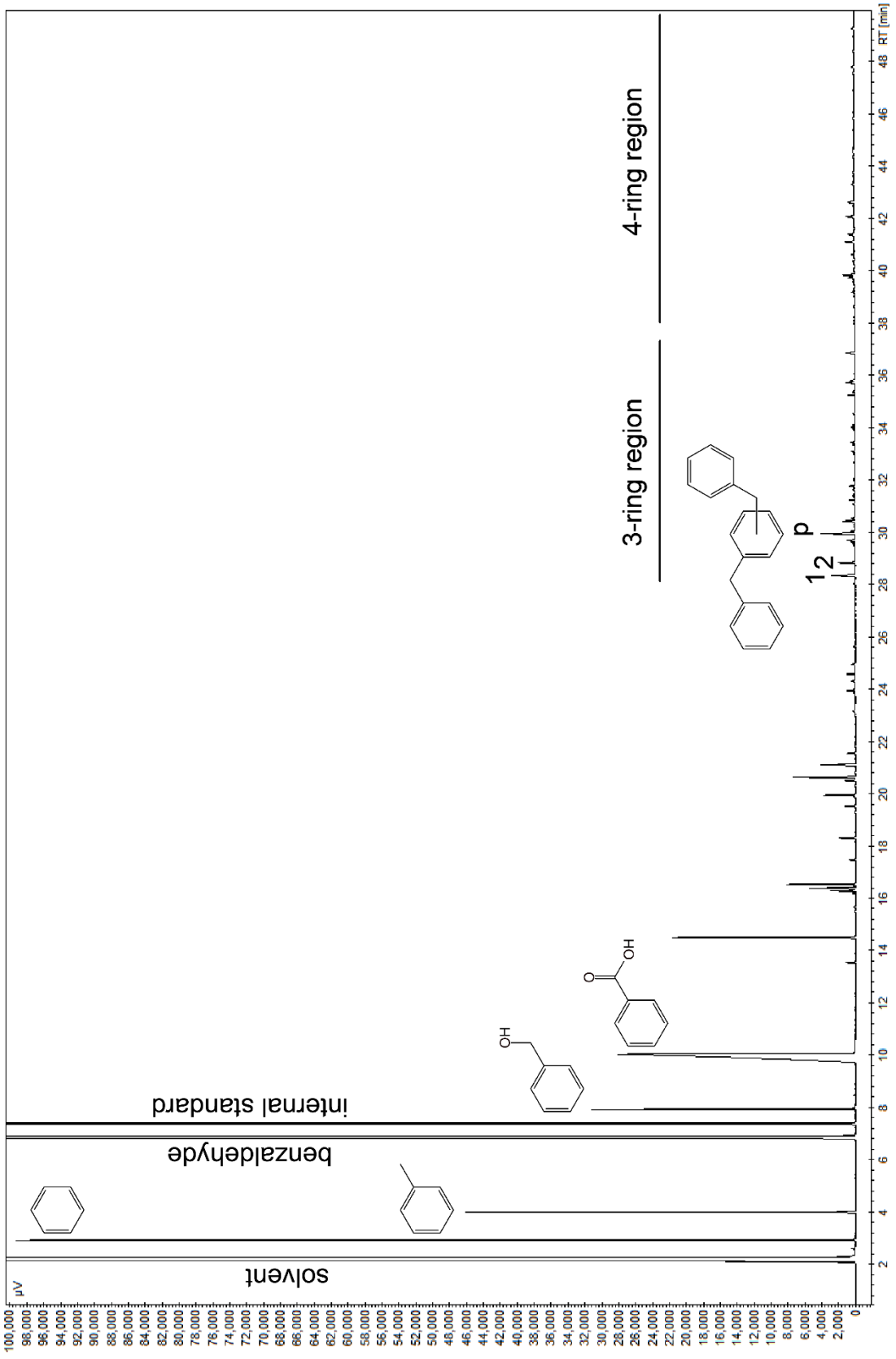
solvent
benzaldehyde
internal standard
3-ring region
4-ring region
1
2
p
OH
O
OH
µV
RT [min]

Figure C1. Typical chromatogram from benzaldehyde experiments (300 °C, 0.1 molal starting concentration, 453 hours). Selected peaks are labelled with the structure of the analyte; isomers of dibenzylbenzene are labelled as dibenzylbenzene-1, dibenzylbenzene-2, or *para*-dibenylbenzene (i.e., 1,4-dibenzylbenzene) corresponding to Table 8. Approximate three-ring and four-ring regions are indicated with horizontal bars.

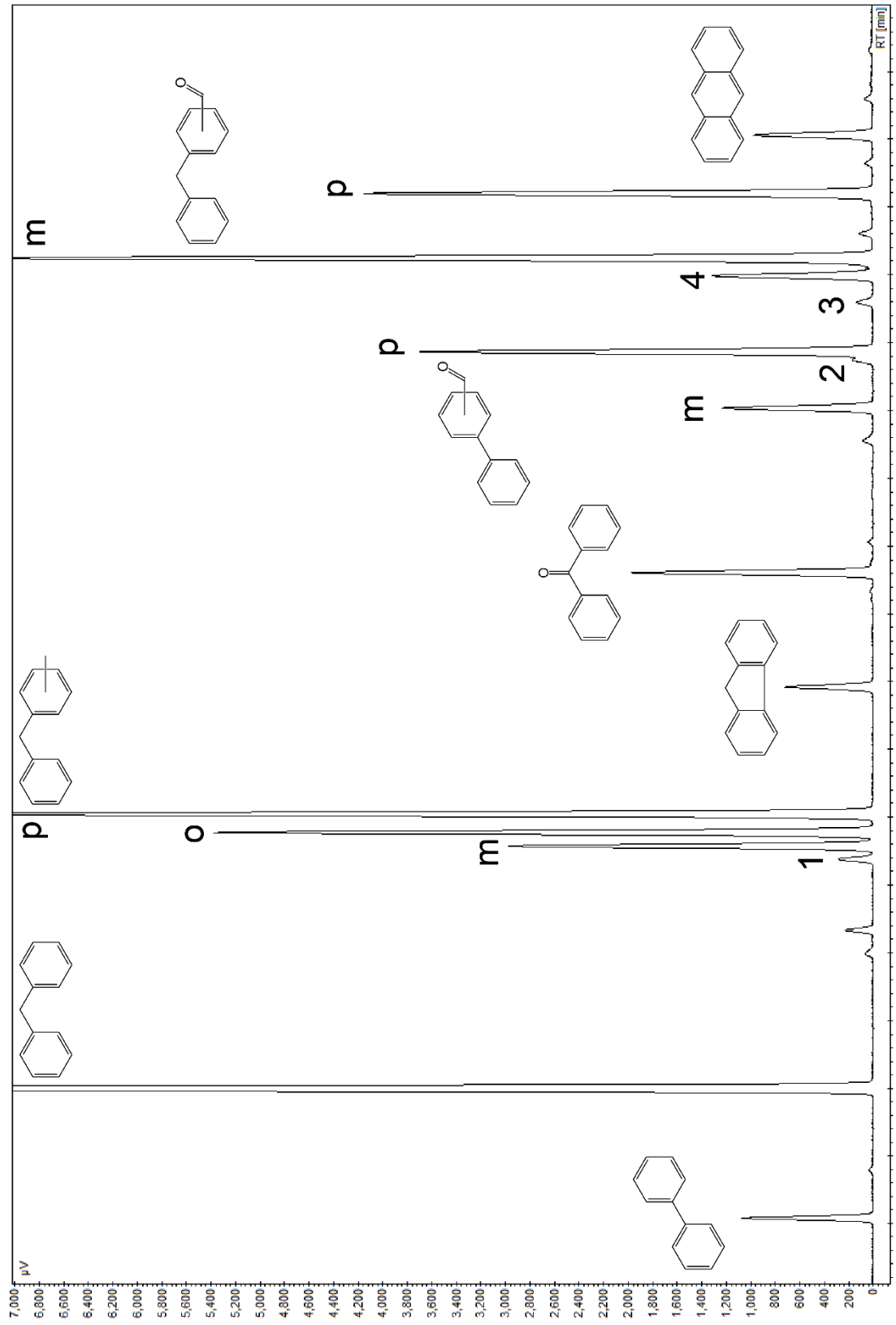
μV
RT [min]
p
o
m
1
p
m
2
3
4
p
m

Figure C2. Two-ring region of chromatogram in Figure C1 with the structure of identified analytes indicated. Isomers are labelled as ortho, meta, or para. Numbered peaks are as follows: 1, bibenzyl; 2, *trans*-stilbene; 3, phenylacetophenone; 4, 9-fluorenone.

BIOGRAPHICAL SKETCH

Kristopher Michael Fecteau was born July 22nd, 1986 in Portland, Maine, United States, the first child of Timothy and Karen Fecteau of Westbrook, Maine. He attended Westbrook public schools (Prides Corner, Congin, Wescott Jr. High, and Westbrook High) graduating 12th in the class of 2004. Initially attending the University of Maine (Orono), he transferred to the University of Southern Maine (USM) in Portland, graduating *summa cum laude* with a Bachelor of Science degree in biology in 2008. He then also earned a Bachelor of Science degree in chemistry *summa cum laude* in 2009 at USM before beginning a doctor of philosophy program in chemistry at Arizona State University. He is a member of the TriBeta, GoldenKey, and PhiKappaPhi honor societies as well as the American Chemical Society and American Geophysical Union.